CHARACTERIZATION OF BIOTHERAPEUTIC PRODUCTS

EDITED BY: Anurag S. Rathore, Christopher Mark Smales and Andras Guttman
PUBLISHED IN: Frontiers in Bioengineering and Biotechnology and
Frontiers in Chemistry

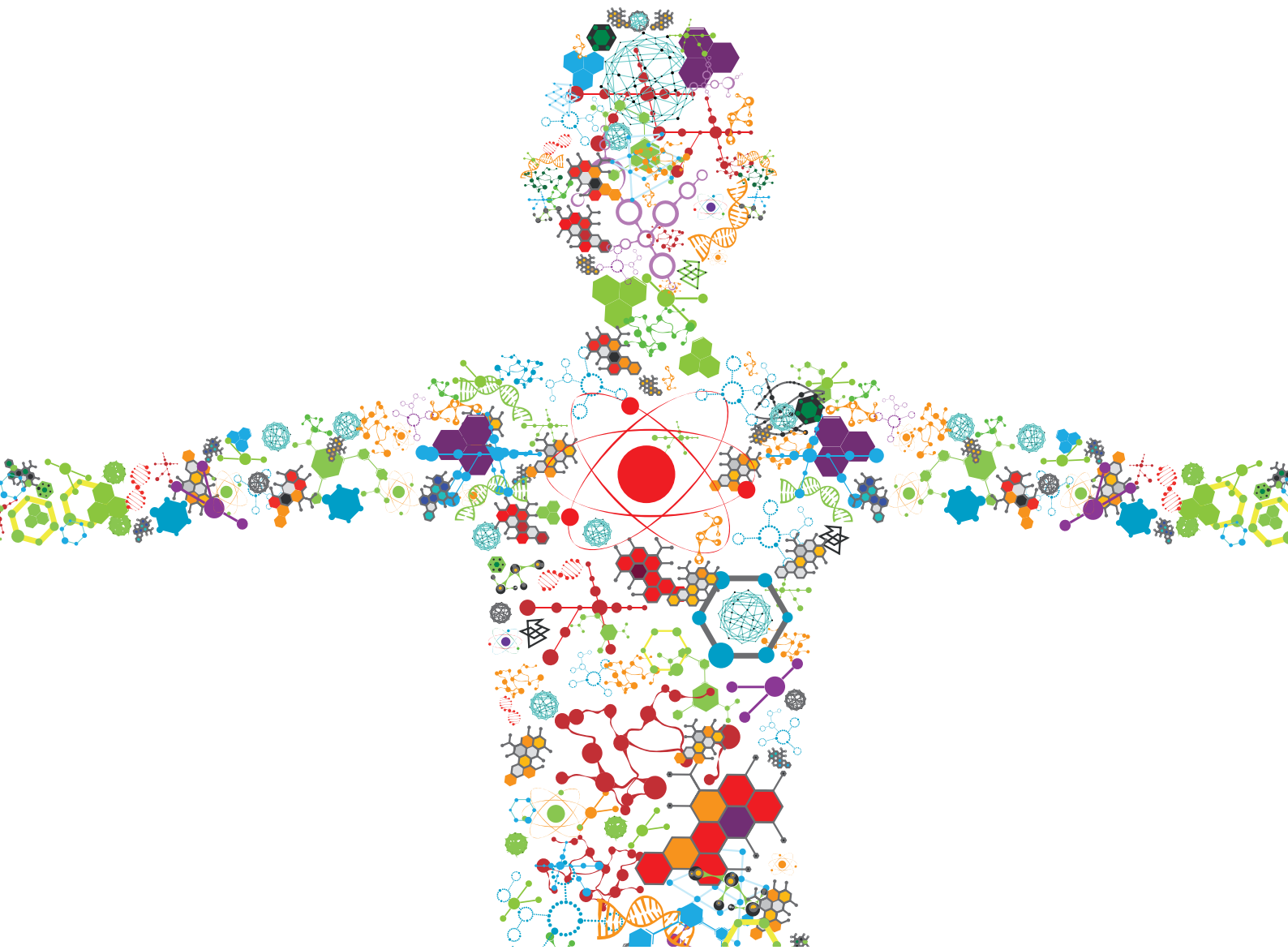

frontiers Research Topics

frontiers

ISSN 1664-8714
ISBN 978-2-83250-475-8
DOI 10.3389/978-2-83250-475-8

About Frontiers

Frontiers is more than just an open-access publisher of scholarly articles: it is a pioneering approach to the world of academia, radically improving the way scholarly research is managed. The grand vision of Frontiers is a world where all people have an equal opportunity to seek, share and generate knowledge. Frontiers provides immediate and permanent online open access to all its publications, but this alone is not enough to realize our grand goals.

Frontiers Journal Series

The Frontiers Journal Series is a multi-tier and interdisciplinary set of open-access, online journals, promising a paradigm shift from the current review, selection and dissemination processes in academic publishing. All Frontiers journals are driven by researchers for researchers; therefore, they constitute a service to the scholarly community. At the same time, the Frontiers Journal Series operates on a revolutionary invention, the tiered publishing system, initially addressing specific communities of scholars, and gradually climbing up to broader public understanding, thus serving the interests of the lay society, too.

Dedication to Quality

Each Frontiers article is a landmark of the highest quality, thanks to genuinely collaborative interactions between authors and review editors, who include some of the world's best academicians. Research must be certified by peers before entering a stream of knowledge that may eventually reach the public - and shape society; therefore, Frontiers only applies the most rigorous and unbiased reviews.
Frontiers revolutionizes research publishing by freely delivering the most outstanding research, evaluated with no bias from both the academic and social point of view. By applying the most advanced information technologies, Frontiers is catapulting scholarly publishing into a new generation.

What are Frontiers Research Topics?

Frontiers Research Topics are very popular trademarks of the Frontiers Journals Series: they are collections of at least ten articles, all centered on a particular subject. With their unique mix of varied contributions from Original Research to Review Articles, Frontiers Research Topics unify the most influential researchers, the latest key findings and historical advances in a hot research area! Find out more on how to host your own Frontiers Research Topic or contribute to one as an author by contacting the Frontiers Editorial Office: frontiersin.org/about/contact

CHARACTERIZATION OF BIOTHERAPEUTIC PRODUCTS

Topic Editors:
Anurag S. Rathore, Indian Institute of Technology Delhi, India
Christopher Mark Smales, University of Kent, United Kingdom
Andras Guttman, University of Pannonia, Hungary

Citation: Rathore, A. S., Smales, C. M., Guttman, A., eds. (2022). Characterization of Biotherapeutic Products. Lausanne: Frontiers Media SA.
doi: 10.3389/978-2-83250-475-8

Table of Contents

frontiers | Frontiers in Bioengineering and Biotechnology

TYPE Editorial
PUBLISHED 27 September 2022
DOI 10.3389/fbioe.2022.993262

OPEN ACCESS

EDITED AND REVIEWED BY
Michel Eppink,
Wageningen University and Research, Netherlands

*CORRESPONDENCE
Anurag S. Rathore,
asrathore@biotechcmz.com

SPECIALTY SECTION
This article was submitted to Bioprocess Engineering, a section of the journal Frontiers in Bioengineering and Biotechnology

RECEIVED 13 July 2022
ACCEPTED 30 August 2022
PUBLISHED 27 September 2022

CITATION
Rathore AS, Smales CM and Guttman A (2022), Editorial: Characterization of biotherapeutic products.
Front. Bioeng. Biotechnol. 10:993262.
doi: 10.3389/fbioe.2022.993262

Editorial: Characterization of biotherapeutic products

Anurag S. Rathore[1]*, C. Mark Smales[2] and Andras Guttman[3]

[1]Indian Institute of Technology Delhi, New Delhi, India, [2]School of Biosciences, Division of Natural Sciences, University of Kent, Canterbury, United Kingdom, [3]Horváth Csaba Memorial Laboratory of Bioseparation Sciences, Research Center for Molecular Medicine, Faculty of Medicine, Doctoral School of Molecular Medicine, University of Debrecen, Debrecen, Hungary

KEYWORDS

biotherapeutics, analytical characterisation, biosimilarity assessment, critical quality attributes (CQAs), post translational modifications (PTMs), virus like particles (VLPs)

Editorial on the Research Topic
Characterization of biotherapeutic products

Characterization of biotherapeutic products is a key aspect and requirement of their successful development and commercialization. The complexity of biotech products and processes, alongside our limited understanding of how quality attributes that define a biotherapeutic impact the product's safety and/or efficacy in the clinic remain major impediments to more predictive bioprocess development that manufacturers and regulators face. Recombinant biotherapeutic proteins are large, complex molecules and require sophisticated analytical and functional characterization methods to define their critical quality attributes and to understand how these are influenced by process and cell host changes.

In view of the above, this Research Topic aims to describe current best analytical characterisation practices of biotherapeutic products and how these can be utilised to enhance yield, quality and safety of such products. Nupur et al. offer a review of key advancements in the global regulatory landscape with respect to biosimilar approvals and also catalogue biosimilarity assessment studies for recombinant DNA products available in the public domain (Nupur et al.). Recent advancements in analytical methods, orthogonal techniques, and platforms for biosimilar characterization are covered. The review offers a comprehensive catalogue for published biosimilarity assessment studies with details on the analytical platform(s) used and critical quality attributes (CQAs) covered for multiple biotherapeutic products.

Characterization of biotherapeutic products is known to offer challenges, originating from the fact that these are extremely complex products, in particular mAbs. Chouquet et al. present recombinant production of two IgM models (IgM617 and IgM012) in pentameric as well as hexameric states and the evaluation of their polymer distribution using different biophysical methods (analytical ultracentrifugation, size exclusion chromatography coupled to multi-angle laser light scattering, mass photometry, and transmission electron microscopy) (Chouquet et al.). Each IgM construct is defined by a specific expression and purification pattern with different sample quality. Nevertheless,

both purified IgMs were able to activate complement in a C1q-dependent manner. Importantly, BioLayer Interferometry (BLI) was used for characterizing the kinetics of C1q binding to recombinant IgMs. The authors show that recombinant IgMs possess similar C1q-binding properties as IgMs purified from human plasma. Further, Singh and Lee employed a two-step strategy for targeted glycan analysis of a mAb expressed in Chinese hamster ovary (CHO) cells (Singh and Lee). The first step was to create a custom library of the glycans of interest independent of glucose units values (thereby eliminating the need for a calibration curve) and instead uses accurate mass and retention time (RT) as primary search variables. The second step is to perform targeted glycan screening using the custom-built library. The developed workflow has been applied to the targeted glycan analysis of a mAb expressed in CHO for 1) cell line selection, 2) characterizing the day-wise glycan evolution in a model mAb during a fed-batch culture, 3) assessing the impact of different media conditions on glycosylation, and 4) evaluating the impact of two different process conditions on glycosylation changes in a model mAb grown in a bioreactor. Taken together, the data presented in this study provides insights into the sources of glycan heterogeneity in a model mAb that are seen during its commercial manufacturing.

Coghlan et al. address the important topic of post translational modifications (PTMs), in particular shuffled disulfide bonds (Coghlan et al.). This quality attribute has been linked to decreased potency and increased immunogenicity of protein therapeutics. To gain deeper understanding the authors designed and further optimized a semi-automated LC-MS/MS method for disulfide bond characterization on two IgG1 protein therapeutics—rituximab and bevacizumab. They also compared originator vs. biosimilar versions of the two therapeutics to determine if there were notable variations in disulfide shuffling and overall degradation between the originator and biosimilar drug products. Their data exhibited differences in how the two proteins degraded with bevacizumab demonstrating an increase in degradation whilst rituximab maintained the same level throughout the incubation. Across all methods, the originator and biosimilar drugs performed similarly.

Novel analytical methods and approaches are central to analytical characterization of biotherapeutic products. Ling et al. present a method based on Raman spectroscopy that combines extreme point sort transformation with a long short-term memory (LSTM) network algorithm for identification of therapeutic mAbs (Ling et al.). A total of 15 therapeutic mAbs were used in this study. The results indicated that the present method had good robustness against spectral peak drift, random noise and fluorescence interference. The authors conclude that the extreme point sort transformation combined with the LSTM network algorithm enables the characteristic extraction of the therapeutic mAb Raman spectrum and that the proposed method is suitable for rapid identification of therapeutic mAbs. Further, Szabo et al. introduce a capillary gel electrophoresis based workflow for 1) size heterogeneity analysis to determine the presence/absence of the non-glycosylated heavy chain (NGHC) fragment (SDS-CGE), 2) capillary gel isoelectric focusing for possible N-glycosylation mediated charge heterogeneity determination, e.g., for excess sialylation and finally, 3) capillary gel electrophoresis for N-glycosylation profiling and sequencing (Szabo et al.). Their results show the presence of negligible amount of non-glycosylated heavy chain (NGHC), while 25% acidic charge variants were detected. Comprehensive N-glycosylation characterization revealed the occurrence of approximately 8.2% core-afucosylated complex and 17% galactosylated N-linked oligosaccharides, suggesting the possible existence of antibody dependent cell mediated cytotoxicity (ADCC) effector function in addition to the generally considered neutralizing effect of bamlanivimab, the first anti-spike neutralizing monoclonal antibody, which got an emergency use authorization from the FDA for COVID-19 treatment.

Viruses and virus like particles (VLPs) seem to present challenges during their analytical characterization. Carvalho et al. evaluated several biophysical and biochemical methods for thorough characterization of monovalent and pentavalent influenza virus like particles (VLPs) from diverse groups (A and B) and subtypes (H1 and H3) produced in insect cells using the baculovirus expression vector system (IC-BEVS) (Carvalho et al.). Particle size distribution and purity profiles were monitored during the purification process using two complementary technologies—nanoparticle tracking analysis (NTA) and tunable resistive pulse sensing (TRPS). VLP surface charge at the selected process pH was also assessed by this last technique. The morphology of the VLP (size, shape, and presence of hemagglutinin spikes) was evaluated using transmission electron microscopy. Circular dichroism was used to assess VLPs' thermal stability. Total protein, DNA, and baculovirus content were also assessed. This study shows robustness and generic applicability of the tools and methods evaluated, independent of VLP valency and group/subtype. Further, Powers et al. present a detailed characterization study that was conducted to enable understanding of a pivotal physicochemical test for adenoviral based therapeutics (Powers et al.). Anion-exchange high performance liquid chromatography (AEX-HPLC) was used to measure viral particle concentration, product purity and surface charge in a high-throughput manner. During product development of an adenoviral-based therapeutic, an accelerated stability study was performed and showed changes in each of the AEX-HPLC reportable attributes. These changes also correlated with a decrease in product infectivity prompting a detailed characterization of the impurity and mechanism of the surface charge change. Characterization experiments identified the impurity as a free hexon trimer, suggesting that capsid

degradation could be contributing to both the impurity and reduced particle concentration. Additional mass spectrometry characterization identified deamidation of specific hexon residues to be associated with the external surface charge modification observed upon thermal stress conditions. To demonstrate a causal relationship between deamidation and surface charge changes observed by AEX-HPLC, site-directed mutagenesis experiments were performed. Through this approach, it was concluded that deamidation of asparagine 414 was responsible for the surface charge alteration observed in the AEX-HPLC profile but was not associated with the reduction in infectivity. Finally, Mullins et al. present results from characterization of recombinant chimpanzee adenovirus C68 low and high-density particles (Mullins et al.). The authors observed differential infectivity and product yield between two recombinant chimpanzee adenovirus C68 constructs whose primary difference was genome length. To determine a possible reason for this outcome, they characterized the proportion and composition of the empty and packaged capsids. Both analytical ultracentrifugation (AUC) and differential centrifugation sedimentation (DCS, a rapid and quantitative method for measuring adenoviral packaging variants) were employed for an initial assessment of genome packaging and showed multiple species whose abundance deviated between the virus builds but not manufacturing campaigns. Identity of the packaging variants was confirmed by charge detection mass spectrometry (CDMS), the first known application of this technique to analyze adenoviral species. The empty and packaged capsid populations were separated via preparative ultracentrifugation and then combined into a series of mixtures. These mixtures showed that the oft-utilized denaturing A260 adenoviral particle titer method will underestimate the actual particle titer by as much as three-fold depending on the empty/full ratio. In contrast, liquid chromatography with fluorescence detection proved to be a superior viral particle titer measurement methodology.

Overall, we expect this Research Topic to be of interest to those involved in characterization of biotherapeutic products.

Author contributions

All authors listed have made a substantial, direct, and intellectual contribution to the work and approved it for publication.

Conflict of interest

The authors declare that the research was conducted in the absence of any commercial or financial relationships that could be construed as a potential conflict of interest.

Publisher's note

frontiers in Bioengineering and Biotechnology

ORIGINAL RESEARCH
published: 04 November 2021
doi: 10.3389/fbioe.2021.753480

Characterization of Recombinant Chimpanzee Adenovirus C68 Low and High-Density Particles: Impact on Determination of Viral Particle Titer

*Elise K. Mullins[1], Thomas W. Powers[1], Jim Zobel[1], Kory M. Clawson[1], Lauren F. Barnes[2], Benjamin E. Draper[3], Qin Zou[1], Joseph J. Binder[4], Stanley Dai[5], Kun Zhang[1], Olga Friese[1], Herbert A. Runnels[1], Martin F. Jarrold[2] and Lawrence C. Thompson[1]**

[1]Analytical Research and Development, Biotherapeutic Pharmaceutical Sciences, Pfizer Inc., Chesterfield, MO, United States, [2]Chemistry Department, Indiana University, Bloomington, IN, United States, [3]Megadalton Solutions, Bloomington, IN, United States, [4]Cancer Vaccines and Immunotherapies, Pfizer Inc., San Diego, CA, United States, [5]Nektar Therapeutics, San Francisco, CA, United States

OPEN ACCESS

Edited by:
Christopher Mark Smales,
University of Kent, United Kingdom

Reviewed by:
Xiaobo Liu,
Guangdong Technion-Israel Institute of Technology (GTIIT), China
Yu-Cai He,
Changzhou University, China

***Correspondence:**
Lawrence C. Thompson
Lawrence.Thompson@pfizer.com

Specialty section:
This article was submitted to Bioprocess Engineering, a section of the journal Frontiers in Bioengineering and Biotechnology

Received: 04 August 2021
Accepted: 20 October 2021
Published: 04 November 2021

Citation:
Mullins EK, Powers TW, Zobel J, Clawson KM, Barnes LF, Draper BE, Zou Q, Binder JJ, Dai S, Zhang K, Friese O, Runnels HA, Jarrold MF and Thompson LC (2021) Characterization of Recombinant Chimpanzee Adenovirus C68 Low and High-Density Particles: Impact on Determination of Viral Particle Titer. Front. Bioeng. Biotechnol. 9:753480. doi: 10.3389/fbioe.2021.753480

We observed differential infectivity and product yield between two recombinant chimpanzee adenovirus C68 constructs whose primary difference was genome length. To determine a possible reason for this outcome, we characterized the proportion and composition of the empty and packaged capsids. Both analytical ultracentrifugation (AUC) and differential centrifugation sedimentation (DCS, a rapid and quantitative method for measuring adenoviral packaging variants) were employed for an initial assessment of genome packaging and showed multiple species whose abundance deviated between the virus builds but not manufacturing campaigns. Identity of the packaging variants was confirmed by charge detection mass spectrometry (CDMS), the first known application of this technique to analyze adenovirus. The empty and packaged capsid populations were separated via preparative ultracentrifugation and then combined into a series of mixtures. These mixtures showed the oft-utilized denaturing A260 adenoviral particle titer method will underestimate the actual particle titer by as much as three-fold depending on the empty/full ratio. In contrast, liquid chromatography with fluorescence detection proves to be a superior viral particle titer methodology.

Keywords: non-human primate, adenovirus, AEX-HPLC, analytical ultracentrifugation, differential centrifugation sedimentation, charge detection mass spectrometry, low density viral particles, viral particle titer

Abbreviations: AUC, analytical ultracentrifugation; DCS, differential centrifugation sedimentation; CDMS, charge detection mass spectrometry; ARM, adenovirus reference material; A260, absorbance at 260 nm; UV, ultra-violet; AEX-HPLC, anion-exchange high performance liquid chromatography; DNA, deoxyribonucleic acids; qPCR, quantitative polymerase chain reaction; DLS, dynamic light scattering; EM, electron microscopy; RPM, revolutions per minute; CsCl, cesium chloride; mL, milliliters; HEK293, cell line derived from human embryonic kidney cells; IFU, infectivity units; VP, viral particles; RP-HPLC, reversed-phase high performance liquid chromatography; ACN, acetonitrile; TFA, trifluoroacetic acid; ELIT, electrostatic linear ion trap; FFT, fast Fourier transforms; MDa, megadalton; mM, millimolar; SDS, sodium dodecyl sulfate; kb, kilobases; LC-MS, liquid chromatography coupled to mass spectrometry.

INTRODUCTION

Non-human primate adenoviral vectors are attractive therapeutic vectors as they share similar beneficial characteristics of human adenovirus like robust antigen expression, but with reduced levels of neutralizing antibodies (Capone et al., 2013; Cheng et al., 2015; Zhang et al., 2017; Zhao et al., 2018). Recent successes using these constructs include modified chimpanzee adenovirus type 3 ebolavirus vaccine (cAd3-EBO) (Stanley et al., 2014; Ledgerwood et al., 2017) and replication-deficient simian adenoviral vectored vaccine ChAdOx1 nCoV-19 against SARS-CoV-2 (Folegatti et al., 2020; Ewer et al., 2021; Putter, 2021).

Fundamentally, recombinant viral vectors have a genomic composition different than native virus. For adenoviral constructs, this often means replacement of the E1 gene, possibly the E3 or other genes with the genetic payload of choice (Farina et al., 2001; Tatsis et al., 2006). These alterations as well as changes in manufacturing, including scale and/or process, can have an impact on the ordered construction of a viral particle during adenovirus maturation (Mangel and San Martín, 2014; Ahi and Mittal, 2016). The final product could contain capsids without genomes (unpackaged/empty), with complete genomes (packaged/full) or myriad intermediates in between (Vellekamp et al., 2001; Sutjipto et al., 2005).

Numerous techniques are available to provide this capsid content information (i.e., empty, partially packaged or fully packaged). The most commonly applied intact capsid approaches are dynamic light scattering (DLS) (Kondylis et al., 2019), electron microscopy (EM) (Kondylis et al., 2019), AUC (Berkowitz and Philo, 2007; Berkowitz, 2008; Yang et al., 2008) and DCS (Bondoc and Fitzpatrick, 1998; Shih et al., 2010). They can measure a range of viral particle populations from low density immature particles up to high mass aggregates. Capsid protein analysis via reversed-phase high performance liquid chromatography (RP-HPLC) can also parse out particle maturity via analysis of viral protein content and processing (Lehmberg et al., 1999; Vellekamp et al., 2001; Chelius et al., 2002; Takahashi et al., 2006). In addition to the more routine techniques, additional-state-of-the-art techniques, including charge detection mass spectrometry (CDMS) (Contino and Jarrold, 2013; Pierson et al., 2016; Draper et al., 2018; Draper and Jarrold, 2019) are available for direct mass determination of intact viral particles (Kondylis et al., 2019; Werle et al., 2021).

The current study was initiated to evaluate the performance of all of these techniques to elucidate particle content on two chimpanzee adenovirus C68 (Farina et al., 2001; Cohen et al., 2002; Xiang et al., 2002; Tatsis et al., 2006) constructs (heretofore known as AdC68 #1 and #2). AdC68 #1 and #2 each contain tumor antigens cloned in place of E1 and E3, but due to differing inserted genes, the resulting recombinant viruses contain genomes of disparate lengths. Throughout this study, we showed that DCS, AUC, and A260/A280 ratio were able to elucidate particle content while RP-HPLC and CDMS provided valuable orthogonal information. A byproduct of this investigation was the important observation that genome packaging ratios have a pronounced impact on viral particle titer accuracy via the denaturing A260 method (Maizel et al., 1968b). We demonstrate that for adenovirus products with some level of empty capsids, viral particle concentration determined by AEX-HPLC (Shabram et al., 1997; Blanche et al., 2000; Klyushnichenko et al., 2001; Kuhn et al., 2007; Whitfield et al., 2009) using native protein fluorescence detection is superior, as the technique generates an unbiased, total viral particle titer.

MATERIALS AND METHODS

Formulation

AdC68 was formulated in A195 buffer (Evans et al., 2004): 10 mM Tris, 75 mM NaCl, 5% w/v sucrose, 0.02% (w/v) polysorbate 80, 1.0mM $MgCl_2$, 0.1 mM EDTA, 0.5% (v/v) ethanol, 10 mM L-histidine, pH 7.4.

Human Adenovirus Type 5 Reference Material (ARM)

The Human Adenovirus Type 5 Reference Material was purchased from the ATCC ARM working group (Hutchins et al., 2000; Hutchins, 2002; Berkowitz, 2008). It is a highly characterized material, containing nearly 100% packaged capsids. This allows it to function as a standard to which all other adenovirus reference materials can be quantitated against.

Analytical Ultracentrifugation per Sedimentation Velocity

The samples were run in triplicate using a Beckman Coulter Analytical Ultracentrifuge Proteome XL/I at 5,000 RPM at 20°C. Data was collected on both the interference and absorbance at 260 nm, then 50 scans were used for analysis. The resulting data was analyzed using Sedfit (ver.15.01b) to generate c(s) size distribution plots. Sednterp (ver. 1.09) was used to determine the solvent viscosity and density.

Differential Centrifugation Sedimentation via Disc Centrifuge

The differential centrifugation sedimentation technique utilizes a disc spun up to 24,000 rpm. A sucrose gradient was added to the disc that ranged from 8 to 24% sucrose. AdC68 samples were then injected into the disc for separation within the sucrose gradient into empty, intermediate, and full/mature species based on their density. The method reports relative percent full, empty, and intermediate species.

Preparative Ultracentrifugation

AdC68 particles were separated by cesium chloride (CsCl) density gradient ultracentrifugation. Ultracentrifugation tubes were loaded with 5 ml of 4 M CsCl underneath 18 ml of 2.2 M CsCl. Viral particles (15.5 ml) were gently overlayed on top of the CsCl, and the tubes were spun at 25,000 rpm for 17 h at 4°C in an SW28 rotor in an Optima XPN-80 Ultracentrifuge (Beckman Coultre). Two visible bands were pulled with 3 ml syringes and transferred to dialysis cassettes with 10,000 Da molecular weight

cutoff. Viral particles in the high-and-low density bands were separately dialyzed twice in A195 buffer for 4 h at 4°C before further analysis.

Cell Culturing

Cultures of HEK293 cells (Cell biolabs, Catalog No. AD-100) were grown in a flask containing Dulbecco's modified medium (Gibco, Catalog No. 11995) supplemented with 10% Heat Inactivated Fetal Bovine Serum (Gibco, Catalog No. 10082) and 1x Penicillin-Streptomycin (Gibco, Catalog No. 15140) in a 5% CO_2 atmosphere at 37°C.

Determination of the Adenoviral Infectivity by a Cell-Based Adenovirus Titer Immunoassay

This method was developed internally in Pfizer to monitor the adenovirus sample infectivity. In this assay, HEK293 cells were seeded into a 24-well flat bottom cell culture plate at 2.2E5 cells/well and then incubated in a 37°C, 5% CO2 incubator. A dilution series of adenovirus sample was prepared in cell culture medium. The dilution series was then added to the wells of the cell assay plate about 1 h after cell seeding. The assay plate was then incubated for 2 days. Following infection, the adenovirus will express the viral proteins including Hexon proteins. The cells were then fixed with cold methanol at -20°C and then stained with a polyclonal antibody against adenovirus Hexon proteins. Positive stained cells in assay wells were counted under microscope fitted with a 10x lens. The cell assay plate wells that contains 7 to 79 stained cells per view field were recorded and used to calculate the adenovirus sample infectivity, reported as IFU/ml as well as vp/IFU.

Intact Protein RP-HPLC of Low and High-Density Fractions

The RP-HPLC method provides a capsid protein map. The samples were denatured with ACN and TFA, then separated on a Phenomenex Jupiter C4, 5μm, 2 × 150mm, 300Å analytical column. Detection is performed with UV at 214 nm to provide chromatograms that can be visually compared for peak consistency.

CDMS of Low and High-Density Fractions

In CDMS the m/z and charge of individual ions are simultaneously measured and then multiplied to give the mass. The CDMS instrument employed here has been described in detail elsewhere (Contino and Jarrold, 2013; Draper et al., 2018; Draper and Jarrold, 2019). Briefly, ions generated by nanoelectrospray, enter the instrument though a metal capillary and pass through several differentially-pumped stages to remove the ions from the ambient gas flow. The resulting ions are accelerated and focused into a hemispherical deflection energy analyzer which transmits a narrow band of ion kinetic energies. The ions are then focused into an electrostatic linear ion trap (ELIT) which consists of two endcaps that can be switched between reflection and transmission mode. Trapped ions oscillate between the endcaps. A detection cylinder placed between the endcaps picks up the charge induced by the oscillating ions. The resulting signal is digitized and analyzed by fast Fourier transforms. The oscillation frequency is related to the ion's m/z and the charge is obtained from the FFT magnitude.

The adenovirus samples were stored in a -80°C freezer prior to analysis. Aliquots were thawed at room temperature and prepared for analysis in a class II biosafety cabinet (NuAire LabGard ES type A2). The sample was desalted and buffer exchanged via size exclusion chromatography (Micro Bio-Spin P-6 Gel Columns, Bio-Rad) into a 200 mM ammonium acetate (Honeywell 631-31-8). Measurements were performed for thousands of ions over a span of 30–45 min and then the masses were binned (0.5 MDa bins) to give the mass spectrum.

Stability Sample Degradation Description

Approximately 120 ml each of AdC68 #1 material and 120 ml of AdC68 #2 material were added to respective Nalgene bottles. A 10 ml aliquot of each was pulled and frozen at -70°C to function as T0 material. The remaining material was held in a 25°C incubator. Consecutive 10 ml aliquots of each construct were pulled at 1, 2, 4, 8, and 12 weeks. Each aliquot was stored at -70°C to be used for further analytics.

Particle Mixtures

AdC68 #1 development drug substance lot was separated by CsCl into low and high-density particle fractions. AEX was used to determine the viral particle concentration for each of the isolated bands. The concentration of the high-density band was 8.0E11 VP/mL and the concentration of the low-density band was 3.8E11 VP/mL. Both samples were diluted to 2E11 VP/mL to then make a range of empty and full particle mixtures at the same particle concentration. The samples were aliquoted at 1.5 ml volumes and frozen at –70°C to be used for analytical testing.

AEX-HPLC of Stability Samples for A260/280 & Mixtures FLD + A260

The AEX-HPLC method is used to determine product purity and virus particle concentration. Relative retention time is also measured which correlates to changes in surface charge. In this case, a high affinity, anion exchange column (GE Healthcare, Resource Q, 1 ml 15 μm, 6.4 × 30 mm, Part No. 17-1177-01) was used to separate the AdC68 and impurities. AdC68 samples are diluted with formulation buffer and analyzed against a standard curve that runs from 0.25E11 VP/mL to 3.0E11 VP/mL. Elution of the bound molecules is achieved using a salt gradient with a flow rate of 1.0 ml/min over the course of 30 min. Molecules are analyzed using fluorescence detection with a 280 nm excitation and 320 nm emission, as well as UV detection at 260 nm. Relative purity is determined by comparing area counts of the eluting peaks and is reported as a percent of the total area for all peaks. Particle quantitation is achieved by correlation of the unknowns to a standard curve. Relative retention time (acidic shift) is measured by comparing the average elution time of all standards to that of the sample.

Denaturing A260 & A280 Measurements

Adenovirus samples were disrupted via a 1% SDS solution for approximately 15 min. After denaturation, the samples are

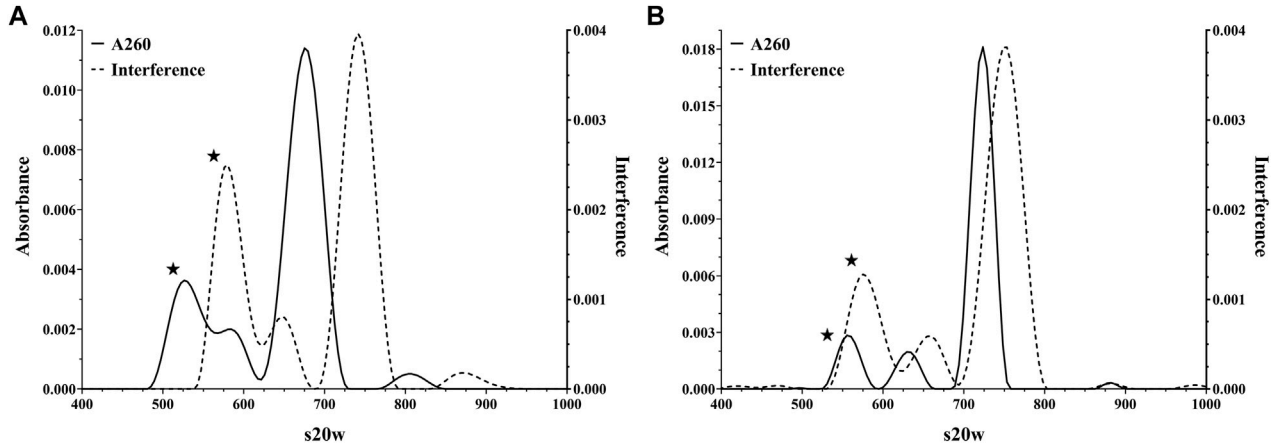

FIGURE 1 | Representative Analytical Ultracentrifugation analyses of AdC68 construct #1 (Panel A) and #2 (Panel B) showing detection at both the absorbance (260 nm) and interference channels.

TABLE 1 | Analytical Ultracentrifugation and Differential Centrifugation Sedimentation quantification of AdC68 viral particle isoforms using interference and light scattering detection, respectively.

AdC68	AUC				DCS			
	Empty (%)	Intermediate (%)	Full (%)	Aggregates (%)	Empty (%)	Intermediate (%)	Full (%)	Aggregates (%)
#1	32	10	56	3	30	14	56	nd
#2	21	9	68	1	21	8	71	nd

"nd" denotes not detected.

transferred to a cuvette and analyzed at 260 and 280 nm. The appropriate Beer's Law equation is used to calculate concentration using the 260 nm measurement. A purity ratio is also calculated using both the 260 and 280 nm absorbances.

RESULTS

After construction, AdC68 #1 and #2 contained genomes of 34.8 and 36.4kb, respectively. Even though the manufacturing processes for these constructs were comparable, unique features appeared between them. Firstly, the AdC68 #1 per particle infectivity was about twice that of AdC68 #2 (data not shown). Secondly, manufacturing yields for AdC68 #2 campaigns were about twice that of AdC68 #1 (data not shown). Lastly, the constructs yielded different absorbances at 260 nm with similar particle numbers (data not shown) suggesting that genome packaging varied between them. Further investigation was initiated to ascertain viral particle attributes including integrity and content.

Particle Content Investigation

Dynamic light scattering (DLS) and electron microscopy (EM) were employed to confirm particle integrity and both showed that the constructs contained uniform, monomeric viral particles of the expected diameter (data not shown).

AUC, as the gold standard, and then DCS, as an orthogonal approach, were performed to examine the particle content. As shown in **Figure 1**, the AUC demonstrates that these materials contain capsids of various sedimentation coefficients consistent with a heterogeneous genomic content, and the constructs varied from each other in the fractional amount of each form (**Table 1**). In addition to leveraging the interference signal for quantitation, absorbance data at 260 nm were collected to give additional insight into capsid composition (i.e., capsids containing DNA would exhibit a stronger signal at 260 nm). As highlighted in **Figure 1**, the population with the smallest sedimentation coefficient exhibited a wide disparity between its absorbance and interference signals while the other three populations were in harmony. The fact that this population displayed lower absorbance relative to interference signal suggested these capsids likely did not contain a genome. These data, in addition to previous studies (Berkowitz and Philo, 2007; Berkowitz, 2008), supported the initial labeling of the capsid populations as empty, intermediate, full, and aggregates (**Table 1**).

As with the AUC interference channel, the light scattering employed by DCS (Bondoc and Fitzpatrick, 1998; Shih et al., 2010) is unbiased by the presence or absence of a genome. Therefore, when assessing particles of uniform size by DCS, the amount of light scattering is a direct correlation to particle number (Hohl et al., 2017). A qualitative comparison indicated a

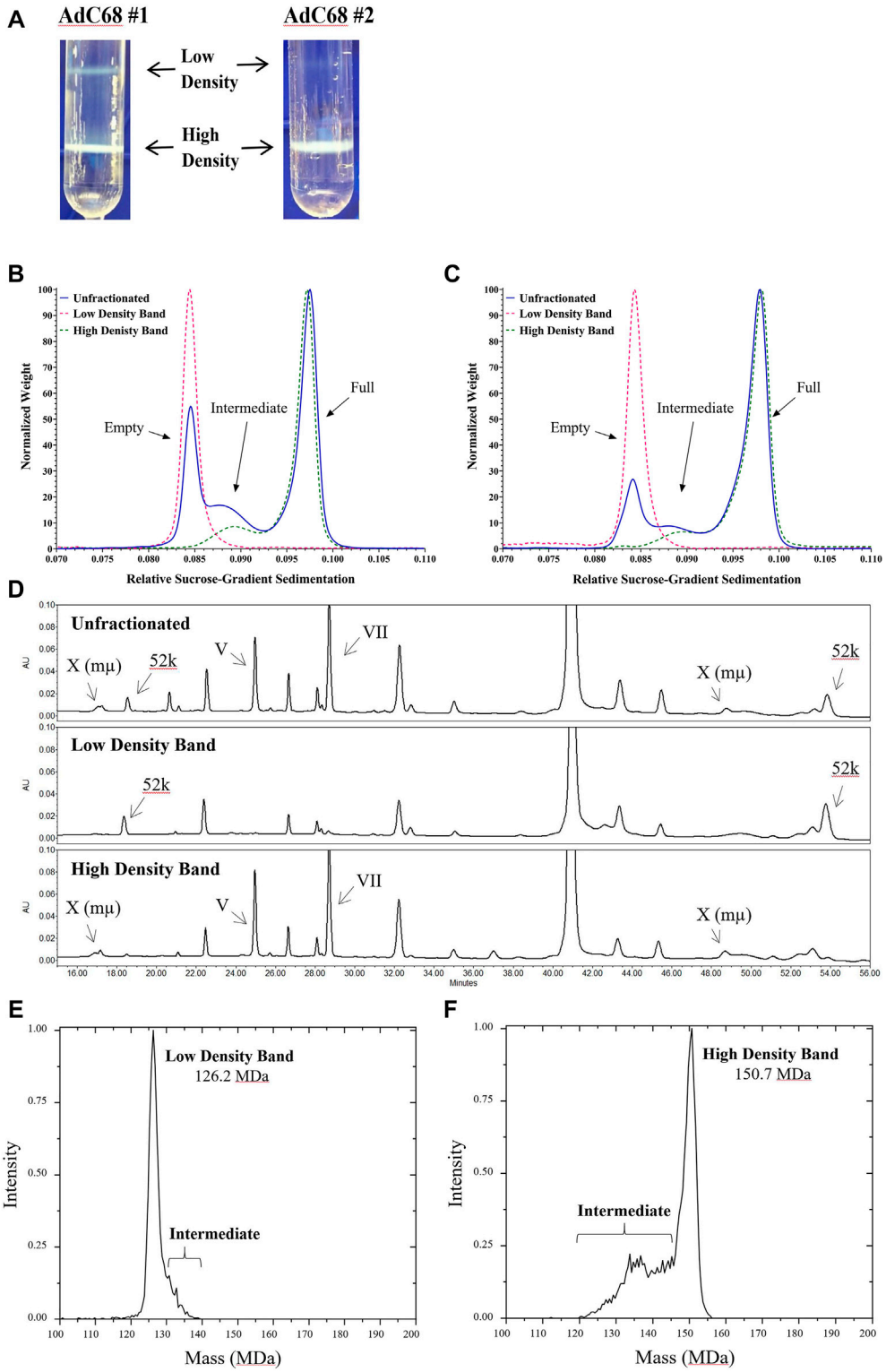

FIGURE 2 | Analysis of preparative ultracentrifugation bands for AdC68 #1 and #2. Panel A is a representative picture of the CsCl preparative fractionation. Panels B and C are DCS overlays of the unfractionated and low/high density fractions for AdC68 #1 and #2, respectively. Panel D is a Reversed Phased High Performance Liquid Chromatography stacked-plot of the proteome content for AdC68 #1 unfractionated and low density/high density fractions. Panel E and Panel F are Charge Detection Mass Spectrometry spectra of the AdC68 #1 low/high density fractions showing the experimentally determined molecular masses, respectively.

TABLE 2 | Infectivity of both the low/high density viral particle fractions for AdC68 #1 and #2.

AdC68	IFU/mL	Vp/IFU
#1	Low Density Particles	251,966[a]
	High Density Particles	55
#2	Low Density Particles	19,234[a]
	High Density Particles	123

[a]*Extrapolated beyond calibrated method range.*

good alignment between DCS data and AUC interference data (**Table 1**). Furthermore, the DCS data also confirmed that AdC68 #1 contained a higher percentage of empty capsids than AdC68 #2 (**Table 1**).

Together, these data demonstrated that both constructs formed particles of appropriate size and shape, but AdC68 #1 contained significantly more low-density (empty) capsids than AdC68 #2. This trait was consistent among several batches of both constructs (data not shown) suggesting this was a feature of these embodiments.

Empty/Full Capsid Isolation and Analysis

Since column chromatography was used as the primary purification technique for these materials, as opposed to density centrifugation, the presence of genome packaging variants in the final material was unsurprising. To further study these variants and confirm the initial peak identifications, materials were fractionated by CsCl density ultracentrifugation (Prage et al., 1972; Burlingham et al., 1974; Daniell, 1976; Tibbetts and Giam, 1979; Tóth et al., 1982; Vellekamp et al., 2001; Sutjipto et al., 2005). The net result was two viral particle populations aptly labeled as the low-density band and the high-density band (**Figure 2A**). Presumably these represented primarily "genome-free or empty" capsids and the "genome-containing or full/mature" capsids, respectively.

The fractions were extracted from the CsCl gradient and evaluated. A negative staining EM investigation showed the typical patterns (Sutjipto et al., 2005) seen for empty and full/mature capsids, respectively (data not shown). Tests for infectivity (**Table 2**) showed that the particles from the low-density fraction exhibited extremely low infectivity as expected (Burlingham et al., 1974; Daniell, 1976) while the particles from the high-density fraction displayed infectivity ratios in line with expectations for the product and recombinant chimpanzee adenovirus (Roy et al., 2004). DCS analysis (**Figure 2B, C**) revealed that the particles from the low-density fraction aligned with the previously labeled empty capsid region and that the particles from the high-density fraction contained both the previously labeled intermediate and full capsid region.

Reversed phase high performance liquid chromatography (RP-HPLC) (Vellekamp et al., 2001; Lehmberg et al., 1999; Chelius et al., 2002; Takahashi et al., 2006) of AdC68 #1 (**Figure 2D**) revealed that the low-density material contained the 52 k protein which is known to be associated only with empty capsids (Sutjipto et al., 2005; Condezo et al., 2015; Ahi and Mittal, 2016) while the high-density material contained proteins V, VII and X, all of which are hallmarks for mature/full capsids (Ahi and Mittal, 2016). Protein identifications were consistent with internal LC-MS characterization and profiles observed in literature (Lehmberg et al., 1999; Chelius et al., 2002; Takahashi et al., 2006). AdC68 #2 had similar results (data not shown).

Finally, CDMS was employed to determine the masses of the low and high-density fractions and confirm the presence of empty and fully packaged capsids. **Figure 2E, F** show the CDMS spectra for the low-density and high-density bands of Ad68 #1, respectively. The primary mass of the high-density band is 150.7 MDa, which is in range with the generally accepted mass for adenovirus mature/full particles of 150 MDa (van Oostrum and Burnett, 1985; Rux and Burnett, 2004). The theoretical mass of an adenoviral particle without a genome is ~127 MDa which is in close alignment to the primary mass of the low-density band: 126.2 MDa. As with DCS, the CDMS data suggests that the high-density fraction contains a majority of the intermediate capsid species. Furthermore, these data support the assignments of empty, intermediate, and full capsids in **Figure 2C** and **Figure 2D**.

Together these data definitively establish that the high-density and low-density bands primarily contain capsids with and without genomes, respectively. However, neither population was 100% homogeneous. The preparation of these highly enriched materials offered the opportunity to investigate the capabilities of different analytical tools to quantify viral particles with varied numbers of empty and full capsids.

Empty/Full Capsid Mixture and Viral Particle Quantification Study

To estimate the impact of empty particles on particle content methods, a series of mixtures of the low and high-density materials were produced and evaluated by several analytical methods. AEX-HPLC was used to measure the viral particle titers for AdC68 #1 100% low-density and 100% high-density parent fractions. Based on those concentrations, theoretical mixtures were created as listed in **Table 3**. Those mixtures were then analyzed on DCS to determine relative percentages of empty, intermediate, and mature/full species. As shown in **Table 3**, the output from the DCS confirmed the targeted mixtures. Since DCS signal intensity is a direct readout of total particle number, the viral particle concentrations of the parent low and high-density fractions measured by AEX-HPLC using intrinsic protein fluorescence must have been accurately determined.

To finalize the data set, denaturing A260/280 nm measurements were performed as described (Materials and Methods). As shown in **Table 3**, A260/280 ratio increases from 0.746 up to 1.307. These values were consistent with adenoviral preparations containing primarily empty/immature to mature/full viral capsids (Prage et al., 1972; Burlingham et al., 1974; Daniell, 1976; Tóth et al., 1982; Vellekamp et al., 2001; Sweeney and Hennessey, 2002; Sutjipto et al., 2005; Berkowitz, 2008). Interestingly, the raw denaturing A260 value increases almost 3-fold over the range of samples which are known to have the same viral particle number (**Table 3**).

TABLE 3 | Differential Centrifugation Sedimentation analyses and 260/280 absorbance measurements of AdC68 #1 low/high density viral particle fractions as well as mixtures of said fractions.

Mixture	DCS band percentage			Absorbance units		
	Empty	Intermediate	Full	260 nm	280 nm	Ratio
100% High Density	nd	10.8	89.2	0.234	0.179	1.307
90% High & 10% Low Density	8.9	10.9	80.2	0.209	0.161	1.299
80% High & 20% Low Density	19.4	9.7	71.0	0.199	0.158	1.265
70% High & 30% Low Density	31.6	7.6	60.8	0.175	0.145	1.204
60% High & 40% Low Density	40.0	7.6	52.4	0.162	0.141	1.154
50% High & 50% Low Density	51.0	5.4	43.6	0.152	0.137	1.112
40% High & 60% Low Density	60.3	5.0	34.7	0.140	0.133	1.047
30% High & 70% Low Density	69.2	3.0	25.9	0.123	0.124	0.990
20% High & 80% Low Density	79.5	3.6	16.9	0.106	0.117	0.908
10% High & 90% Low Density	88.4	3.3	8.3	0.092	0.111	0.830
100% Low Density	100	nd	nd	0.080	0.108	0.746

"nd" denotes not detected.

This bias can also be observed in overlays of the A260 and fluorescence channels of AEX-HPLC intact particle analyses (**Figure 3**). As expected for the human ARM which is known to contain a high percentage of packaged capsids (Hutchins et al., 2000; Hutchins, 2002; Berkowitz, 2008), both the A260 (**Figure 3A**) and fluorescence AEX-HPLC (**Figure 3B**) channels show commensurate, concentration-dependent increase in signal. However, when the empty/full capsid mixtures (known to contain similar viral particle titers) were studied, the response factors for these two detection modes did not align (**Figure 3C, D**). For all mixtures, signal from the fluorescence channel was concordant while that from the A260 channel increased in proportion to the percentage of high-density particles. The overall ~2.5 fold increase in response was comparable to that of the denaturing A260 measurement with the difference between them probably related to light scattering effects from analyses of the intact particles.

Based on this data, application of the denaturing 260 nm based concentration calculation is not sufficient for determining the particle titer of the adenovirus constructs used in this study, primarily due to the large abundance of empty capsids.

Viral Particle Stability Study

In addition to assessing particle content, an additional aim was to determine how genome content and size impacted capsid stability. The relative stability for these two materials was explored through an accelerated stability hold followed by DCS and AEX-HPLC time-point measurements. **Figure 4A, B** clearly show that the empty capsid population decreased dramatically such that by the end of the second week of the study, only a fractional amount of that species remained. Limited stability of empty capsids compared to full capsids is consistent with previous observations (Prage et al., 1972; Burlingham et al., 1974; Tibbetts and Giam, 1979; Tóth et al., 1982).

The stability profile of the fully packaged capsid populations deviate significantly. AdC68 #1 exhibited a steady decrease in intact particle number and infectivity (data not shown) such that only ~25% of the initial capsid number remained after 12 weeks (**Figure 4A**). In contrast, AdC68 #2 was more resistant to degradation, taking up to 4 weeks before any discernable particle loss was detected. By 12 weeks, > 50% of the particles remain intact (**Figure 4B**) and infectious (data not shown).

The AEX-HPLC measurements showed a biphasic result for viral particle titer consistent with rapid depletion of empty capsids followed by a gradual disappearance of the full capsids (data not shown). These data also indicated that breakdown of AdC68 #2 particles was at a reduced rate compared to AdC68 #1 (data not shown).

Both data sets were consistent and indicated these AdC68 builds show differential stability profiles. Interestingly, these data convey another deficiency in the denaturing A260 concentration method compared to AEX-HPLC. Because the viral particles are disrupted prior to quantification, the A260 method is blind to degradation and not a useful measurement of stability.

DISCUSSION

Construction of a recombinant, replication deficient adenovirus is a delicate operation. A balance must be struck between removal of the replication machinery and insertion of the therapeutic material while maintaining a genome size optimal for packaging and stability (Saha et al., 2014). These two constructs exhibited differences in infectivity ratios, stability profiles, production yields and genome packaging: an outcome which is almost certainly due, at least in part, to divergent genome lengths. However, in many ways, the variability in quality attributes between constructs is inconsequential insomuch as target profiles for the individual builds can be maintained. To maintain said profile, an analytical package must be developed that can measure the associated quality attributes. This study focused on two attributes specifically, capsid content and viral particle concentration.

Viral Particle Content Analysis (Ie. Genome Packaging Profile)

The majority of the viral particle content tools presented in this manuscript harken back to the past 50 or so years of

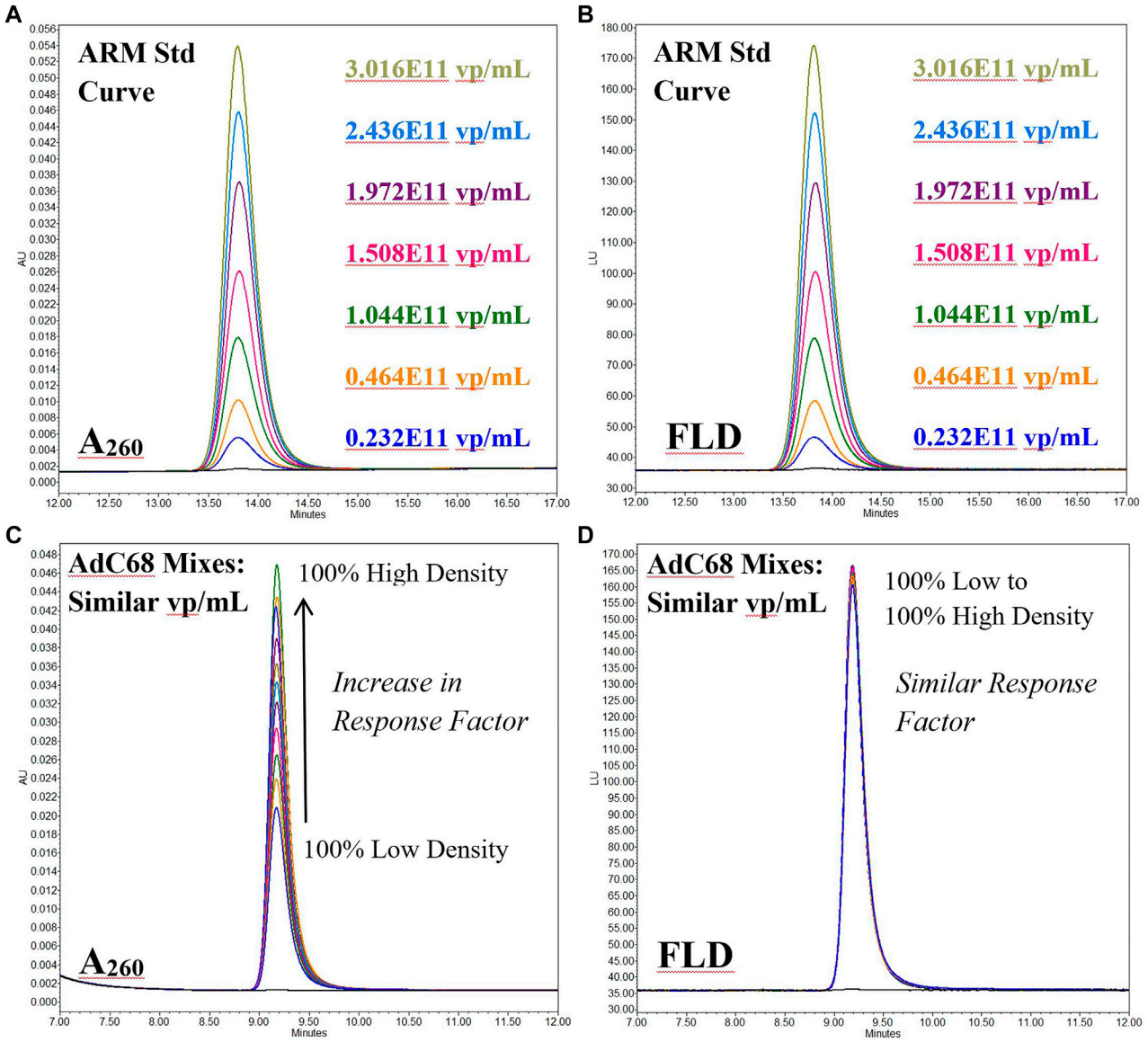

FIGURE 3 | Anion Exchange High Performance Liquid Chromatography overlays of the fluorescence (FLD) and 260 nm absorbance (A_{260}) channels for both Human Ad5 Reference Material (Panels A & B) and mixtures of AdC68 low/high density viral particle fractions (Panels C & D). The Human Ad5 Reference Material data is a serial dilution and shows a similar response factor for both channels. The AdC68 mixtures give an increasing response factor on the 260 nm channel for samples of the similar particle # but differing particle density while that for the fluorescence channel is consistent among all samples.

adenovirus characterization. From the early days of density gradient ultracentrifugation to separate differentially packaged capsids followed by SDS-PAGE to examine the protein content (Prage et al., 1972; Burlingham et al., 1974; Daniell, 1976; Tibbetts and Giam, 1979; Tóth et al., 1982), to substitution of SDS-PAGE with RP-HPLC and mass spectrometry (Lehmberg et al., 1999; Vellekamp et al., 2001; Chelius et al., 2002; Takahashi et al., 2006; Benevento et al., 2014; Perez-Berna et al., 2014; van Tricht et al., 2018) and rounding out with direct content analysis via AUC and DCS (Bondoc and Fitzpatrick, 1998; Berkowitz and Philo, 2007; Berkowitz, 2008; Yang et al., 2008; Shih et al., 2010). The outlier is the introduction of direct measurement of adenoviral mass via CDMS, something that would have been thought almost impossible just a few years ago.

When it comes to direct viral particle content analysis, AUC is the current gold standard, however, it has drawbacks including low sample throughput, high volume sample burn, and complex mathematical data analyses. In this study, DCS gave comparable results while being a more user-friendly technique for daily capsid content analysis. DCS gives results in ~15 min using ~100 µl of material.

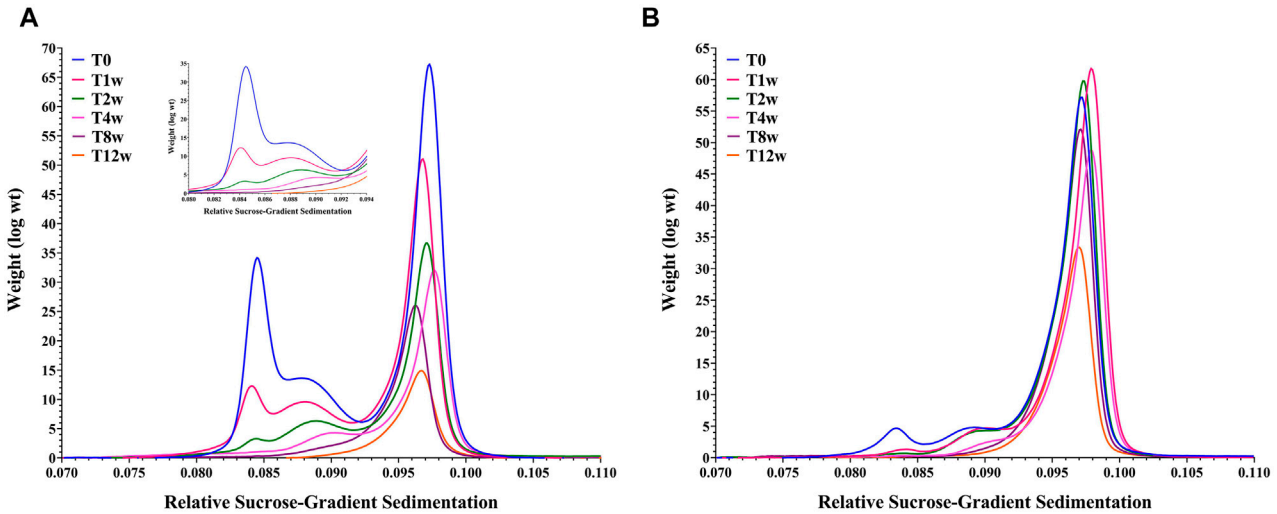

FIGURE 4 | Overlay of Differential Centrifugation Sedimentation data for an AdC68 #1 (Panel A) and AdC68 #2 (Panel B) accelerated stability time course.

CDMS, though currently conducted on prototype instrumentation, is gaining in popularity as a biotherapeutic characterization tool (Pansieri et al., 2020; Wörner et al., 2020; Miller et al., 2021). As with DCS, CDMS is able to obtain information using relatively low volumes of material, an advantage for viral applications. While CDMS was not used to quantitate particle content for the mixtures in this study, the data included represent a proof of concept that the technology could be used for such purposes. A similar study was performed on AAV capsids, which demonstrated that CDMS was highly complementary to AUC (Werle et al., 2021).

Viral Particle Concentration Determination

Even though the exact number of critical quality attributes associated with any pharmaceutical product may vary, all must include a measure of quantity (Center for Drug Evaluatio, 1999), often called strength or concentration, that can be determined accurately throughout product lifetime. The historical approach for adenovirus utilizes UV absorbance at 260 nm of denatured particles via the extinction coefficient determined by Maizel et al. (1968b). Though the exact value of the extinction coefficient has been revisited (Sweeney and Hennessey, 2002), the ease of this determination has made it a staple in adenoviral laboratories.

All told, while the denaturing 260 nm based concentration calculation is sufficient for initial viral particle titering for materials like human ARM (Berkowitz, 2008) and other constructs with a low percentage of empty capsids, the accuracy of this approach wanes as the percentage of empty capsids increases. Thus, in the pharmaceutical space, adequate understanding of the properties of the adenovirus material should be understood before attempting to use the A260 measurement. Specifically, adenovirus applications that have empty and intermediate capsids should avoid use of the A260 measurement or at minimum complement that analyses with AEX-HPLC quantification.

To avoid the empty capsid interference, dose and titering can be determined by counting viral genomes using PCR tools (Thomas et al., 2007; Crettaz et al., 2008; Gallaher and Berk, 2013). Though these methods are more specific in terms of determining DNA amount, they can be biased due to off-targeting of truncated genomes (intermediate particles) that may contain the chosen PCR amplicon. In addition, as with denaturing A260, information about particle integrity is lost so these measurements have little value monitoring particle stability.

In general, a technique that is not biased from the particle content should be implemented for viral particle titer measurements. This allows for consistent particle quantification, regardless of the construct design or implementation of density or charge based purification. The AEX-HPLC method described in this manuscript is a robust tool for accurately counting capsids because the fluorescence detection is blind to viral particle maturity. The one drawback to this method is that it is necessary to have reference standard to quantify against. To this end, the work of the Adenovirus Reference Material Working Group (Hutchins et al., 2000; Hutchins, 2002) created a singular standard to which all other materials can be bridged.

CONCLUSION

From the early days of its study, adenovirus was shown to generate heterogenous packaging populations (Smith, 1965a; Smith, 1965b; Maizel et al., 1968a). This observation generated numerous studies of adenoviral particle maturation leading to a well defined model for capsid assembly (Ahi and Mittal, 2016). However, unlike adeno-associated virus-based gene therapies, where capsid genome packaging ratio is of particular interest because of its clinical significance (Wright, 2008; Wright, 2014a; Wright, 2014b), its impact on adenovirus has had less scrutiny. Here we show that at minimum, this ratio can have considerable

influence on viral particle titering depending on the method chosen. It will also impact the stability and infectivity profiles. In total, a comprehensive adenoviral analytical control strategy is not complete without a robust accounting of the capsid packaging profile.

DATA AVAILABILITY STATEMENT

The datasets presented in this article are not readily available because Raw data may be deemed proprietary by legal. Requests to access the datasets should be directed to lawrence.thompson@pfizer.com.

AUTHOR CONTRIBUTIONS

EM, TP, JZ, JB, KZ and LT designed the study. EM, TP, JZ, KC, LB, BD, SD, KZ and LT performed the experiments. TP, EM, JZ, KC, LB, BD, JB, KZ, QZ, OF, HR, MJ and LT analyzed the results. TP, EM, KZ and LT wrote the manuscript. All authors contributed to the research and reviewed the manuscript.

FUNDING

Funded as part of ongoing research and development within Worldwide Research, Development and Medical by Pfizer, Inc.

REFERENCES

Ahi, Y. S., and Mittal, S. K. (2016). Components of Adenovirus Genome Packaging. *Front. Microbiol.* 7, 1503. doi:10.3389/fmicb.2016.01503

Benevento, M., Di Palma, S., Snijder, J., Moyer, C. L., Reddy, V. S., Nemerow, G. R., et al. (2014). Adenovirus Composition, Proteolysis, and Disassembly Studied by In-Depth Qualitative and Quantitative Proteomics. *J. Biol. Chem.* 289 (16), 11421–11430. doi:10.1074/jbc.m113.537498

Berkowitz, S. A. (2008). Determining the Concentration and the Absorptivity Factor at 260 Nm in Sodium Dodecyl Sulfate of the Adenovirus Reference Material Using Analytical Ultracentrifugation. *Anal. Biochem.* 380 (1), 152–154. doi:10.1016/j.ab.2008.05.014

Berkowitz, S. A., and Philo, J. S. (2007). Monitoring the Homogeneity of Adenovirus Preparations (A Gene Therapy Delivery System) Using Analytical Ultracentrifugation. *Anal. Biochem.* 362 (1), 16–37. doi:10.1016/j.ab.2006.11.031

Blanche, F., Cameron, B., Barbot, A., Ferrero, L., Guillemin, T., Guyot, S., et al. (2000). An Improved Anion-Exchange HPLC Method for the Detection and Purification of Adenoviral Particles. *Gene Ther.* 7 (12), 1055–1062. doi:10.1038/sj.gt.3301190

Bondoc, L., and Fitzpatrick, S. (1998). Size Distribution Analysis of Recombinant Adenovirus Using Disc Centrifugation. *JIMB* 20, 317–322. doi:10.1038/sj.jim.2900529

Burlingham, B. T., Brown, D. T., and Doerfler, W. (1974). Incomplete Particles of Adenovirus. I. Characteristics of the DNA Associated with Incomplete Adenovirions of Types 2 and 12. *Virology* 60 (2), 419–430. doi:10.1016/0042-6822(74)90336-5

Capone, S., D'Alise, A. M., Ammendola, V., Colloca, S., Cortese, R., Nicosia, A., et al. (2013). Development of Chimpanzee Adenoviruses as Vaccine Vectors: Challenges and Successes Emerging from Clinical Trials. *Expert Rev. Vaccin.* 12 (4), 379–393. doi:10.1586/erv.13.15

Center for Drug Evaluation and Research, ICH, Q6B Specifications: Test Procedures and Acceptance Criteria for Biotechnological/Biological Products. 1999, International Conference on Harmonisation of Technical Requirements for Registration of Pharmaceuticals for Human Use.

Chelius, D., Hühmer, A. F. R., Shieh, C. H., Lehmberg, E., Traina, J. A., Slattery, T. K., et al. (2002). Analysis of the Adenovirus Type 5 Proteome by Liquid Chromatography and Tandem Mass Spectrometry Methods. *J. Proteome Res.* 1 (6), 501–513. doi:10.1021/pr025528c

Cheng, C., Wang, L., Ko, S.-Y., Kong, W.-P., Schmidt, S. D., Gall, J. G. D., et al. (2015). Combination Recombinant Simian or Chimpanzee Adenoviral Vectors for Vaccine Development. *Vaccine* 33 (51), 7344–7351. doi:10.1016/j.vaccine.2015.10.023

Cohen, C. J., Xiang, Z. Q., Gao, G. P., Ertl, H. C. J., Wilson, J. M., and Bergelson, J. M. , Chimpanzee Adenovirus CV-68 Adapted as a Gene Delivery Vector Interacts with the Coxsackievirus and Adenovirus Receptor. *J. Gen. Virol.*, 2002. 83(Pt 1): p. 151–155.doi:10.1099/0022-1317-83-1-151

Condezo, G. N., Marabini, R., Ayora, S., Carazo, J. M., Alba, R., Chillón, M., et al. (2015). Structures of Adenovirus Incomplete Particles Clarify Capsid Architecture and Show Maturation Changes of Packaging Protein L1 52/55k. *J. Virol.* 89 (18), 9653–9664. doi:10.1128/jvi.01453-15

Contino, N. C., and Jarrold, M. F. (2013). Charge Detection Mass Spectrometry for Single Ions with a Limit of Detection of 30 Charges. *Int. J. Mass Spectrom.* 345-347, 153–159. doi:10.1016/j.ijms.2012.07.010

Crettaz, J., Olague, C., Vales, A., Aurrekoetxea, I., Berraondo, P., Otano, I., et al. (2008). Characterization of High-Capacity Adenovirus Production by the Quantitative Real-Time Polymerase Chain Reaction: a Comparative Study of Different Titration Methods. *J. Gene Med.* 10 (10), 1092–1101. doi:10.1002/jgm.1236

Daniell, E. (1976). Genome Structure of Incomplete Particles of Adenovirus. *J. Virol.* 19 (2), 685–708. doi:10.1128/jvi.19.2.685-708.1976

Draper, B. E., Anthony, S. N., and Jarrold, M. F. (2018). The FUNPET-A New Hybrid Ion Funnel-Ion Carpet Atmospheric Pressure Interface for the Simultaneous Transmission of a Broad Mass Range. *J. Am. Soc. Mass. Spectrom.* 29 (11), 2160–2172. doi:10.1007/s13361-018-2038-3

Draper, B. E., and Jarrold, M. F. (2019). Real-Time Analysis and Signal Optimization for Charge Detection Mass Spectrometry. *J. Am. Soc. Mass. Spectrom.* 30 (6), 898–904. doi:10.1007/s13361-019-02172-z

Evans, R. K., Nawrocki, D. K., Isopi, L. A., Williams, D. M., Casimiro, D. R., Chin, S., et al. (2004). Development of Stable Liquid Formulations for Adenovirus-Based Vaccines. *J. Pharm. Sci.* 93 (10), 2458–2475. doi:10.1002/jps.20157

Ewer, K. J., Barrett, J. R., Belij-Rammerstorfer, S., Sharpe, H., Makinson, R., Morter, R., et al. (2021). T Cell and Antibody Responses Induced by a Single Dose of ChAdOx1 nCoV-19 (AZD1222) Vaccine in a Phase 1/2 Clinical Trial. *Nat. Med.* 27 (2), 270–278. doi:10.1038/s41591-020-01194-5

Farina, S. F., Gao, G.-p., Xiang, Z. Q., Rux, J. J., Burnett, R. M., Alvira, M. R., et al. (2001). Replication-defective Vector Based on a Chimpanzee Adenovirus. *J. Virol.* 75 (23), 11603–11613. doi:10.1128/jvi.75.23.11603-11613.2001

Folegatti, P. M., Ewer, K. J., Aley, P. K., Angus, B., Becker, S., Belij-Rammerstorfer, S., et al. (2020). Safety and Immunogenicity of the ChAdOx1 nCoV-19 Vaccine against SARS-CoV-2: a Preliminary Report of a Phase 1/2, Single-Blind, Randomised Controlled Trial. *Lancet* 396 (10249), 467–478. doi:10.1016/S0140-6736(20)31604-4

Gallaher, S. D., and Berk, A. J. (2013). A Rapid Q-PCR Titration Protocol for Adenovirus and Helper-dependent Adenovirus Vectors that Produces Biologically Relevant Results. *J. Virol. Methods* 192 (1-2), 28–38. doi:10.1016/j.jviromet.2013.04.013

Hohl, A., Ramms, A. S., Dohmen, C., Mantwill, K., Bielmeier, A., Kolk, A., et al. (2017). Adenovirus Particle Quantification in Cell Lysates Using Light Scattering. *Hum. Gene Ther. Methods* 28 (5), 268–276. doi:10.1089/hgtb.2017.052

Hutchins, B. (2002). Development of a Reference Material for Characterizing Adenovirus Vectors. *Bioprocess J.* 1 (1), 25–29. doi:10.12665/j11.hutchins

Hutchins, B., Sajjadi, N., Seaver, S., Shepherd, A., Bauer, S. R., Simek, S., et al. (2000). Working toward an Adenoviral Vector Testing Standard. *Mol. Ther.* 2 (6), 532–534. doi:10.1006/mthe.2000.0217

Klyushnichenko, V., Bernier, A., Kamen, A., and Harmsen, E. (2001). Improved High-Performance Liquid Chromatographic Method in the Analysis of

Adenovirus Particles. *J. Chromatogr. B Biomed. Sci. Appl.* 755 (1-2), 27–36. doi:10.1016/s0378-4347(00)00597-1

Kondylis, P., Schlicksup, C. J., Zlotnick, A., and Jacobson, S. C. (2019). Analytical Techniques to Characterize the Structure, Properties, and Assembly of Virus Capsids. *Anal. Chem.* 91 (1), 622–636. doi:10.1021/acs.analchem.8b04824

Kuhn, I., Larsen, B., Gross, C., and Hermiston, T. (2007). High-performance Liquid Chromatography Method for Rapid Assessment of Viral Particle Number in Crude Adenoviral Lysates of Mixed Serotype. *Gene Ther.* 14 (2), 180–184. doi:10.1038/sj.gt.3302851

Ledgerwood, J. E., DeZure, A. D., Stanley, D. A., Coates, E. E., Novik, L., Enama, M. E., et al. (2017). Chimpanzee Adenovirus Vector Ebola Vaccine. *N. Engl. J. Med.* 376 (10), 928–938. doi:10.1056/nejmoa1410863

Lehmberg, E., Traina, J. A., Chakel, J. A., Chang, R.-J., Parkman, M., McCaman, M. T., et al. (1999). Reversed-phase High-Performance Liquid Chromatographic Assay for the Adenovirus Type 5 Proteome. *J. Chromatogr. B: Biomed. Sci. Appl.* 732 (2), 411–423. doi:10.1016/s0378-4347(99)00316-3

Maizel, J. V., Jr., White, D. O., and Scharff, M. D. (1968a). The Polypeptides of Adenovirus II. Soluble proteins, cores, top components and the structure of the virion. *Virology* 36 (1), 126–136. doi:10.1016/0042-6822(68)90122-0

Maizel, J. V., Jr., White, D. O., and Scharff, M. D. (1968b). The Polypeptides of Adenovirus. I. Evidence for Multiple Protein Components in the Virion and a Comparison of Types 2, 7A, and 12. *Virology* 36 (1), 115–125. doi:10.1016/0042-6822(68)90121-9

Mangel, W., and San Martín, C. (2014). Structure, Function and Dynamics in Adenovirus Maturation. *Viruses* 6 (11), 4536–4570. doi:10.3390/v6114536

Miller, L. M., Barnes, L. F., Raab, S. A., Draper, B. E., El-Baba, T. J., Lutomski, C. A., et al. (2021). Heterogeneity of Glycan Processing on Trimeric SARS-CoV-2 Spike Protein Revealed by Charge Detection Mass Spectrometry. *J. Am. Chem. Soc.* 143 (10), 3959–3966. doi:10.1021/jacs.1c00353

Pansieri, J., Iashchishyn, I. A., Fakhouri, H., Ostojić, L., Malisauskas, M., Musteikyte, G., et al. (2020). Templating S100A9 Amyloids on Aβ Fibrillar Surfaces Revealed by Charge Detection Mass Spectrometry, Microscopy, Kinetic and Microfluidic Analyses. *Chem. Sci.* 11 (27), 7031–7039. doi:10.1039/c9sc05905a

Perez-Berna, A. J., Mangel, W. F., McGrath, W. J., Graziano, V., Flint, J., and San Martin, C. (2014). Processing of the L1 52/55k Protein by the Adenovirus Protease: a New Substrate and New Insights into Virion Maturation. *J. Virol.* 88 (3), 1513–1524. doi:10.1128/jvi.02884-13

Pierson, E. E., Keifer, D. Z., Asokan, A., and Jarrold, M. F. (2016). Resolving Adeno-Associated Viral Particle Diversity with Charge Detection Mass Spectrometry. *Anal. Chem.* 88 (13), 6718–6725. doi:10.1021/acs.analchem.6b00883

Prage, L., Höglund, S., and Philipson, L. (1972). Structural Proteins of Adenoviruses 8. Characterization of incomplete particles of adenovirus type 3. *Virology* 49 (3), 745–757. doi:10.1016/0042-6822(72)90531-4

Putter, J. S. (2021). Immunotherapy for COVID-19: Evolving Treatment of Viral Infection and Associated Adverse Immunological Reactions. *Transfus. Apher. Sci.* 60 (2), 103093. doi:10.1016/j.transci.2021.103093

Roy, S., Gao, G., Lu, Y., Zhou, X., Lock, M., Calcedo, R., et al. (2004). Characterization of a Family of Chimpanzee Adenoviruses and Development of Molecular Clones for Gene Transfer Vectors. *Hum. Gene Ther.* 15 (5), 519–530. doi:10.1089/10430340460745838

Rux, J. J., and Burnett, R. M. (2004). Adenovirus Structure. *Hum. Gene Ther.* 15 (12), 1167–1176. doi:10.1089/hum.2004.15.1167

Saha, B., Wong, C., and Parks, R. (2014). The Adenovirus Genome Contributes to the Structural Stability of the Virion. *Viruses* 6 (9), 3563–3583. doi:10.3390/v6093563

Shabram, P. W., Giroux, D. D., Goudreau, A. M., Gregory, R. J., Horn, M. T., Huyghe, B. G., et al. (1997). Analytical Anion-Exchange HPLC of Recombinant Type-5 Adenoviral Particles. *Hum. Gene Ther.* 8 (4), 453–465. doi:10.1089/hum.1997.8.4-453

Shih, S.-J., and Yagami, M. (2010). Validation of a Quantitative Method for Detection of Adenovirus Aggregation. *Bioprocessing J.* 9 (2), 25–33. doi:10.12665/j92.shih

Smith, K. O. (1965). Studies on Adenovirus-12. I. Quantitative Correlations between Some Physical, Antigenic and Infectious Properties. *J. Immunol.* 94, 976–989.

Smith, K. O. (1965). Cyclic Structure of Adenovirus DNA. *Science* 148 (3666), 100–102. doi:10.1126/science.148.3666.100

Stanley, D. A., Honko, A. N., Asiedu, C., Trefry, J. C., Lau-Kilby, A. W., Johnson, J. C., et al. (2014). Chimpanzee Adenovirus Vaccine Generates Acute and Durable Protective Immunity against Ebolavirus challenge. *Nat. Med.* 20 (10), 1126–1129. doi:10.1038/nm.3702

Sutjipto, S., Ravindran, S., Cornell, D., Liu, Y.-H., Horn, M., Schluep, T., et al. (2005). Characterization of Empty Capsids from a Conditionally Replicating Adenovirus for Gene Therapy. *Hum. Gene Ther.* 16 (1), 109–125. doi:10.1089/hum.2005.16.109

Sweeney, J. A., and Hennessey, J. P., Jr. (2002). Evaluation of Accuracy and Precision of Adenovirus Absorptivity at 260 Nm under Conditions of Complete DNA Disruption. *Virology* 295 (2), 284–288. doi:10.1006/viro.2002.1406

Takahashi, E., Cohen, S. L., Tsai, P. K., and Sweeney, J. A. (2006). Quantitation of Adenovirus Type 5 Empty Capsids. *Anal. Biochem.* 349 (2), 208–217. doi:10.1016/j.ab.2005.11.014

Tatsis, N., Tesema, L., Robinson, E. R., Giles-Davis, W., McCoy, K., Gao, G. P., et al. (2006). Chimpanzee-origin Adenovirus Vectors as Vaccine Carriers. *Gene Ther.* 13 (5), 421–429. doi:10.1038/sj.gt.3302675

Thomas, M. A., Lichtenstein, D. L., Krajcsi, P., and Wold, W. S. (2007). A Real-Time PCR Method to Rapidly Titer Adenovirus Stocks. *Methods Mol. Med.* 130, 185–192. doi:10.1385/1-59745-166-5:185

Tibbetts, C., and Giam, C. Z. (1979). *In Vitro* association of Empty Adenovirus Capsids with Double-Stranded DNA. *J. Virol.* 32 (3), 995–1005. doi:10.1128/jvi.32.3.995-1005.1979

Tóth, M., Taródi, B., and Béládi, I. (1982). Preparative Separation of Intact Incomplete and Empty Adenovirus Type 2 Particles. *Acta Virol.* 26 (4), 217–220.

van Oostrum, J., and Burnett, R. M. (1985). Molecular Composition of the Adenovirus Type 2 Virion. *J. Virol.* 56 (2), 439–448. doi:10.1128/jvi.56.2.439-448.1985

van Tricht, E., de Raadt, P., Verwilligen, A., Schenning, M., Backus, H., Germano, M., et al. (2018). Fast, Selective and Quantitative Protein Profiling of Adenovirus-Vector Based Vaccines by Ultra-performance Liquid Chromatography. *J. Chromatogr. A* 1581-1582, 25–32. doi:10.1016/j.chroma.2018.10.045

Vellekamp, G., Porter, F. W., Sutjipto, S., Cutler, C., Bondoc, L., Liu, Y.-H., et al. (2001). Empty Capsids in Column-Purified Recombinant Adenovirus Preparations. *Hum. Gene Ther.* 12 (15), 1923–1936. doi:10.1089/104303401753153974

Werle, A., Powers, T. W., Zobel, J. F., Wappelhorst, C. N., Jarrold, M. F., Lyktey, N. A., et al. (2021). Comparison of Analytical Techniques to Quantitate the Capsid Content of Adeno-Associated Viral Vectors. *Mol. Ther. Methods Clin. Dev.* 23, 254–262. doi:10.1016/j.omtm.2021.08.009

Whitfield, R. J., Battom, S. E., Barut, M., Gilham, D. E., and Ball, P. D. (2009). Rapid High-Performance Liquid Chromatographic Analysis of Adenovirus Type 5 Particles with a Prototype Anion-Exchange Analytical Monolith Column. *J. Chromatogr. A* 1216 (13), 2725–2729. doi:10.1016/j.chroma.2008.11.010

Wörner, T. P., Snijder, J., Bennett, A., Agbandje-McKenna, M., Makarov, A. A., and Heck, A. J. R. (2020). Resolving Heterogeneous Macromolecular Assemblies by Orbitrap-Based Single-Particle Charge Detection Mass Spectrometry. *Nat. Methods* 17 (4), 395–398. doi:10.1038/s41592-020-0770-7

Wright, J. F. (2014). AAV Empty Capsids: for Better or for Worse? *Mol. Ther.* 22 (1), 1–2. doi:10.1038/mt.2013.268

Wright, J. F. (2008). Manufacturing and Characterizing AAV-Based Vectors for Use in Clinical Studies. *Gene Ther.* 15 (11), 840–848. doi:10.1038/gt.2008.65

Wright, J. (2014). Product-Related Impurities in Clinical-Grade Recombinant AAV Vectors: Characterization and Risk Assessment. *Biomedicines* 2 (1), 80–97. doi:10.3390/biomedicines2010080

Xiang, Z., Gao, G., Reyes-Sandoval, A., Cohen, C. J., Li, Y., Bergelson, J. M., et al. (2002). Novel, Chimpanzee Serotype 68-based Adenoviral Vaccine Carrier for

Induction of Antibodies to a Transgene Product. *J. Virol.* 76 (6), 2667–2675. doi:10.1128/jvi.76.6.2667-2675.2002

Yang, X., Agarwala, S., Ravindran, S., and Vellekamp, G. (2008). Determination of Particle Heterogeneity and Stability of Recombinant Adenovirus by Analytical Ultracentrifugation in CsCl Gradients. *J. Pharm. Sci.* 97 (2), 746–763. doi:10.1002/jps.21008

Zhang, C., Chi, Y., and Zhou, D. (2017). Development of Novel Vaccines against Infectious Diseases Based on Chimpanzee Adenoviral Vector. *Methods Mol. Biol.* 1581, 3–13. doi:10.1007/978-1-4939-6869-5_1

Zhao, H., Xu, C., Luo, X., Wei, F., Wang, N., Shi, H., et al. (2018). Seroprevalence of Neutralizing Antibodies against Human Adenovirus Type-5 and Chimpanzee Adenovirus Type-68 in Cancer Patients. *Front. Immunol.* 9, 335. doi:10.3389/fimmu.2018.00335

Conflict of Interest: Authors EKM, TWP, JZ, KMC, QC, KZ, OF, HAR, LCT and JJB were employed by Pfizer Inc. Author BED was employed by Megadalton Solutions. Author SD was employed by Nektar Therapeutics.

The remaining authors declare that the research was conducted in the absence of any commercial or financial relationships that could be construed as a potential conflict of interest.

Publisher's Note: All claims expressed in this article are solely those of the authors and do not necessarily represent those of their affiliated organizations, or those of the publisher, the editors and the reviewers. Any product that may be evaluated in this article, or claim that may be made by its manufacturer, is not guaranteed or endorsed by the publisher.

frontiers in Bioengineering and Biotechnology

ORIGINAL RESEARCH
published: 11 January 2022
doi: 10.3389/fbioe.2021.805788

Characterization of Monoclonal Antibody Glycan Heterogeneity Using Hydrophilic Interaction Liquid Chromatography-Mass Spectrometry

Sumit K. Singh[1,2] *and Kelvin H. Lee*[1]*

[1]Department of Chemical and Biomolecular Engineering, University of Delaware, Newark, DE, United States, [2]School of Biochemical Engineering, Indian Institute of Technology (BHU) Varanasi, Varanasi, India

Glycosylation is a critical quality attribute of monoclonal antibody (mAb) therapeutics. Hydrophilic interaction liquid chromatography-mass spectrometry (HILIC-MS) is an invaluable technology for the characterization of protein glycosylation. HILIC/MS-based glycan analysis relies on the library search using Glucose Units (GU) and accurate mass (AM) as the primary search parameters for identification. However, GU-based identifications are gradient-dependent and are not suitable for applications where separation gradients need to be optimized to analyze complex samples or achieve higher throughput. Additionally, the workflow requires calibration curves (using dextran ladder) to be generated for each analysis campaign, which in turn, are used to derive the GU values of the separated glycan species. To overcome this limitation, we employed a two-step strategy for targeted glycan analysis of a mAb expressed in Chinese Hamster Ovary (CHO) cells. The first step is to create a custom library of the glycans of interest independent of GU values (thereby eliminating the need for a calibration curve) and instead uses AM and retention time (RT) as the primary search variables. The second step is to perform targeted glycan screening using the custom-built library. The developed workflow was applied for targeted glycan analysis of a mAb expressed in CHO for 1) cell line selection 2) characterizing the day-wise glycan evolution in a model mAb during a fed-batch culture, 3) assessing the impact of different media conditions on glycosylation, and 4) evaluating the impact of two different process conditions on glycosylation changes in a model mAb grown in a bioreactor. Taken together, the data presented in this study provides insights into the sources of glycan heterogeneity in a model mAb that are seen during its commercial manufacturing.

Keywords: glycosylation, glycan, monoclonal antibody, CHO cell, hydrophilic interaction liquid chromatography

OPEN ACCESS

Edited by:
Christopher Mark Smales, University of Kent, United Kingdom

Reviewed by:
Stuart Haslam, Imperial College London, United Kingdom
Alexander D. Frey, Aalto University, Finland

***Correspondence:**
Kelvin H. Lee
khl@udel.edu

Specialty section:
This article was submitted to Bioprocess Engineering, a section of the journal Frontiers in Bioengineering and Biotechnology

Received: *31 October 2021*
Accepted: *15 December 2021*
Published: *11 January 2022*

Citation:
Singh SK and Lee KH (2022) Characterization of Monoclonal Antibody Glycan Heterogeneity Using Hydrophilic Interaction Liquid Chromatography-Mass Spectrometry. Front. Bioeng. Biotechnol. 9:805788. doi: 10.3389/fbioe.2021.805788

1 INTRODUCTION

Monoclonal antibodies (mAbs) are the fastest-growing modality in the biopharmaceutical industry with application towards treating many diseases including cancer (Grilo and Mantalaris, 2019). An important feature of mAbs that is crucial for safety and efficacy is glycosylation (Eon-Duval et al., 2012). About two-thirds of all the approved biologics include glycosylation as a key post-translational modification bears testimony to its importance in the development of biologics (Walsh, 2018).

The most common type of glycosylation observed in mAbs is N-glycosylation. In this type of glycosylation, glycans are attached to the nitrogen atom of an Asparagine (Asn) residue with a consensus sequence of Asn-X-Ser/Thr, where X is any amino acid except proline (Schwarz and Aebi, 2011). Moreover, N-glycans also possess a common five-membered trimannosyl chitobiose core, to which N-acetylglucosamine, galactose, and sialic acid get added in a probabilistic fashion, resulting in considerable observed glycan complexity and heterogeneity (Fisher et al., 2019). The overwhelming diversity of possible glycan types on a mAb necessitates analytical methods that can characterize the mAb glycosylation at different levels of protein architecture (Jensen et al., 2012; Reusch et al., 2015a; Reusch et al., 2015b). These include analysis at the level of intact proteins, protein subunits, peptides, and released glycans often utilizing liquid chromatography with mass spectrometry and/or fluorescence detection (Kaur, 2021). In addition, other approaches include capillary electrophoresis-mass spectrometry (CE-MS), capillary electrophoresis-laser induced fluorescence detection (LIF), high-performance anion-exchange chromatography with pulsed amperometric detection (HPAEC-PAD), and/or nuclear magnetic resonance (NMR) spectroscopy (Duivelshof et al., 2019).

Among the available analytical methods for glycosylation analysis, a common approach is to release the glycans from the protein by hydrolyzing the side-chain amide group of the asparagine residue of the protein by treating the analyte with Peptide-N-glycosidase F (PNGase F) enzyme (Hilliard et al., 2017). The released glycans are either permethylated, reduced, or labeled with a fluorophore dye before analysis with LC-MS to enhance the optical detection and MS ionization efficiency (Jensen et al., 2012). Chromatographic analysis of glycans is typically performed with hydrophilic-interaction chromatography (HILIC) because of the relatively lower back pressure (due to high fraction of organic solvents during separation) making the analysis amenable to the use of ultra-high-performance liquid chromatographic columns (Lauber et al., 2015). This fact, in turn, facilitates improved resolution under the separation conditions.

HILIC-MS analysis involves the identification of each of the glycans by conversion of the retention time to Glucose Units (GU) (Domann et al., 2007). The GU values of each of the glycans is a specific property of the fluorescent tag used for labeling, and therefore each tag will have a unique GU value for a particular glycan. The most widely used commercial fluorescent tag that is currently used for released glycan analysis is RapiFlour-MS (RFMS), because its properties enable rapid labeling, high sensitivity FLR measurements, and improved MS ionization in the positive mode of operation (Hilliard et al., 2017). Other commonly used fluorescent tags include 2-aminobenzamide (2-AB), 2-aminoanthranilic acid (2-AA), and 4-aminobenzoic acid 2-(diethylamino)ethyl ester (Zhou et al., 2017). While the released glycan assays using GU-based identification followed by confirmation using mass spectrometry have certainly improved analytical performance, this workflow is gradient-dependent (works only with the gradient used for generating the search library). As such, the GU-based glycan workflows are not well-suited for applications where separation gradients need to be optimized to analyze complex samples or achieve higher throughput.

In this work, we developed an alternative workflow that overcomes this limitation by using accurate mass (AM) as the primary search parameter. For this, the search library (from Waters Corp) was modified by removing the GU-information and incorporating the AM data for all the glycan candidates in the search library. Next, the retention time data were included for the glycans of interest as a confirmatory screening variable. Finally, the workflow was applied for screens of the following: 1) cell line selection 2) characterizing the day-wise glycan evolution in a model mAb during a fed-batch culture, 3) assessing the impact of different media conditions on glycosylation, and 4) evaluating the impact of two different process conditions on glycosylation changes in a model mAb grown in a bioreactor.

2 MATERIALS AND METHODS

2.1 Monoclonal Antibody Fed-Batch Cell Culture

Recombinant CHO-K1 Clone A11 expressing the anti-HIV antibody VRC01 (IgG1) was obtained from the Vaccine Research Center at the National Institutes of Health (NIH). Working cell bank cells (1 ml: 90% media and 10% DMSO frozen in liquid nitrogen) were thawed directly into 125 ml vented shake flasks with 30 ml working volume containing ActiPro medium (GE Healthcare) with 6 mM L-glutamine (Sigma-Aldrich) (media 1) and a parallel bank was thawed using a proprietary chemically-defined Medium 2, and a proprietary chemically-defined Medium 3. Cultures were maintained in a 5% CO_2 incubator at 37°C in a 1-inch orbital shaker at 135 rpm. Cells were passaged five times, in the exponential growth phase (every 2–3 days) to a target cell density of 0.4×10^6 cells/ml, before inoculation into the fed-batch.

Fed-batch was carried out in shake flasks and ambr250 bioreactors (Sartorius) using the appropriate feeds for each medium and cells harvested at day 14 or 70% viability whichever came first.

2.2 Protein-A Purification

The mAb from the different cell lines were purified from the cell culture harvest fluid using a 5 ml HiTrap Protein-A HP column (Cat. 17040201, GE Healthcare, Uppsala, Sweden). Briefly, protein A column was equilibrated with 50 mM phosphate containing 150 mM NaCl, pH 7.5 (5CV). Next, the cell culture harvest was loaded onto the column such that a residence time of 4 min was obtained. The column was subsequently washed with the equilibration buffer (2CV). Elution was performed using 100 mM glycine buffer, pH 3 (1.5CV). Before subsequent loading, the column was reconditioned using washing with 2 M NaCl (2CV) and 0.5 M NaOH (2CV). The concentration of the elute was determined using UV-Spectrophotometer (Cat. ND-2000, Thermo Fisher) by recording the absorbance at 280 nm. The samples were buffer exchanged into water +0.1% formic acid before mass spectrometric analysis.

2.3 Glycan Analysis With Library Searching

2.3.1 Glycan Release

Briefly, the purified samples were concentrated to 2 mg/ml in water +0.1% formic acid. A 7.5 ml aliquot (15 mg) was diluted with 15.3 ml of water. To this, a 6 ml of a 5% RapiGest solution (Cat. 186002123, Waters) was added. The solution was heated at 95°C for 5 min and then cooled to the ambient temperature. Next, a 1.2 ml aliquot of Rapid PNGase F was added and mixed by aspiration. The sample solution was incubated at 55°C for 5 min and cooled at room temperature for 5 min.

2.3.2 Glycan Labeling

Following the deglycosylation from the mAb, the released glycans were labeled with RapiFluor-MS™ (RFMS). A 24-reaction kit was used and the RFMS reagent (23 mg) was dissolved in 131 ml of anhydrous DMF. A 12 ml aliquot of this solution was added to the deglycosylation mixture and mixed by aspiration. The labeling reaction was allowed to proceed at room temperature for 5 min. The reaction was then quenched with the diluting reaction mixture with a 360 µl aliquot of acetonitrile (ACN).

2.3.3 Glycan Purification

The labeled glycans were purified using a HILIC µ-elution plate. The wells of the µ-elution plate were conditioned with 200 µl aliquots of water (three times). The steps in purifying the labeled glycans from other byproducts involve the following steps: equilibration with 200 µl of 85% ACN, sample loading (~400 µl), wash with 1% formic acid, 90% ACN, and finally elution with 30 µl SPE Elution Buffer (200 mM ammonium acetate in 5% ACN). The eluate was diluted with 310 µl of GlycoWorks SPE diluent (DMF/ACN) and mixed by aspiration.

2.3.4 UPLC-MS

The purified glycans from the above step were separated on a Waters ACQUITY UPLC system® using Waters ACQUITY UPLC Glycan BEH Amide column (2.1 × 150 mm, 1.7 mm particle size, 130 Å pore size). A 50 mM ammonium formate solution (pH = 4.4) was used as mobile phase A and a 100% ACN solution was used as mobile phase B. Other parameters for chromatographic separation of glycans included column temperature: 60°C and 75–54% gradient of mobile phase B over 35 min at a flow rate of 0.4 ml/min. The separated glycans were detected using a fluorescence (FLR) detector with an excitation wavelength of 265 nm and an emission wavelength of 425 nm. MS data were recorded on a Bioaccord® Waters MS system operated in positive ion mode. MS parameters included: m/z range: 50–2000, capillary voltage: 1.5 kV, cone voltage: 45 V. The MS was calibrated using ACQUITY RDa calibrant and wash solution (Cat. 186009012, Waters) and lock mass calibration was performed using ACQUITY RDa lock mass solution (Cat. No. 186009012, Waters).

2.3.5 Data Analysis

The glycan peak annotation was performed using the Glycan Assay (FLR with MS confirmation) workflow within UNIFI. Initially, a calibration curve is constructed by running a dextran ladder labeled with RFMS (Cat No. 186007982, Waters) using the above-described method conditions. The components of the dextran ladder, G4 through G12 with the expected retention times are noted. Next, the retention times of the released glycans are converted into GU values using the calibration curve. The GU values of the assigned species are then matched with the potential glycan structures in the RFMS glycan GU scientific library in UNIFI with a GU tolerance of 0.2 units and mass error of 15 ppm. The relative abundance of any mass confirmed glycan species was determined from the dividing FLR peak area of that species with the total summed peak area of all the identified glycans. Statistical analysis for comparing mAb glycosylation from different cell lines was done by two-way ANOVA using Tukey post-test with Graphpad software version 8.4.

3 RESULTS

3.1 Glycan Analysis of VRC01 mAb Using the Standard Method

The glycan analysis of the VRC01 using the standard library search method resulted in the identification of 53 confirmed N-glycans, out of which 44 were assigned based on both GU values and accurate mass, while the remaining nine glycan species were annotated based on GU values alone (**Figure 1**). These nine glycan species were low abundance glycans (<2%) and co-eluted with a more abundant glycan species that potentially resulted in suppression of its mass spectrum. **Table 1** lists out the identified glycans with their corresponding normalized abundances expressed as the total area of the FLR peak. The relative abundances of these glycans spanned in the range from 0.1% (A2[3]G(4)1S(6)1) to 11.92% (F(6)A2G(4)2S(3,3)2). A total of 18 glycans were base-line resolved, while 35 glycans co-eluted with a more abundant species but were identified and mass-confirmed with this method. Out of the 53 identified glycans, 25 were complex biantennary, 12 were complex triantennary, five were complex tetra antennary, five were high mannose, and six were hybrid glycans. The individual glycan species identified for the VRC01 mAb were grouped into various glycan attributes and are shown in **Figure 2**. The percentage calculated is the sum of individual normalized amounts (**Table 1**) for each glycan species contributing to the overall abundance of a given attribute. As it is evident from **Figure 2**, the majority of glycans are complex biantennary glycans (~57%). High mannose forms also constitute ~13.2% of the overall glycans of VRC01 indicating the presence of immature glycoforms. Of the total identified VRC01 glycans, ~70% of the glycans were galactosylated, ~51% of them were terminally sialylated, and ~68% were core-fucosylated. The higher levels of sialylation observed in VRC01 is an unusual feature generally not observed with mAbs, thereby suggesting it to be an important quality attribute of VRC01. The heavy sialylation level seen in the VRC01 was attributed to glycans occupying the light chain that comprised of heterogenous population of bi-, tri-, and tetraantennary, core fucosylated complex galactosylated and terminally sialylated glycans.

Based on the VRC01 glycan profile using the standard analysis method, 12 glycan species were selected for the monitoring using

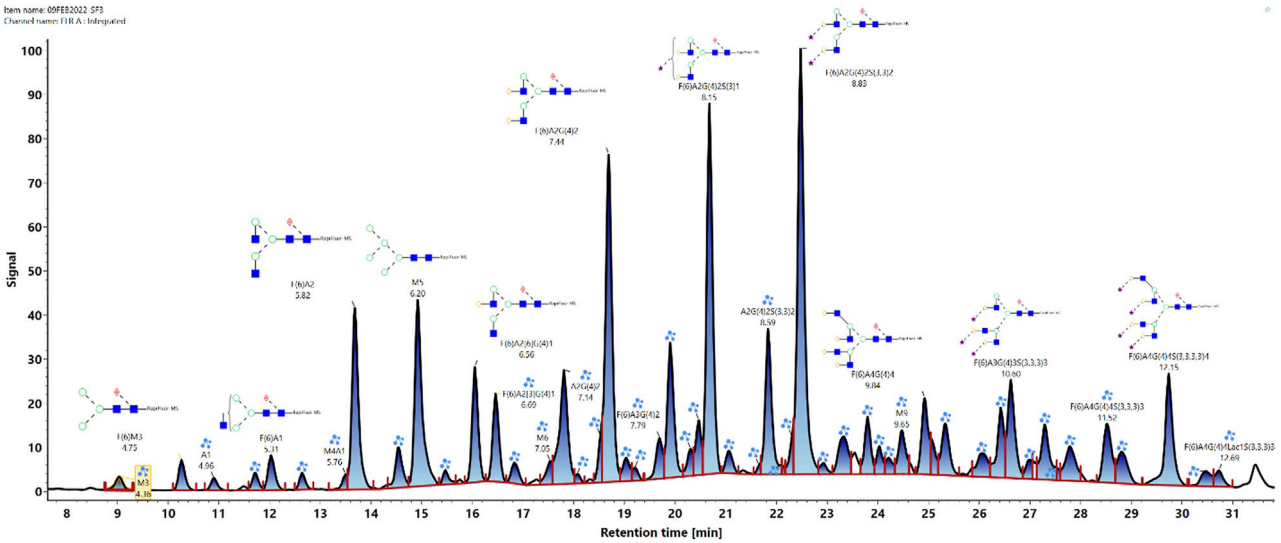

FIGURE 1 | Released N-glycan map from the FLR channel of the HILIC- UPLC-FLR-MS analysis of VRC01 mAb. In total 53 glycans were identified and annotated (44 were identified and annotated based on GU and accurate mass, while 9 of them were based only on GU values).

the glycan screening method (highlighted in **Table 1**). The selection of these species was made based on the relative % amount, with each of these glycan species present in an amount greater than or equal to 3%. Cumulatively, these 12 glycan species constitute ~65% of overall VRC01 glycans.

3.2 Glycan Screening Method

The first step in the development of the glycan screening method was to prepare a library of glycan species devoid of GU value information. This step was accomplished by deleting the corresponding GU values of each of the glycan species from the existing waters-commercial glycan library. The Waters commercial glycan library contains GU values of 168 N-linked glycans derived from trastuzumab, infliximab, etanercept, NISTmAb, human serum polyclonal IgG, mouse serum polyclonal IgG, erythropoietin, bovine fetuin, and yeast invertase (Hilliard et al., 2017). The rationale of choosing these glycoproteins for the generation of glycan search library was two-fold: 1) to comprehensively cover the three classes of N-linked glycans namely, high mannose, complex, and hybrid structures; and 2) to provide the extensive coverage of the N-linked glycans that are routinely attached to the therapeutic mAbs and other biopharmaceutical products. Each of these glycans in the commercial library contains information about the corresponding GU values and accurate mass information. The glycan screening library, therefore, is composed of these 168 N-linked glycan species with their only corresponding accurate mass information (**Supplementary Table S1**). Further, the retention time information of the VRC01 glycan species that are shortlisted for screening was updated to the glycan screening method from the standard run. We note that accurate mass will be used as a primary search variable while the retention time of the glycan species is to be used as a confirmatory variable in the glycan screening method. The retention time information needs to be updated for each separation gradient used for the glycan analysis.

3.3 Comparison of VRC01 Glycosylation From Four Different Clones

Several clonal CHO cell lines expressing VRC01 mAb were evaluated for the following criterion: the clone should have maximum viable cell densities ranging between 1.0–2.0 × 10^7 cells/ml and enough volumetric productivity over a standard 14 days fed-batch platform process to ensure that enough material for analysis of N-linked glycans was generated for analysis. Further, the glycan profile should be within a range that allows for any change to be reliably measured in every aspect of the glycosylation profile: galactosylation, fucosylation, sialylation, and high mannose content.

We conducted eight independent fed-batch experiments using the glycan screening method to select one out of the four available clones (two replicates for each clone) for further evaluation. Each of the clones exhibited different volumetric productivities and were developed using a DHFR-based MTX selection system and the detail of their development is provided in a recent publication (Nmagu et al., 2021). The clones, specifically A11, CP24, CP19, and CP 35 demonstrated titers of 1,770, 1,550, 750, and 61 mg/L (Nmagu et al., 2021).

The glycosylation profiles of VRC01 from these clones show large reproducible differences in the levels of sialylation, galactosylation, and fucosylation. As shown in **Figure 3**, the highest producing clone A11, exhibited maximum relative abundance of the levels of sialylation (~24%), galactosylation (55%), and fucosylation (50%). On the other hand, the lowest

TABLE 1 | List of the confirmed N-glycans derived from VRC01 mAb analyzed in the study. Also included are the observed retention times, normalized abundance (% amount), expected and observed GU values, expected and observed masses, the predominant charge state, and the response units. The highlighted glycan species are those that are shortlisted to be monitored using the screening workflow.

SL. No	Component name	Observed RT (min)	Glycan units	Observed mass (Da)	% Amount (%)	Expected glycan units	Expected mass (Da)	Charge	Response
1	M3	9.04	4.3583	1,221.507	0.43	4.3633	1,221.502	2	31886133
2	F(6)M3	10.27	4.752	1,367.564	0.81	4.7617	1,367.56	2	60887988
3	A1	10.9	4.9581	1,424.587	0.33	4.9699	1,424.582	2	24741016
4	M4	11.72	5.2148	1,383.558	0.46	5.3077	1,383.555	2	34666288
5	F(6)A1	12.03	5.3126	1,570.643	1	5.2906	1,570.64	2	75026269
6	A2	12.64	5.5003	1,627.665	0.42	5.4619	1,627.661	2	31299243
7	M4A1	13.5	5.7619	1,586.637	0.32	5.7402	1,586.635	2	24184490
8	F(6)A2	13.68	5.8169	1,773.727	4.98	5.7879	1,773.719	2	3.74E+08
9	F(6)A1[3]G(4)1	14.54	6.0808	1,732.698	1.24	6.095	1,732.692	2	93050430
10	M5	14.92	6.1996	1,545.611	5.75	6.1692	1,545.608	2	4.31E+08
11	A2[3]G(4)1	15.47	6.3716	1,789.718	0.36	6.29	1,789.714	2	27222853
12	F(6)A2[6]G(4)1	16.05	6.559	1,935.777	2.87	6.5337	1,935.772	2	2.15E+08
13	F(6)A2[3]G(4)1	16.46	6.6921	1,935.779	2.3	6.6633	1,935.772	2	1.72E+08
14	F(6)A2[6]BG(4)1	16.83	6.8134	2,138.856	0.66	6.8	2,138.851	2	49258887
15	M6	17.54	7.0486	1,707.662	0.61	7.1138	1,707.661	2	45834299
16	A2G(4)2	17.81	7.1397	1,951.772	4.05	7.0955	1,951.767	2	3.04E+08
17	M6 D1	18.07	7.2303	854.8377	0.21	7.14	821.7959	2	15499336
18	A2BG(4)2	18.52	7.3836	2,154.865	0.78	7.35	2,154.846	3	58458127
19	F(6)A2G(4)2	18.69	7.4413	2,097.832	8.91	7.4266	2,097.825	2	6.68E+08
20	M5A1G(4)1	19.03	7.5596	1,910.739	0.69	7.431	1,910.74	2	51800792
21	F(6)A2BG(4)2	19.21	7.6232	2,300.913	0.31	7.605	2,300.904	3	23189435
22	F(6)A3G(4)2	19.69	7.7936	2,300.912	1.15	7.7585	2,300.904	3	86301406
23	F(6)A2[6]G(4)1S(6)1	19.9	7.8696	2,226.876	3.7	7.84	2,226.867	2	2.77E+08
24	M7 D1	20.3	8.0131	1,869.719	0.65	8.0285	1,869.714	2	48971172
25	A2G(4)2S(3)1	20.47	8.0732	748.6280	1.29	8.06	729.282	2	96888102
26	F(6)A2G(4)2S(3)1	20.68	8.1502	2,388.927	9.36	8.124	2,388.92	2	7.01E+08
27	F(6)A2[3]G(4)1Sg(6)1	21.06	8.2939	2,242.868	0.65	8.3057	2,242.862	2	48619741
28	F(6)A2G(4)2S(6)1	21.65	8.5146	1,195.4673	0.14	8.55	1,394.5757	2	10806796
29	A2G(4)2S(3,3)2	21.83	8.5856	2,533.966	3.97	8.57	2,533.958	3	2.97E+08
30	A2[3]G(4)1S(6)1	22.11	8.6935	694.6104	0.1	8.69	586.5778	2	7558824
31	F(6)A2BG(4)2S(6)1	22.3	8.7666	2,592.009	0.67	8.82	2,591.999	3	50024309
32	F(6)A2G(4)2S(3,3)2	22.47	8.8339	2,680.025	11.92	8.85	2,680.016	3	8.94E+08
33	A2G(4)2S(3,6)2	22.92	9.0107	2,533.965	0.33	9	2,533.958	3	24788235
34	A3G(4)3S(3)1	23.33	9.1737	2,608.012	1.57	9.23	2,607.994	3	1.18E+08
35	A2G(4)2S(6,6)2	23.8	9.3668	845.6598	1.48	9.415	869.3230	2	1.11E+08
36	F(6)A3G(4)3S(3)1	24.02	9.4614	2,754.06	0.68	9.538	2,754.052	2	50906409
37	F(6)A2G(4)2S(6,6)2	24.21	9.5405	2,680.015	0.47	9.69	2,680.016	2	35023310
38	M9	24.47	9.6488	2,193.825	1.32	9.6667	2,193.819	2	98775879
39	F(6)A4G(4)4	24.92	9.8416	2,828.098	2.12	9.915	2,828.089	3	1.59E+08
40	F(6)A3Lac3	25.05	9.8994	1,537.1048	0.68	9.91	1,529.1198	2	50960194
41	F(6)A3G(4)3Lac1	25.33	10.019	2,828.1	1.72	10.015	2,828.089	3	1.29E+08
42	A3S(6)1G(4,4,3)3S(3,6)2	26.04	10.3369	3,190.18	1.1	10.31	3,190.185	3	82361071
43	M10 a3D1,a3D3,a2D4(2)	26.42	10.5103	2,355.882	2	10.53	2,355.872	2	1.5E+08
44	F(6)A3G(4)3S(3,3,3)3	26.62	10.6002	3,336.262	2.97	10.6267	3,336.243	3	2.23E+08
45	A3G(4)3S(3,3,6)3	26.99	10.774	2,879.0101	0.51	10.72	2,862.6845	3	38209650
46	F(6)A3G(4)2Ga(3)2Sg(6)1	27.29	10.9168	978.3740	1.99	10.94	940.687	2	1.49E+08
47	F(6)A4G(4)4Lac1	27.53	11.0304	3,193.235	0.14	11.01	3,193.221	3	10417180
48	F(6)A3G(4)3Lac2	27.79	11.1559	1,065.41	1.52	11.16	1,059.7256	2	1.14E+08
49	F(6)A4G(4)4S(3,3,3)3	28.52	11.5199	3,701.393	2.02	11.52	3,701.375	3	1.51E+08
50	F(6)A3G(4) 3Lac1S(3,3,3)3	28.81	11.666	3,701.389	1.39	11.71	3,701.375	3	1.04E+08
51	F(6)A4G(4)4S(3,3,3,3)4	29.73	12.148	3,992.491	3.7	12.17	3,992.471	3	2.77E+08
52	F(6)A3G(4) 3Lac2S(3,3,3)3	30.47	12.5441	4,066.515	0.66	12.52	4,066.508	3	49654386
53	F(6)A4G(4) 4Lac1S(3,3,3)3	30.73	12.6875	4,066.512	0.54	12.7	4,066.508	3	40618466

Abbreviations: F, fucose; G, galactose; A1, monoantennary; A2, biantennary; Sg, N-glycolylneuraminic acid; Ga, a1,3-linked galactose.

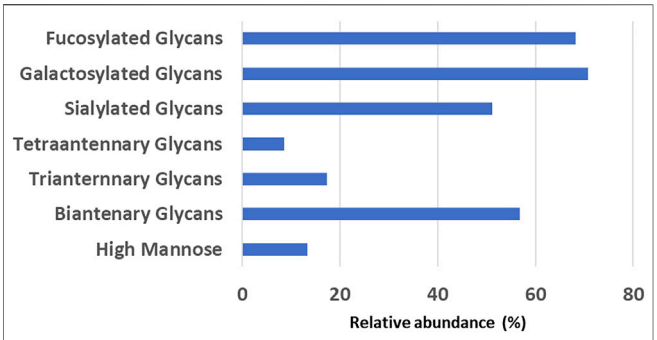

FIGURE 2 | The relative abundance levels of various glycan attributes obtained by summing the corresponding normalized abundance levels for each glycan species that possess that attribute (listed in **Table 1**).

producing clone CP35 exhibited the lowest relative abundance of sialylation (10%), galactosylation (35%), and fucosylation (25%). The intermediate producer clones, CP19 and CP24, resulted in relative levels of sialylation, and fucosylation that were less than A11, but higher than CP35. The galactosylation levels in CP24 and CP35 clones were 33.9 ± 1.97 and 36.9 ± 4.36, thereby indicating that the changes are not statistically significant between these 2 cell lines. However, it was found that while the productivity of CP24 cell lines was more than CP19, the levels of the sialylation, galactosylation, and fucosylation were higher in CP19 indicating that the glycosylation levels does not follow a linear relationship with the productivity of the clone. All four clones exhibited different glycan profiles indicating variability in the glycan processing machinery potentially attributed to differential availability of nucleotide sugars, glycan precursors, conformational steric hindrance, and metabolic activity of each clone.

There was no significant difference in the levels of the high mannose glycoforms (M5 forms) in VRC01 from any of the four clones indicating that the structural diversification from the immature high mannose N-glycans into relatively more processed and functionally mature forms consisting of hybrid and complex N- glycans subtypes did take place, regardless of the differences in the productivity of the clones. All clones exhibited similar viable cell density and viability profiles through day 3 before diverging, likely as a result of innate clonal variations. Clone CP35 seemed to diverge the most as it exhibited the highest VCD with nearly 50% greater cell density during exponential growth. This increase in exponential growth for CP35, correlated

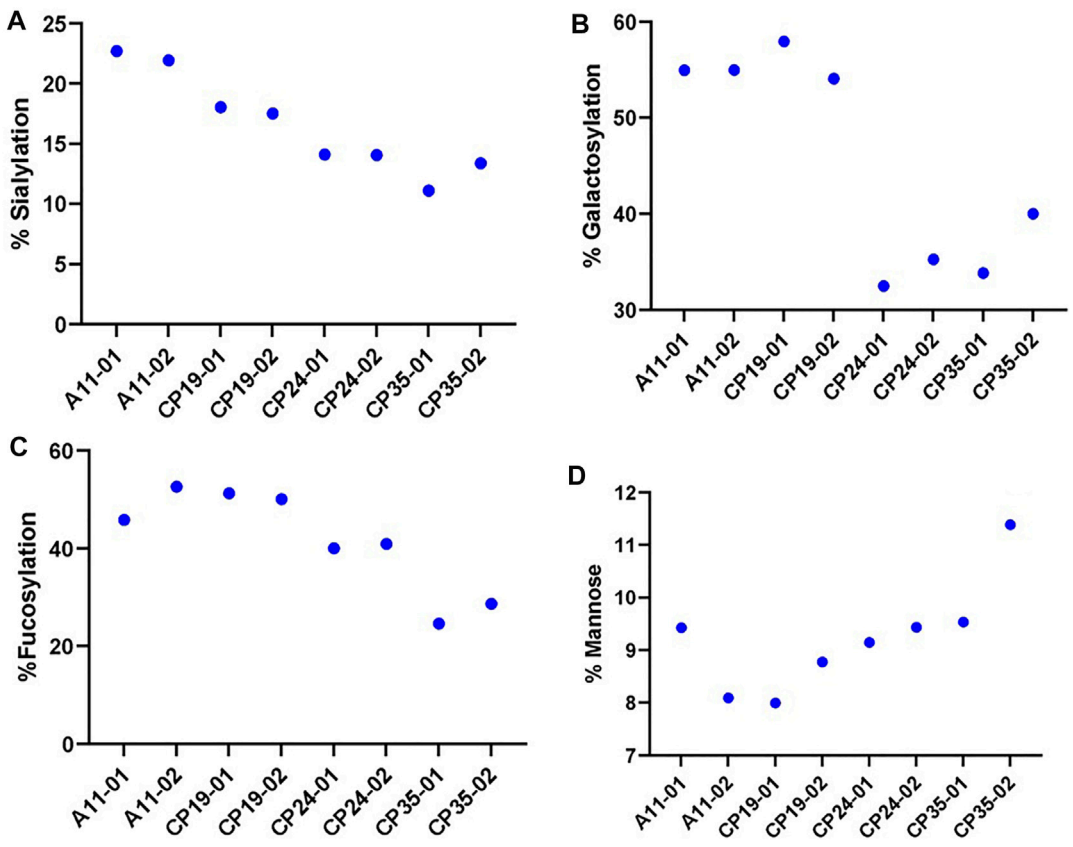

FIGURE 3 | The relative levels of various glycan attribute. **(A)** Sialylation, **(B)** Galactosylation, **(C)** Fucosylation and **(D)** Mannose content for four different CHO clones (A11, CP19, CP24, and CP35) expressing VRC01 mAb in a 12 days long fed-culture. The suffix 01 and 02 represents the biological replicates for each of the clone.

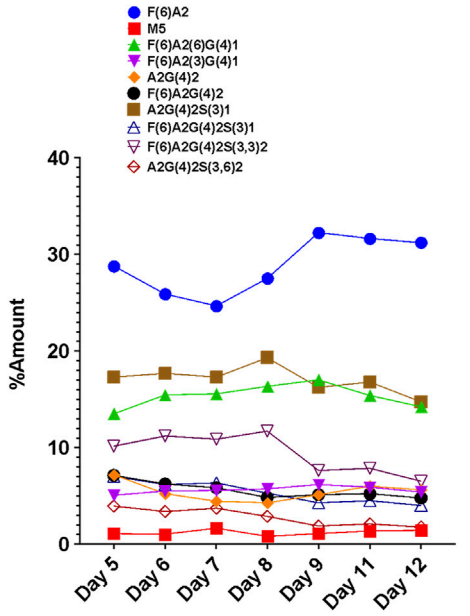

FIGURE 4 | Day-wise evolution of various glycan species of the VRC01 mAb expressed using A11 CHO cell line in fed-batch culture.

with greater glucose/nutrient consumption and lactate production which may be associated with apoptosis, leading to a shortened fed-batch culture duration in comparison to the other cell clones. Meanwhile, clone A11 showed slightly greater late culture viability than CP19 and CP24, and A11 had a distinctively lower lactate profile than the other cell clones. Based on these characteristics, the A11 clone was selected for further studies to explore glycosylation dynamics of VRC01 under different culture conditions.

3.4 Day-Wise Evolution of VRC01 Glycans in a Fed-Batch CHO Cell Culture

The A11 CHO clone was cultivated in a 14 days fed-batch cell culture process, carried out in a 25 ml shake flask. HILIC was used for VRC01 glycan analysis from cell-culture harvest samples collected on different days across exponential growth (days 5, 7, and 8) and the stationary production phase (days 9 and 11) (Nmagu et al., 2021). The individual glycan structures were then grouped into major glycosylated species, namely high mannose, galactosylated, sialylated, fucosylated, and afucosylated species.

The FLR traces of the monitored glycans of the VRC01 for the respective days are shown in **Figure 4**. On day 5, all 12 monitored glycans species were detected and identified, though some were low abundance. With the increasing cell culture duration until day 8, the relative abundance of certain glycan species such as F(6)A2, F(6)A2(6)G(4)1, F(6)A2(3)G(4)1, increased. However, the amounts of F(6)A2G(4)2, F(6)A2G(4)2S(3)1, F(6)A2G(4)2S(3,3)2, A2G(4)2S(3)1 remained relatively constant from day 5 to day 8 (growth phase). From day 8 onwards, the relative abundances of the latter glycan species started decreasing, while the former glycans remained unchanged. The relative abundance of the M5 species remained the same throughout the cell culture period. These data are consistent with a bottleneck in the VRC01 glycosylation that is not in the ability to convert high mannose into low mannose (and followed by the subsequent extension of the glycosylation network in the Golgi), but with steps leading to the transfer of galactosyl and sialyl transfer might be the rate-limiting step in overall glycosylation reaction of the VRC01 in CHO cells. The relatively constant levels of glycoforms such as A2G(4)2S(3)1, F(6) A2G(4)2S(3)1, F(6)A2G(4)2S(3,3)2, and A2G(4)2S(3,6)2 (all of them representing terminally sialylated forms) was observed during the cell culture phase when the viable cell density (VCD) was increasing. However, as the VCD started to decline from day 8 onwards, the relative abundances of the sialylated glycoforms also started decreasing. This decrease in the levels of sialylated glycans at later days of the cell culture (beyond day 8) might be attributed either to the availability of necessary nucleotide sugar donors (NSDs) or the expression levels of the enzymes responsible for the transfer of sialic acid to the growing glycosylation network on the VRC01, or both.

3.5 Comparison of VRC01 Glycosylation Grown in Three Different Media

The workflow was used for the assessment of the impact of the different cell culture media on the VRC01 glycosylation characteristics. Here, the VRC01 mAb were expressed in a fed-batch CHO culture in both bioreactor and the shake-flask modes of operation in three different media (Media 1, 2, and 3). As shown in **Figure 5A**, glycans of the VRC01 grown in Media 1 and 2 show similar relative abundances. In contrast, we observed a lower abundance of all glycan species from samples grown in Medium 3 as evidenced by the signal intensity in **Figure 5A**. The Man 5 species was ~27 and ~52% less in Media 2 and 3, respectively, as compared to that of Medium 1. Similarly, the afucosylated content (mainly from the A2G(4)2 and A2G(4)2S(3,3)2 species) constituted 11.2, 14.9, and 15.6% respectively in Media 1, 2, and 3. Another significant difference in the VRC01 glycosylation that was seen across the three media was in levels of sialylation which exhibited the following trend: sialylation (Medium 3)> sialylation (Medium 2) > sialylation (Medium 1). The increase in sialylation in Media 2 and 3 were attributed to the increase in the relative abundances of following glycan species in Media 2 and 3, respectively as compared that in Medium 1: F(6)A2[6]G(4)1S(6)1 (25.6 and 29.9%), F(6)A2G(4)2S(3)1 (17 and 28.2%), A2G(4)2S(3,3)2 (39.6 and 62%), F(6)A2G(4)2S(3,3)2 (49.2 and 59.3%), F(6)A3G(4)3S(3,3,3)3 (15.3 and 50%), and F(6)A4G(4)4S(3,3,3,3)4 (57 and 56%). Thus, we generally observed a modest increase in the levels of mono-sialylation, and a significant increase in the levels of di-, tri-, and tetra-sialylation of VRC01 glycans in Media 2 and 3, respectively as compared to Medium 1. In addition, consistent with this trend, a modest increase of 12.7 and 21.2% were noted in the levels of galactosylation of VRC01 grown in Media 2 and 3 as compared to Medium 1 (**Figure 5B**).

The low levels of high mannose glycans along with higher levels of afucosylated glycans seen in Media 2 and 3 as compared to Medium 1 suggests a positive impact of cell culture medium

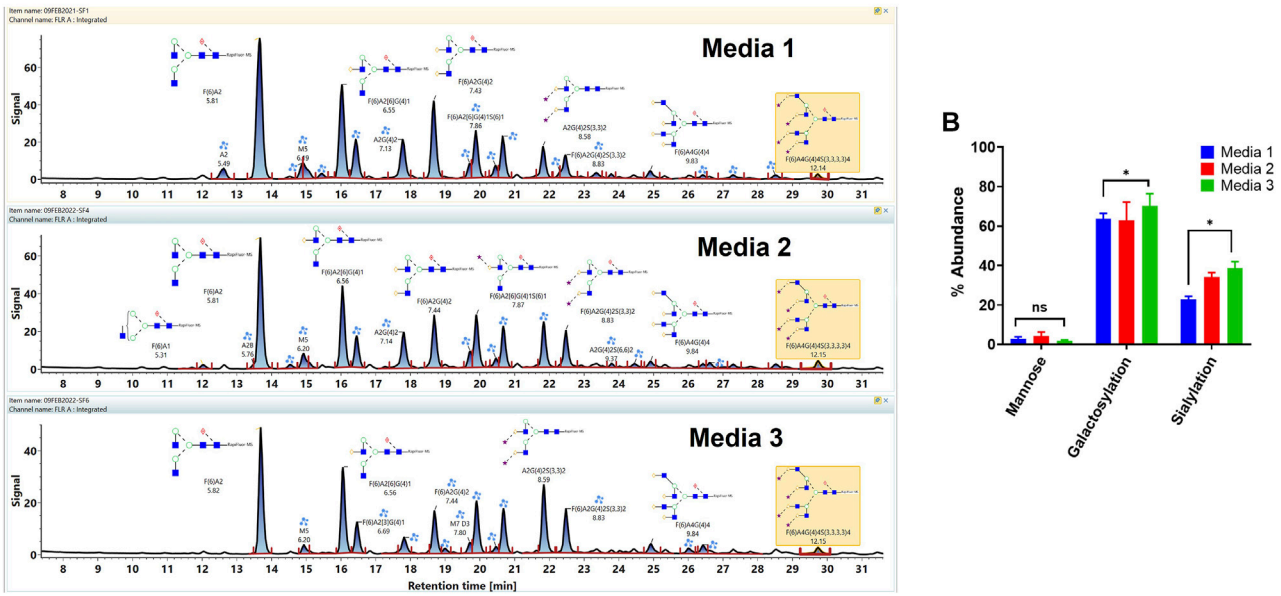

FIGURE 5 | (A) Released glycan map (FLR trace) of the VRC01 expressed using A11 clone in three different media. **(B)** Relative abundance of various glycan attributes of VRC01 grown in the three different media.

composition on the product quality attribute of VRC01 in the former as compared to the latter. The presence of high mannose glycans in biotherapeutics has been correlated with their rapid clearance in the body resulting in decreased half-life of the molecule. Similarly, a positive correlation between the levels of afucosylated glycans and the antibody-mediated cell cytotoxicity has been established. Recently, a positive correlation in the levels of sialylation and anti-inflammatory activity has also been observed for several mAbs.

3.6 Comparison of VRC01 Glycosylation Grown Under Two Different Process Conditions

Finally, the glycan profile of VRC01 grown in the Ambr250 bioreactor under two different process conditions was assessed using a glycan screening workflow. The two processes differed from each other in terms of the feedback loop used for DO control over the course of the cell culture (**Supplementary Figure S1**). The processes are referred to as 2-level DO and 6-level DO, respectively.

As seen in **Figure 6**, there are substantial differences in the glycosylation profiles of the VRC01 expressed under these two conditions. The 6-level DO process resulted in the presence of greater than ~10-fold higher mannose forms in the VRC01 than the 2-level DO process. This difference is evident from the presence of M5, M7, and M9 forms (peaks 2, 7, 12 in **Figure 6A**) in the former and was completely absent (except trace levels of M5) in the latter. Even though the overall galactosylation levels of the VRC01 from both processes were similar, several compositional differences of individual glycan forms were also noted between the two processes. For example, while the ratio of peak areas of G1F isoforms (peaks 3 and 4) is 3:1 for the 2-level DO process, it is almost 1:1 for the 6-level DO process. However, the G2F species (peak 6) is significantly higher in abundance in the 6-level DO process than the 2-level DO process, thereby compensating for the decrease in the G1F form. There was no significant change in the sialylated forms (peaks 8, 9,10, and 11), which resulted in a similar level of overall sialylation in the VRC01 from both processes.

Thus, the workflow can highlight the impact of process changes on the observed glycan heterogeneity of mAbs from CHO cell cultures.

4 DISCUSSION

A major consideration with the CHO-based mAb production is the need to assess the glycan heterogeneity. Several factors, including process parameters, media and feed compositions, cell culture duration, and feeding strategy impacts glycan heterogeneity (Batra and Rathore, 2016). It is important to understand the source of glycan heterogeneity during mAb production to devise strategies to minimize the glycosylation variations observed during manufacturing. Towards this goal, an analytical method that can provide a comprehensive mAb glycosylation profile by separating and resolving as many glycan species as possible is of significant interest. The current approach of performing such an analysis is by the enzymatic release of the glycans from the mAbs followed by their separation and detection using LC-FLR-MS (Hilliard et al., 2017).

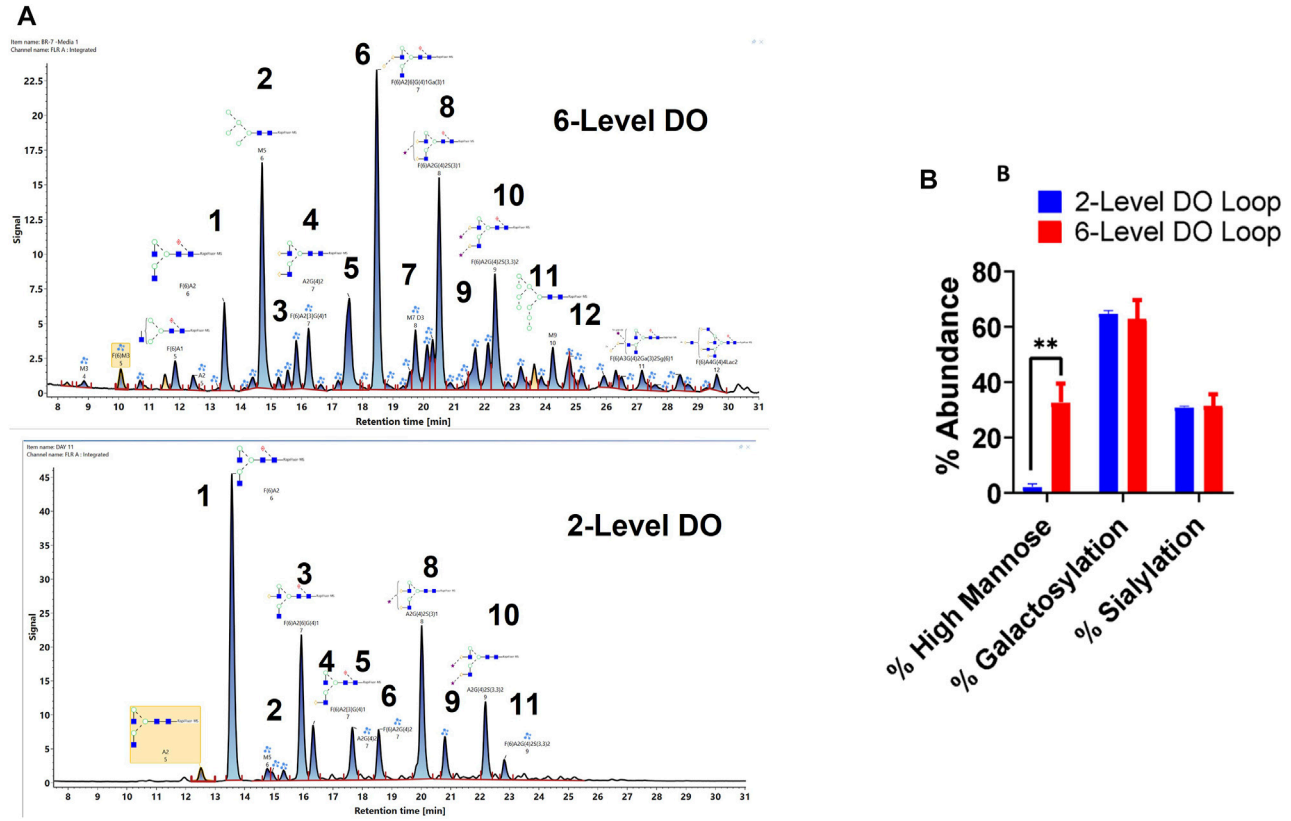

FIGURE 6 | (A) Released glycan map (FLR trace) of the VRC01 expressed using A11 clone using two different processes in Ambr 250 bioreactor. **(B)** Relative abundance of various glycan attributes of VRC01 grown under the two process conditions.

In the present study, a screening method for glycan analysis is developed that leverages the accurate mass and retention time of the glycan species for their identification and annotation. The proposed method has an advantage over the existing released glycan workflows regarding its ability to optimize the separation gradient that can help improve the resolving power of the chromatography. Additionally, the method does not require calibration using the dextran ladder for each analysis campaign as only the accurate mass and retention time is used for identification and annotation of the glycan species in the released glycan map, thus the method offers advantages as a screening approach as a surrogate to other methods that may be validated.

The method was applied to understand the glycan heterogeneity of VRC01 under various processing conditions. The existing literature attributes cell culture duration as one of the most dominant factors that bring about changes in the N-glycan distribution, gene expression profiles, metabolic states, and changes in the cell cycle (Bibila and Robinson, 1995; Hossler et al., 2009; Pacis et al., 2011). A general trend that is observed for different host cell lines, mAbs, and feeding strategies is an increase in the specific productivity with a simultaneous decrease in the levels of galactosylation over the course of typical fed-batch cell culture (Madabhushi et al., 2021). The decrease in the levels of galactosylation is more pronounced towards the end of the culture (Sumit et al., 2019). Our observations are consistent with this trend. The enhanced protein secretion capacity (at higher specific productivity) potentially corresponds to shorter Golgi residence time, but at the same time limits the glycosylation reactions leading to incomplete processing of the glycosylation resulting in lower galactosylation levels (Hossler et al., 2007; Kantardjieff et al., 2010; Val et al., 2016). However, our data on the glycosylation profiles of the VRC01 mAb expressed in CHO cell lines with a wide range of cell-specific productivities shows that the least productive clone also had the lowest galactosylation levels. This observation suggests that there are additional molecular mechanisms that may contribute.

Endogenous human IgG1 contains <1% of high mannose glycans (Mastrangeli et al., 2020). In contrast, recombinant therapeutic mAbs include ~10% high mannose glycans (Goetze et al., 2011). Thus, there is interest in limiting excessive high mannose glycan formation in IgGs during commercial manufacturing (Mastrangeli et al., 2020). Current trends in biopharmaceutical manufacturing such as process intensification, development of fully humanized mAbs, growth in biosimilar products, development of high concentration mAb formulations, and the emergence of next-generation biopharmaceuticals such as anti-drug conjugates and bispecific antibodies, necessitates the control of high mannose content as a

critical aspect in the process development (Berkel et al., 2009; Shi and Goudar, 2014; Feinberg et al., 2017; Sumit et al., 2019; Talbot et al., 2019; Mastrangeli et al., 2020).

Our analysis of the range of process conditions, cell lines, cell culture duration, and feed conditions indicate that high mannose glycans in VRC01 are unaffected by clone-specific productivity differences, standard commercial medium feeds (unless specific additives are used that are known to influence the high mannose glycan formation) and even the cell culture duration. However, under different DO control conditions in an AMBR250 bioreactor, it was found that there was a 10-fold increase in the high mannose content. The most abundant high-mannose structure observed was the M5 form, along with M3, M4, M6, M7, and M9 forms that were present in relatively very low abundance as compared to the M5 form. The occurrence of Man 5 glycans could potentially be attributed either by the action of mannosidases in the Golgi complex or from an incomplete/truncated biosynthesis of lipid linked oligosaccharides (LLO) in the endoplasmic reticulum (ER) (Breitling and Aebi, 2013; Mastrangeli et al., 2020). The M6, M7 glycans also could be an outcome of inefficient glycan processing in the Golgi complex, although they could also originate from incomplete LLO biosynthesis. Inefficient ER processing, potentially originating from a bottleneck in the availability of nucleotide sugar substrates such as UDP-GlcNAc and UDP-Man in the ER, thereby creating an imbalance in the protein folding and synthesis rates (Jiménez del Val et al., 2013; Mastrangeli et al., 2020) could also be a causative factor leading to the accumulation of high mannose glycans. Other process conditions that have been reported to cause ER stress during CHO cell cultures include a combination of factors such as temperature, pH, trace metals (zinc, copper), specific media supplements (Choline, spermine, ornithine) (Kang et al., 2015; Sou et al., 2015; Kuwae et al., 2018; Graham et al., 2019). In addition, there are reports in the literature showing that the extended cell culture durations also lead to less processing of glycans resulting in high mannose glycans (Jiang et al., 2018). Similarly, the impact of cell-specific productivity on the high mannose content is generally attributed to steric hinderance effects in the enzymatic processes, making the impact product-specific and less generalizable (Hills et al., 2001).

Another important mAb glycan attribute is the level of fucosylation. The high levels of fucosylation impose steric hindrance around the glycosylation site and thus inhibit the interaction of the Fc domain of the mAb with the Fc receptors on the effector cells leading to low antibody-dependent cell-mediated cytotoxicity (ADCC) (Pereira et al., 2018). However, existing data on commercial mAbs indicate only <10% of the recombinant mAbs as being non-fucosylated (Yamane-Ohnuki and Satoh, 2009). The most common strategies employed to reduce mAb fucosylation includes the use of engineered cell lines lacking the enzyme (α-1,6 fructosyltransferase) or overexpressing β(1-4)-N-acetylglucosaminyltransferase III gene (GnTIII), use of glycoside inhibitor kifunensine, and zinc finer mediated knockdown of fucose transport gene (Mimura et al., 2018). mAb fucosylation can also be varied by controlling the cell culture osmolarity and pH, where an inverse correlation exists (Konno et al., 2012). Here, we observed that the less-productive clone (CP35) also had the lowest fucosylation levels—consistent with observations from others. Also, the fucosylation level was observed to decrease with the loss in the cell viability at later days of cell culture (potentially due to accumulation of the lactate and ammonia that impacts the cell culture pH). The three different media used in the cell culture did not impact levels of the VRC01 fucosylation.

Together, our results illustrate that clonal variability, cell culture duration, media and feed, and process conditions together impact VRC01 mAb glycan heterogeneity. The reasons for glycan heterogeneity are multi-factorial and strategies to obtain a particular level of a particular glycoform towards achieving the desired product quality requires knowledge and adjustment of these parameters. The analytical method reported in this work provides a step towards elucidating and determining the complex relationship between process variables and glycosylation. Additional studies expanding on the data obtained from this study using multi-omic approaches will provide additional insights into the sources of glycan heterogeneity of mAbs during CHO cell culture and thereby aid in robust process development to control the glycosylation attributes to the desired levels.

5 CONCLUSION

The present study reports the development of a HILIC based glycan screening method for characterization of mAb glycosylation**.** The method employs the accurate mass of the glycans as the primary search variable and retention time as the confirmatory variable. The method was employed to study the source of glycan heterogeneity in a model IgG1 mAb, VRC01. It was determined that clonal heterogeneity, cell culture duration, and the process conditions impact several glycan attributes such as galactosylation, sialylation, fucosylation, and high mannose forms. Overall, the analytical method and glycosylation data presented here can guide in-depth analysis and process development to optimize the levels of VRC01 glycosylation for the desired product quality.

DATA AVAILABILITY STATEMENT

The original contributions presented in the study are included in the article/**Supplementary Material**, further inquiries can be directed to the corresponding author.

AUTHOR CONTRIBUTIONS

SS conceived the work, executed experiments, and analyzed data. KL conceived the work, sponsored the work, and analyzed data. All authors contributed to manuscript revision, read, and approved the submitted version.

FUNDING

The work has been supported, in part, by the National Science Foundation (1624698, 1736123) and NIST (70NANB17H002).

ACKNOWLEDGMENTS

The authors would like to thank Douglas Ngmau for providing the VRC01 samples from the fed-batch study using CHO clones of different productivity. The authors thank Dr. Hussain Dahodwala for providing VR01 samples from CHO cells cultivated in three different media. Additionally, we would like to thank Michael Daly from Waters Corporation for his help in troubleshooting the mass spectrometry experiments for glycan analysis at various points in this study and also the NIH-NIAID for sharing of cells.

SUPPLEMENTARY MATERIAL

The Supplementary Material for this article can be found online at: https://www.frontiersin.org/articles/10.3389/fbioe.2021.805788/full#supplementary-material

REFERENCES

Batra, J., and Rathore, A. S. (2016). Glycosylation of Monoclonal Antibody Products: Current Status and Future Prospects. *Biotechnol. Prog.* 32, 1091–1102. doi:10.1002/BTPR.2366

Bibila, T. A., and Robinson, D. K. (1995). In Pursuit of the Optimal Fed-Batch Process for Monoclonal Antibody Production. *Biotechnol. Prog.* 11, 1–13. doi:10.1021/BP00031A001

Breitling, J., and Aebi, M. (2013). N-linked Protein Glycosylation in the Endoplasmic Reticulum. *Cold Spring Harbor Perspect. Biol.* 5, a013359. doi:10.1101/cshperspect.a013359

Domann, P. J., Pardos-Pardos, A. C., Fernandes, D. L., Spencer, D. I. R., Radcliffe, C. M., Royle, L., et al. (2007). Separation-based Glycoprofiling Approaches Using Fluorescent Labels. *Proteomics* 7, 70–76. doi:10.1002/PMIC.200700640

Duivelshof, B. L., Jiskoot, W., Beck, A., Veuthey, J.-L., Guillarme, D., and D'Atri, V. (2019). Glycosylation of Biosimilars: Recent Advances in Analytical Characterization and Clinical Implications. *Analytica Chim. Acta* 1089, 1–18. doi:10.1016/J.ACA.2019.08.044

Eon-Duval, A., Broly, H., Gleixner, R., Eon-Duval, A., Broly, H., Gleixner, R., et al. (2012). Quality Attributes of Recombinant Therapeutic Proteins: An Assessment of Impact on Safety and Efficacy as Part of a Quality by Design Development Approach. *Biotechnol. Prog.* 28, 608–622. doi:10.1002/btpr.1548

Feinberg, H., Jégouzo, S. A. F., Rex, M. J., Drickamer, K., Weis, W. I., and Taylor, M. E. (2017). Mechanism of Pathogen Recognition by Human Dectin-2. *J. Biol. Chem.* 292, 13402–13414. doi:10.1074/JBC.M117.799080

Fisher, P., Thomas-Oates, J., Wood, A. J., and Ungar, D. (2019). The N-Glycosylation Processing Potential of the Mammalian Golgi Apparatus. *Front. Cell Dev. Biol.* 7, 157. doi:10.3389/fcell.2019.00157

Goetze, A. M., Liu, Y. D., Zhang, Z., Shah, B., Lee, E., Bondarenko, P. V., et al. (2011). High-mannose Glycans on the Fc Region of Therapeutic IgG Antibodies Increase Serum Clearance in Humans. *Glycobiology* 21, 949–959. doi:10.1093/GLYCOB/CWR027

Graham, R. J., Bhatia, H., and Yoon, S. (2019). Consequences of Trace Metal Variability and Supplementation on Chinese Hamster Ovary (CHO) Cell Culture Performance: A Review of Key Mechanisms and Considerations. *Biotechnol. Bioeng.* 116, 3446–3456. doi:10.1002/BIT.27140

Grilo, A. L., and Mantalaris, A. (2019). The Increasingly Human and Profitable Monoclonal Antibody Market. *Trends Biotechnol.* 37, 9–16. doi:10.1016/J.TIBTECH.2018.05.014

Hilliard, M., William, R. A., Jr., Alley, W. R., McManus, C. A., Yu, Y. Q., Hallinan, S., et al. (2017). Glycan Characterization of the NIST RM Monoclonal Antibody Using a Total Analytical Solution: From Sample Preparation to Data Analysis. *MAbs* 9, 1349–1359. doi:10.1080/19420862.2017.1377381

Hills, A. E., Patel, A., Boyd, P., and James, D. C. (2001). Metabolic Control of Recombinant Monoclonal antibodyN-Glycosylation in GS-NS0 Cells. *Biotechnol. Bioeng.* 75, 239–251. doi:10.1002/BIT.10022

Hossler, P., Khattak, S. F., and Li, Z. J. (2009). Optimal and Consistent Protein Glycosylation in Mammalian Cell Culture. *Glycobiology* 19, 936–949. doi:10.1093/glycob/cwp079

Hossler, P., Mulukutla, B. C., and Hu, W.-S. (2007). Systems Analysis of N-Glycan Processing in Mammalian Cells. *PLoS One* 2, e713. doi:10.1371/JOURNAL.PONE.0000713

Jensen, P. H., Karlsson, N. G., Kolarich, D., and Packer, N. H. (2012). Structural Analysis of N- and O-Glycans Released from Glycoproteins. *Nat. Protoc.* 7 (7), 1299–1310. doi:10.1038/nprot.2012.063

Jiang, R., Chen, H., and Xu, S. (2018). pH Excursions Impact CHO Cell Culture Performance and Antibody N-Linked Glycosylation. *Bioproc. Biosyst. Eng.* 41, 1731–1741. doi:10.1007/S00449-018-1996-Y

Jiménez del Val, I., Constantinou, A., Dell, A., Haslam, S., Polizzi, K. M., and Kontoravdi, C. (2013). A Quantitative and Mechanistic Model for Monoclonal Antibody Glycosylation as a Function of Nutrient Availability during Cell Culture. *BMC Proc.* 7, O10. doi:10.1186/1753-6561-7-s6-o10

Jimenez del Val, I., Fan, Y., and Weilguny, D. (2016). Dynamics of Immature mAb Glycoform Secretion during CHO Cell Culture: An Integrated Modelling Framework. *Biotechnol. J.* 11, 610–623. doi:10.1002/BIOT.201400663

Kang, S., Zhang, Z., Richardson, J., Shah, B., Gupta, S., Huang, C.-J., et al. (2015). Metabolic Markers Associated with High Mannose Glycan Levels of Therapeutic Recombinant Monoclonal Antibodies. *J. Biotechnol.* 203, 22–31. doi:10.1016/J.JBIOTEC.2015.03.002

Kantardjieff, A., Jacob, N. M., Yee, J. C., Epstein, E., Kok, Y.-J., Philp, R., et al. (2010). Transcriptome and Proteome Analysis of Chinese Hamster Ovary Cells under Low Temperature and Butyrate Treatment. *J. Biotechnol.* 145, 143–159. doi:10.1016/J.JBIOTEC.2009.09.008

Kaur, H. (2021). Characterization of Glycosylation in Monoclonal Antibodies and its Importance in Therapeutic Antibody Development. *Crit. Rev. Biotechnol.* 41, 300–315. doi:10.1080/07388551.2020.1869684

Konno, Y., Kobayashi, Y., Takahashi, K., Takahashi, E., Sakae, S., Wakitani, M., et al. (2012). Fucose Content of Monoclonal Antibodies Can Be Controlled by Culture Medium Osmolality for High Antibody-dependent Cellular Cytotoxicity. *Cytotechnology* 64, 249–265. doi:10.1007/S10616-011-9377-2

Kuwae, S., Miyakawa, I., and Doi, T. (2018). Development of a Chemically Defined Platform Fed-Batch Culture media for Monoclonal Antibody-Producing CHO Cell Lines with Optimized Choline Content. *Cytotechnology* 70, 939–948. doi:10.1007/S10616-017-0185-1

Lauber, M. A., Yu, Y.-Q., Brousmiche, D. W., Hua, Z., Koza, S. M., Magnelli, P., et al. (2015). Rapid Preparation of Released N-Glycans for HILIC Analysis Using a Labeling Reagent that Facilitates Sensitive Fluorescence and ESI-MS Detection. *Anal. Chem.* 87, 5401–5409. doi:10.1021/ACS.ANALCHEM.5B00758

Madabhushi, S. R., Podtelezhnikov, A. A., Murgolo, N., Xu, S., and Lin, H. (2021). Understanding the Effect of Increased Cell Specific Productivity on Galactosylation of Monoclonal Antibodies Produced Using Chinese Hamster Ovary Cells. *J. Biotechnol.* 329, 92–103. doi:10.1016/J.JBIOTEC.2021.01.023

Mastrangeli, R., Audino, M. C., Palinsky, W., Broly, H., and Bierau, H. (2020). The Formidable Challenge of Controlling High Mannose-type N-Glycans in Therapeutic mAbs. *Trends Biotechnol.* 38, 1154–1168. doi:10.1016/J.TIBTECH.2020.05.009

Mimura, Y., Katoh, T., Saldova, R., O'Flaherty, R., Izumi, T., Mimura-Kimura, Y., et al. (2018). Glycosylation Engineering of Therapeutic IgG Antibodies:

Challenges for the Safety, Functionality and Efficacy. *Protein Cell* 9, 47–62. doi:10.1007/s13238-017-0433-3

Nmagu, D., Singh, S. K., and Lee, K. H. (2021). "Creation of Monoclonal Antibody Expressing CHO Cell Lines Grown With Sodium Butyrate and Characterization of Resulting Antibody Glycosylation," in *Methods in Enzymology* (Cambridge, MA: Academic Press), 267–295. doi:10.1016/BS.MIE.2021.06.039

Pacis, E., Yu, M., Autsen, J., Bayer, R., and Li, F. (2011). Effects of Cell Culture Conditions on Antibody N-Linked Glycosylation-What Affects High Mannose 5 Glycoform. *Biotechnol. Bioeng.* 108, 2348–2358. doi:10.1002/BIT.23200

Pereira, N. A., Chan, K. F., Lin, P. C., and Song, Z. (2018). The "Less-Is-More" in Therapeutic Antibodies: Afucosylated Anti-cancer Antibodies with Enhanced Antibody-dependent Cellular Cytotoxicity. *MAbs* 10, 693–711. doi:10.1080/19420862.2018.1466767

Reusch, D., Haberger, M., Falck, D., Peter, B., Maier, B., Gassner, J., et al. (2015a). Comparison of Methods for the Analysis of Therapeutic Immunoglobulin G Fc-Glycosylation Profiles-Part 2: Mass Spectrometric Methods. *MAbs* 7, 732–742. doi:10.1080/19420862.2015.1045173

Reusch, D., Haberger, M., Maier, B., Maier, M., Kloseck, R., Zimmermann, B., et al. (2015b). Comparison of Methods for the Analysis of Therapeutic Immunoglobulin G Fc-Glycosylation Profiles-Part 1: Separation-Based Methods. *MAbs* 7, 167–179. doi:10.4161/19420862.2014.986000

Schwarz, F., and Aebi, M. (2011). Mechanisms and Principles of N-Linked Protein Glycosylation. *Curr. Opin. Struct. Biol.* 21, 576–582. doi:10.1016/J.SBI.2011.08.005

Shi, H. H., and Goudar, C. T. (2014). Recent Advances in the Understanding of Biological Implications and Modulation Methodologies of Monoclonal Antibody N-Linked High Mannose Glycans. *Biotechnol. Bioeng.* 111, 1907–1919. doi:10.1002/BIT.25318

Sou, S. N., Sellick, C., Lee, K., Mason, A., Kyriakopoulos, S., Polizzi, K. M., et al. (2015). How Does Mild Hypothermia Affect Monoclonal Antibody Glycosylation? *Biotechnol. Bioeng.* 112, 1165–1176. doi:10.1002/BIT.25524

Sumit, M., Dolatshahi, S., Chu, A.-H. A., Cote, K., Scarcelli, J. J., Marshall, J. K., et al. (2019). Dissecting N-Glycosylation Dynamics in Chinese Hamster Ovary Cells Fed-Batch Cultures Using Time Course Omics Analyses. *iScience* 12, 102–120. doi:10.1016/J.ISCI.2019.01.006

Talbot, N. E., Mead, E. J., Davies, S. A., Uddin, S., and Smales, C. M. (2019). Application of ER Stress Biomarkers to Predict Formulated Monoclonal Antibody Stability. *Biotechnol. J.* 14, 1900024. doi:10.1002/BIOT.201900024

van Berkel, P. H. C., Gerritsen, J., Perdok, G., Valbjørn, J., Vink, T., van de Winkel, J. G. J., et al. (2009). N-linked Glycosylation Is an Important Parameter for Optimal Selection of Cell Lines Producing Biopharmaceutical Human IgG. *Biotechnol. Prog.* 25, 244–251. doi:10.1002/BTPR.92

Walsh, G. (2018). Biopharmaceutical Benchmarks 2018. *Nat. Biotechnol.* 36, 1136–1145. doi:10.1038/nbt.4305

Yamane-Ohnuki, N., and Satoh, M. (2009). Production of Therapeutic Antibodies with Controlled Fucosylation. *mAbs* 1, 230–236. doi:10.4161/MABS.1.3.8328

Zhou, S., Huang, Y., Dong, X., Peng, W., Veillon, L., Kitagawa, D. A. S., et al. (2017). Isomeric Separation of Permethylated Glycans by Porous Graphitic Carbon (PGC)-LC-MS/MS at High Temperatures. *Anal. Chem.* 89, 6590–6597. doi:10.1021/acs.analchem.7b00747

Conflict of Interest: The authors declare that the research was conducted in the absence of any commercial or financial relationships that could be construed as a potential conflict of interest.

Publisher's Note: All claims expressed in this article are solely those of the authors and do not necessarily represent those of their affiliated organizations, or those of the publisher, the editors and the reviewers. Any product that may be evaluated in this article, or claim that may be made by its manufacturer, is not guaranteed or endorsed by the publisher.

frontiers in Bioengineering and Biotechnology

REVIEW
published: 09 February 2022
doi: 10.3389/fbioe.2022.832059

Analytical Similarity Assessment of Biosimilars: Global Regulatory Landscape, Recent Studies and Major Advancements in Orthogonal Platforms

Neh Nupur[1†], *Srishti Joshi*[1†], *Davy Gulliarme*[2,3] *and Anurag S. Rathore*[1*]

[1]*Department of Chemical Engineering, IIT Delhi, Hauz Khas, New Delhi, India,* [2]*Institute of Pharmaceutical Sciences of Western Switzerland (ISPSO), University of Geneva, Geneva, Switzerland,* [3]*School of Pharmaceutical Sciences, University of Geneva, Geneva, Switzerland*

OPEN ACCESS

Edited by:
Christoph Herwig, Vienna University of Technology, Austria

Reviewed by:
Chang-Han Lee, Seoul National University, South Korea
Ana Margarida Goncalves Carvalho Dias, New University of Lisbon, Portugal

***Correspondence:**
Anurag S. Rathore
asrathore@biotechcmz.com

[†]*These authors have contributed equally to this work and share first authorship*

Specialty section:
This article was submitted to Bioprocess Engineering, a section of the journal Frontiers in Bioengineering and Biotechnology

Received: *09 December 2021*
Accepted: *07 January 2022*
Published: *09 February 2022*

Citation:
Nupur N, Joshi S, Gulliarme D and Rathore AS (2022) Analytical Similarity Assessment of Biosimilars: Global Regulatory Landscape, Recent Studies and Major Advancements in Orthogonal Platforms. Front. Bioeng. Biotechnol. 10:832059. doi: 10.3389/fbioe.2022.832059

Biopharmaceuticals are one of the fastest-growing sectors in the biotechnology industry. Within the umbrella of biopharmaceuticals, the biosimilar segment is expanding with currently over 200 approved biosimilars, globally. The key step towards achieving a successful biosimilar approval is to establish analytical and clinical biosimilarity with the innovator. The objective of an analytical biosimilarity study is to demonstrate a highly similar profile with respect to variations in critical quality attributes (CQAs) of the biosimilar product, and these variations must lie within the range set by the innovator. This comprises a detailed comparative structural and functional characterization using appropriate, validated analytical methods to fingerprint the molecule and helps reduce the economic burden towards regulatory requirement of extensive preclinical/clinical similarity data, thus making biotechnological drugs more affordable. In the last decade, biosimilar manufacturing and associated regulations have become more established, leading to numerous approvals. Biosimilarity assessment exercises conducted towards approval are also published more frequently in the public domain. Consequently, some technical advancements in analytical sciences have also percolated to applications in analytical biosimilarity assessment. Keeping this in mind, this review aims at providing a holistic view of progresses in biosimilar analysis and approval. In this review, we have summarized the major developments in the global regulatory landscape with respect to biosimilar approvals and also catalogued biosimilarity assessment studies for recombinant DNA products available in the public domain. We have also covered recent advancements in analytical methods, orthogonal techniques, and platforms for biosimilar characterization, since 2015. The review specifically aims to serve as a comprehensive catalog for published biosimilarity assessment studies with details on analytical platform used and critical quality attributes (CQAs) covered for multiple biotherapeutic products. Through this compilation, the emergent evolution of techniques with respect to each CQA has also been charted and discussed. Lastly, the information resource of published biosimilarity assessment studies, created during literature search is anticipated to serve as a helpful reference for biopharmaceutical scientists and biosimilar developers.

Keywords: analytical similarity, biosimilars, critical quality attributes, orthogonal analytical tools, regulatory guidelines

1 INTRODUCTION

Biologics or biotherapeutics are rDNA products used to diagnose, prevent, treat, and cure medical conditions and include a diverse category of products (i.e., proteins, enzymes, peptides, vaccines to name a few). Biotherapeutics are structurally complex compared to small molecules (USFDA, 2018). Currently, biopharmaceuticals are one of the fastest-growing sectors in the biotechnology industry. In the last decade, the landscape for biologics has evolved at an accelerated rate globally with market size of USD 254.9 billion as of 2017 and expected to reach USD 580.5 billion by 2026 at a Compound Annual Growth Rate (CAGR[1]) of 9.5% (2018–2026) (Global, 2018).

As the innovator (aka originator/reference) molecule reaches patent cliff, it paves way for commercialization of biosimilars which are "highly similar" to the innovator in terms of structure and function, notwithstanding minor variations in clinically inactive components and should have no clinically meaningful differences in terms of safety, purity, and potency of the drug product (DP[2]) (USFDA, 2019). This needs to be thoroughly characterized during product development. The product attributes that are critical to the safety, efficacy, and potency of the product are classified as critical quality attributes (CQAs) (Eon-Duval et al., 2012). This exercise that is conducted to establish comparability between the reference product and its intended biosimilar is known as similarity assessment (aka biosimilarity) and comprises detailed comparative physicochemical and functional characterization using appropriate, validated analytical methods (Nupur et al., 2016, 2018; Joshi and Rathore, 2020). As structural attributes are molecule-dependent, CQAs may vary to a certain degree amongst the different modalities. For example, glycosylation is typically a CQA for proteins produced in the eukaryotic systems, such as monoclonal antibodies (mAbs) produced in the mammalian cells. For therapeutics with prokaryotic hosts (such as *Escherichia coli*), glycosylation is not an attribute of concern. Hence, requirements for analytical platforms for characterization and biosimilarity assessments are tailored to be modality-specific and within the larger domain of rDNA products, so are the regulatory requirements. Analytical platforms play a dynamic role in biopharmaceutical and biosimilar manufacturing and in general serves to control/monitor the process. A typical bioprocess train for biosimilar development and associated analysis commonly required at different stages of manufacturing are illustrated in **Figure 1**.

The requirement of unambiguous biosimilarity demonstration brings us to the concept of orthogonality. Implementation of orthogonal tools (differing in their principle of operation) is invaluable to demonstrate unambiguity in the comparative profiles of CQAs, especially in the cases where the primary technique is qualitative or the CQA is dynamic (i.e., cannot be mapped completely by one technique). The United States Food and Drug Administration (USFDA) non-binding guidance for industry on "Development of Therapeutic Protein Biosimilars: Comparative Analytical Assessment and Other Quality-Related Considerations," quotes that "methods that use different physicochemical or biological principles to assess the same attribute are especially valuable, because they provide independent data to support the quality of that attribute" and have pointed out the importance of adding orthogonal tools to analytical assessment (USFDA, 2019). A classic example of this is size variants, where orthogonal analytical techniques have been widely employed to 1) cover the breadth of the size range (soluble aggregates < sub visible < visible < insoluble aggregates) and 2) to independently quantify size aggregates in the same size range (orthogonal tools for size variants assessment are discussed in **Section 2.2.4.1**). Other attributes exemplifying the use of orthogonal tools include higher-order structure (HOS), glycosylation, and charge variants (discussed under **Section 4**).

Analytical characterization of CQAs for different modalities has been reviewed in some publications (Fekete et al., 2013, 2016; Jacobs et al., 2016, 2017; Santos-Neto et al., 2021). However, the current review focuses on major developments in regulatory approvals and orthogonal analytical platforms for biosimilarity assessment. The global regulatory landscape with respect to biosimilar approvals as well as that in the analytical platforms for similarity studies (till July 2021) has been summarized, with particular focus on progress made in the last 5 years (since 2015). Finally, a discussion on evolution and future trajectory of analytical similarity platforms is also presented. Overall, this review serves as a useful repository of references to help biosimilar manufacturers in designing suitable analytical platforms for similarity studies.

All abbreviations appearing in this publication, including supplementary information have been tabulated as **Supplementary Table S1**. Definitions and meanings of domain specific terminology have been listed in **Supplementary Table S2**.

2. GLOBAL LANDSCAPE ON BIOSIMILAR APPROVALS

Following the patent cliff of certain innovator products and the growing support from the major regulatory agencies, there has been a steady increase in the number of biosimilar approvals. At present, region and country-specific biosimilar regulatory pathways and guidance are at different stages of development and implementation (Rathore and Bhargava, 2020; 2021a; 2021b; 2021c). There is a growing interest in increasing global harmonization of the regulatory guidelines for biosimilar development including selection of the reference product, nomenclature, and the design of analytical, non-clinical, or clinical biosimilarity studies. A global agreement on the regulatory requirement for the biosimilars would facilitate standardization of product quality and is likely to positively impact the reception and acceptance of biosimilars worldwide

[1]CAGR is a geometric progression ratio that provides a constant rate of return over the time period.

[2]DP is the finished dosage form, for example, a tablet, capsule or solution that contains an active pharmaceutical ingredient, generally, but not necessarily, in association with inactive ingredients.

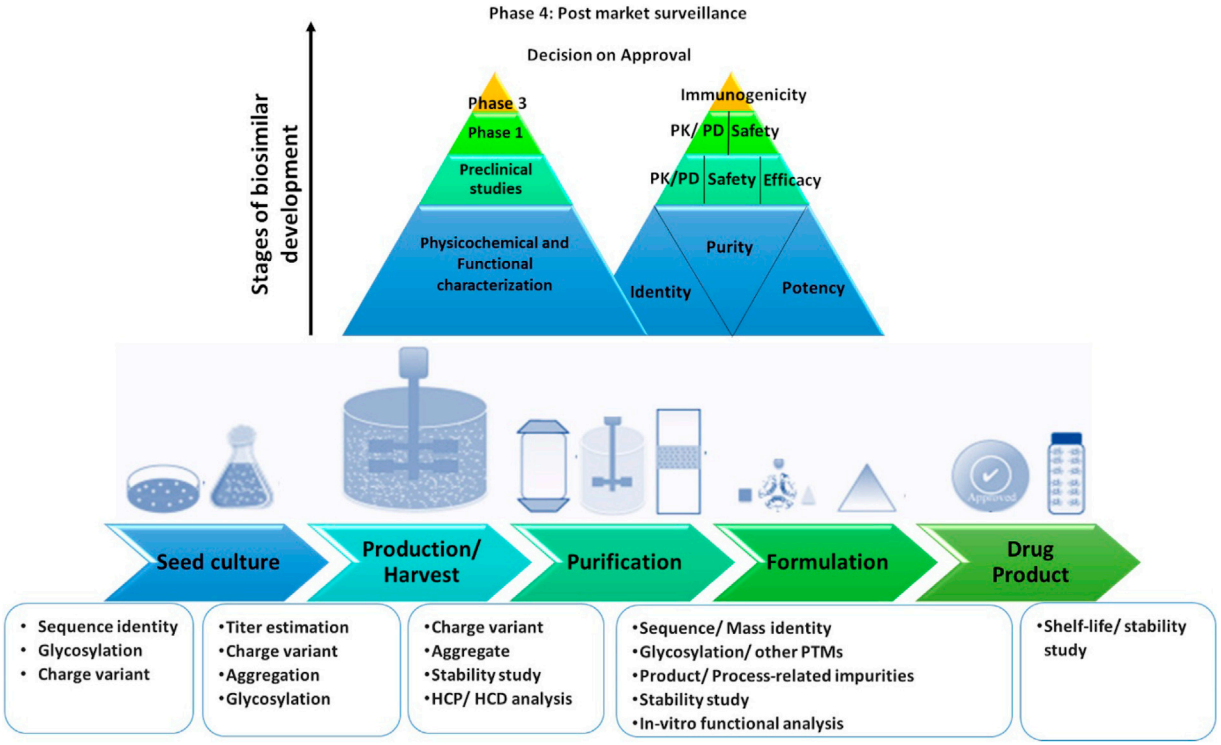

FIGURE 1 | Bioprocess train with multiple stages of development during biosimilar manufacturing. PK, Pharmacokinetics; PD, Pharmacodynamics; PTM, Post translational modifications; HCP, Host Cell Protein; HCD, Host Cell DNA.

(WHO, 2009, 2013; Kang H.-N. et al., 2020). A brief region and country-wise account of global status on regulatory guidelines for biosimilar approvals are presented in **Table 1**.

The European Medicines Agency (EMA) pioneered the legal framework and regulatory approval pathway for biosimilars in 2005, paving the way for other jurisdictions around the globe (Gherghescu and Delgado-Charro, 2020). In alignment with the International Council for Harmonization (ICH) guidelines, the EMA's "Guideline on Similar Biological Medicinal Products" states that similarity to the innovator needs to be established in terms of quality characteristics, biological activity, safety, and efficacy based on a comprehensive, head-to-head biosimilarity exercise for characterization of the quality of the DP and the approval is subjected to the totality-of-evidence presented (EMA, 1996, 1999, 2005; CHMP, 2005, 2014). The World Health Organization (WHO) adopted similar guidelines on the evaluation of Similar Biotherapeutic Products (SBPs) in 2009 to ensure better access to safe and effective SBPs worldwide through global harmonization of the regulatory framework for licensure (WHO, 2009). The WHO laid the foundation for other regulatory authorities to introduce their respective guidelines by giving to the national regulatory authorities (NRAs) the flexibility to adapt approval pathways according to their needs. Around the same time, Biologics Price Competition and Innovation Act (BPCI) were developed in the US that initiated the biosimilar approval pathway under USFDA. Since then, several countries have laid down and implemented a regulatory framework for biosimilar approval for its commercial use within their jurisdiction (**Table 1**). All guidance documents thus far emphasize the demonstration of biosimilarity *via* extensive structural and functional characterization followed by non-clinical, pharmacokinetic, and clinical studies. The degree of biosimilarity with respect to product quality determines the scope and breadth of the required non-clinical and clinical data, on a case-by-case basis, dependent on the product class/ modality. The comparative clinical studies are encouraged to be specifically developed to rule out clinically relevant differences in safety or efficacy between the biosimilar and the innovator, in order to confirm biosimilarity (WHO, 2013).

The global regulatory landscape continues to evolve in response to the mushrooming biosimilar industry, with close to 600 approved biosimilars for 45 reference products in over 50 countries, to date. In addition to **Table 1**, a comprehensive region/country-wise list of mAb and non-mAb biosimilar approvals has been tabulated in **Supplementary Table S3**. Due to several factors such as clinical indications, market size, patent cliffs, and the need for affordable alternatives, mAbs constitute a major segment in the overall biosimilars portfolio. This is evidenced by a total of 249 biosimilars that currently populate the market for 12 reference products. Of these, the leading mAbs include anti-HER2 trastuzumab (60), anti-CD20 rituximab (53), anti-TNF α adalimumab (38) and infliximab (33), and anti-VEGF bevacizumab (31), and the anti-TNF Fc-fusion protein, etanercept (26) (**Figure 2A**). The majority of these approvals

TABLE 1 | A region/country-wise account of regulatory guidelines for biosimilar approvals to dateJuly, 2021.

Region	Countries	Regulatory agency	Year	Adopted from/Aligned with	Biosimilar approvals (till date)	References
Europe	European Union	European Medical Agency (EMA)	2005	Committee for Medicinal Products for Human Use and International Council for Harmonization (ICH)	69	EMA (1996), EMA (1999),EMA (2005), EMA (2020), CHMP (2005), CHMP (2014)
North America	United States (US)	Food and Drug Administration (FDA)	Initiated in 2010 and finalized in 2015	Biologics Price Competition and Innovation Act, 2010 for Biologic License Application and Section 351(a) and 351(k) of the Public Health Service Act	34	USFDA (2015), USFDA (2019), USFDA (2021)
	Canada	Biologics and Genetic Therapies Directorate under Health Canada	Initiated in 2010 and finalized in 2016	EMA, USFDA, and WHO	26	Canada (2016), Wojtyra (2021)
Asia	Japan	Pharmaceuticals and Medical Devices Agency	2009	EMA	28	PMDA (2020), Rathore and Bhargava (2021a)
	South Korea	Ministry of Food and Drug Safety	Initiated in 2009 and finalized in 2014	EMA and WHO	15	MFDS (2020), Rathore and Bhargava (2021a)
	India	Central Drugs Standard Control Organization and the Review Committee on Genetic Manipulation	Initiated in 2012 and revised in 2016	EMA and USFDA	103	DBT (2016), CDSCO (2020), Rathore and Bhargava (2021a)
	China	Center for Drug Evaluation under National Medical Products Administration	Initiated in 2014 and finalized in 2015	EMA and USFDA	14	GaBI (2021), Rathore and Bhargava (2021a)
	Malaysia	National Pharmaceutical Regulatory Agency	Initiated in 2008 and reframed in 2009	EMA and WHO	25	NPRA (2021), Rathore and Bhargava (2021a)
	Indonesia	National Agency for Drug and Food Control	2015	ICH and EMA	20	Kang et al. (2021), Rathore and Bhargava (2021a)
	Singapore	Health Products Regulation Group	2009	EMA	7	
	Thailand	Food and Drug Administration	2013	WHO	13	
	Iran	Food and Drug Organization under Ministry of Health and Medical Education	2014	WHO	26	
	Jordan	Food and Drug Administration	2015	EMA	9	
	Russia	Министерство здравоохранения Российской Федерации; Rosminzdrav, Minzdrav			34	GaBI (2020), Kang et al. (2021)
Australia	Australia	Therapeutic Goods Administration	Initiated in 2008, finalized in 2013 and revised in 2018	EMA	26	TGA (2018), Health (2021)
Latin America	Argentina	Administracion Nacional de Medicamentos, Alimentos y Tecnologıa Medica	2008	EMA	29	GaBI (2019), Ortiz-Prado et al. (2020), Rathore and Bhargava (2021b)
	Brazil	Agencia Nacional de Vigilancia Sanitaria	2010	WHO	21	
	Mexico	Federal Commission for the Protection against Sanitary Risks	Initiated in 2011 and reframed in 2013		6	
	Peru	Ministerio de Salud	2016	WHO, FDA, and EMA	5	
	Colombia	Ministerio de Salud y Proteccion Social	2013		3	
	Chile	Agencia Nacional de Medicamentos	Initiated in 2011 and finalized in 2014		15	
	Venezuela	Instituto Nacional de Higiene “Rafael Rangel”	2012		1	
	Cuba	Center for State Control on the Quality of Drugs	2011	WHO	16	

(Continued on following page)

TABLE 1 | (*Continued*) A region/country-wise account of regulatory guidelines for biosimilar approvals to dateJuly, 2021.

Region	Countries	Regulatory agency	Year	Adopted from/Aligned with	Biosimilar approvals (till date)	References
Africa	Egypt	Central Administration for Pharmaceutical Affairs with National Organization for Research and Control of Biologics under Egyptian Drug Authority	2013		4	Pategou (2020), Kang et al. (2021)
	Ghana	Food and Drugs Authority	Initiated in 2013 and reframed in 2019		13	
	South Africa	South African Health Product Regulatory Authority	Initiated in 2010 and reframed in 2014	EMA	2	

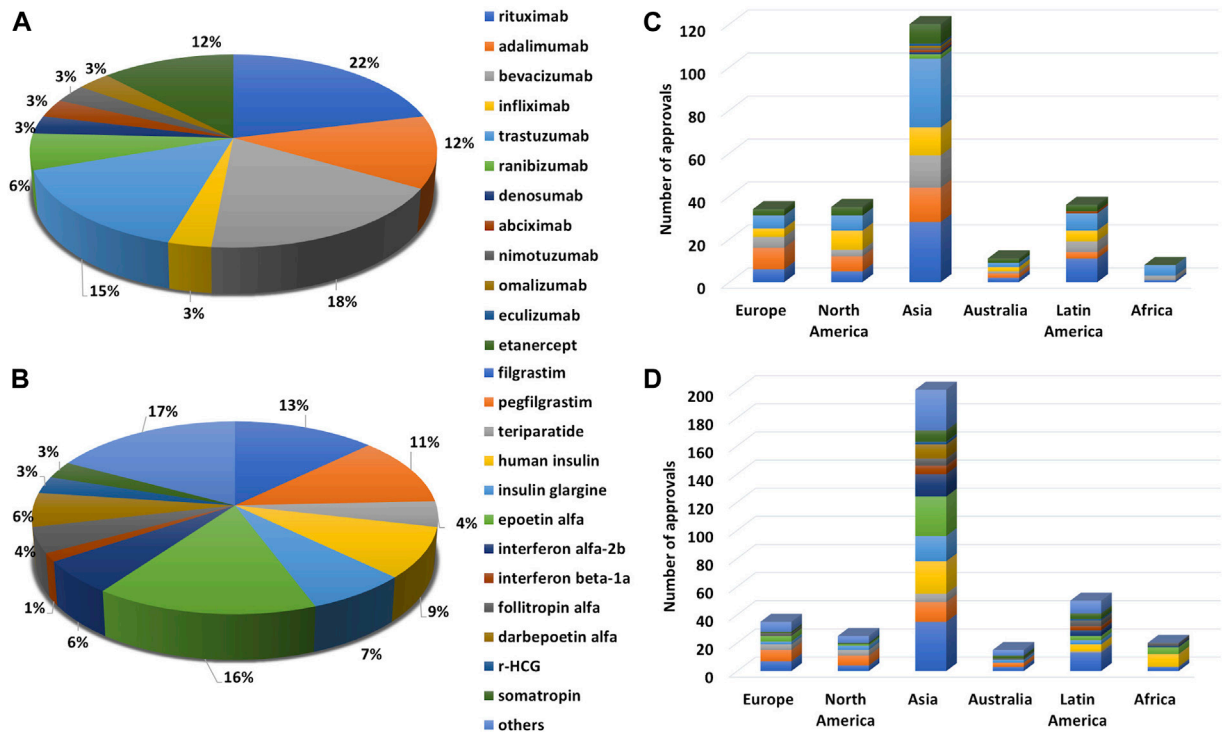

FIGURE 2 | Trend in biosimilar approval for different modalities depicted as percentage of total approvals for a given biologic under **(A)** mAbs and **(B)** non-mAbs and global biosimilar approvals (in numbers) across continents i.e., Europe, North America, Asia, Australia, Latin America, and Africa for **(C)** mAbs and **(D)** non-mAbs.

have been granted in Asia (50%) followed by Latin America (15%), Europe (14%), North America (14%), Australia (4%), and Africa (3%) (**Figure 2B**). Taking the rest of the modalities together as non-mAbs, a total of 348 biosimilars for 33 reference products belonging to filgrastim (65, GCSF receptor binding) followed by epoetin alfa (41, JAK-STAT receptor binding), human insulin (37, insulin receptor binding), peg-filgrastim (32, GCSF receptor binding), insulin glargine (28, insulin receptor binding), and interferon alfa-2b (21, IFN-α/β receptor binding) have been approved so far (**Figure 2C**). The geographic spread of these approvals is similar to that of mAbs with a maximum number of biosimilar approvals granted in Asia (58%) followed by Latin America (15%), Europe (10%), North America (7%), Africa (6%) and Australia (4%) (**Figure 2D**).

Recent patent expirations (2020-21) include ranibizumab (2020-US) and eculizumab (2020-US, 2021-EU). Other major

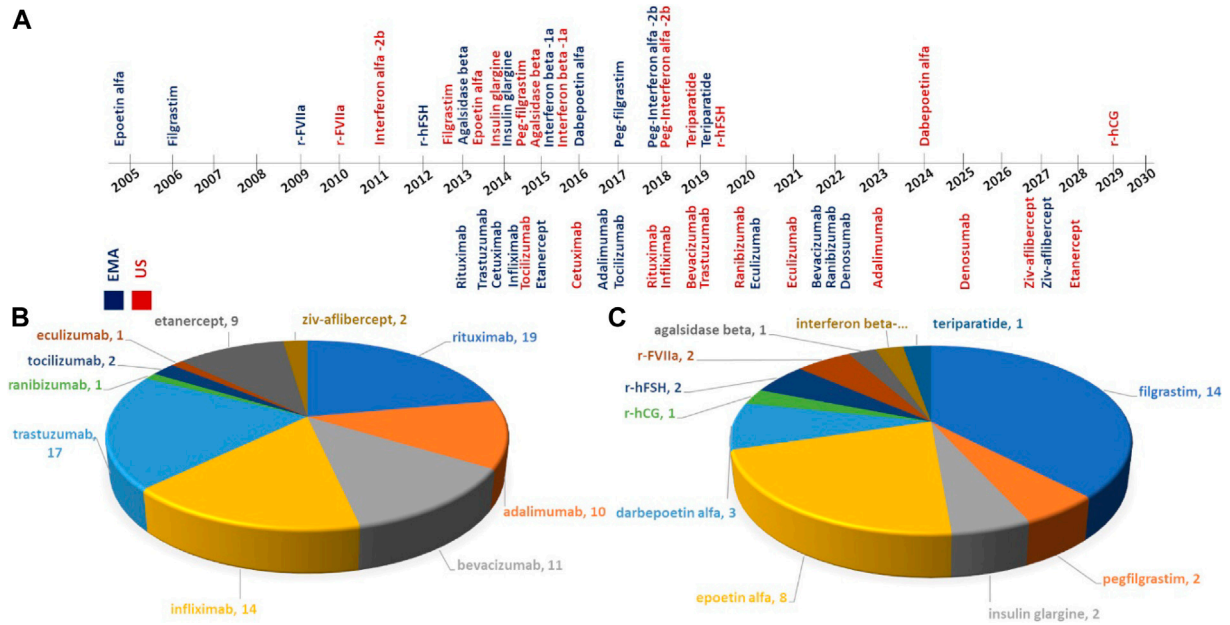

FIGURE 3 | (A) Timeline on patent expirations of reference products in European Medicines Agency; EMA (Moorkens et al., 2020) and U.S. Food and Drug Administration; USFDA (Derbyshire and Shina, 2019), publications on analytical similarity studies for biosimilars under **(B)** mAbs, and **(C)** non-mAbs.

biologics including blockbuster drugs nearing patent cliff in this decade include Bevacizumab (2022-EU), ranibizumab (2022-EU), Denosumab (EU-2020), adalimumab (US-2023), Denosumab (US-2025), Ziv-aflibercept (EU/US-2021 and Etanercept (2028-US) for mAb based biologics and Dabepoetin alpha (2024-US) and r-hCG (2029-US) in non-mAb biologics (**Figure 3A**).

The affordability of biosimilars largely depends on remissions in clinical studies granted on the basis of analytical and functional biosimilarity assessment data presented to the regulators. Despite a large number of approvals, public availability of information related to biosimilarity assessment is scattered and limited. Here, we have collected information with respect to analytical biosimilarity studies published as peer-reviewed research articles and offer a comprehensive account of the same in the following section.

2.1 Analytical Biosimilarity Assessment in the Published Literature

Head-to-head structural and functional biosimilarity assessment is a non-trivial, resource-intensive exercise since there is a need to use multiple methods for analytical and functional characterization. Most regulatory guidelines recommend the use of a gamut of orthogonal, high-resolution, analytical tools for qualitative and quantitative characterization of CQAs. Although several biosimilars have been approved to date, publicly available repositories of published literature on analytical biosimilarity studies remain limited (Ishii-Watabe and Kuwabara, 2019; Alsamil et al., 2020; Ratih et al., 2021; Safdar et al., 2021). In this section, we have focused on peer-reviewed analytical biosimilarity studies published so far, with a focus on analytical platforms used for characterization of each CQA. The methodology adopted for the selection of relevant publications from search engines has been detailed in **Supplementary Material**. The final database consisted of 116 publications presenting analytical biosimilarity studies for approved/intended biosimilars available in the public domain with details on the CQAs assessed and analytical tools used to date (**Supplementary Table S4**).

To the best of our knowledge, the first peer-reviewed biosimilarity study was published in 2006 where biophysical comparability of Epoetin alfa was carried out comparing the analytical profiles of Eprex® (prefilled syringes) with the innovator, namely Epogen®. It is a recombinant human erythropoietin that stimulates red blood cell production and is approved by FDA for use in treatment of anemia due to chronic kidney disease or cancer treatments. (Deechongkit et al., 2006). The innovator product Epogen® manufactured by Amgen reached patent cliff in 2005 in Europe and 2013 in US following which several biosimilars and intended copies have entered the markets. The market for the molecule continues to grow (USD9,243.12 million in 2020), and is projected to reach USD14,414.59 million by 2028. The annual sales of Epogen®, the innovator product was reported at 598 million USD for financial year 2020 (Amgen, 2021; Nerkar et al., 2021). Since epoetin alpha, 10 mAbs and 15 non mAbs have reached the patent cliff in either the US or EMA and the peer-reviewed biosimilarity studies have been published for most off-patent products (**Figure 3A**, **Supplementary Table S5**). About 80 analytical biosimilarity studies covering 8 off-patent mAbs (i.e., rituximab, trastuzumab, bevacizumab, infliximab, adalimumab,

ranibizumab, tocilizumab, and eculizumab) and 2 Fc-fusion proteins (i.e., etanercept and ziv-aflibercept) have been published so far (till July 2021). Interestingly, there are few instances where analytical studies have been published for the parent molecule (ziv-aflibercept) yet to reach patent expiration (due date 2027) (Hermosilla et al., 2020; Shen et al., 2021). Similarly, in the case of non-mAbs, 36 analytical biosimilarity studies covering 11 non-mAbs (i.e., filgrastim, peg-filgrastim, epoetin-α, darbepoetin-α, interferon-β, recombinant activated factor VII (rFVIIa), insulin glargine, recombinant human follicle stimulating hormone (r-FSH), agalsidase-β, recombinant human chorionic gonadotropin (r-hCG), and teriparatide) are accessible in the public domain (till July 2021). The most represented molecules in these studies include rituximab (19), trastuzumab (17), filgrastim (14), infliximab (14), bevacizumab (11), adalimumab (10), and etanercept (9) (**Figures 3B, C**).

Broadly, the most relevant CQAs of biotherapeutic products can be categorized under primary structure, higher-order structures (HOS), glycosylation (eukaryotic hosts), product-related variants, and process-related variants. The primary structure is further divided into intact/subunit mass analysis, amino acid sequence/peptide mapping, and disulfide bridge/free sulfhydryl group; HOS into the secondary structure, tertiary structure, and conformational stability; glycosylation into oligosaccharide pattern, glycopeptide mapping, and monosaccharide/sialic acid content; product-related variants into size variants, charge variants and related proteins arising out of post-translational modifications, i.e., aggregates, fragments, C-terminal lysine loss, N-terminal pyroglutamate cyclization, methionine oxidation, asparagine deamidation, aspartate isomerization, glycation, phosphorylation, acetylation, acylation, misfolding and process-related variants into host cell proteins (HCPs) and host cell DNA (HCD). A minimum requirement of at least one technique under each of the above-mentioned categories is mandatory for assessment, except in cases where the nature of the therapeutic of interest allows for the exclusion of analyzing certain attributes. For example, biosimilars expressed in *E. coli* do not require glycosylation analysis as the expression system is not capable of performing glycosylation.

For interested readers, a comprehensive account of CQA-wise and tool-wise analytical biosimilarity studies in published literature covering orthogonal analytical tools has been tabulated in **Supplementary Table S6**. From published studies, most assessed CQAs were primary structure (peptide mapping/amino acid sequence covered in 76 studies), followed by product-related variants (size variants covered in 75 studies), HOS (tertiary structure covered in 63 studies), and glycosylation (58 studies). This is not surprising as biosimilarity exhibited across the structural hierarchy is indicative of preservation of the functionality and hence efficacy of the intended biosimilar.

While assessing biosimilarity, one is really looking at the structural fingerprint of the biosimilar DP/DS and comparing it to the innovator. The strength of the evidence gathered is hence directly dependent on the resolution and sensitivity of the techniques employed. Moreover, in certain instances, one technique *per* attribute may not be sufficient as the attribute in question may be multi-faceted and hence requires multiple orthogonal tools. HOS and size variants are two such examples. Hence orthogonal tools serve as a means to 1) corroborate evidence for biosimilarity and 2) map multiple facets of a complex attribute independently, with an overall aim of reducing ambiguity. Having said that, there is significant commonality in CQAs for therapeutic molecules as elements of structural identity and integrity such as primary and HOS which are applicable to all proteins. Therefore, primarily the biosimilarity platforms consist of established biophysical techniques used in protein characterization. Over time and follow-on technical advancements, orthogonal assessment means have corroborated the skeleton of analytical characterization platforms (**Figure 4**). Major technical developments since 2015 have been outlined and discussed below.

2.2 Recent Advancements and Orthogonality in Analytical Similarity Assessment

As outlined in the USFDA guidelines on the comparative analytical assessment of biosimilars, detailed analysis of CQAs should be conducted using orthogonal analytical platforms including both established biophysical tools and new technologies, since each technique has its own merits and demerits (USFDA, 2019). The development of methods and techniques for orthogonal assessment of CQAs is hence a burgeoning field and over the years, some of these methods and techniques have been adopted for routine biosimilarity studies (**Supplementary Tables S6, S7** and **Figure 4**). In comparison to other CQAs, HOS and/or stability are the most represented with respect to publications reporting application of a new technology/technique for comparative analysis of biotherapeutics (covered in 28 studies) followed by glycan profiling (covered in 21 studies), charge variants (covered in 15 studies), peptide mapping (covered in 11 studies), size variants (covered in seven studies), and other attributes (other PTMs, glycation, disulfide bond, free sulfhydryl content, HCPs, and effector binding). Data acquisition aside, there has also been an increase in publications related to the application of advanced statistical methods for the evaluation of chromatography/spectroscopy data for comparative analysis (nine studies).

2.2.1 Primary Structure

Confirmation of primary structure involves mapping of the amino-acid sequence (sequence identity) and measuring the exact mass (mass-identity) of the biosimilar compared to the innovator (**Figure 5**). Sequence identity can be established by both Edman degradation and mass spectrometry (MS). Edman degradation, a traditional tool that involves successive removal of N-terminal amino acids by chemical methods, has featured in several publications across the years (Lee et al., 2013; Crobu et al., 2014). However, MS has increasingly become the more popular technique for both sequence and mass identity due to its sensitivity, versatility, fast turnaround and enhanced resolution. Moreover, additional information related to

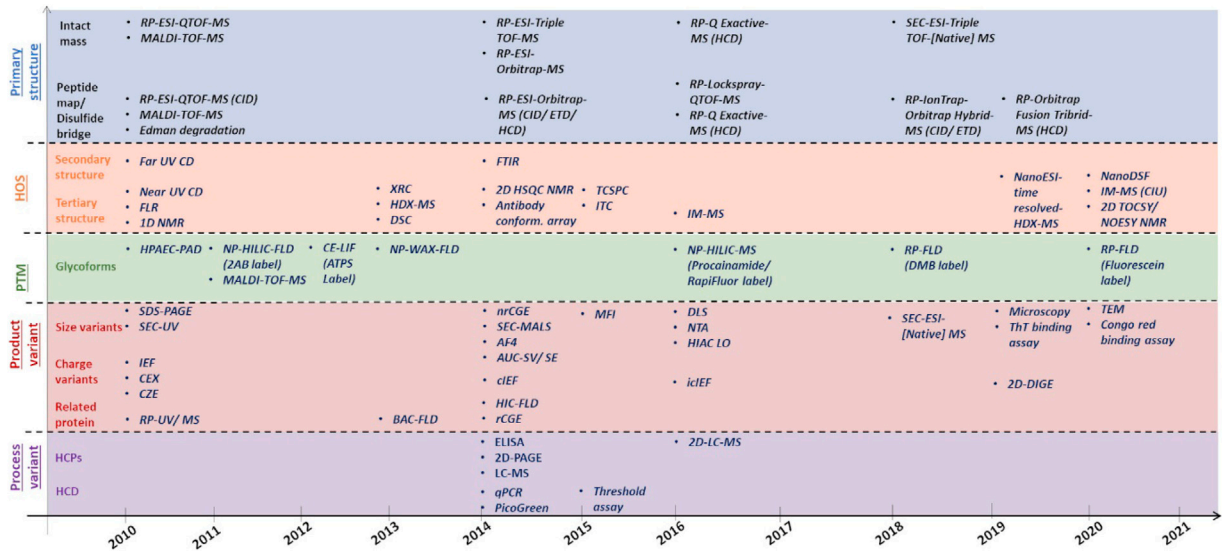

FIGURE 4 | Evolutionary timeline of analytical platforms used for different CQAs i.e., primary structure, HOS, glycosylation, product-related and process-related variant with respect to analytical biosimilarity assessment.

glycosylation and other PTMs can also be obtained through MS within a single analysis (Singleton, 2014). Over the years, MS platforms that have been featured in analytical similarity assessment publications for primary structure analysis include MALDI-TOF-MS, RP-ESI-QTOF-MS, RP-ESI-IonTrap/ Orbitrap/Q-Exactive-MS, LC-ESI-QTOF-[Native] MS (**Figure 4**, **Supplementary Table S4**).

For intact mass analysis, there have been recent advancements in developing LC-ESI-[Native] MS-based methods that offer an orthogonal alternative to traditional denaturing RP-ESI-MS where other LC modalities (such as SEC, HIC or IEX) are explored to determine intact mass with possible sequence variants under non-denaturing (native) conditions to identify biologically active species and monitor protein dynamics. SEC-ESI-QTOF-MS has been employed in analytical biosimilarity assessment of biosimilar candidates of Amgen's bevacizumab (ABP 215) (Seo et al., 2018) and infliximab (ABP 710) (Saleem et al., 2020), Sun Pharma's rituximab (SB-02) (Singh et al., 2018) and Celtrion's infliximab (CT-P13) (Hermosilla et al., 2019) compared to the respective innovators. The advantage of SEC-MS over RP-MS is that the native structure is preserved, and so the information gained is not only a comparison on exact mass, but also of the higher-order structure of the intended biosimilar. In acknowledgment of this, a host of native MS-based analyses such as native-MS, ion mobility (IM)-MS, and time-resolved hydrogen-deuterium exchange (HDX)-MS have been employed to provide an unambiguous assessment of the structural, dynamic, and chemical biosimilarity for Apobiologix's bevacizumab biosimilar (Brown et al., 2019) (**Supplementary Table S4**).

For peptide mapping, the constant evolution of peptide ion fragmentation types, such as electron-transfer dissociation (ETD) and/or Higher-energy C-trap dissociation (HCD) versus collision-induced dissociation (CID) along with the use of LC-QTOF, LC-Ion-Trap-Orbitrap and LC-Q-Exactive-Orbitrap MS has resulted in improvements in accurate identification and quantification of sequence variants and mutations. In two different studies, complete sequence coverage (100%) was obtained after trypsin/Lys-C digestion by targeted and non-targeted comparison of the tryptic map for comparing trastuzumab biosimilars (Chen et al., 2013). Also, stable isotope labeling by amino acids in cell culture (SILAC) by dimethyl labeling [i.e., 2CH2 (rituximab) and 2CD2 (RNAi-mediated rituximab)] were used to detect sequence variants along with disulfide linkages, PTMs, and mutations (Li et al., 2013). LC-QTOF has been used for the complete amino acid sequence analysis of Celtrion's infliximab (Remsima®) (Jung et al., 2014), trastuzumab (CT-P6) (Lee J. et al., 2018), rituximab (CT-P10) (Lee K. H. et al., 2018), Sun Pharma's rituximab (SB-02) (Singh et al., 2018) and Intas's peg-filgrastim (INTP5) (Shekhawat et al., 2019) biosimilars. Similarly, in recent years LC-Ion-Trap/Orbitrap Hybrid MS has been employed for characterization of certain biosimilars such as Amgen's bevacizumab (ABP 215) (Seo et al., 2018), rituximab (ABP 798) (Seo et al., 2020), infliximab (ABP 710) (Saleem et al., 2020), and Kyowa's adalimumab (Hulio®: FKB327) (Schreiber et al., 2020) biosimilars, and LC-Q-Exactive-Orbitrap-MS was used for China's bevacizumab (BVZ-BC) (company name not indicated in associated publication) (Yu et al., 2020) and Amgen's eculizumab (ABP 959) (Hutterer et al., 2021) biosimilars, to determine similar amino acid sequence, PTM profiles, and disulfide linkages compared to the respective innovators.

RP-based peptide mapping has certain limitations including poor retention of small/hydrophilic peptides, limited peak capacity, and reduced sample throughput due to the need for

re-equilibration between separations. This has largely been addressed through multi-dimensional LC platforms such as 2D-LC. Application of comprehensive two-dimensional liquid chromatography (2D-LC or LC × LC) as a tool for peptide mapping for trastuzumab has been demonstrated (Vanhoenacker et al., 2015). The method addresses identity, purity, and comparability of trastuzumab *via* three different combinations of LC × LC namely SCX, RP, and HILIC in the first dimension coupled with RP in the second dimension, respectively. In other studies, application of 2D-LC-MS has been demonstrated for antibody digests, with online-column digestion, followed by Orbitrap-MS for targeted peptide monitoring and chemometrics (Pérez-Robles et al., 2017; Shatat et al., 2018) (**Supplementary Table S7**).

Due to its sensitivity and dynamic range, more work is being done towards maximizing the capability of LC-MS-based formats through a more holistic characterization/comparability strategy including multiple levels of analysis (intact, subunit as well as peptides level). These multi-attribute methods (MAM) use a combination of high mass accuracy/high-resolution MS along with automated identification and relative quantification of the attributes (peptide mapping, glycopeptide, deamidation, and oxidation) with dedicated software. A head-to-head biosimilarity of trastuzumab and cetuximab with biosimilar candidates has been demonstrated at all levels including peptides and glycopeptides produced by enzymatic digestions (e.g., trypsin, Lys-C, Asp-N, pepsin) and analyzed on nanoLC-QTOF-MS (Beck et al., 2015). MAM formats have also been demonstrated on formats such as LC-Orbitrap-MS. With respect to biosimilarity assessment, the new peak detection feature of the method has particular applicability as it automatizes the identification of new peaks in tested samples (Rogers et al., 2015, 2018) (**Supplementary Table S7**). The method has since been adopted in QC to release testing and MAM consortium has been formed to harmonize best practices and generate methodologies in the facilitation of the widespread integration of the MAM platform in QC labs (Millán-Martín et al., 2020). Recently, industry-wide inter-laboratory study (28 participating labs) using pre-digested samples of the NISTmAb RM 8671 and pre-defined experimental protocol has been conducted to test the robustness of MAM methods (Mouchahoir et al., 2021) (**Supplementary Table S7**). A version of the methods suitable for process development has been successfully implemented in three Sanofi sites with automatization of sample preparation as well as data interpretation (Song et al., 2021).

Other orthogonal platforms for primary structure assessment include MALDI-TOF-MS which offers a unique alternative to ESI-TOF-MS by producing less complicated spectra due to multiple charging and provides a significant tolerance against salts for fast and easy sample preparation. Few studies have reported the use of MALDI-TOF-MS for peptide mapping and disulfide bridging analysis of non-innovator versions, e.g., etanercept (AVG01) (Maity et al., 2011), TNFR-hyFc fusion protein (Lee et al., 2013), filgrastim (BK0023) (Crobu et al., 2014), and filgrastim (EP2006) (Sörgel et al., 2015) (**Supplementary Table S4**). In one of the study, chemometrics-based "nearness similarity index" was applied, as a mathematical comparison method applicable to complex mass spectrometric data, particularly in peptide maps obtained by MALDI-TOF-MS (Pérez-Robles et al., 2017) (**Supplementary Table S7**). The method was applied to identify changes in long-term stability assessment of infliximab and rituximab and should be applicable in biocomparability studies.

2.2.2 Higher-Order Structure

Higher-order structure (HOS) is an umbrella term for three-dimensional (3D) conformations and includes multiple levels of structural hierarchies (i.e., secondary, tertiary and, quaternary). The concept of orthogonality is perhaps most celebrated for HOS characterization, since no one tool can map HOS in its entirety, hence multiple orthogonal tools are used for each level. Here, we have highlighted the evolution of orthogonality in published biosimilarity assessment studies (**Figure 4**) and discussed methods and techniques developed that have shown application towards biosimilarity assessment (**Supplementary Table S7**).

2.2.2.1 Secondary Structure

Initial biosimilarity assessment studies published on comparability of Eprex® (epoetin-α), Nivestim™ and Zarzio® (filgrastim) to their respective reference products showed secondary structure comparability through overlay of far ultraviolet circular dichroism (far UV CD) spectra (Deechongkit et al., 2006; Skrlin et al., 2010; Srgel et al., 2010). Later, Fourier transform infrared (FTIR) spectroscopy has also been incorporated either instead of or more commonly as an orthogonal assessment technique (Jung et al., 2014; Liu et al., 2016). Portfolio of biosimilars where CD and/or FTIR has been used for evaluation of secondary structure biosimilarity to reference product is quite diverse and includes both mAb and non-mAb products (**Supplementary Table S4**).

Lately, deconvolution of CD spectra (Fazel et al., 2019; Hermosilla et al., 2020) and IR absorption spectra (1700–1,600 cm^{-1}) (Lee et al., 2019; Shekhawat et al., 2019) using different software (K2D2, BeStSel, OriginPro, etc.) have been successfully used to quantitate secondary conformations (i.e., alpha-helix, beta-sheet, or random coil).

2.2.2.2 Tertiary Structure

Tertiary structures are 3D conformations. Near UV CD (250–300 nm) and fluorescence (FLR) spectroscopy have been traditionally the methods of choice for tertiary structure determination. In biosimilarity studies, these two techniques have been used either individually or together (Moro Pérez et al., 2019; Zhang et al., 2020). However, there have been limited studies involving the use of X-ray crystallography (XRC), a traditional technique for protein structural studies at the near-atomic level, as it works well only with proteins that can be crystallized, it requires expensive instrumentation, trained operators, and extensive time for analysis (Lerch et al., 2020). If we look at the evolution of HOS assessment in biosimilarity studies (**Figure 4**), the timeline is peppered with multiple orthogonal techniques such as single dimension NMR (Visser et al., 2013; Sörgel et al., 2015; Montacir et al., 2017), multi-

dimension NMR (Shekhawat et al., 2019; Bor Tekdemir et al., 2020; Kovács et al., 2020), HDX-MS (Cho et al., 2016; Brokx et al., 2017; Brown et al., 2019), IM-MS (Fang et al., 2016; Montacir et al., 2017, 2018), antibody conformational array (Jung et al., 2014; Hong et al., 2017), aptamer-based enzyme linked aptasorbent assay (Wildner et al., 2019), and small angle X-ray scattering (SAXS) (Narvekar et al., 2020) (**Supplementary Table S4**). Of these, NMR has emerged as the new gold standard for HOS assessment with more than 10 published biosimilarity studies published with either 1D, or 1D and 2D as a part of the analytical platform (**Supplementary Table S4**).

The popularity of NMR is also evident by the fact that by 2016, 15% of BLAs to USFDA included HDX-MS and NMR data for HOS characterization (USFDA, 2016). NMR is one of the high-resolution biophysical techniques for obtaining information regarding protein structure, dynamics, and flexibility at the atomic level by mapping the individual atoms linkage with each other in the 3D space. However, its application for large molecules such as mAbs has been limited until recently. ^{1}H NMR has been implemented for HOS assessment, where pulsed-field gradient stimulated echo (PGSTE) experiment has been used to generate highly resolved spectra of intact mAbs in formulation buffers (Poppe et al., 2015) (**Supplementary Table S7**). Based on differences in the translational diffusion coefficients of molecules in the NMR sample, virtually all other undesired signals arising from water and excipients could be removed. The PROFILE method has since been implemented for similarity assessment studies with the application of chemometrics for statistical analysis of similarity.

Following 1D NMR, the applicability of 2D formats has also shown great promise in biosimilarity assessment, where two different isotopes have been used to generate each spectrum (^{13}C, ^{1}H, ^{15}N usually) and provide a series of ^{1}H or ^{13}C spectra, represented as a 2D diagram reflective of the HOS. Sophisticated sample preparation (radioactive labeling) required for NMR, along with the long acquisition time has been addressed in these studies along with characterization of different heterogeneities (charge variants, size, PTMs, glycosylation) present within the formulation. Seminal work in this field with respect to method validation and standardization for characterization of mAb-based modalities has been carried out by, or in association with NIST and made available as a series of publications (Arbogast et al., 2015, 2016, 2017; Brinson and Marino, 2019; Brinson et al., 2020; Sheen et al., 2020) (**Supplementary Table S7**). Recent studies have shown structural elucidation of mAbs at natural abundance *via* 2D-^{13}C NMR in as little as 30 min, along with evidence for high correlation of spectra from individual Fab and Fc fragments with intact mAb (Arbogast et al., 2015), as well as application of chemometrics for NMR spectral analysis and biosimilarity studies (both 1D and 2D-NMR) (Arbogast et al., 2016, 2017; Japelj et al., 2016; Chen et al., 2018; Brinson et al., 2020; Sheen et al., 2020) (**Supplementary Table S7**). In addition to HOS, NMR has also been shown as an orthogonal tool for the assessment of size variants in biotherapeutics (Patil et al., 2017; Joshi et al., 2021) (**Supplementary Table S7**). In the last couple of years, more work has been done on the identification of PTMs through NMR, although suitability for comparative analysis is yet to be demonstrated (Hinterholzer et al., 2019, 2020) (**Supplementary Table S7**).

Another orthogonal technique for dynamic HOS comparability is HDX-MS. It elucidates protein conformational dynamics, protein folding, and protein-ligand interactions. HDX-MS relies on the coupling of low-temperature UHPLC with the sensitivity and resolution of MS to determine the locations and rates of amide hydrogen deuterium uptake. In the last 5 years, there has been methodological advances w.r.t range of temperature required for HDX experiments, method reproducibility, significance testing, and application of HDX-MS for similarity assessments. This includes the optimization of HDX-MS methodology based on manual solid-phase extraction to allow a fast and simplified conformational analysis of proteins under pharmaceutically relevant formulation conditions as demonstrated on interferon-β-1a in-formulation samples (E. Nazari et al., 2016) (**Supplementary Table S7**).

Similar to the development of NMR methods for biopharmaceutical analysis, an interlaboratory method validation study to evaluate the reproducibility of HDX-MS has also been conducted (Hudgens et al., 2019) (**Supplementary Table S7**). The study determined the reproducibility of continuous-labeling, bottom-up HDX-MS measurements from the Fab fragment of NISTmAb reference material (PDB: 5K8A) in an inter-laboratory comparison study comprising 15 laboratories (Cummins et al., 2016) (**Supplementary Table S7**).

Harmonization of HDX-MS methodology for biopharmaceutical analysis has also led to studies exploring the application of statistics for fast and unbiased data analysis. For example, to eliminate subjectivity and reliably identify significant differences in HDX-MS measurements, null measurements were performed and compared the application of individual tests of significance with Bonferroni correction and globally estimated significance limit (ΔHX) to evaluate the risk (i.e., falsely classifying a difference as significant) and power (i.e., failing to classify a true difference as significant) associated with different statistical analysis approaches (**Supplementary Table S7**). Combining these two approaches, hybrid statistical analysis was suggested, based on volcano plots that simultaneously decreased the risk of false positives and retained superior power. However, as these methods are not directly applicable in a comparative analysis setup, the authors demonstrated adoption of a univariate two one-sided tests (TOST) equivalence testing method for biosimilarity assessment. Using this method, the group was able to statistically distinguish between 5% deglycosylated NISTmAb and its unmodified reference material (Hageman et al., 2021).

2.2.2.3 Conformational Stability

Conformational stability is measured as the change in enthalpy due to variation in physical and chemical properties of a molecule as a function of temperature and/or time. Thermal denaturation by variable temperature (VT)-CD has been traditionally used to

study conformational stability as well as folding/unfolding mechanisms (Levy et al., 2014; Halim et al., 2018; Hermosilla et al., 2019) (**Supplementary Table S4**). Over the years, differential scanning calorimetry (DSC) has gained popularity as a fast and sensitive tool to measure thermodynamic stability and thermal unfolding pattern, where conformational changes are reflected as changes in characteristic transition/melting temperatures (*T*m) of one or multiple protein domains (Visser et al., 2013; Magnenat et al., 2017; Lee et al., 2019) (**Supplementary Table S4**). In recent times, time-correlated single-photon counting (TCSPC) is being used as an orthogonal technique to DSC to measure fluorescence lifetime distributions by the time-resolved intensity decay of protein (López-Morales et al., 2015; Mendoza-Macedo et al., 2016; Cerutti et al., 2019) (**Supplementary Table S4**). Other orthogonal tools include a fast, robust, low volume technique, i.e., nano differential scanning fluorimetry (nanoDSF) based on changes in intrinsic fluorescence upon thermal denaturation in a label-free fashion (Joshi et al., 2020; Wen et al., 2020) and IM-MS with collision-induced unfolding (CIU) (Kang et al., 2020b; 2020c) with limited applications so far (**Supplementary Table S4**).

2.2.3 Glycosylation

Glycosylation is an enzymatic PTM that occurs in proteins of eukaryotic origin (mAbs, Fc-fusion proteins, and others such as epoetin-α). These exist in multiple glycoforms and exhibit complex micro-as well as macro-heterogeneity (Higel et al., 2016). A multi-level characterization strategy is generally adopted for glycan profiling, i.e., glycoprotein, glycopeptides, and released glycan levels that employs different LC-MS approaches with adaptations in sample preparation (reduction/digestion/derivatization) and mode of chromatography [RP/hydrophilic interaction chromatography (HILIC)] to suit the analyte size (intact/reduced/glycopeptide/released glycan) (Krull et al., 2020; Duivelshof et al., 2021) (**Figure 4**). Glycan characterization at the intact and reduced level follows a typical LC-MS routine workflow with minimal sample preparation. Released glycan analysis on the other hand is a fairly complex exercise with multiple steps in sample preparation followed by acquisition and detection through HILIC-FLD/MS. In earlier biosimilarity assessment publications, traditional labels, i.e., 2-aminobenzoic acid (2AA), 2-aminobenzamide (2AB), or 4-amino-N-(2-diethylaminoethyl) benzamide (procainamide) have been used (Lauber et al., 2015; Reusch et al., 2015) for sample preparation. The most common label that has been used in biosimilarity studies published so far is 2AB (**Supplementary Table S4**). In recent studies, use of novel commercial labels such as Glycoworks™ or *Rapi*Fluor-MS™ with superior performance in terms of speed, sample preparation, fluorescence (FL) signal, and ionization efficiency have been used (Keser et al., 2018). Bioimilarity studies using RapiFluor-HILIC-FLD/MS for different biosimilar candidates include Celltrion's infliximab (Inflectra®) (Fang et al., 2016; Duivelshof et al., 2021), Shanghai Henlius's rituximab (HLX01) (Xu et al., 2019), and trastuzumab (HLX02) (Xie et al., 2020), Biocad's rituximab (Acellbia®), where 32 glycoforms were detected by tandem MS, while only 13 glycoforms were detected by HILIC-FLD (Kang et al., 2020c), and China's ziv-aflibercept (Shen et al., 2021) (**Supplementary Table S4**).

For quantification of individual monosaccharides, High-performance anion-exchange chromatography-pulsed amperometric detection (HPAEC-PAD) has been the preferred technique (Bruggink et al., 2005), followed by RP-FLD after labeling with 1, 2-diamino-4, 5-methylenedioxy-benzenedihydrochloride (DMB) or fluorescein (Higel et al., 2013). Biosimilarity studies using HPAEC-PAD and RP-FLD have been detailed in the **Supplementary Table S4**.

For most chromatography-based analysis (irrespective of the attribute), Capillary Electrophoresis (CE) is often the popular orthogonal technique of choice. Recent advances in various CE modes have made it more user-friendly and versatile for glycan analysis. However, LC remains the preferred separation technique in similarity assessments. Examples of similarity assessments with orthogonal use of CZE (8-aminopyrene-1, 3, 6-trisulfonate, APTS labeling) and laser-induced fluorescence (LIF) detection to HILIC-FLD include China's etanercept (company name not mentioned in associated publication) (Tan et al., 2012) and Probiomed's trastuzumab (López-Morales et al., 2015) and 10 different mAbs (Giorgetti et al., 2018). The applicability of capillary gel electrophoresis (CGE) for quantitative glycosimilarity assessment has been demonstrated for etanercept biosimilars (Borza et al., 2018) (**Supplementary Table S4**).

The high cost *per* analysis, long analysis time, and a need for sophisticated instrumentation as well as skill set required for data analysis have increased the need for orthogonal tools for glycan profiling. To address this, there has been an increase in the exploration of simpler glycan analysis formats utilizing spectroscopic tools such as RAMAN and FTIR wherein minimal sample preparation is required and chemometric methods are applied for data analysis. In one such study, RAMAN was used as a Process Analytical Technology (PAT) tool for monitoring glycosylation site occupancy in CHO cell cultures in real-time, indicating method developability for similarity assessment as a possibility in near future (Li et al., 2018) (**Supplementary Table S7**). In another recent study the utility of FTIR has been demonstrated for inter-batch or inter-sample comparison of monosaccharide profiles (Derenne et al., 2020) (**Supplementary Table S7**). The methodology is based on a statistical (PCA) comparison of FTIR spectra (4,000 and 600 cm^{-1}) of buffer exchanged glyco-therapeutics (to remove noise from excipients). The group mapped the FTIR fingerprint of 17 mAbs and found that it is not only sensitive to large differences such as the presence or absence of several monosaccharides but also to smaller modifications of the glycan and monosaccharide content. Another spectroscopic tool proposed for glycan profiling is NMR. In a proof of concept study, a "middle-down" NMR approach was conducted for identification of domain-specific glycosylation of mAbs without cleavage of the glycan moieties *via* sub-unit analysis of denatured Fc domain (Peng et al., 2018) (**Supplementary Table S7**). Chemical shift assignments from commercial standard glycans were obtained at ^{13}C natural abundance and allowed for

unambiguous determination of the chemical structure, glycosidic linkage position, and anomeric configuration of each monosaccharide in the major N-glycan scaffolds found in mAb molecules.

Another alternative/orthogonal glycan identification technique is lectin-microarray. Lectins are naturally occurring carbohydrate-binding proteins with affinities for specific sugar groups and due to this property, have found recent commercial application in glycan profiling for biotherapeutics. In a study, the utility as well as a high degree of orthogonality of commercial GlycoScope lectin microarray kit to three standard released glycan methods (HILIC-FLD of 2AA and 2AB labeling, HPAEC-PAD) have been demonstrated in an inter-lot comparability study (Cook et al., 2015) (**Supplementary Table S7**). The microarray platform comprised the microarray kit (microarray slides with Cy3-labelled goat anti-human-Fc antibody, IgG calibration standard, and components to prepare antibody exposure solution and bind/wash and block solutions) along with companion software for data interpretation and analysis.

Analysis of released glycans requires specific curated libraries for accurate annotation. Here, we would like to highlight two studies dealing with glycan data management, interpretation and analysis. The first study talks about the orthogonal application for structural annotation of N-glycan in a capillary electropherogram using GUcal software (Jarvas et al., 2015) (**Supplementary Table S7**). The second study describes a novel software, namley MoFi, which integrates hybrid MS data (intact and glycopeptide level) to assign glycan and PTMs to deconvoluted intact protein spectra (Skala et al., 2018) (**Supplementary Table S7**). The software first determines all monosaccharide/PTM compositions that are consistent with the residual masses derived from a deconvoluted spectrum of an intact glycoprotein, thereafter combining these primary annotations with a site-specific glycan library, generated through peptide mapping experiments. The software is unique in its data utilization approach and is capable of adding a new dimension of information to routine intact mass analysis, thereby making it more informative. The authors acknowledge the suitability of MoFi in GMP regulated biopharmaceutical analysis and it would indeed be interesting to evaluate its performance for biosimilarity assessment. Both MoFi and GUcal are freely available online.

2.2.4 Product-Related Variants and Impurities

Product-related variants and impurities corresponds to heterogeneities formed during bioprocess manufacturing, handling, and storage including size-based heterogeneities (aggregates, fragments, and sub-visible/visible particles), charge based heterogeneities (acidic and basic variants), and other product modifications (reduced, oxidized, glycated, misfolded proteins, etc.). Impurity profiling is a prerequisite during biosimilar development and specifications are set vis-à-vis the innovator for product-related variants subjected to case-by-case evaluation depending on the nature of the variant (EMA, 1999).

2.2.4.1 Aggregates/Fragments

Aggregation/fragmentation occur due to protein unfolding of hydrophobic patches with environmental changes during various stages of the manufacturing process and may elicit immunogenic responses if present in significant amounts (Ratanji et al., 2014). The spectrum of aggregate size ranges between soluble aggregates to visible precipitates, depending upon exposure to various stresses (i.e., shear, thermal, chemical, freeze-thaw, etc.) and duration of exposure. Hence, its assessment involves the use of multiple orthogonal tools (**Figure 4**). Size exclusion chromatography (SEC)-UV is the method of choice. It can quantify soluble aggregates/fragments (1–100 nm) and offers rapid analysis, excellent resolution, robustness, and reproducibility. More recently SEC has been augmented with multi-angle light scattering (MALS) for measuring the size, i.e., molar mass and root-mean-square (RMS) radius (also called the radius of gyration, R_g) of the different molecular species separated by SEC (Flores-Ortiz et al., 2014; Lee K. H. et al., 2018; Singh et al., 2018; Seo et al., 2020).

Protein loss due to stationary phase interactions and salt-induced aggregation/dissociation are common issues observed during SEC analysis. Hence, sedimentation velocity-analytical ultracentrifugation (SV-AUC), a matrix-free alternative to SEC, has been employed to quantitatively measure the size distribution. Researchers have proposed a validated AUC method and demonstrated its robustness as an orthogonal tool for similarity assessment of rituximab biosimilar product (Patil et al., 2020). However, AUC is not yet considered a technology that can be used for routine analysis, due to expensive instrumentation as well as challenging and time-intensive methods. While sodium dodecyl sulfate-polyacrylamide gel electrophoresis (SDS-PAGE) is still being used, it is qualitative in nature with limited sensitivity. CE-SDS, an automated version of SDS-PAGE in capillary format, is an orthogonal technique to SEC, particularly useful in quantifying fragments, partially reduced and non-glycosylated proteins (Shi et al., 2012; Wagner et al., 2020). Similarity studies with usage of SEC-UV/MALS, SV-AUC and CE-SDS include biosimilar candidates of Celtrion's infliximab (Remsima®) (Jung et al., 2014), trastuzumab (CT-P6) (Lee J. et al., 2018) and rituximab (CT-P10: Truxima™) (Lee K. H. et al., 2018), and Amgen's adalimumab (ABP 501) (Liu et al., 2016), bevacizumab (ABP 215) (Seo et al., 2018), infliximab (ABP 710) (Saleem et al., 2020), rituximab (ABP 798) (Seo et al., 2020) and eculizumab (ABP 959) (Hutterer et al., 2021) (**Supplementary Table S4**).

During SEC, insoluble aggregates/particles either elute out through the void volume or retain on the pre-column filter, hence needs to be analyzed using other techniques. These particles are categorized into sub-visible (1–100 μm) and sub-micron (100 nm-1 μm) particles depending on particle size. Sub-visible particles are analyzed by light obscuration (LO) in high accuracy (HIAC) liquid particle counter and micro-flow imaging (MFI). LO, an indirect optical method, is used to measure particle size distribution (PSD) of particles >10 μm but underestimates smaller transparent particle populations, and cannot distinguish sub-populations (Narhi et al., 2009).

Hence, more recently MFI is preferably used either singly or in conjunction with LO as an orthogonal technique for result validation (Sharma et al., 2010). Sub-micron particles are analyzed by dynamic light scattering (DLS) and field flow fractionation (FFF) or asymmetrical field flow fractionation (AF4). DLS is a semi-quantitative tool that determines PSD in the 1 nm–5 μm range, but cannot measure accurate size (Ahrer et al., 2003). AF4 is a no matrix alternative tool orthogonal to SEC-UV/MALS, and DLS for aggregates >1 nm which can be coupled with various detectors and enable analysis under native conditions (Contado, 2017). Few similarity studies have used all of the above multiple orthogonal platforms, i.e., LO, MFI, DLS and FFF in conjunction with SEC-UV/MALS, AUC, CE-SDS, for aggregate analysis. Examples include Amgen's adalimumab (ABP 501) (Liu et al., 2016), bevacizumab (ABP 215) (Seo et al., 2018), trastuzumab (ABP 980) (Hutterer et al., 2019), infliximab (ABP 710) (Saleem et al., 2020), and rituximab (ABP 798) (Seo et al., 2020) (**Supplementary Table S4**).

In addition to the established repertoire of tools above mentioned, DOSY-NMR has been demonstrated to be applicable for insulin and mAb-based formulations (Patil et al., 2017; Joshi et al., 2021). For mAbs, the relevance of DOSY-NMR for realistic hydrodynamic measurement has been demonstrated, where size estimations were found to be closer to computationally calculated radii of the published X-ray diffraction structures on Fab and Fc (Joshi et al., 2021) (**Supplementary Table S7**). Due to the highly heterogeneous nature of HMWs (in terms of shape and size), species-specific quantification is challenging (Hermosilla et al., 2020) (**Supplementary Table S7**). As a possible solution, researchers have developed a semi-automated electron microscopy (EM)-based method that involves semi-automated, size-based clustering of different protein species from micrographs. Demonstrating its applicability on mAbs, the method was shown to automatically select a highly heterogeneous population of aggregates for a given sample and perform a size-based classification (number of aggregates of each species vs size of radius for the species) (Kumar et al., 2020) (**Supplementary Table S7**). Nanoparticle tracking analysis (NTA), a non-destructive, high resolving real-time monitoring technique to measure the number-based PSD of particles >30 nm, has found limited mention in similarity studies thus far (Moreno et al., 2016; Arvinte et al., 2019) (**Supplementary Table S7**).

2.2.4.2 Charge Variants

Charge variants are differently charged proteoforms formed in different colloidal matrices (i.e., culture media, in-process buffers, or formulation) during various stages of the manufacturing process. Charge variants are considered key-quality attributes (kQAs) and an ongoing scientific debate is prominent on its inclusion as a CQA (DBT, 2016; Singh et al., 2016). Over the years, cation exchange (CEX) chromatography has been the preferred tool for charged variant analysis as it offers rapid analysis, suitable resolution, robustness, and reproducibility (Joshi et al., 2015). Few similarity studies include Amgen's bevacizumab (ABP 215) (Seo et al., 2018), rituximab (ABP 798) (Seo et al., 2020) and infliximab (ABP 710) (Saleem et al., 2020). Similar to other chromatography based analysis, CE serves as a rapid, high-performance alternative tool orthogonal to CEX (Moritz et al., 2015) and has been employed in biosimilarity assessments such as for Sun Pharma's rhCG (SB005) (Thennati et al., 2018) and rituximab (SB-02) (Singh et al., 2018) (**Supplementary Table S4**). Further, the application of different modes of CE and hyphenation of CEX or CE with MS, have introduced more orthogonal tools to the analytical armory with respect to charge variant analysis (Gahoual et al., 2014; Haselberg et al., 2018). Capillary isoelectric focusing (cIEF), an extension to gel IEF in a capillary format, offers a pI based separation of charged species in a pH gradient in response to an electric field with higher resolution, lesser sample volume requirement, and faster sample analysis (Zhao and Chen, 2014; Suba et al., 2015). Image capillary isoelectric focusing (icIEF) allows the cIEF process to be "imaged" in real-time using whole-column imaging detection (WCID) technology. While, cIEF has been employed for charge profiling of biosimilar candidates of Amgen's adalimumab (ABP 501) (Liu et al., 2016) and bevacizumab (ABP 215) (Seo et al., 2018), and Probiomed S.A. de C.V.'s rituximab (Kikuzubam) (Miranda-Hernandez et al., 2015), etanercept (Infinitam®) (Miranda-Hernández et al., 2016), trastuzumab-Probiomed (López-Morales et al., 2015) and infliximab-Probiomed (Velasco-Velázquez et al., 2017); examples of biosimilarity platforms with icIEF include Pfizer's infliximab (PF-06438179) (Derzi et al., 2016) and adalimumab (PF-06410293) (Derzi et al., 2020), Zhejiang Hisun's tocilizumab (HS628) (Miao et al., 2017), Samsung Bioepis's infliximab (SB2) (Hong et al., 2017) and adalimumab (SB5) (Lee et al., 2019), and Shanghai Henlius's rituximab (HLX01) (Xu et al., 2019), trastuzumab (HLX02) (Xie et al., 2020) and adalimumab (HLX03) (Zhang et al., 2020) (**Supplementary Table S4**).

Hyphenation of CEX/CE with MS either offline or *via* modifying the buffer system to use MS-compatible volatile salts (ammonium acetate/formate) has expanded the information gained by CEX/CE alone (Biacchi et al., 2015). The low flow operation of the microfluidic systems for CE-MS significantly boosts MS sensitivity and increased the dynamic range, even with sample amounts as low as 1 ng. Recently, 2 studies by Carillo et al., and Fussl et al., have demonstrated the application of commercially available microfluidic ZipChip microfluidic CE-MS technology for characterization of native charge variant profile complex mAbs such as cetuximab (Carillo et al., 2020; Fussl et al., 2020). Within the 1D-LC analysis format, there has been an increase in the development of MS-compatible CEX methods and direct online coupling of CEX to MS using volatile salt-based pH gradients, giving rise to Native CEX-MS. This has been demonstrated by multiple groups with variations in the stationary phase (weak and strong ion exchangers) and MS platforms (ESI-MS, IM-MS, and orbitrap) for trastuzumab, adalimumab, infliximab, bevacizumab, and cetuximab (Bailey et al., 2018; Füssl et al., 2018; Sankaran et al., 2018; Jaag et al., 2021; Murisier et al., 2021) (**Supplementary Table S7**).

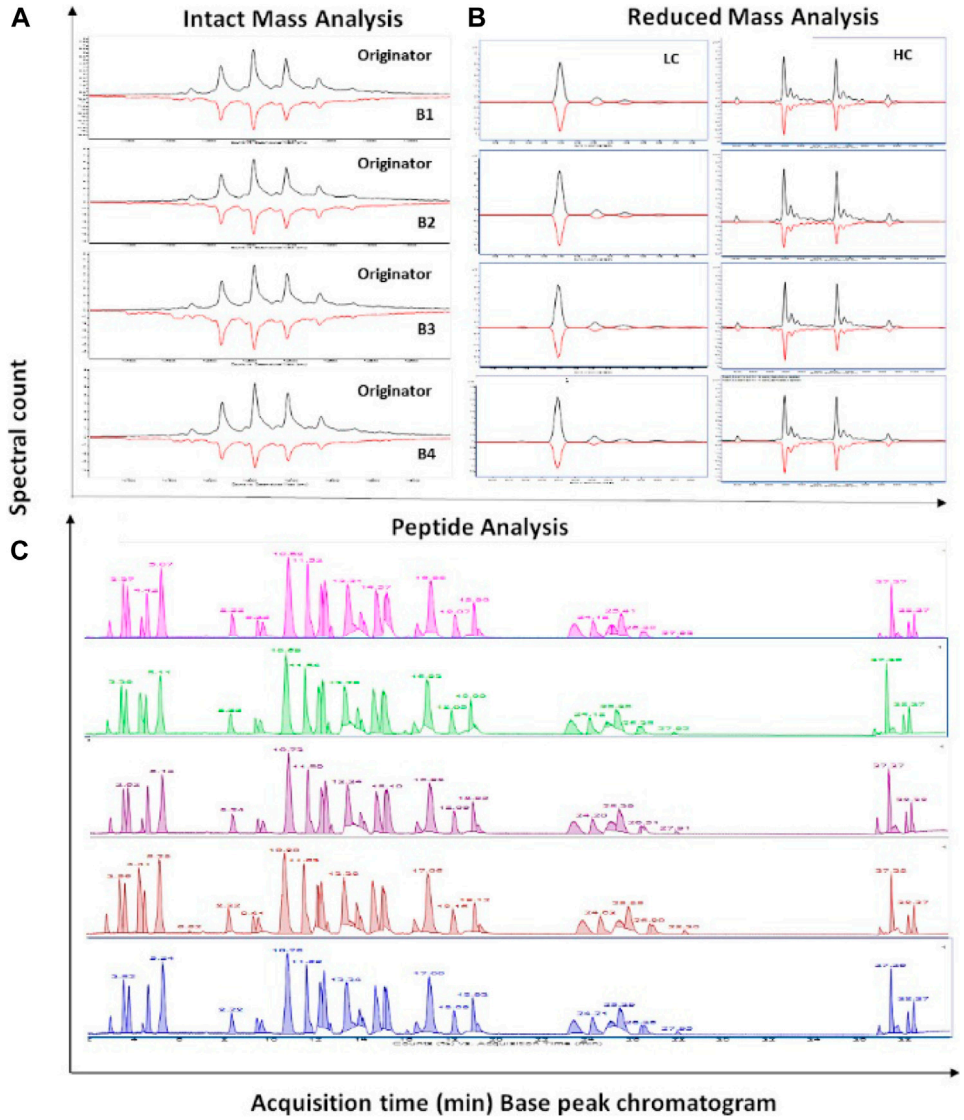

FIGURE 5 | RP-LC-MS based primary structure biosimilarity assessment of trastuzumab originator and biosimilars as adapted from Joshi and Rathore, 2020. **(A)** mirror plot of Intact profile, **(B)** mirror plot of reduced profile and **(C)** stacked chromatograms of trastuzumab biosimilars compared with originator.

Multidimensional platforms such as 2D-LC with CEX in first dimension followed by an MS-compatible second dimension, i.e., RP (desalting improves peak capacity and MS compatibility) have also been incorporated in biosimilarity (Alvarez et al., 2011; Stoll et al., 2015) (**Supplementary Table S7**). More such applications for similarity assessment of biosimilars have also been shown for cetuximab, trastuzumab, and infliximab (Sorensen et al., 2016).

2.2.4.3 Other Product Modifications

Non-enzymatic PTMs include modifications such as oxidation, phosphorylation, sulfation, acetylation, methylation, and hydroxylation, that are formed during multiple stages of the manufacturing process. Liquid chromatography offers unparalleled selectivity towards the characterization of PTMs and the quantitation of related molecular variants and impurities. RP-HPLC with UV/FLD is the preferred technique for quantifying oxidized and reduced species (Brokx et al., 2017; Bor Tekdemir et al., 2020). It has also been efficiently coupled with MS platforms for site-specific identification and relative quantification (Lee K. H. et al., 2018; Saleem et al., 2020). Hydrophobic interaction chromatography (HIC) (Flores-Ortiz et al., 2014; Hassett et al., 2018) with UV/FLD for molecular variants, i.e., oxidized, deamidated with isomerization and/or succinimide formation, proteolytic fragments and misfolded species, and boronate affinity chromatography (BAC) (Visser et al., 2013; Singh et al., 2018) with FLD for glycated species have been less widely used for the separation of product-related variants (**Supplementary Table S4**). It must be noted that HIC is highly suitable to monitor oxidation, but for deamidation/isomerization, it is much less efficient than IEX.

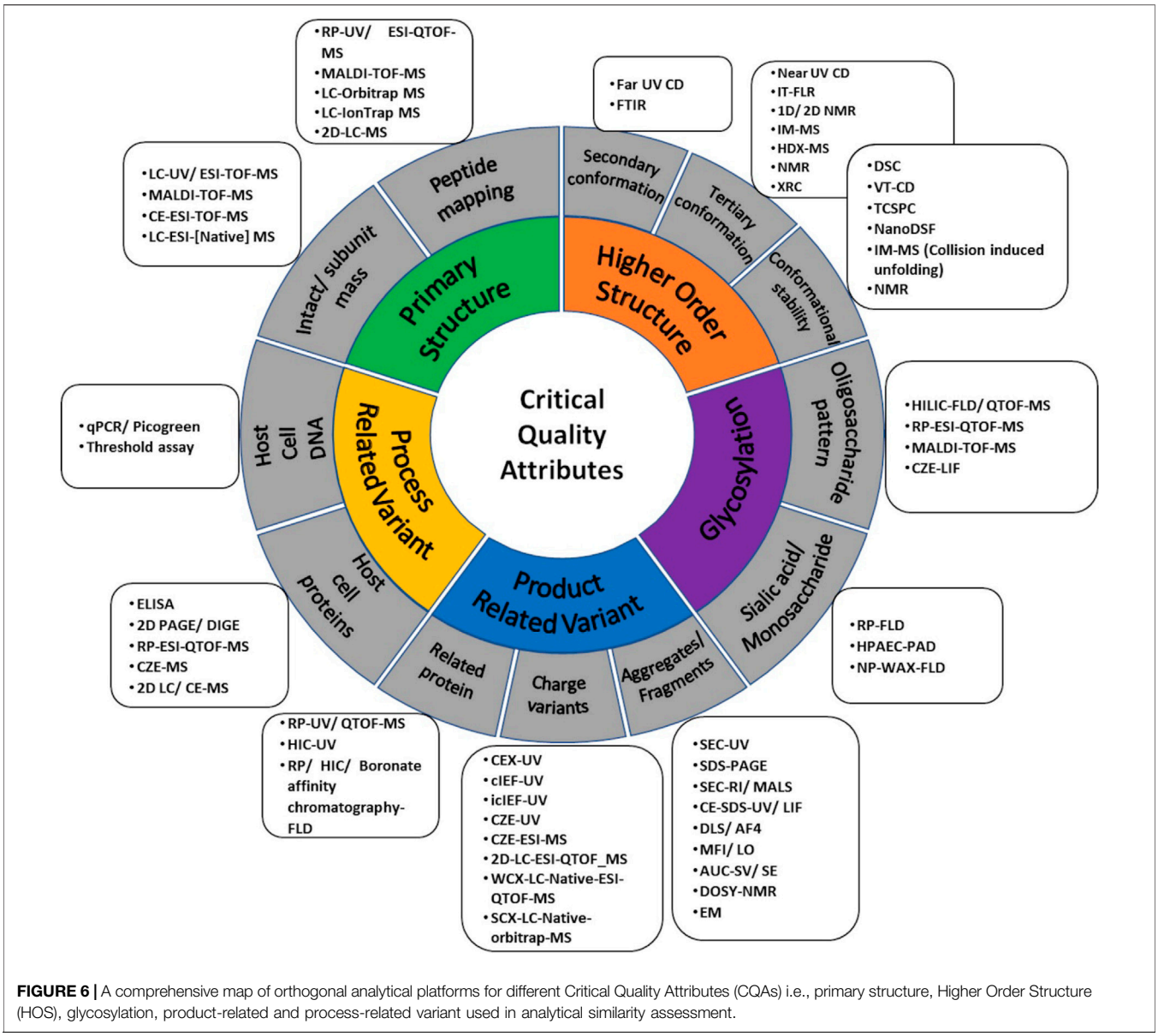

FIGURE 6 | A comprehensive map of orthogonal analytical platforms for different Critical Quality Attributes (CQAs) i.e., primary structure, Higher Order Structure (HOS), glycosylation, product-related and process-related variant used in analytical similarity assessment.

2.2.5 Process-Related Variants

Process-related variants, also called process residuals, include cell substrates, e.g., HCPs, HCD, cell culture, and downstream processing residuals. Enzyme-linked immunosorbent assay (ELISA) and real-time or quantitative PCR (qPCR using SYBR green, PicoGreen) have been consistently used as the method of choice for HCP and HCD detection and quantitation, respectively, in biosimilarity studies due to its high sensitivity, high throughput, and relative ease of use (Magalhaes et al., 2016; Xu et al., 2019; Xie et al., 2020) (**Supplementary Table S4**). Few publications have listed Threshold™ assays for HCD detection of filgrastim (EP2006; ≤200 pg/mg) (Sörgel et al., 2015) and adalimumab (FKB327; <2 pg/mg) (Schreiber et al., 2020) biosimilars (**Supplementary Table S4**).

Specific to HCP analysis, orthogonal methods are coming into picture, since identification of individual HCPs is gaining importance in addition to measuring the overall amount of the HCPs Due to the complex nature of the HCP mixture, qualitative methods such as ELISA are being replaced in favor of proteomic techniques such as 2D-gel electrophoresis and LC-MS/MS-based platforms. In two studies, three orthogonal methods, i.e., ELISA, 2D-PAGE/DIGE, and LC-MS/2D-LC-MS^E were used to identify, quantify and compare HCPs present in in-house filgrastim (Rathore and Bhambure, 2014) and Amgen′s adalimumab (ABP 501) (Liu et al., 2016) biosimilars with respect to the innovators (**Supplementary Table S4**). Due to the limited separation efficiency of LC-based systems, 2D-LC (high-pH RP/low-pH RP)-IM-MS^E platform have been explored for comparing HCP profiles between Celltrion's infliximab biosimilar (Inflectra®) and Remicade® especially significant for co-eluting peptides (Fang et al., 2016) (**Supplementary Table S4**). Finally, orthogonal LC-

MS platforms such as CZE-ESI-MS/MS have been successful in identification of a greater number of HCPs compared to LC-MS/MS (Zhu et al., 2016; Kumar et al., 2021).

2.2.5.1 Statistics in Analytical Biosimilarity Assessment

While the analytical biosimilarity platforms have seen significant evolution over the years with respect to the techniques employed and orthogonal assessment of CQAs, data analysis has remained traditional for a large part, depending on comparison of information in the form of X-Y plots and charts. Recent conversations on statistical inference of biosimilarity have opened following USFDA's, now retracted draft guidance on "Statistical Approaches to Evaluate Analytical Similarity." The draft guidance suggested risk and criticality-based segregation of CQAs into tiers and the application of tier-based statistical tools for ascertaining confidence in similarity for a given analytical dataset (USFDA, 2017). Application of tier-based statistical assessment has thereafter been demonstrated in recent biosimilarity assessments of biosimilar candidates for Celltrion's trastuzumab (CT-P6) (Lee J. et al., 2018), Samsung Bioepis's adalimumab (SB5) (Lee et al., 2019) Shanghai Henlius's rituximab (HLX01) (Xu et al., 2019), adalimumab (HLX03) (Zhang et al., 2020), and Roche China's bevacizumab (BVZ-BC) (Yu et al., 2020) (**Supplementary Table S4**). Along the same line of thought, statistical alternatives to similarity evaluation in cases where multiple reference products exist (EU-approved and US-licensed) have been proposed such as the use of simultaneous confidence approach as a possible means to reconcile the biosimilarity between the reference products as using it as a whole in comparison to the intended biosimilar (Zheng et al., 2019) (**Supplementary Table S7**). Studies comparing test procedures using confidence intervals for recently developed methods as well as other previously developed methods applied for demonstrating analytical biosimilarity have also been published (Burdick et al., 2017; Wang and Chow, 2017; Quiroz et al., 2019; Chen and Hsiao, 2020) (**Supplementary Table S7**). Comparative signature diagrams (CSDs) has been explored as an orthogonal visualization technique for analytical data sets in the form of colored contour plots (Kim et al., 2016) (**Supplementary Table S7**). However, these studies do not address orthogonal ways to analyze the raw data. As far as orthogonal strategies for raw data evaluation go, the application of multivariate data analysis (MVDA) techniques such as principal component analysis (PCA) has been applied to spectroscopy data from NMR and MS towards an unbiased spectral comparison of products (Arbogast et al., 2017; Chen et al., 2018; Shatat et al., 2018; Hassan et al., 2019; Brinson et al., 2020; Wang et al., 2020) (**Supplementary Table S7**). What remains yet unexplored, is the application of advanced statistics towards a holistic, multi-technique, multi-attribute biosimilarity assessment that also incorporates the impact of criticality of a CQA on relevance of a given data. In addition, application of statistics towards a scoring strategy for biosimilars has also yet to be demonstrated. Some examples of biosimilar scoring strategies limited to single instrument data have been published in recent times. These include a study where multivariate data analysis method based on JMP® software (SAS Institute Inc.) was developed to assess the glycosylation pattern similarity of antibody candidates from different conditions and scoring was done based on specific distance between the biosimilar and the reference product (Xu et al., 2021) (**Supplementary Table S7**). Another, single attribute-based scoring strategy has been used to list the different glycosylation related CQAs (gCQAs) and then describe calculations for establishing two different similarity scores, namely profile similarity score and compositional similarity score. The mean of these two scores has been defined as the final Glycosimilarity Index (GI) (Szekrenyes et al., 2020) (**Supplementary Table S7**).

3 CONCLUSION

Biosimilars are targeted to be an affordable alternative for expensive innovator biologics. However, reaching the goal of affordability without compromising with quality is challenging and requires a collaborative effort from manufacturers and regulators, guided by subject matter experts. For emerging biosimilar manufacturers and pharmaceutical manufactures that are expanding their offerings in the biosimilar domain, there is a steep learning curve with regards to successful manufacturing of biosimilars as translational learnings from the pharmaceutical sector are limited. Therefore, in the interest of affordability, it is important to build an informative corpus of common knowledge regarding all aspects of biosimilar development. This review is a step in that direction.

Over the years, as blockbuster drugs reach patent expiry, there has been a steady increase in the number of biosimilar approvals in all the major jurisdictions, especially for mAbs. There has also been an increase in published biosimilarity assessment studies. However, it does not yet commensurate with the rate of approvals and more such assessments need to be published through peer-reviewed pathways. The number of approvals as well as published assessments is likely to go up as global guidelines on interchangeability evolve and there is more market acceptance for these products. The data presented in peer-reviewed similarity assessment studies are representative of the total data generated during a similarity exercise and thus a good indicator of the percolation of new technologies from R&D stage to incorporation in the analytical platform to increase complementarity or orthogonality. Putting together all the tools that have either been used in similarity assessments or for which application towards similarity has been indicated, a comprehensive map of analytical platform, including orthogonal tools, has been built as an outcome of the literature survey done in this review (**Figure 6**).

As there is a cost attached with the incorporation of any new technology in the similarity assessment platform, common/well established tools and techniques that can be applied across the CQA spectrum are likely to be preferred. So far, the evolution of similarity assessment platforms reflects a growing acceptance of hyphenated platforms (separation x detection) with MS being the prevalent end-point detector. This is followed by advancements in spectroscopy, such as the inclusion of NMR for whole molecule analysis.

Recent technological advancements with respect to the application of 2D-NMR, multidimensional chromatography, HDX-MS, and spectroscopy in the characterization of CQAs with several publications on method standardization of these techniques towards similarity assessment have populated the scholastic space. However, to facilitate affordability, future similarity assessment exercises need to be more lightweight with respect to the number of tools and more diverse and information-intensive with respect to characterization. A possible solution seems to emerge in the form of MAMs. Indeed, there is a growing trend towards establishing multi-attribute monitoring and analysis methods for process control and purity analysis. Current MAMs are MS-based and applicable on digested proteins and MAM developments in whole molecule assessments in formulation conditions *via* LC-MS or spectroscopy platforms are a welcome move for similarity assessments.

We hope that the repositories provided as tables in the main text as well as Supplementary Information acts as a useful go to source for biopharmaceutical scientists, academicians, interested regulators as well as manufacturers, for the purpose of designing analytical similarity assessment platforms, decision making on tools to invest in, common methodologies to be adopted and also for general understanding of biosimilar and similarity landscape.

AUTHOR CONTRIBUTIONS

NN: Methodology, Investigation, Analysis, Writing- original draft. SJ: Methodology, Investigation, Analysis, Writing-original draft. DG: review and editing. AR: Conceptualization, Supervision, Project administration, Writing—review and editing, Funding acquisition and Resources.

FUNDING

This work was funded by the Center of Excellence for Biopharmaceutical Technology grant under the Department of Biotechnology, Government of India (BT/COE/34/SP15097/2015). Agilent was not involved in the study design, collection, analysis, interpretation of data, the writing of this article or the decision to submit it for publication.

ACKNOWLEDGMENTS

The authors would also like to thank Agilent Technologies India Private Limited for funding this research as part of its corporate social responsibility initiative.

SUPPLEMENTARY MATERIAL

The Supplementary Material for this article can be found online at: https://www.frontiersin.org/articles/10.3389/fbioe.2022.832059/full#supplementary-material

REFERENCES

Ahrer, K., Buchacher, A., Iberer, G., Josic, D., and Jungbauer, A. (2003). Analysis of Aggregates of Human Immunoglobulin G Using Size-Exclusion Chromatography, Static and Dynamic Light Scattering. *J. Chromatogr. A* 1009, 89–96. doi:10.1016/S0021-9673(03)00433-3

Alsamil, A. M., Giezen, T. J., Egberts, T. C., Leufkens, H. G., Vulto, A. G., van der Plas, M. R., et al. (2020). Reporting of Quality Attributes in Scientific Publications Presenting Biosimilarity Assessments of (Intended) Biosimilars: a Systematic Literature Review. *Eur. J. Pharm. Sci.* 154, 105501. doi:10.1016/j.ejps.2020.105501

Alvarez, M., Tremintin, G., Wang, J., Eng, M., Kao, Y.-H., Jeong, J., et al. (2011). On-line Characterization of Monoclonal Antibody Variants by Liquid Chromatography-Mass Spectrometry Operating in a Two-Dimensional Format. *Anal. Biochem.* 419, 17–25. doi:10.1016/j.ab.2011.07.033

Amgen (2021). *Amgen Reports Fourth Quarter and Full Year 2020 Financial Results.* New York: P R Newswire. Available at: https://www.prnewswire.com/news-releases/amgen-reports-fourth-quarter-and-full-year-2020-financial-results-301220622.html (Accessed January 6, 2022).

Arbogast, L. W., Brinson, R. G., Formolo, T., Hoopes, J. T., and Marino, J. P. (2016). 2D 1HN, 15N Correlated NMR Methods at Natural Abundance for Obtaining Structural Maps and Statistical Comparability of Monoclonal Antibodies. *Pharm. Res.* 33, 462–475. doi:10.1007/s11095-015-1802-3

Arbogast, L. W., Brinson, R. G., and Marino, J. P. (2015). Mapping Monoclonal Antibody Structure by 2D 13C NMR at Natural Abundance. *Anal. Chem.* 87, 3556–3561. doi:10.1021/ac504804m

Arbogast, L. W., Delaglio, F., Schiel, J. E., and Marino, J. P. (2017). Multivariate Analysis of Two-Dimensional 1H, 13C Methyl NMR Spectra of Monoclonal Antibody Therapeutics to Facilitate Assessment of Higher Order Structure. *Anal. Chem.* 89, 11839–11845. doi:10.1021/acs.analchem.7b03571

Arvinte, T., Palais, C., Poirier, E., Cudd, A., Rajendran, S., Brokx, S., et al. (2019). Part 1: Physicochemical Characterization of Bevacizumab in Undiluted 25 mg/mL Drug Product Solutions: Comparison of Originator with a Biosimilar Candidate. *J. Pharm. Biomed. Anal.* 175, 112742. doi:10.1016/j.jpba.2019.06.039

Bailey, A. O., Han, G., Phung, W., Gazis, P., Sutton, J., Josephs, J. L., et al. (2018). Charge Variant Native Mass Spectrometry Benefits Mass Precision and Dynamic Range of Monoclonal Antibody Intact Mass Analysis. *MAbs* 10, 1214–1225. doi:10.1080/19420862.2018.1521131

Beck, A., Debaene, F., Diemer, H., Wagner-Rousset, E., Colas, O., DorsselaerVan, A. V., et al. (2015). Cutting-edge Mass Spectrometry Characterization of Originator, Biosimilar and Biobetter Antibodies. *J. Mass. Spectrom.* 50, 285–297. doi:10.1002/jms.3554

Biacchi, M., Gahoual, R., Said, N., Beck, A., Leize-Wagner, E., and François, Y.-N. (2015). Glycoform Separation and Characterization of Cetuximab Variants by Middle-Up Off-Line Capillary Zone Electrophoresis-UV/Electrospray Ionization-MS. *Anal. Chem.* 87, 6240–6250. doi:10.1021/acs.analchem.5b00928

Bor Tekdemir, Z., Seckin, A. I., Kacar, T., Yilmaz, E., and Bekiroglu, S. (2020). Evaluation of Structural, Biological, and Functional Similarity of Biosimilar Granulocyte Colony Stimulating Factor to its Reference Product. *Pharm. Res.* 37. doi:10.1007/s11095-020-02932-7

Borza, B., Szigeti, M., Szekrenyes, A., Hajba, L., and Guttman, A. (2018). Glycosimilarity Assessment of Biotherapeutics 1: Quantitative Comparison of the N -glycosylation of the Innovator and a Biosimilar Version of Etanercept. *J. Pharm. Biomed. Anal.* 153, 182–185. doi:10.1016/j.jpba.2018.02.021

Brinson, R. G., Elliott, K. W., Arbogast, L. W., Sheen, D. A., Giddens, J. P., Marino, J. P., et al. (2020). Principal Component Analysis for Automated Classification of 2D Spectra and Interferograms of Protein Therapeutics: Influence of Noise, Reconstruction Details, and Data Preparation. *J. Biomol. NMR* 74, 643–656. doi:10.1007/s10858-020-00332-y

Brinson, R. G., and Marino, J. P. (2019). 2D J-Correlated Proton NMR Experiments for Structural Fingerprinting of Biotherapeutics. *J. Magn. Reson.* 307, 106581. doi:10.1016/j.jmr.2019.106581

Brokx, S., Scrocchi, L., Shah, N., and Dowd, J. (2017). A Demonstration of Analytical Similarity Comparing a Proposed Biosimilar Pegfilgrastim and Reference Pegfilgrastim. *Biologicals* 48, 28–38. doi:10.1016/j.biologicals.2017.06.001

Brown, K. A., Rajendran, S., Dowd, J., and Wilson, D. J. (2019). Rapid Characterization of Structural and Functional Similarity for a Candidate Bevacizumab (Avastin) Biosimilar Using a Multipronged Mass-spectrometry-based Approach. *Drug Test. Anal.* 11, 1207–1217. doi:10.1002/dta.2609

Bruggink, C., Maurer, R., Herrmann, H., Cavalli, S., and Hoefler, F. (2005). Analysis of Carbohydrates by Anion Exchange Chromatography and Mass Spectrometry. *J. Chromatogr. A* 1085, 104–109. doi:10.1016/j.chroma.2005.03.108

Burdick, R., Coffey, T., Gutka, H., Gratzl, G., Conlon, H. D., Huang, C.-T., et al. (2017). Statistical Approaches to Assess Biosimilarity from Analytical Data. *AAPS J.* 19, 4–14. doi:10.1208/s12248-016-9968-0

Canada (2016). *Guidance Document: Information and Submission Requirements for Biosimilar Biologic Drugs*.

Carillo, S., Jakes, C., and Bones, J. (2020). In-depth Analysis of Monoclonal Antibodies Using Microfluidic Capillary Electrophoresis and Native Mass Spectrometry. *J. Pharm. Biomed. Anal.* 185, 113218. doi:10.1016/j.jpba.2020.113218

CDSCO (2020). *List of New Drugs (R-DNA Origin) Approved for Manufacture and Marketing in India*. Available at: https://www.cdsco.gov.in/opencms/opencms/en/biologicals/rDNA/(Accessed June 9, 2021).

Cerutti, M. L., Pesce, A., Bès, C., and Seigelchifer, M. (2019). Physicochemical and Biological Characterization of RTXM83, a New Rituximab Biosimilar. *BioDrugs* 33, 307–319. doi:10.1007/s40259-019-00349-2

Chen, C., and Hsiao, C. F. (2020). Use of Tolerance Intervals for Assessing Biosimilarity. *Stat. Med.* 39, 3806–3822. doi:10.1002/SIM.8695

Chen, K., Park, J., Li, F., Patil, S. M., and Keire, D. A. (2018). Chemometric Methods to Quantify 1D and 2D NMR Spectral Differences Among Similar Protein Therapeutics. *AAPS PharmSciTech* 19, 1011–1019. doi:10.1208/s12249-017-0911-1

Chen, S.-L., Wu, S.-L., Huang, L.-J., Huang, J.-B., and Chen, S.-H. (2013). A Global Comparability Approach for Biosimilar Monoclonal Antibodies Using LC-Tandem MS Based Proteomics. *J. Pharm. Biomed. Anal.* 80, 126–135. doi:10.1016/j.jpba.2013.02.040

CHMP (2014). *Committee for Medicinal Products for Human Use (CHMP): Guideline on Similar Biological Medicinal Products - Revision 1*. Available at: www.ema.europa.eu/contact (Accessed July 1, 2021).

CHMP (2005). *Committee for Medicinal Products for Human Use (CHMP): Guideline on Similar Biological Medicinal Products*.

Cho, I. H., Lee, N., Song, D., Jung, S. Y., Bou-Assaf, G., Sosic, Z., et al. (2016). Evaluation of the Structural, Physicochemical, and Biological Characteristics of SB4, a Biosimilar of Etanercept. *MAbs* 8, 1136–1155. doi:10.1080/19420862.2016.1193659

Contado, C. (2017). Field Flow Fractionation Techniques to Explore the "Nano-World". *Anal. Bioanal. Chem.* 409, 2501–2518. doi:10.1007/s00216-017-0180-6

Cook, M. C., Kaldas, S. J., Muradia, G., Rosu-Myles, M., and Kunkel, J. P. (2015). Comparison of Orthogonal Chromatographic and Lectin-Affinity Microarray Methods for Glycan Profiling of a Therapeutic Monoclonal Antibody. *J. Chromatogr. B* 997, 162–178. doi:10.1016/j.jchromb.2015.05.035

Crobu, D., Spinetti, G., Schrepfer, R., Tonon, G., Jotti, G. S., Onali, P., et al. (2014). Preclinical and Clinical Phase I Studies of a New Recombinant Filgrastim (BK0023) in Comparison with Neupogen®. *BMC Pharmacol. Toxicol.* 15, 7. doi:10.1186/2050-6511-15-7

Cummins, D. J., Espada, A., Novick, S. J., Molina-Martin, M., Stites, R. E., Espinosa, J. F., et al. (2016). Two-Site Evaluation of the Repeatability and Precision of an Automated Dual-Column Hydrogen/Deuterium Exchange Mass Spectrometry Platform. *Anal. Chem.* 88, 6607–6614. doi:10.1021/acs.analchem.6b01650

DBT (2016). *CDSCO: Guidelines on Similar Biologics: Regulatory Requirements for Marketing Authorization in India*. Available at: https://nib.gov.in/NIB-DBT2016.pdf (Accessed June 9, 2021).

Deechongkit, S., Aoki, K. H., Park, S. S., and Kerwin, B. A. (2006). Biophysical Comparability of the Same Protein from Different Manufacturers: A Case Study Using Epoetin Alfa from Epogen and Eprex. *J. Pharm. Sci.* 95, 1931–1943. doi:10.1002/jps.20649

Derbyshire, M., and Shina, S. (2019). Patent Expiry Dates for Biologicals: 2018 Update. *Gabi J.* 8, 24–31. doi:10.5639/gabij.2019.0801.003

Derenne, A., Derfoufi, K.-M., Cowper, B., Delporte, C., and Goormaghtigh, E. (2020). FTIR Spectroscopy as an Analytical Tool to Compare Glycosylation in Therapeutic Monoclonal Antibodies. *Analytica Chim. Acta* 1112, 62–71. doi:10.1016/j.aca.2020.03.038

Derzi, M., Johnson, T. R., Shoieb, A. M., Conlon, H. D., Sharpe, P., Saati, A., et al. (2016). Nonclinical Evaluation of PF-06438179: A Potential Biosimilar to Remicade (Infliximab). *Adv. Ther.* 33, 1964–1982. doi:10.1007/s12325-016-0403-9

Derzi, M., Shoieb, A. M., Ripp, S. L., Finch, G. L., Lorello, L. G., O'Neil, S. P., et al. (2020). Comparative Nonclinical Assessments of the Biosimilar PF-06410293 and Originator Adalimumab. *Regul. Toxicol. Pharmacol.* 112, 104587. doi:10.1016/j.yrtph.2020.104587

Duivelshof, B. L., Denorme, S., Sandra, K., Liu, X., Beck, A., Lauber, M. A., et al. (2021). Quantitative N-Glycan Profiling of Therapeutic Monoclonal Antibodies Performed by Middle-Up Level HILIC-HRMS Analysis. *Pharmaceutics* 13 (13), 1744. doi:10.3390/PHARMACEUTICS13111744

EMA (1996). *ICH Topic Q5C: Quality of Biotechnological Products: Stability Testing of Biotechnological/Biological Products*. Available at: https://www.ema.europa.eu/en/documents/scientific-guideline/ich-topic-q-5-c-quality-biotechnological-products-stability-testing-biotechnological/biological-products_en.pdf (Accessed June 9, 2021).

EMA (2005). *ICH Topic Q5E: Comparability of Biotechnological/Biological Products*.

EMA (1999). *ICH Topic Q6B Specifications: Test Procedures and Acceptance Criteria for Biotechnological/Biological Products*. Available at: https://www.ema.europa.eu/en/documents/scientific-guideline/ich-q-6-b-test-procedures-acceptance-criteria-biotechnological/biological-products-step-5_en.pdf (Accessed June 9, 2021).

EMA (2020). *Medicines: European Medicines Agency*. Available at: https://www.ema.europa.eu/en/medicines/search_api_aggregation_ema_medicine_types/field_ema_med_biosimilar (Accessed June 9, 2021).

E. Nazari, Z. Z., van de Weert, M., Bou-Assaf, G., Houde, D., Weiskopf, A., and D. Rand, K. K. (2016). Rapid Conformational Analysis of Protein Drugs in Formulation by Hydrogen/Deuterium Exchange Mass Spectrometry. *J. Pharm. Sci.* 105, 3269–3277. doi:10.1016/j.xphs.2016.07.006

Eon-Duval, A., Broly, H., and Gleixner, R. (2012). Quality Attributes of Recombinant Therapeutic Proteins: an Assessment of Impact on Safety and Efficacy as Part of a Quality by Design Development Approach. *Biotechnol. Prog.* 28, 608–622. doi:10.1002/BTPR.1548

Fang, J., Doneanu, C., Alley, W. R., Yu, Y. Q., Beck, A., and Chen, W. (2016). Advanced Assessment of the Physicochemical Characteristics of Remicade and Inflectra by Sensitive LC/MS Techniques. *MAbs* 8, 1021–1034. doi:10.1080/19420862.2016.1193661

Fazel, R., Guan, Y., Vaziri, B., Krisp, C., Heikaus, L., Saadati, A., et al. (2019). Structural and *In Vitro* Functional Comparability Analysis of Altebrel, a Proposed Etanercept Biosimilar: Focus on Primary Sequence and Glycosylation. *Pharmaceuticals* 12, 14. doi:10.3390/ph12010014

Fekete, S., Gassner, A.-L., Rudaz, S., Schappler, J., and Guillarme, D. (2013). Analytical Strategies for the Characterization of Therapeutic Monoclonal Antibodies. *Trac Trends Anal. Chem.* 42, 74–83. doi:10.1016/j.trac.2012.09.012

Fekete, S., Guillarme, D., Sandra, P., and Sandra, K. (2016). Chromatographic, Electrophoretic, and Mass Spectrometric Methods for the Analytical Characterization of Protein Biopharmaceuticals. *Anal. Chem.* 88, 480–507. doi:10.1021/acs.analchem.5b04561

Flores-Ortiz, L. F., Campos-García, V. R., Perdomo-Abúndez, F. C., Pérez, N. O., and Medina-Rivero, E. (2014). Physicochemical Properties of Rituximab. *J. Liquid Chromatogr. Relat. Tech.* 37, 1438–1452. doi:10.1080/10826076.2013.794738

Füssl, F., Cook, K., Scheffler, K., Farrell, A., Mittermayr, S., and Bones, J. (2018). Charge Variant Analysis of Monoclonal Antibodies Using Direct Coupled pH Gradient Cation Exchange Chromatography to High-Resolution Native Mass Spectrometry. *Anal. Chem.* 90, 4669–4676. doi:10.1021/acs.analchem.7b05241

Füssl, F., Trappe, A., Carillo, S., Jakes, C., and Bones, J. (2020). Comparative Elucidation of Cetuximab Heterogeneity on the Intact Protein Level by Cation

Exchange Chromatography and Capillary Electrophoresis Coupled to Mass Spectrometry. *Anal. Chem.* 92, 5431–5438. doi:10.1021/acs.analchem.0c00185

GaBI (2021). *Copy Biologicals Approved in China*. Available at: https://www.gabionline.net/biosimilars/general/copy-biologicals-approved-in-china (Accessed July 17, 2021).

GaBI (2020). *Non-originator Biologicals Approved in Russia*. Available at: https://www.gabionline.net/biosimilars/general/Non-originator-biologicals-approved-in-Russia (Accessed July 17, 2021).

GaBI (2019). *Similar Biotherapeutic Products Approved and Marketed in Latin America*. Available at: https://gabionline.net/biosimilars/general/Similar-biotherapeutic-products-approved-and-marketed-in-Latin-America (Accessed July 17, 2021).

Gahoual, R., Biacchi, M., Chicher, J., Kuhn, L., Hammann, P., Beck, A., et al. (2014). Monoclonal Antibodies Biosimilarity Assessment Using Transient Isotachophoresis Capillary Zone Electrophoresis-Tandem Mass Spectrometry. *MAbs* 6, 1464–1473. doi:10.4161/mabs.36305

Gherghescu, I., and Delgado-Charro, M. B. (2020). The Biosimilar Landscape: An Overview of Regulatory Approvals by the EMA and FDA. *Pharmaceutics* 13 (13), 48. doi:10.3390/PHARMACEUTICS13010048

Giorgetti, J., D'Atri, V., Canonge, J., Lechner, A., Guillarme, D., Colas, O., et al. (2018). Monoclonal Antibody N-Glycosylation Profiling Using Capillary Electrophoresis - Mass Spectrometry: Assessment and Method Validation. *Talanta* 178, 530–537. doi:10.1016/j.talanta.2017.09.083

Global (2018). *Report on Global Biologics Market Size, Market Share, Application Analysis, Regional Outlook, Growth Trends, Key Players, Competitive Strategies and Forecasts, 2018 to 2026*. Available at: https://www.researchandmarkets.com/reports/4564281/global-biologics-market-size-market-share (Accessed April 27, 2021).

Hageman, T. S., Wrigley, M. S., and Weis, D. D. (2021). Statistical Equivalence Testing of Higher-Order Protein Structures with Differential Hydrogen Exchange-Mass Spectrometry (HX-MS). *Anal. Chem.* 93, 6980–6988. doi:10.1021/acs.analchem.0c05279

Halim, L. A., Márquez, M., Maas-Bakker, R. F., Castañeda-Hernández, G., Jiskoot, W., and Schellekens, H. (2018). Quality Comparison of Biosimilar and Copy Filgrastim Products with the Innovator Product. *Pharm. Res.* 35. doi:10.1007/s11095-018-2491-5

Haselberg, R., De Vijlder, T., Heukers, R., Smit, M. J., Romijn, E. P., Somsen, G. W., et al. (2018). Heterogeneity Assessment of Antibody-Derived Therapeutics at the Intact and Middle-Up Level by Low-Flow Sheathless Capillary Electrophoresis-Mass Spectrometry. *Analytica Chim. Acta* 1044, 181–190. doi:10.1016/j.aca.2018.08.024

Hassan, L. A., Shatat, S. M., Eltanany, B. M., Al-Ghobashy, M. A., and Abbas, S. S. (2019). Stability and Biosimilarity Assessment of Infliximab Using an Orthogonal Testing Protocol and Statistically-Guided Interpretation of Peptide Mapping. *Anal. Methods* 11, 3198–3211. doi:10.1039/c9ay00903e

Hassett, B., Scheinberg, M., Castañeda-Hernández, G., Li, M., Rao, U. R. K., Singh, E., et al. (2018). Variability of Intended Copies for Etanercept (Enbrel): Data on Multiple Batches of Seven Products. *MAbs* 10, 166–176. doi:10.1080/19420862.2017.1387346

Health (2021). *Department of Health: Which Biosimilar Medicines Are Available in Australia?* Available at: https://www1.health.gov.au/internet/main/publishing.nsf/Content/biosimilar-which-medicines-are-available-in-australia (Accessed June 9, 2021).

Hermosilla, J., Pérez-Robles, R., Salmerón-García, A., Casares, S., Cabeza, J., Bones, J., et al. (2020). Comprehensive Biophysical and Functional Study of Ziv-Aflibercept: Characterization and Forced Degradation. *Sci. Rep.* 10, 1–13. doi:10.1038/s41598-020-59465-7

Hermosilla, J., Sánchez-Martín, R., Pérez-Robles, R., Salmerón-García, A., Casares, S., Cabeza, J., et al. (2019). Comparative Stability Studies of Different Infliximab and Biosimilar CT-P13 Clinical Solutions by Combined Use of Physicochemical Analytical Techniques and Enzyme-Linked Immunosorbent Assay (ELISA). *BioDrugs* 33, 193–205. doi:10.1007/s40259-019-00342-9

Higel, F., Demelbauer, U., Seidl, A., Friess, W., and Sörgel, F. (2013). Reversed-phase Liquid-Chromatographic Mass Spectrometric N-Glycan Analysis of Biopharmaceuticals. *Anal. Bioanal. Chem.* 405 (405), 2481–2493. doi:10.1007/S00216-012-6690-3

Higel, F., Seidl, A., Sörgel, F., and Friess, W. (2016). N-glycosylation Heterogeneity and the Influence on Structure, Function and Pharmacokinetics of Monoclonal Antibodies and Fc Fusion Proteins. *Eur. J. Pharmaceutics Biopharmaceutics* 100, 94–100. doi:10.1016/j.ejpb.2016.01.005

Hinterholzer, A., Stanojlovic, V., Cabrele, C., and Schubert, M. (2019). Unambiguous Identification of Pyroglutamate in Full-Length Biopharmaceutical Monoclonal Antibodies by NMR Spectroscopy. *Anal. Chem.* 91, 14299–14305. doi:10.1021/acs.analchem.9b02513

Hinterholzer, A., Stanojlovic, V., Regl, C., Huber, C. G., Cabrele, C., and Schubert, M. (2020). Identification and Quantification of Oxidation Products in Full-Length Biotherapeutic Antibodies by NMR Spectroscopy. *Anal. Chem.* 92, 9666–9673. doi:10.1021/acs.analchem.0c00965

Hong, J., Lee, Y., Lee, C., Eo, S., Kim, S., Lee, N., et al. (2017). Physicochemical and Biological Characterization of SB2, a Biosimilar of Remicade (Infliximab). *MAbs* 9, 365–383. doi:10.1080/19420862.2016.1264550

Hudgens, J. W., Gallagher, E. S., Karageorgos, I., Anderson, K. W., Filliben, J. J., Huang, R. Y.-C., et al. (2019). Interlaboratory Comparison of Hydrogen-Deuterium Exchange Mass Spectrometry Measurements of the Fab Fragment of NISTmAb. *Anal. Chem.* 91, 7336–7345. doi:10.1021/ACS.ANALCHEM.9B01100

Hutterer, K. M., Ip, A., Kuhns, S., Cao, S., Wikström, M., and Liu, J. (2021). Analytical Similarity Assessment of ABP 959 in Comparison with Eculizumab Reference Product. *BioDrugs* 35, 563–577. doi:10.1007/S40259-021-00492-9

Hutterer, K. M., Polozova, A., Kuhns, S., McBride, H. J., Cao, X., and Liu, J. (2019). Assessing Analytical and Functional Similarity of Proposed Amgen Biosimilar ABP 980 to Trastuzumab. *BioDrugs* 33, 321–333. doi:10.1007/s40259-019-00350-9

Ishii-Watabe, A., and Kuwabara, T. (2019). Biosimilarity Assessment of Biosimilar Therapeutic Monoclonal Antibodies. *Drug Metab. Pharmacokinet.* 34, 64–70. doi:10.1016/j.dmpk.2018.11.004

Jaag, S., Shirokikh, M., and Lämmerhofer, M. (2021). Charge Variant Analysis of Protein-Based Biopharmaceuticals Using Two-Dimensional Liquid Chromatography Hyphenated to Mass Spectrometry. *J. Chromatogr. A* 1636, 461786. doi:10.1016/j.chroma.2020.461786

Jacobs, I., Ewesuedo, R., Lula, S., and Zacharchuk, C. (2017). Biosimilars for the Treatment of Cancer: A Systematic Review of Published Evidence. *BioDrugs* 31, 1–36. doi:10.1007/s40259-016-0207-0

Jacobs, I., Petersel, D., Shane, L. G., Ng, C.-K., Kirchhoff, C., Finch, G., et al. (2016). Monoclonal Antibody and Fusion Protein Biosimilars across Therapeutic Areas: A Systematic Review of Published Evidence. *BioDrugs* 30 (30), 489–523. doi:10.1007/S40259-016-0199-9

Japelj, B., Ilc, G., Marušič, J., Senčar, J., Kuzman, D., and Plavec, J. (2016). Biosimilar Structural Comparability Assessment by NMR: From Small Proteins to Monoclonal Antibodies. *Sci. Rep.* 6, 1–12. doi:10.1038/srep32201

Jarvas, G., Szigeti, M., and Guttman, A. (2015). GUcal: An Integrated Application for Capillary Electrophoresis Based Glycan Analysis. *Electrophoresis* 36, 3094–3096. doi:10.1002/elps.201500397

Joshi, S., Khatri, L. R., Kumar, A., and Rathore, A. S. (2021). Monitoring Size and Oligomeric-State Distribution of Therapeutic mAbs by NMR and DLS: Trastuzumab as a Case Study. *J. Pharm. Biomed. Anal.* 195, 113841. doi:10.1016/j.jpba.2020.113841

Joshi, S., Maharana, C., and Rathore, A. S. (2020). An Application of Nano Differential Scanning Fluorimetry for Higher Order Structure Assessment between mAb Originator and Biosimilars: Trastuzumab and Rituximab as Case Studies. *J. Pharm. Biomed. Anal.* 186, 113270. doi:10.1016/j.jpba.2020.113270

Joshi, S., and Rathore, A. S. (2020). Assessment of Structural and Functional Comparability of Biosimilar Products: Trastuzumab as a Case Study. *BioDrugs* 34, 209–223. doi:10.1007/s40259-020-00404-3

Joshi, V., Kumar, V., and Rathore, A. S. (2015). Rapid Analysis of Charge Variants of Monoclonal Antibodies Using Non-linear Salt Gradient in Cation-Exchange High Performance Liquid Chromatography. *J. Chromatogr. A* 1406, 175–185. doi:10.1016/j.chroma.2015.06.015

Jung, S. K., Lee, K. H., Jeon, J. W., Lee, J. W., Kwon, B. O., Kim, Y. J., et al. (2014). Physicochemical Characterization of Remsima. *MAbs* 6, 1163–1177. doi:10.4161/mabs.32221

Kang, H.-N., Thorpe, R., Knezevic, I., Blades, C. D. R. Z., Casas Levano, M., Chew, J. Y., et al. (2020a). The Regulatory Landscape of Biosimilars: WHO Efforts and

Progress Made from 2009 to 2019. *Biologicals* 65, 1–9. doi:10.1016/j.biologicals.2020.02.005

Kang, H. N., Thorpe, R., Knezevic, I., Casas Levano, M., Chilufya, M. B., Chirachanakul, P., et al. (2021). Regulatory Challenges with Biosimilars: an Update from 20 Countries. *Ann. N.Y. Acad. Sci.* 1491, 42–59. doi:10.1111/nyas.14522

Kang, J., Halseth, T., Vallejo, D., Najafabadi, Z. I., Sen, K. I., Ford, M., et al. (2020b). Assessment of Biosimilarity under Native and Heat-Stressed Conditions: Rituximab, Bevacizumab, and Trastuzumab Originators and Biosimilars. *Anal. Bioanal. Chem.* 412, 763–775. doi:10.1007/s00216-019-02298-9

Kang, J., Kim, S. Y., Vallejo, D., Hageman, T. S., White, D. R., Benet, A., et al. (2020c). Multifaceted Assessment of Rituximab Biosimilarity: The Impact of Glycan Microheterogeneity on Fc Function. *Eur. J. Pharmaceutics Biopharmaceutics* 146, 111–124. doi:10.1016/j.ejpb.2019.12.003

Keser, T., Pavić, T., Lauc, G., and Gornik, O. (2018). Comparison of 2-aminobenzamide, Procainamide and RapiFluor-MS as Derivatizing Agents for High-Throughput HILIC-UPLC-FLR-MS N-Glycan Analysis. *Front. Chem.* 6, 324. doi:10.3389/fchem.2018.00324

Kim, J. H., Joshi, S. B., Esfandiary, R., Iyer, V., Bishop, S. M., Volkin, D. B., et al. (2016). Improved Comparative Signature Diagrams to Evaluate Similarity of Storage Stability Profiles of Different IgG1 mAbs. *J. Pharm. Sci.* 105, 1028–1035. doi:10.1016/j.xphs.2016.01.008

Kovács, P., Schäfer, T., Háda, V., Hevér, H., Klingelhöfer, S., Nebel, M., et al. (2020). Comparative Physicochemical and Biological Characterisation of the Similar Biological Medicinal Product Teriparatide and its Reference Medicinal Product. *BioDrugs* 34, 65–75. doi:10.1007/s40259-019-00386-x

Krull, I., Rathore, A. S., and Budholiya, N. (2020). *A Review of Recent Developments in Analytical Characterization of Glycosylation in Therapeutic Proteins*. Cranbury, NJ: LCGC North Am., 30–37. Available at: https://www.chromatographyonline.com/view/review-recent-developments-analytical-characterization-glycosylation-therapeutic-proteins (Accessed June 9, 2021).

Kumar, M., Pant, A., Bansal, R., Pandey, A., Gomes, J., Khare, K., et al. (2020). Electron Microscopy-Based Semi-automated Characterization of Aggregation in Monoclonal Antibody Products. *Comput. Struct. Biotechnol. J.* 18, 1458–1465. doi:10.1016/j.csbj.2020.06.009

Kumar, R., Shah, R. L., Ahmad, S., and Rathore, A. S. (2021). Harnessing the Power of Electrophoresis and Chromatography: Offline Coupling of Reverse Phase Liquid Chromatography-capillary Zone Electrophoresis-tandem Mass Spectrometry for Analysis of Host Cell Proteins in Monoclonal Antibody Producing CHO Cell Line. *Electrophoresis* 42, 735–741. doi:10.1002/elps.202000252

Lauber, M. A., Yu, Y.-Q., Brousmiche, D. W., Hua, Z., Koza, S. M., Magnelli, P., et al. (2015). Rapid Preparation of Released N-Glycans for HILIC Analysis Using a Labeling Reagent that Facilitates Sensitive Fluorescence and ESI-MS Detection. *Anal. Chem.* 87, 5401–5409. doi:10.1021/acs.analchem.5b00758

Lee, J.-H., Yeo, J., Park, H. S., Sung, G., Lee, S. H., Yang, S. H., et al. (2013). Biochemical Characterization of a New Recombinant TNF Receptor-hyFc Fusion Protein Expressed in CHO Cells. *Protein Expr. Purif.* 87, 17–26. doi:10.1016/j.pep.2012.09.001

Lee, J., Kang, H. A., Bae, J. S., Kim, K. D., Lee, K. H., Lim, K. J., et al. (2018a). Evaluation of Analytical Similarity between Trastuzumab Biosimilar CT-P6 and Reference Product Using Statistical Analyses. *MAbs* 10, 547–571. doi:10.1080/19420862.2018.1440170

Lee, K. H., Lee, J., Bae, J. S., Kim, Y. J., Kang, H. A., Kim, S. H., et al. (2018b). Analytical Similarity Assessment of Rituximab Biosimilar CT-P10 to Reference Medicinal Product. *MAbs* 10, 380–396. doi:10.1080/19420862.2018.1433976

Lee, N., Lee, J. J., Yang, H., Baek, S., Kim, S., Kim, S., et al. (2019). Evaluation of Similar Quality Attribute Characteristics in SB5 and Reference Product of Adalimumab. *MAbs* 11, 129–144. doi:10.1080/19420862.2018.1530920

Lerch, T. F., Sharpe, P., Mayclin, S. J., Edwards, T. E., Polleck, S., Rouse, J. C., et al. (2020). Crystal Structures of PF-06438179/GP1111, an Infliximab Biosimilar. *BioDrugs* 34, 77–87. doi:10.1007/s40259-019-00390-1

Levy, M. J., Gucinski, A. C., Sommers, C. D., Ghasriani, H., Wang, B., Keire, D. A., et al. (2014). Analytical Techniques and Bioactivity Assays to Compare the Structure and Function of Filgrastim (Granulocyte-colony Stimulating Factor) Therapeutics from Different Manufacturers. *Anal. Bioanal. Chem.* 406, 6559–6567. doi:10.1007/s00216-013-7469-x

Li, C., Rossomando, A., Wu, S.-L., and Karger, B. L. (2013). Comparability Analysis of Anti-CD20 Commercial (Rituximab) and RNAi-Mediated Fucosylated Antibodies by Two LC-MS Approaches. *MAbs* 5, 565–575. doi:10.4161/mabs.24814

Li, M.-Y., Ebel, B., Paris, C., Chauchard, F., Guedon, E., and Marc, A. (2018). Real-time Monitoring of Antibody Glycosylation Site Occupancy by *In Situ* Raman Spectroscopy during Bioreactor CHO Cell Cultures. *Biotechnol. Prog.* 34, 486–493. doi:10.1002/btpr.2604

Liu, J., Eris, T., Li, C., Cao, S., and Kuhns, S. (2016). Assessing Analytical Similarity of Proposed Amgen Biosimilar ABP 501 to Adalimumab. *BioDrugs* 30, 321–338. doi:10.1007/s40259-016-0184-3

López-Morales, C. A., Miranda-Hernández, M. P., Juárez-Bayardo, L. C., Ramírez-Ibáñez, N. D., Romero-Díaz, A. J., Piña-Lara, N., et al. (2015). Physicochemical and Biological Characterization of a Biosimilar Trastuzumab. *Biomed. Res. Int.* 2015, 1–10. doi:10.1155/2015/427235

Magalhaes, V., Mantovani, M., Caruso, C., Facchini, F., Pascon, R., and Cagnacci, P. (2016). Physicochemical and Biological Comparison of the First Brazilian Biosimilar Filgrastim with its Reference Product. *Bs* 6, 45–60. doi:10.2147/bs.s107898

Magnenat, L., Palmese, A., Fremaux, C., D'Amici, F., Terlizzese, M., Rossi, M., et al. (2017). Demonstration of Physicochemical and Functional Similarity between the Proposed Biosimilar Adalimumab MSB11022 and Humira. *MAbs* 9, 127–139. doi:10.1080/19420862.2016.1259046

Maity, S., Ullanat, R., Lahiri, S., Shekar, S., Sodhan, G., Vyas, A., et al. (2011). A Non-innovator Version of Etanercept for Treatment of Arthritis. *Biologicals* 39, 384–395. doi:10.1016/j.biologicals.2011.08.014

Mendoza-Macedo, K., Romero-Díaz, A. J., Miranda-Hernández, M. P., Campos-García, V. R., Ramírez-Ibañez, N. D., Juárez-Bayardo, L. C., et al. (2016). Characterization and Comparability of Biosimilars: A Filgrastim Case of Study and Regulatory Perspectives for Latin America. *Electron. J. Biotechnol.* 24, 63–69. doi:10.1016/j.ejbt.2016.10.003

MFDS (2020). *Biosimilar: Minisry of Food and Drug Safety*. Available at: https://www.mfds.go.kr/eng/wpge/m_37/de011024l001.do (Accessed June 9, 2021).

Miao, S., Fan, L., Zhao, L., Ding, D., Liu, X., Wang, H., et al. (2017). Physicochemical and Biological Characterization of the Proposed Biosimilar Tocilizumab. *Biomed. Res. Int.* 2017, 1–13. doi:10.1155/2017/4926168

Millán-Martín, S., Jakes, C., Carillo, S., Buchanan, T., Guender, M., Kristensen, D. B., et al. (2020). Inter-laboratory Study of an Optimised Peptide Mapping Workflow Using Automated Trypsin Digestion for Monitoring Monoclonal Antibody Product Quality Attributes. *Anal. Bioanal. Chem.* 412, 6833–6848. doi:10.1007/s00216-020-02809-z

Miranda-Hernández, M. P., López-Morales, C. A., Perdomo-Abúndez, F. C., Salazar-Flores, R. D., Ramírez-Ibanez, N. D., Pérez, N. O., et al. (2016). New Alternatives for Autoimmune Disease Treatments: Physicochemical and Clinical Comparability of Biosimilar Etanercept. *J. Immunol. Res.* 2016, 1–9. doi:10.1155/2016/9697080

Miranda-Hernández, M. P., López-Morales, C. A., Ramírez-Ibáñez, N. D., Piña-Lara, N., Pérez, N. O., Molina-Pérez, A., et al. (2015). Assessment of Physicochemical Properties of Rituximab Related to its Immunomodulatory Activity. *J. Immunol. Res.* 2015, 1–10. doi:10.1155/2015/910763

Montacir, O., Montacir, H., Eravci, M., Springer, A., Hinderlich, S., Saadati, A., et al. (2017). Comparability Study of Rituximab Originator and Follow-On Biopharmaceutical. *J. Pharm. Biomed. Anal.* 140, 239–251. doi:10.1016/j.jpba.2017.03.029

Montacir, O., Montacir, H., Springer, A., Hinderlich, S., Mahboudi, F., Saadati, A., et al. (2018). Physicochemical Characterization, Glycosylation Pattern and Biosimilarity Assessment of the Fusion Protein Etanercept. *Protein J.* 37, 164–179. doi:10.1007/s10930-018-9757-y

Moorkens, E., Vulto, A. G., and Huys, I. (2020). An Overview of Patents on Therapeutic Monoclonal Antibodies in Europe: Are They a Hurdle to Biosimilar Market Entry? *mAbs* 12, 1743517. doi:10.1080/19420862.2020.1743517

Moreno, M. R., Tabitha, T. S., Nirmal, J., Radhakrishnan, K., Yee, C. H., Lim, S., et al. (2016). Study of Stability and Biophysical Characterization of Ranibizumab and Aflibercept. *Eur. J. Pharmaceutics Biopharmaceutics* 108, 156–167. doi:10.1016/j.ejpb.2016.09.003

Moritz, B., Schnaible, V., Kiessig, S., Heyne, A., Wild, M., Finkler, C., et al. (2015). Evaluation of Capillary Zone Electrophoresis for Charge Heterogeneity Testing

of Monoclonal Antibodies. *J. Chromatogr. B* 983-984, 101–110. doi:10.1016/j.jchromb.2014.12.024

Moro Pérez, L., Rodríguez Taño, A. d. l. C., Martín Márquez, L. R., Gómez Pérez, J. A., Valle Garay, A., and Blanco Santana, R. (2019). Rodríguez Taño, A. de la C., Martín Márquez, L. R., Gómez Pérez, J. A., Garay, A. V., and Santana, R. BConformational characterization of a novel anti-HER2 candidate antibody. *PLoS ONE* 14, e0215442. doi:10.1371/journal.pone.0215442

Mouchahoir, T., Schiel, J. E., Rogers, R., Heckert, A., Place, B. J., Ammerman, A., et al. (2021). New Peak Detection Performance Metrics from the MAM Consortium Interlaboratory Study. *J. Am. Soc. Mass. Spectrom.* 32, 913–928. doi:10.1021/JASMS.0C00415

Murisier, A., Duivelshof, B. L., Fekete, S., Bourquin, J., Schmudlach, A., Lauber, M. A., et al. (2021). Towards a Simple On-Line Coupling of Ion Exchange Chromatography and Native Mass Spectrometry for the Detailed Characterization of Monoclonal Antibodies. *J. Chromatogr. A* 1655, 462499. doi:10.1016/j.chroma.2021.462499

Narhi, L., Jiang, Y., Cao, S., Benedek, K., and Shnek, D. (2009). A Critical Review of Analytical Methods for Subvisible and Visible Particles. *Cpb* 10, 373–381. doi:10.2174/138920109788488905

Narvekar, A., Gawali, S. L., Hassan, P. A., Jain, R., and Dandekar, P. (2020). pH Dependent Aggregation and Conformation Changes of Rituximab Using SAXS and its Comparison with the Standard Regulatory Approach of Biophysical Characterization. *Int. J. Biol. Macromolecules* 164, 3084–3097. doi:10.1016/j.ijbiomac.2020.08.148

Nerkar, S., Darandale, M., and Sumant, O. (2021). *Erythropoietin Drugs Market by Product Type (Epoetin-Alfa, Epoetin-Beta, and Darbepoetin-Alfa, Others) and Application (Hematology, Kidney Disorder, Cancer, Others): Global Opportunity Analysis and Industry Forecast, 2021–2028*. Pune, India: Allied Mark. Res. Available at: https://www.alliedmarketresearch.com/erythropoietin-market (Accessed January 6, 2022).

NPRA (2021). *Biosimilars Approved*. Available at: https://www.npra.gov.my/index.php/en/informationen/new-products-indication/biosimilars-approved.html (Accessed July 17, 2021).

Nupur, N., Chhabra, N., Dash, R., and Rathore, A. S. (2018). Assessment of Structural and Functional Similarity of Biosimilar Products: Rituximab as a Case Study. *MAbs* 10, 143–158. doi:10.1080/19420862.2017.1402996

Nupur, N., Singh, S. K., Narula, G., and Rathore, A. S. (2016). Assessing Analytical Comparability of Biosimilars: GCSF as a Case Study. *J. Chromatogr. B* 1032, 165–171. doi:10.1016/j.jchromb.2016.05.027

Ortiz-Prado, E., Ponce-Zea, J., Vasconez, J. E., Castillo, D., Checa-Jaramilloz, D. C., Rodríguez-Burneo, N., et al. (2020). Current Trends for Biosimilars in the Latin American Market. *Gabi J.* 9, 64–74. doi:10.5639/gabij.2020.0902.011

Pategou, J. (2020). *Africa's Biosimilar Landscape Outlook Current Challenges*. Available at: https://www.biosimilardevelopment.com/doc/africa-s-biosimilar-landscape-outlook-current-challenges-0001 (Accessed July 1, 2021).

Patil, S. M., Keire, D. A., and Chen, K. (2017). Comparison of NMR and Dynamic Light Scattering for Measuring Diffusion Coefficients of Formulated Insulin: Implications for Particle Size Distribution Measurements in Drug Products. *AAPS J.* 19, 1760–1766. doi:10.1208/s12248-017-0127-z

Patil, S. M., Nguyen, J., Keire, D. A., and Chen, K. (2020). Sedimentation Velocity Analytical Ultracentrifugation Analysis of Marketed Rituximab Drug Product Size Distribution. *Pharm. Res.* 37 (37), 1–14. doi:10.1007/S11095-020-02961-2

Peng, J., Patil, S. M., Keire, D. A., and Chen, K. (2018). Chemical Structure and Composition of Major Glycans Covalently Linked to Therapeutic Monoclonal Antibodies by Middle-Down Nuclear Magnetic Resonance. *Anal. Chem.* 90, 11016–11024. doi:10.1021/acs.analchem.8b02637

Pérez-Robles, R., Navas, N., Medina-Rodríguez, S., and Cuadros-Rodríguez, L. (2017). Method for the Comparison of Complex Matrix Assisted Laser Desorption Ionization-Time of Flight Mass Spectra. Stability of Therapeutical Monoclonal Antibodies. *Chemometrics Intell. Lab. Syst.* 170, 58–67. doi:10.1016/j.chemolab.2017.09.008

PMDA (2020). *List of Approved Products: Pharmaceuticals and Medical Devices Agency*. Available at: https://www.pmda.go.jp/english/review-services/reviews/approved-information/drugs/0002.html (Accessed June 9, 2021).

Poppe, L., Jordan, J. B., Rogers, G., and Schnier, P. D. (2015). On the Analytical Superiority of 1D NMR for Fingerprinting the Higher Order Structure of Protein Therapeutics Compared to Multidimensional NMR Methods. *Anal. Chem.* 87, 5539–5545. doi:10.1021/acs.analchem.5b00950

Quiroz, J., Montes, R., Shi, H., and Roychoudhury, S. (2019). A Comparative Study of Confidence Intervals to Assess Biosimilarity from Analytical Data. *Pharm. Stat.* 18, 316–328. doi:10.1002/pst.1925

Ratanji, K. D., Derrick, J. P., Dearman, R. J., and Kimber, I. (2014). Immunogenicity of Therapeutic Proteins: Influence of Aggregation. *J. Immunotoxicology* 11, 99–109. doi:10.3109/1547691X.2013.821564

Rathore, A. S., and Bhambure, R. (2014). Establishing Analytical Comparability for "Biosimilars": Filgrastim as a Case Study. *Anal. Bioanal. Chem.* 406, 6569–6576. doi:10.1007/s00216-014-7887-4

Rathore, A. S., and Bhargava, A. (2020). Biosimilars in Developed Economies: Overview, Status, and Regulatory Considerations. *Regul. Toxicol. Pharmacol.* 110, 104525. doi:10.1016/j.yrtph.2019.104525

Rathore, A. S., and Bhargava, A. (2021a). Regulatory Considerations in Biosimilars: Asia pacific Regions. *Prep. Biochem. Biotechnol.* 51, 1–8. doi:10.1080/10826068.2020.1815061

Rathore, A. S., and Bhargava, A. (2021b). Regulatory Considerations in Biosimilars: Latin America Region. *Prep. Biochem. Biotechnol.* 51, 201–206. doi:10.1080/10826068.2021.1876729

Rathore, A. S., and Bhargava, A. (2021c). Regulatory Considerations in Biosimilars: Middle East and Africa Regions. *Prep. Biochem. Biotechnol.* 51, 731–737. doi:10.1080/10826068.2021.1959346

Ratih, R., Asmari, M., Abdel-Megied, A. M., Elbarbry, F., and El Deeb, S. (2021). Biosimilars: Review of Regulatory, Manufacturing, Analytical Aspects and beyond. *Microchemical J.* 165, 106143. doi:10.1016/j.microc.2021.106143

Reusch, D., Haberger, M., Maier, B., Maier, M., Kloseck, R., Zimmermann, B., et al. (2015). Comparison of Methods for the Analysis of Therapeutic Immunoglobulin G Fc-Glycosylation Profiles-Part 1: Separation-Based Methods. *MAbs* 7, 167–179. doi:10.4161/19420862.2014.986000

Rogers, R. S., Abernathy, M., Richardson, D. D., Rouse, J. C., Sperry, J. B., Swann, P., et al. (2018). A View on the Importance of "Multi-Attribute Method" for Measuring Purity of Biopharmaceuticals and Improving Overall Control Strategy. *Aaps J.* 20. doi:10.1208/s12248-017-0168-3

Rogers, R. S., Nightlinger, N. S., Livingston, B., Campbell, P., Bailey, R., and Balland, A. (2015). Development of a Quantitative Mass Spectrometry Multi-Attribute Method for Characterization, Quality Control Testing and Disposition of Biologics. *MAbs* 7, 881–890. doi:10.1080/19420862.2015.1069454

Safdar, A., Butt, M. H., Ahmad, A., and Zaman, M. (2021). Progress in Oncology Biosimilars till 2020: Scrutinizing Comparative Studies of Biosimilar Monoclonal Antibodies. *J. Oncol. Pharm. Pract.* 27, 107815522110160–107815522111204. doi:10.1177/10781552211016083

Saleem, R., Cantin, G., Wikström, M., Bolton, G., Kuhns, S., McBride, H. J., et al. (2020). Analytical and Functional Similarity Assessment of ABP 710, a Biosimilar to Infliximab Reference Product. *Pharm. Res.* 37, 1–23. doi:10.1007/s11095-020-02816-w

Sankaran, P. K., Kabadi, P. G., Honnappa, C. G., Subbarao, M., Pai, H. V., Adhikary, L., et al. (2018). Identification and Quantification of Product-Related Quality Attributes in Bio-Therapeutic Monoclonal Antibody via a Simple, and Robust Cation-Exchange HPLC Method Compatible with Direct Online Detection of UV and Native ESI-QTOF-MS Analysis. *J. Chromatogr. B* 1102-1103, 83–95. doi:10.1016/j.jchromb.2018.10.019

Santos-Neto, J. F., Oliveira, F. O., Hodel, K. V. S., Fonseca, L. M. S., Badaró, R., and MacHado, B. A. S. (2021). Technological Advancements in Monoclonal Antibodies. *Scientific World J.* 2021, 1–19. doi:10.1155/2021/6663708

Schreiber, S., Yamamoto, K., Muniz, R., and Iwura, T. (2020). Physicochemical Analysis and Biological Characterization of FKB327 as a Biosimilar to Adalimumab. *Pharmacol. Res. Perspect.* 8. doi:10.1002/prp2.604

Seo, N., Huang, Z., Kuhns, S., Sweet, H., Cao, S., Wikström, M., et al. (2020). Analytical and Functional Similarity of Biosimilar ABP 798 with Rituximab Reference Product. *Biologicals* 68, 79–91. doi:10.1016/j.biologicals.2020.08.002

Seo, N., Polozova, A., Zhang, M., Yates, Z., Cao, S., Li, H., et al. (2018). Analytical and Functional Similarity of Amgen Biosimilar ABP 215 to Bevacizumab. *MAbs* 10, 678–691. doi:10.1080/19420862.2018.1452580

Sharma, D. K., King, D., Oma, P., and Merchant, C. (2010). Micro-flow Imaging: Flow Microscopy Applied to Sub-visible Particulate Analysis in Protein Formulations. *AAPS J.* 12, 455–464. doi:10.1208/s12248-010-9205-1

Shatat, S. M., Eltanany, B. M., Mohamed, A. A., Al-Ghobashy, M. A., Fathalla, F. A., and Abbas, S. S. (2018). Coupling of On-Column Trypsin Digestion-Peptide Mapping and Principal Component Analysis for Stability and Biosimilarity Assessment of Recombinant Human Growth Hormone. *J. Chromatogr. B* 1072, 105–115. doi:10.1016/j.jchromb.2017.11.007

Sheen, D. A., Shen, V. K., Brinson, R. G., Arbogast, L. W., Marino, J. P., and Delaglio, F. (2020). Chemometric Outlier Classification of 2D-NMR Spectra to Enable Higher Order Structure Characterization of Protein Therapeutics. *Chemometrics Intell. Lab. Syst.* 199, 103973. doi:10.1016/j.chemolab.2020.103973

Shekhawat, R., Shah, C. K., Patel, A., Srinivasan, S., Kapoor, P., Patel, S., et al. (2019). Structural Similarity, Characterization of Poly Ethylene Glycol Linkage and Identification of Product Related Variants in Biosimilar Pegfilgrastim. *PLoS ONE* 14, e0212622. doi:10.1371/journal.pone.0212622

Shen, Z., Wang, Y., Xu, H., Zhang, Q., Sha, C., Sun, B., et al. (2021). Analytical Comparability Assessment on Glycosylation of Ziv-Aflibercept and the Biosimilar Candidate. *Int. J. Biol. Macromolecules* 180, 494–509. doi:10.1016/j.ijbiomac.2021.03.020

Shi, Y., Li, Z., and Lin, J. (2012). Advantages of CE-SDS over SDS-PAGE in mAb Purity Analysis. *Anal. Methods* 4, 1637–1642. doi:10.1039/c2ay25208b

Singh, S. K., Narula, G., and Rathore, A. S. (2016). Should Charge Variants of Monoclonal Antibody Therapeutics Be Considered Critical Quality Attributes? *Electrophoresis* 37, 2338–2346. doi:10.1002/elps.201600078

Singh, S. K., Pokalwar, S., Bose, S., Gupta, S., Almal, S., and Ranbhor, R. S. (2018). Structural and Functional Comparability Study of Anti-CD20 Monoclonal Antibody with Reference Product. *Btt* 12, 159–170. doi:10.2147/BTT.S187744

Singleton, C. A. (2014). MS in the Analysis of Biosimilars. *Bioanalysis* 6, 1627–1637. doi:10.4155/bio.14.110

Skala, W., Wohlschlager, T., Senn, S., Huber, G. E., and Huber, C. G. (2018). MoFi: A Software Tool for Annotating Glycoprotein Mass Spectra by Integrating Hybrid Data from the Intact Protein and Glycopeptide Level. *Anal. Chem.* 90, 5728–5736. doi:10.1021/ACS.ANALCHEM.8B00019

Skrlin, A., Radic, I., Vuletic, M., Schwinke, D., Runac, D., Kusalic, T., et al. (2010). Comparison of the Physicochemical Properties of a Biosimilar Filgrastim with Those of Reference Filgrastim. *Biologicals* 38, 557–566. doi:10.1016/j.biologicals.2010.05.002

Song, Y. E., Dubois, H., Hoffmann, M., Deri, S., Fromentin, Y., Wiesner, J., et al. (2021). Automated Mass Spectrometry Multi-Attribute Method Analyses for Process Development and Characterization of mAbs. *J. Chromatogr. B* 1166, 122540. doi:10.1016/j.jchromb.2021.122540

Sorensen, M., Harmes, D. C., Stoll, D. R., Staples, G. O., Fekete, S., Guillarme, D., et al. (2016). Comparison of Originator and Biosimilar Therapeutic Monoclonal Antibodies Using Comprehensive Two-Dimensional Liquid Chromatography Coupled with Time-Of-Flight Mass Spectrometry. *MAbs* 8, 1224–1234. doi:10.1080/19420862.2016.1203497

Sörgel, F., Lerch, H., and Lauber, T. (2010). Physicochemical and Biologic Comparability of a Biosimilar Granulocyte colony-stimulating Factor with its Reference Product. *BioDrugs* 24, 347–357. doi:10.2165/11585100-000000000-00000

Sörgel, F., Schwebig, A., Holzmann, J., Prasch, S., Singh, P., and Kinzig, M. (2015). Comparability of Biosimilar Filgrastim with Originator Filgrastim: Protein Characterization, Pharmacodynamics, and Pharmacokinetics. *BioDrugs* 29, 123–131. doi:10.1007/s40259-015-0124-7

Stoll, D. R., Harmes, D. C., Danforth, J., Wagner, E., Guillarme, D., Fekete, S., et al. (2015). Direct Identification of Rituximab Main Isoforms and Subunit Analysis by Online Selective Comprehensive Two-Dimensional Liquid Chromatography-Mass Spectrometry. *Anal. Chem.* 87, 8307–8315. doi:10.1021/acs.analchem.5b01578

Suba, D., Urbányi, Z., and Salgó, A. (2015). Capillary Isoelectric Focusing Method Development and Validation for Investigation of Recombinant Therapeutic Monoclonal Antibody. *J. Pharm. Biomed. Anal.* 114, 53–61. doi:10.1016/j.jpba.2015.04.037

Szekrenyes, A., Szigeti, M., Dvorakova, V., Jarvas, G., and Guttman, A. (2020). Quantitative Comparison of the N-Glycosylation of Therapeutic Glycoproteins Using the Glycosimilarity Index. A Tutorial. *Trac Trends Anal. Chem.* 122, 115728. doi:10.1016/j.trac.2019.115728

Tan, Q., Guo, Q., Fang, C., Wang, C., Li, B., Wang, H., et al. (2012). Characterization and Comparison of Commercially Available TNF Receptor 2-Fc Fusion Protein Products. *MAbs* 4, 761–774. doi:10.4161/mabs.22276

TGA (2018). *Biosimilar Medicines Regulation: Therapeutic Goods Administration: Version 2.2*. Available at: https://www.tga.gov.au/publication/biosimilar-medicines-regulation (Accessed June 9, 2021).

Thennati, R., Singh, S., Nage, N., Patel, Y., Bose, S., Burade, V., et al. (2018). Analytical Characterization of Recombinant hCG and Comparative Studies with Reference Product. *Btt* 12, 23–35. doi:10.2147/BTT.S141203

USFDA (2018). *Biological Product Definitions*. Available at: https://www.fda.gov/files/drugs/published/Biological-Product-Definitions.pdf (Accessed May 3, 2021).

USFDA (2021). *Biosimilar Product Information*. Available at: https://www.fda.gov/drugs/biosimilars/biosimilar-product-information (Accessed June 9, 2021).

USFDA (2019). *Draft Guidance: Development of Therapeutic Protein Biosimilars: Comparative Analytical Assessment and Other Quality-Related Considerations*.

USFDA (2015). *Guidance for Industry: Quality Considerations in Demonstrating Biosimilarity of a Therapeutic Protein Product to a Reference Product*. Available at: http://www.fda.gov/Drugs/GuidanceComplianceRegulatoryInformation/Guidances/default.htmand/orhttp://www.fda.gov/BiologicsBloodVaccines/GuidanceComplianceRegulatoryInformation/Guidances/default.htm (Accessed June 9, 2021).

USFDA (2016). *Regulatory Consideration for the Characterization of HOS in Biotechnology Products*.

USFDA (2017). *Statistical Approaches to Evaluate Analytical Similarity - Guidance for Industry*. Silver Spring, Maryland: FDA Guid. Ind.

Vanhoenacker, G., Vandenheede, I., David, F., Sandra, P., and Sandra, K. (2015). Comprehensive Two-Dimensional Liquid Chromatography of Therapeutic Monoclonal Antibody Digests. *Anal. Bioanal. Chem.* 407, 355–366. doi:10.1007/s00216-014-8299-1

Velasco-Velázquez, M., Salinas-Jazmín, N., Hisaki-Itaya, E., Cobos-Puc, L., Xolalpa, W., González, G., et al. (2017). Extensive Preclinical Evaluation of an Infliximab Biosimilar Candidate. *Eur. J. Pharm. Sci.* 102, 35–45. doi:10.1016/j.ejps.2017.01.038

Visser, J., Feuerstein, I., Stangler, T., Schmiederer, T., Fritsch, C., and Schiestl, M. (2013). Physicochemical and Functional Comparability between the Proposed Biosimilar Rituximab GP2013 and Originator Rituximab. *BioDrugs* 27, 495–507. doi:10.1007/s40259-013-0036-3

Wagner, E., Colas, O., Chenu, S., Goyon, A., Murisier, A., Cianferani, S., et al. (2020). Determination of Size Variants by CE-SDS for Approved Therapeutic Antibodies: Key Implications of Subclasses and Light Chain Specificities. *J. Pharm. Biomed. Anal.* 184, 113166. doi:10.1016/j.jpba.2020.113166

Wang, D., Park, J., Patil, S. M., Smith, C. J., Leazer, J. L., Keire, D. A., et al. (2020). An NMR-Based Similarity Metric for Higher Order Structure Quality Assessment Among U.S. Marketed Insulin Therapeutics. *J. Pharm. Sci.* 109, 1519–1528. doi:10.1016/j.xphs.2020.01.002

Wang, T., and Chow, S.-C. (2017). On the Establishment of Equivalence Acceptance Criterion in Analytical Similarity Assessment. *J. Biopharm. Stat.* 27, 206–212. doi:10.1080/10543406.2016.1265539

Wen, J., Lord, H., Knutson, N., and Wikström, M. (2020). Nano Differential Scanning Fluorimetry for Comparability Studies of Therapeutic Proteins. *Anal. Biochem.* 593, 113581. doi:10.1016/j.ab.2020.113581

WHO (2013). *Expert Committee on Biological Standardization: Guidelines on Evaluation of Monoclonal Antibodies as Similar Biotherapeutic Products (SBPs) - Annex 2*.

WHO (2009). *Final Expert Committee on Biological Standardization: Guidelines on Evaluation of Similar Biotherapeutic Products (SBPs)*.

Wildner, S., Huber, S., Regl, C., Huber, C. G., Lohrig, U., and Gadermaier, G. (2019). Aptamers as Quality Control Tool for Production, Storage and Biosimilarity of the Anti-CD20 Biopharmaceutical Rituximab. *Sci. Rep.* 9 (9), 1–14. doi:10.1038/s41598-018-37624-1

Wojtyra, U. (2021). *Smart & Biggar: Update on Biosimilars in Canada - April 2021*. Available at: https://www.smartbiggar.ca/insights/publication/update-on-biosimilars-in-canada-april-2021 (Accessed June 9, 2021).

Xie, L., Zhang, E., Xu, Y., Gao, W., Wang, L., Xie, M. H., et al. (2020). Demonstrating Analytical Similarity of Trastuzumab Biosimilar HLX02 to Herceptin with a Panel of Sensitive and Orthogonal Methods Including a

Novel FcγRIIIa Affinity Chromatography Technology. *BioDrugs* 34, 363–379. doi:10.1007/s40259-020-00407-0

Xu, J., Shao, Z., Han, X., Huang, Y., Zou, X., and Shen, Y. (2021). Similarity Assessment by Multivariate Statistics Method Based on the Distance between Biosimilar and Originator. *Bioresour. Bioproc.* 8, 24. doi:10.1186/s40643-021-00378-2

Xu, Y., Xie, L., Zhang, E., Gao, W., Wang, L., Cao, Y., et al. (2019). Physicochemical and Functional Assessments Demonstrating Analytical Similarity between Rituximab Biosimilar HLX01 and the MabThera. *MAbs* 11, 606–620. doi:10.1080/19420862.2019.1578147

Yu, C., Zhang, F., Xu, G., Wu, G., Wang, W., Liu, C., et al. (2020). Analytical Similarity of a Proposed Biosimilar BVZ-BC to Bevacizumab. *Anal. Chem.* 92, 3161–3170. doi:10.1021/acs.analchem.9b04871

Zhang, E., Xie, L., Qin, P., Lu, L., Xu, Y., Gao, W., et al. (2020). Quality by Design-Based Assessment for Analytical Similarity of Adalimumab Biosimilar HLX03 to Humira. *AAPS J.* 22, 1–14. doi:10.1208/s12248-020-00454-z

Zhao, S. S., and Chen, D. D. Y. (2014). Applications of Capillary Electrophoresis in Characterizing Recombinant Protein Therapeutics. *Electrophoresis* 35, 96–108. doi:10.1002/elps.201300372

Zheng, J., Yin, D., Yuan, M., and Chow, S.-C. (2019). Simultaneous Confidence Interval Methods for Analytical Similarity Assessment. *J. Biopharm. Stat.* 29, 920–940. doi:10.1080/10543406.2019.1657142

Zhu, G., Sun, L., Heidbrink-Thompson, J., Kuntumalla, S., Lin, H.-y., Larkin, C. J., et al. (2016). Capillary Zone Electrophoresis Tandem Mass Spectrometry Detects Low Concentration Host Cell Impurities in Monoclonal Antibodies. *Electrophoresis* 37, 616–622. doi:10.1002/elps.201500301

Conflict of Interest: The authors declare that the research was conducted in the absence of any commercial or financial relationships that could be construed as a potential conflict of interest.

Publisher's Note: All claims expressed in this article are solely those of the authors and do not necessarily represent those of their affiliated organizations, or those of the publisher, the editors and the reviewers. Any product that may be evaluated in this article, or claim that may be made by its manufacturer, is not guaranteed or endorsed by the publisher.

frontiers in Bioengineering and Biotechnology

ORIGINAL RESEARCH
published: 18 February 2022
doi: 10.3389/fbioe.2022.805176

Bioanalytics for Influenza Virus-Like Particle Characterization and Process Monitoring

Sofia B. Carvalho[1,2], *Ricardo J. S. Silva*[1,2], *Marcos F. Q. Sousa*[1,2], *Cristina Peixoto*[1,2], *António Roldão*[1,2], *Manuel J. T. Carrondo*[1] *and Paula M. Alves*[1,2]*

[1]*iBET, Instituto de Biologia Experimental e Tecnológica, Oeiras, Portugal,* [2]*Instituto de Tecnologia Química e Biológica António Xavier, Universidade Nova de Lisboa, Oeiras, Portugal*

Virus-like particles (VLPs) are excellent platforms for the development of influenza vaccine candidates. Nonetheless, their characterization is challenging due to VLPs' unique biophysical and biochemical properties. To cope with such complexity, multiple analytical techniques have been developed to date (e.g., single-particle analysis, thermal stability, or quantification assays), most of which are rarely used or have been successfully demonstrated for being applicable for virus particle characterization. In this study, several biophysical and biochemical methods have been evaluated for thorough characterization of monovalent and pentavalent influenza VLPs from diverse groups (A and B) and subtypes (H1 and H3) produced in insect cells using the baculovirus expression vector system (IC-BEVS). Particle size distribution and purity profiles were monitored during the purification process using two complementary technologies — nanoparticle tracking analysis (NTA) and tunable resistive pulse sensing (TRPS). VLP surface charge at the selected process pH was also assessed by this last technique. The morphology of the VLP (size, shape, and presence of hemagglutinin spikes) was evaluated using transmission electron microscopy. Circular dichroism was used to assess VLPs' thermal stability. Total protein, DNA, and baculovirus content were also assessed. All VLPs analyzed exhibited similar size ranges (90–115 nm for NTA and 129–141 nm for TRPS), surface charges (average of −20.4 mV), and morphology (pleomorphic particles resembling influenza virus) exhibiting the presence of HA molecules (spikes) uniformly displayed on M1 protein scaffold. Our data shows that HA titers and purification efficiency in terms of impurity removal and thermal stability were observed to be particle dependent. This study shows robustness and generic applicability of the tools and methods evaluated, independent of VLP valency and group/subtype. Thus, they are most valuable to assist process development and enhance product characterization.

Keywords: influenza, vaccines, virus-like particles, analytical tools, biophysical characterization, biochemical characterization, bioprocess monitoring

OPEN ACCESS

Edited by:
Christopher Mark Smales, University of Kent, United Kingdom

Reviewed by:
Marc G. Aucoin, University of Waterloo, Canada
Hideki Yamaji, Kobe University, Japan

***Correspondence:**
Paula M. Alves
marques@ibet.pt

Specialty section:
This article was submitted to Bioprocess Engineering, a section of the journal Frontiers in Bioengineering and Biotechnology

Received: *29 October 2021*
Accepted: *05 January 2022*
Published: *18 February 2022*

Citation:
Carvalho SB, Silva RJS, Sousa MFQ, Peixoto C, Roldão A, Carrondo MJT and Alves PM (2022) Bioanalytics for Influenza Virus-Like Particle Characterization and Process Monitoring. Front. Bioeng. Biotechnol. 10:805176. doi: 10.3389/fbioe.2022.805176

INTRODUCTION

Influenza VLPs are traditionally composed of hemaglutinin (HA) protein displayed on the surface of M1 protein (the scaffold). They can be composed by HA of only one subtype/strain (i.e., monovalent) or multiple subtypes/strains (i.e., multivalent). These VLPs are enveloped particles, thus they contain host cell proteins (HCP) acquired during the budding process (Vicente et al., 2011). These particles can be produced using several expression systems, namely, *Escherichia coli*, eukaryotic mammalian, insect, and plant cells (Pillet et al., 2016; Tretyakova et al., 2016; Venereo-Sanchez et al., 2016; Huang et al., 2017). The presence of HCP is highly dependent on the expression system used (Venereo-Sanchez et al., 2016). The envelope composition affects particle complexity impacting VLPs' structure and stability (Deng, 2018; González-Domínguez et al., 2020).

The integrity and stability of the VLP, including detection of all HA proteins, should be monitored during the entire bioprocess as VLP degradation can occur at any point during the process. There is a need for a deeper characterization of influenza VLPs and their bioprocess, to provide us more insights on their components and product- and process-related impurities critical for improving manufacturing. However, traditional methods used for influenza viruses are not enough to cope with the VLPs' characterization needs (Thompson et al., 2013; Nooraei et al., 2021). Furthermore, the implementation of several of these methods for influenza VLPs and their optimization for in-process samples and different expression systems is yet not fully accomplished.

Recently, new analytical tools are being developed and efforts are being made to revise methods used in more mature fields or to characterize other types of products (e.g., monoclonal antibodies). A comprehensive toolbox of analytical tools, traditional and modern ones, for the structural, functional, and potency characterization of VLPs was reviewed by Huang et al. (2017) and Nooraei et al. (2021) and are summarized in **Table 1**. The biochemical characterization should consider the determination of VLPs' purity, global charge, and relevant proteins', such as HA and M1, primary amino acid sequence, and molecular mass. In biophysical analysis, parameters such as morphology, size, polydispersity, thermal stability, and aggregation propensity are evaluated. Immunoassays tools have been used for the biological characterization of VLPs by analyzing the binding of functional epitopes of the particles to a panel of specific monoclonal antibodies.

Besides HCP, there are other product-related impurities such as extracellular vesicles (EVs), described for example for HEK293 system (Venereo-Sanchez et al., 2016; Moleirinho et al., 2019), and/or baculoviruses (BV) when using the insect cell system (Margine et al., 2012; Carvalho et al., 2019). Although host cell-derived proteins and particles such as EVs or BV can play a role in the immunological response, they can also pose regulatory issues and should be monitored during the bioprocess (Margine et al., 2012; Thompson et al., 2015; Deng, 2018; Lavado-García et al., 2020). The discrimination of VLPs from impurities such as EVs or BV, which share similar surface properties, requires the use of orthogonal tools for both analytical and purification tasks. Recent advances to these tools are reported elsewhere (Thompson et al., 2013; Carvalho et al., 2016; Moleirinho et al., 2020; Reiter et al., 2020).

In the current work, a set of six different influenza VLPs was expressed using the insect cells — recombinant baculovirus expression vector system (IC-BEVS), exploring distinct valences (i.e. mono- and pentavalent), subtypes (i.e. H1 and H3), and groups (A and B). Biochemical (HA titer and impurities, i.e. total protein, DNA, and baculovirus content) and biophysical (VLP identity, morphology, size distribution, surface charge, structure and stability) analyses were performed using different methods. The main goal was to demonstrate the applicability of the analytical tools used and how they can be applied to bioprocess monitoring and to guide its optimization.

MATERIALS AND METHODS

Cell Line and Culture Media

Insect High Five cells (B85502, ThermoFisher Scientific) were routinely sub-cultured in 500 ml shake flasks (10% working volume) (Corning) to 0.3×10^6 cells/ml inoculum, every 3–4 days, when cell concentration reached $2–3\times10^6$ cells/ml, using Insect X-press medium (BEBP12-730Q, Sartorius). An Innova 44R incubator (New Brunswick) at 27°C and 100 rpm (orbital motion diameter of 2.54 cm) was used.

Baculovirus Amplification

Recombinant baculoviruses containing influenza matrix M1 gene in combination with one or multiple hemagglutinin (HA) genes were generated by RedBiotech AG (Switzerland) using its proprietary rePAX® technology (**Supplementary Table S1**). The promotor used for both HA and M1 was the polh (polyhedrin promoter). HA and M1 protein sequences are described in **Supplementary Table S2**. Amplification of baculovirus stocks was performed as described elsewhere (Vieira et al., 2005). Briefly, Spodoptera frugiperda Sf-9 cells (11496-015, ThermoFisher Scientific) were infected at 1×10^6 cells/ml at a multiplicity of infection (MOI) of 0.1 infectious particles per cell (IP/cell). When cell viability reached 80%–85%, culture bulk was harvested and centrifuged at 200×*g* for 10 min at 4°C. The pellet was discarded, and the supernatant was centrifuged at 2,000×g for 20 min at 4°C. The resulting supernatant was stored at 4°C until further use.

Production of Influenza VLPs

Influenza VLPs were produced in shake flasks (2 L with 10% working volume). Briefly, shake flask cultures were infected at a cell concentration at infection (CCI) of 2×10^6 cells/ml using an MOI of 1 IP/cell. Cell cultures were harvested when cell viability dropped to values around 40%, commonly between 48 h post-infection (hpi) and 72 hpi.

Purification of Influenza VLPs

Influenza VLP purification started with the clarification process that was performed by sequential depth filtration using a D0HC filter (MD0HC23CL3, Merck Millipore) and an Opticap XL150 capsule with 0.5/0.2 µm pore size (KHGES015FF3, Merck Millipore), connected in series. The second step included an

TABLE 1 | Bioanalytics for VLP characterization. Summary of analytical tools used for biochemical, biophysical and biological characterization of VLPs. Reviewed in Huang et al. (2017) and Nooraei et al. (2021).

Biochemical characterization			
Amino acid sequence	**Molecular weight**	**Purity**	**Isoelectric point**
LC-MS (peptide mapping)	SDS-PAGE[a]; WB[a]; MALDI-TOF MS nativeMS	RP-HPLC; SDS-PAGE[a]	iclEF
Biophysical characterization			
Morphology	**Size and polydispersity**	**Stability and aggregation propensity**	**Particle concentration**
TEM[a]; cryo-EM; AFM	TEM; cryo-EM; AFM; TRPS[a]; DLS; NTA[a]; AUC; AF4-MALS	CD[a]; DSC; Cloud point	TRPS[a]; DLS; NTA[a]
Biological characterization			
Antibody binding	**Antigenicity**	**Receptor binding**	
SPR; BLI	ELISA	Hemagglutination assay	

LC-MS, liquid chromatography-mass spectrometry; SDS-PAGE, sodium dodecyl sulfate–polyacrylamide gel electrophoresis; WB, western blot; MALDI-TOF: matrix-assisted laser desorption/ionization–Time of Flight; RP-HPLC, reversed-phase–high-performance liquid chromatography; iclEF, imaged capillary isoelectric focusing; TEM, transmission electron microscopy; cryo-EM, cryogenic electron microscopy; AFM, atomic force microscopy; TRPS, tunable resistive pulse sensing; DLS, dynamic light scattering; NTA, nanoparticle tracking analysis; AUC, analytical ultracentrifugation; AF4-MALS, Asymmetrical flow field-flow fractionation—multi angle light scattering; CD, circular dichroism; DSC, differential scanning calorimetry; SPR, surface plasmon resonance; BLI, biolayer interferometry analysis; ELISA, enzyme-linked immunosorbent assay.
[a]Explored in this work.

anion exchange chromatography by using a Sartobind Q MA 75 (93IEXQ42DB-12V, Sartorius) membrane adsorber, operated in bind/elute mode. The membrane adsorber was equilibrated with 50 mM HEPES, pH 7.0, and 150 mM of NaCl equilibration buffer. The flow rate was set to 5 membrane volume (MV) min^{-1} and the VLPs were collected in the elution step that was performed with 50 mM HEPES, pH 7.0, 1 M NaCl. The Sartobind Q elution pool containing VLPs was concentrated by tangential flow filtration (TFF) conducted using a flat sheet Pellicon XL Ultrafiltration Module Biomax 300 kDa 0.005 m^2 (PXB300C50, Merck Millipore). The membrane module was set up according to the manufacturer's instructions: it was preconditioned with deionized water, to eliminate trace preservatives and equilibrated with 50 mM HEPES, pH 7.0, and 200 mM NaCl (working buffer) before the concentration step. After achieving the desired concentration factor, the TFF loop was completely drained and the VLP retentate was recovered. Ultrafiltration retentate was loaded into a size-exclusion chromatography (SEC) performed using a HiLoad 26/600 Superdex 200 pg column (Cytiva). The column was loaded at a constant flow rate of 5 ml/min. Working buffer was used as eluent and the eluted fractions were collected for further analysis. The elution of influenza VLPs was monitored at 280 nm. The fraction containing the top of the chromatographic peak was collected and considered for further analysis (final). Both Sartobind Q and SEC chromatographies were coupled to an AKTA explorer 150 liquid chromatography system (Cytiva) equipped with UV, conductivity, and pH monitors. System operation and data gathering and analysis were performed using the UNICORN 6.0 software (Cytiva). All purification steps were performed at room temperature (RT) (22°C).

Analytics

Cell Concentration and Viability

Cell concentration and viability were monitored daily using Cedex High-Resolution Cell Analyzer (Roche) or the trypan blue exclusion dye method with a Fuchs–Rosenthal hemocytometer.

Hemagglutination Assay

HA protein content was determined using the hemagglutination assay as described elsewhere (Carvalho et al., 2018; Sequeira et al., 2018). Briefly, samples were serially diluted 1:2 or 1:3 with DPBS(−/−) 1X (14190-169, Gibco) in V-bottom 96-well plates (Thermo Scientific) and gently mixed 1:1 with 1% chicken erythrocytes (Lohmann Tierzucht GmbH). An influenza vaccine (Influvac, Abbott) was used as a positive control, with known concentration. Plates were incubated at 4°C for at least 30 min. Hemagglutination was inspected visually and HA titer was estimated as being the inverse of the highest dilution of the sample that completely inhibited hemagglutination.

Turbidity

To evaluate the efficacy of the clarification step, turbidity of the harvest and clarified samples was measured using a Turbidimeter (2100 Qis Portable HACH).

Tunable Resistive Pulse Sensing

VLP size distribution, particle concentration, and charge (zeta potential) were evaluated using TRPS. These measurements were performed with the qNano (Izon Sciences) equipment and nanopore membranes NP200 (Izon Sciences), rated for particles between 80 and 500 nm. The instrument was set up and calibrated according to the manufacturer's instructions. To calibrate size and particle concentration, carboxylated polystyrene particles with a mode diameter of 340 nm (SKP400E, Izon Science) with a concentration of 6×10^{10} particles/ml were used. All measurements were done using a membrane stretch of 45 mm, a voltage of 0.20 V, and a pressure of 5 mbar. The measurement duration was dependent on the number of particles detected with a minimum of 500 events. Zeta potential measurements were performed using PBS buffer

using calibration particles with a diameter of 220 nm (CPC 200, Izon Science) and a nanopore membrane NP200 (Izon Science). The selected membrane stretch was 45.30 mm. The pressure (P) and voltage (V) calibration points were selected as V1P1, V1P2, V2P1, and V3P1 with V1, V2, and V3 as 0.32, 0.26, and 0.29 V, respectively, and P1 and P2 as 1 and 2 mbar. The zeta potential of VLP samples was measured using V1P1 voltage and pressure setting.

Transmission Electron Microscopy

TEM was used to assess the integrity and morphology of the VLPs after downstream processing (ultrafiltrated retentate and selected SEC fractions). Sample preparation was performed as follows: a drop (5 µl) of each sample was adsorbed onto a formvar coated 150 mesh copper grid from Veco (Science Services) for 2 min. After washing the grid five times with sterile filtered dH_2O, it was soaked in 2% uranyl acetate for 2 min and dried in air at RT (22°C). A Hitachi H-7650 120 kV transmission electron microscope (Hitachi High-Technologies Corporation) was used to analyze the samples.

Nanoparticle Tracking Analysis

VLP concentration and size distribution was measured using the NanoSight NS500 (Nanosight Ltd). Samples were diluted in D-PBS (14190-169, Gibco) to a particle concentration between 10^8 and 10^9 particles/ml to work at the instrument's linear range. All measurements were performed at a controlled temperature of 25°C. Sample videos were analyzed with the Nanoparticle Tracking Analysis (NTA) 3.3 Analytical software. Capture settings (shutter and gain) were adjusted manually for each analysis. For each sample, five captures of 60-s videos were acquired and the total number of particles was considered.

Total Protein Quantification

Total protein content in samples was quantified using the BCA Protein Assay Kit (23225, Thermo Fisher Scientific) following the manufacturer's instructions. Bovine serum albumin (BSA) was used for calibration (23209, Thermo Fisher Scientific). Absorbance at 562 nm was measured on Infinite M200 PRO NanoQuant (Tecan) microplate multimode reader using a clear 96-well microplate (655101, Greiner Bio-One GmbH).

Total dsDNA Quantification

Total dsDNA was determined using the Quant-iT Picogreen dsDNA reagent (P7581, Molecular Probes) according to the manufacturer's instructions. Fluorescence (λ_{exc} = 485 nm, λ_{emiss} = 535 nm) was measured on an Infinite 200 PRO NanoQuant (Tecan) microplate multimode reader using a black 96-well microplate, flat transparent (3915, Corning).

SDS-PAGE and Western Blot Analysis

Influenza M1 and HA proteins in samples before and after purification were identified by SDS-PAGE and Western blot analysis. Samples were incubated at 70°C for 10 min after the addition of loading buffer (LDS sample buffer and reducing agent; ThermoFisher Scientific). Denatured samples were loaded into a 4%–12% NuPAGE Bis-Tris protein gel (ThermoFisher Scientific) using the MOPS running buffer (ThermoFisher Scientific). Loading was performed using 2 µg of total protein per lane and 0.04 µg of HA per lane. SeeBlue Plus2 Prestained Standard (ThermoFisher Scientific) molecular weight markers were used. Samples were resolved for 60 min at a constant voltage (200 V and 400 mA) and transferred to a nitrocellulose membrane using the iBlot system (ThermoFisher Scientific). SDS-PAGE and Western blot membranes were used in duplicate for M1 and HA protein identification. Membranes were blocked for 1 h with 5% (w/v) of dry milk (Merck Millipore) in Tris-buffered saline with 0.1% (w/v) of Tween 20 (T-TBS buffer). After blocking, membranes were incubated overnight at room temperature with the respective primary antibodies (**Supplementary Table S3**).

Western blot detection was performed with the corresponding anti-goat, anti-mouse, or anti-sheep secondary antibody conjugated with alkaline phosphatase for M1 and HA identification (**Supplementary Table S3**). Protein band detection was performed by covering membranes with NBT/BCIP 1-Step (Thermo Scientific) for 10 min; membranes were then scanned with a benchtop scanner device.

Baculovirus Quantification

Baculovirus DNA was extracted and purified using the High Pure Viral Nucleic Acid Kit (Roche Diagnostics) following the manufacturer's instructions. The number of genome copies was quantified by real-time quantitative PCR (qPCR) following the protocol described elsewhere (Vicente et al., 2009). The master mix was prepared using the Light Cycler 480 SYBR Green I Master (04707516001, Roche Diagnostics), a final concentration of 0.5 µM of each primer, for the ie-1 baculovirus gene region and PCR grade water; 96-well white plates (04729692001, Roche Diagnostics) and a LightCycler 480 Instrument II (Roche Molecular Systems, Inc.) were used.

Circular Dichroism Spectroscopy

CD experiments were performed using a Chirascan™ qCD spectrometer (Applied Photophysics). Far UV CD spectra (n = 3) were measured at 20°C with a bandwidth of 1 nm and a time per point of 3 s from 195 to 260 nm. Temperature ramps (n = 1) were recorded by increasing the temperature from 20°C to 95°C from 195 to 260 nm, with a time per point of 0.4 s and spectra acquisition every 1°C. CD spectra at 90°C and 20°C after temperature ramp were also acquired. The HA concentration was 4.5 µg/ml. Temperature ramp melting temperature (Tm) was interpolated applying a sigmoidal regression performed using GraphPad version 9.1.1.

RESULTS

Production of Influenza VLPs

Six different influenza VLPs with distinct valences (i.e. monovalent and pentavalent) and from different groups (A and B) and subtypes (H1 and H3) were produced in insect High Five cells using the baculovirus expression vector system (IC-BEVS). Cell infection and HA protein expression kinetics are shown in **Figure 1**. Cell concentration and viability profiles follow

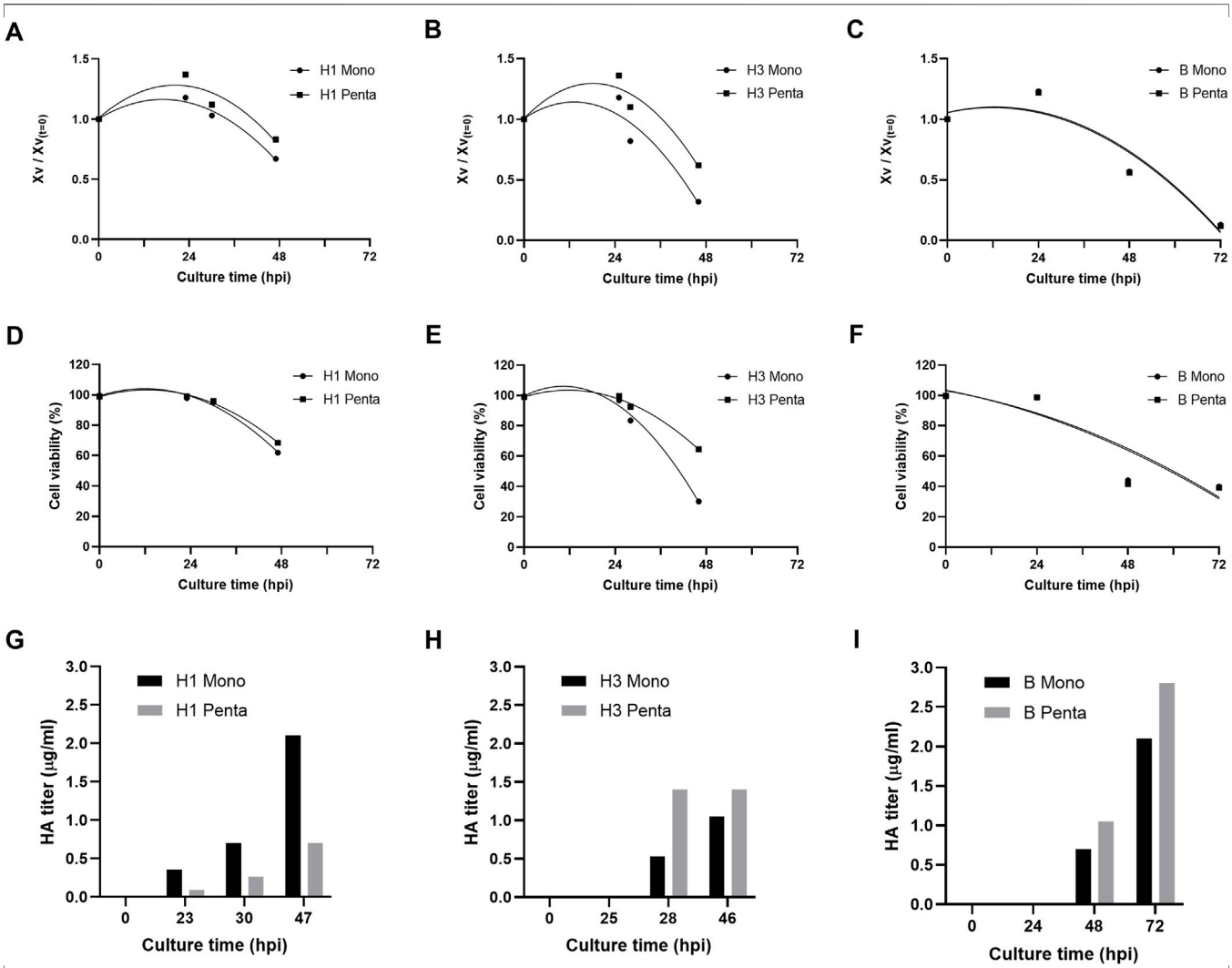

FIGURE 1 | Production of influenza VLPs. **(A–C)** Normalized viable cell concentration during culture time upon infection, hours post-infection (hpi). **(D,E)** Cell viability kinetics (%) upon infection (hpi). **(G–I)** HA titer profile (µg/ml) upon infection (hpi). Data are expressed as a mean of two replicates (n = 2).

similar trends in all groups/subtypes and valences studied, except for group B cultures (i.e. culture time extends to 72 h post-infection (hpi) instead of 48 hpi as in other groups/subtypes) (**Figures 1A–F**). As to protein expression, results suggest that HA titer is group/subtype and valency dependent (**Figures 1G–I**). For example, while the H1 subtype monovalent culture shows higher HA titers compared to pentavalent culture, the opposite occurs for H3 and B. Overall, the highest HA titer was observed for B pentavalent culture, with peak production reached at 72 hpi.

Biochemical Characterization of Influenza VLPs

Identification of Influenza M1 and HA Proteins

To investigate if both HA and M1 proteins are incorporated in the particles, Western blot analysis was performed at the time of harvest in supernatant samples (initial) and after Downstream processing (DSP), using SEC selected fraction (final) (**Figure 2**). HA and M1 proteins were specifically identified in both samples, at the expected molecular weight range (HA MW = 63 kDa, M1 MW = 28 kDa), for all the studied VLPs. For B Penta VLP it was only possible to confirm M1 and HA presence in the lanes loaded according to HA content (**Figure 2F**).

HA Titers and Process-Related Impurities

The ratio HA titer to major process-related impurities (i.e., total DNA, total protein, and baculovirus) at harvest and after purification (i.e., SEC fraction) was assessed for all cultures (**Figure 3**). All ratios are higher for SEC fraction than for harvest, meaning that DSP is increasing HA protein and decreasing impurity content. The HA/DNA ratio (µg/µg) for H1 Mono and H1 Penta VLPs were 0.22 and 0.15 for the harvested samples, respectively (**Figure 3A**). These values increased to 47.06 and 12.82 after purification. H3 Mono and

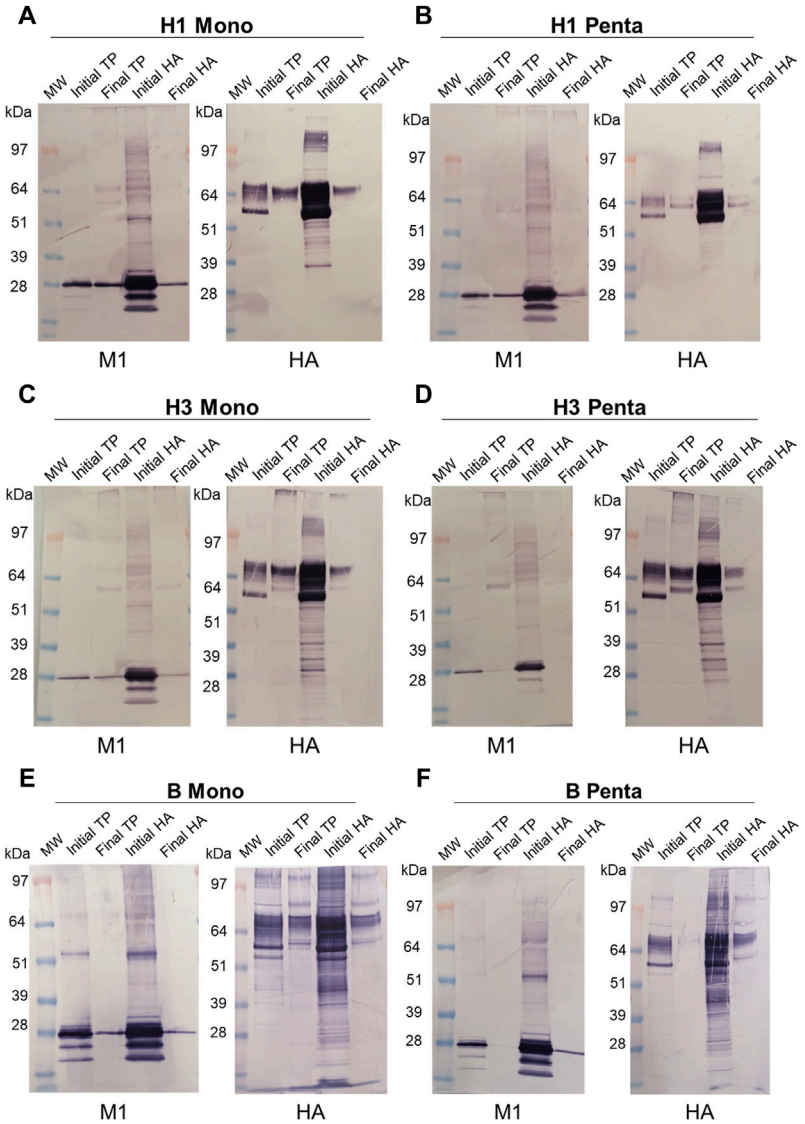

FIGURE 2 | Identification of HA and M1 proteins by Western blot in VLP samples after harvest and after downstream processing (SEC fraction selected). **(A)** H1 Mono VLP, **(B)** H1 Penta VLP, **(C)** H3 Mono VLP, **(D)** H3 Penta VLP, **(E)** B Mono VLP, **(F)** B Penta VLP. MW: molecular weight protein markers; TP: total protein; initial TP: harvest sample loaded by total protein amount; final TP: SEC fraction selected sample loaded by total protein amount; initial HA: harvest sample loaded by HA protein amount; final HA: SEC fraction selected sample loaded by HA protein amount. HA MW = 63 kDa, M1 MW = 28 kDa.

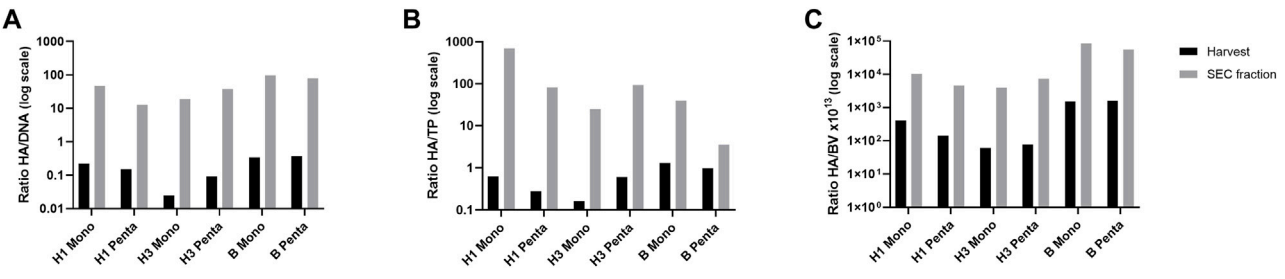

FIGURE 3 | Estimation of HA titers and major process-related impurities. **(A)** HA (μg/ml) to DNA (μg/ml), **(B)** HA (μg/ml) to total protein (mg/ml), and **(C)** HA (μg/ml) to baculovirus concentration (copies/ml × 10^{13}) ratios. Log scale is used for visualization purposes. Black bars represent VLP samples after harvest. Grey bars represent VLP samples after downstream processing (SEC fraction selected).

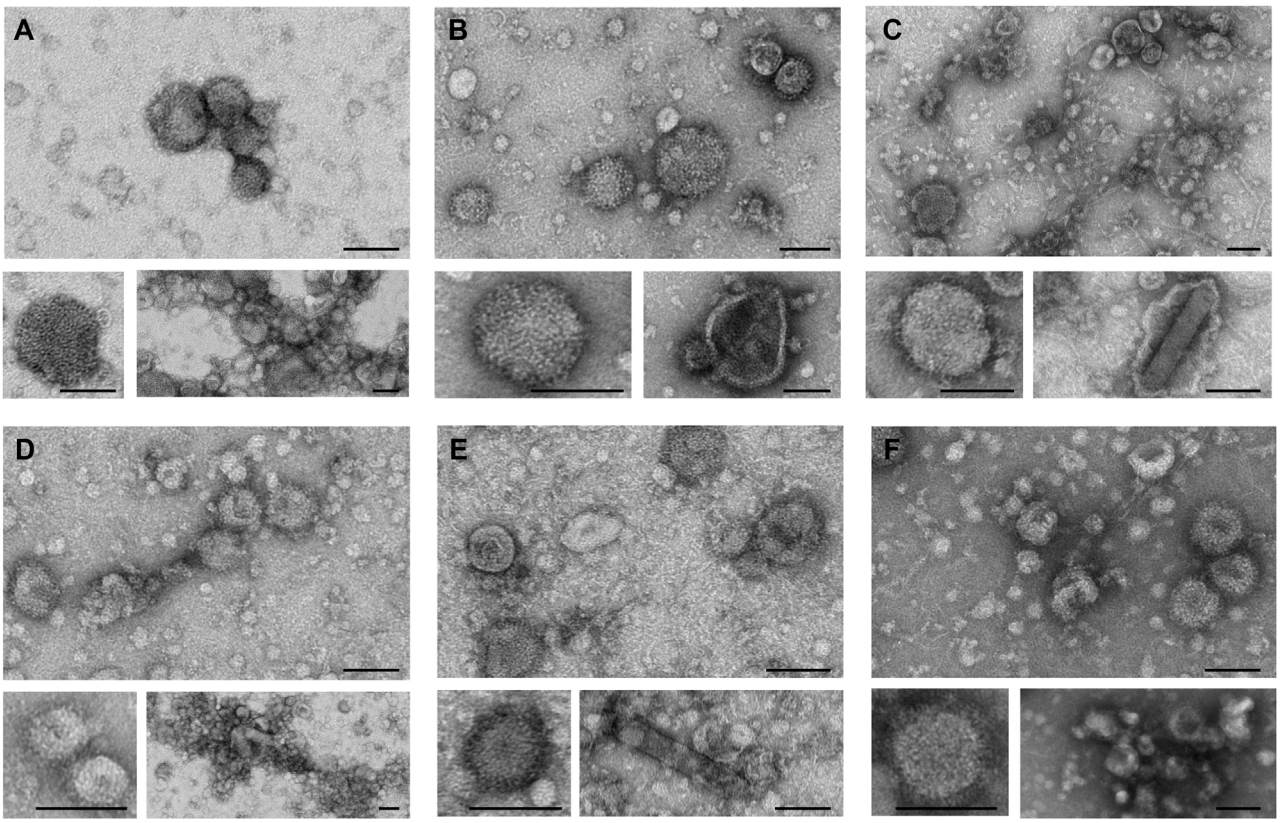

FIGURE 4 | Transmission electron microscopy of purified influenza VLPs. Representative images of TEM analysis depicting VLP size and morphology of purified samples (SEC fraction selected). Top panels show an overview of the analyzed samples; bottom left panels show close up views of individual spherical VLPs presenting the characteristic influenza HA spikes; bottom right panels show the presence of larger and pleomorphic VLPs, aggregates or baculovirus. **(A)** H1 Mono VLP, **(B)** H1 Penta VLP, **(C)** H3 Mono VLP, **(D)** H3 Penta VLP, **(E)** B Mono VLP, **(F)** B Penta VLP. Scale bar, 100 nm.

H3 Penta VLPs have the lowest ratios for the harvest sample, 0.02 and 0.09, respectively. The values increased, after purification, to 19.02 and 38.30. Although the H3 Mono ratio is still one of the lowest, it is not as low as the one obtained for H1 Penta VLP. On the other hand, B VLPs have the highest ratios for both harvest and SEC fractions. B Mono has 0.34 and 97.85 and B Penta 0.37 and 79.31.

In terms of HA/TP ratio (**Figure 3B**), H1 Mono and H1 Penta VLPs were 0.62 and 0.28 at the harvest sample, respectively. For the SEC fraction samples, the ratios obtained for these VLPs were the highest amongst all the studied particles. The H1 Mono value of 694.46 stands out, but the second highest is 82.33 and refers to H1 Penta VLP. Similar to that observed for DNA, the H3 Mono value was 0.16, the lowest obtained for harvest samples, which slightly increases to 24.69 after purification. H3 Penta starts with 0.61, but in this case, the value of the SEC fraction is 93.53, which is much higher than that for the monovalent VLP. Interestingly, for B type VLPs, although the harvest sample ratios are the highest, 1.29 for B Mono and 0.98 for B Penta, the SEC values are not as high as the ones obtained for other VLPs. B Mono presents a ratio of 39.90 and B Penta has the lowest value of 3.57.

The HA/BV ratios (**Figure 3C**) can be grouped according to VLP as they differ by approximately 1 log between type/subtype. H1 Mono and H1 Penta values at the harvest were 4.12×10^{-12} and 1.43×10^{-12}, respectively. After purification, the baculovirus content decreased 25 and 33 times, achieving ratio values of 1.05×10^{-10} and 4.67×10^{-11}, respectively. H3 Mono and H3 Penta VLPs ratios are the lowest for the harvest samples with values of 6.03×10^{-13} and 7.78×10^{-13}, respectively. However, the ratio achieved upon purification was the highest, with values of 4.00×10^{-11} and 7.40×10^{-11}, respectively, and baculovirus content decreased by 66 and 95 times. The highest ratios were obtained for B Mono and B Penta VLPs at both harvests, 1.51×10^{-11} and 1.64×10^{-11}, respectively, and SEC fraction samples, 8.56×10^{-10} and 5.60×10^{-10}, respectively. In these cases, the baculovirus content decreased 57 and 34 times.

Biophysical Characterization of Influenza VLPs

Morphology

TEM analysis was performed to assess the integrity and morphology of the six different influenza VLPs, after the complete DSP (**Figure 4**). Top panels present an overview of each preparation, where the presence of spherical and pleomorphic VLPs can be observed, as well as other types of

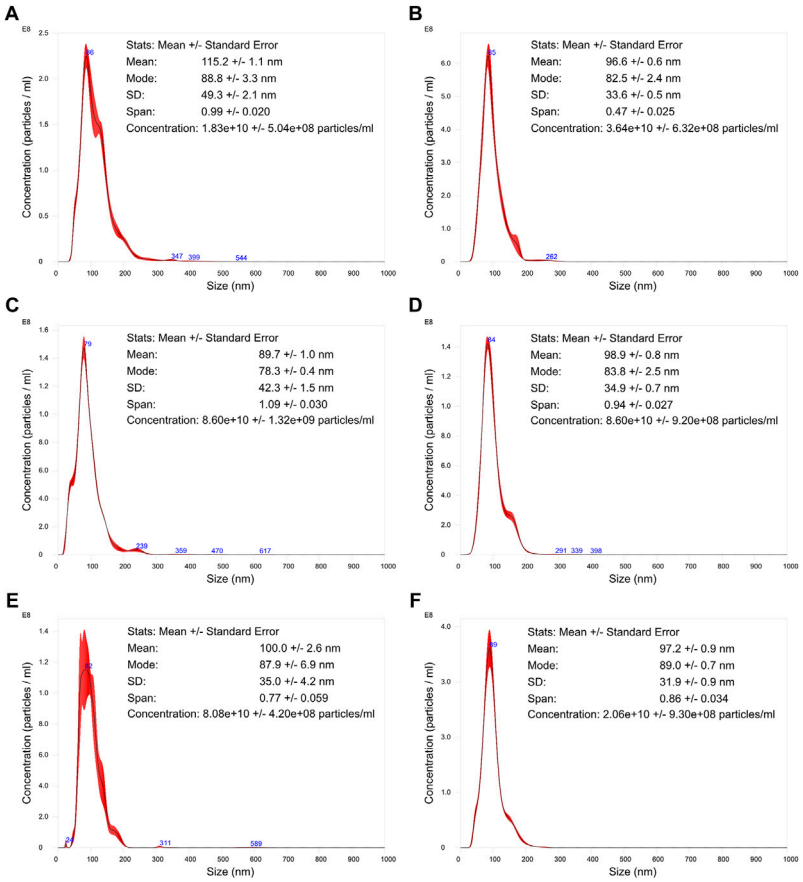

FIGURE 5 | Nanoparticle tracking analysis of influenza VLPs. Particle size distribution analysis of purified samples. The represented distributions are an averaged result of five measurements. The error bars (in red) indicate +/− 1 standard error of the mean. **(A)** H1 Mono VLP, **(B)** H1 Penta VLP, **(C)** H3 Mono VLP, **(D)** H3 Penta VLP, **(E)** B Mono VLP, **(F)** B Penta VLP.

particles and/or vesicles. It is possible to observe ultrastructural details of VLP membranes by zooming in representative images of each preparation (bottom left panels). All particle images revealed the presence of HA spikes, characteristic of influenza viruses. The bottom right panel images represent the type of impurities observed in each preparation. Besides vesicles and/or exosomes that are visible in all VLP preparations, aggregates can be observed in H1 Mono (**Figure 4A**), H3 Penta (**Figure 4D**), and B Penta (**Figure 4F**) samples. The presence of baculovirus in purified VLP samples is exemplified for H3 Mono (**Figure 4C**) and B Mono (**Figure 4E**). Deformed H1 Penta VLPs were also observed (**Figure 4B**).

Concentration, Size Distribution, and Surface Charge

Particle size distribution, concentration, and surface charge were assessed for each VLP purified sample (**Figures 5**, **6**). The particle size distribution determined using TRPS had a mono-modal profile. On the other hand, NTA data suggests a heterogeneous population with three main groups existing: the center group corresponding to a mean value of 79–86 nm and two transitions to lower and higher particle diameters. Mean particle size diameters determined using NTA ranged from 90 to 115 nm, with no visible correlation to monovalent or pentavalent VLPs. A similar observation was obtained with NTA for the mode of the distribution (ranging from 78 to 89 nm). All particle size distributions were positively skewed as their mean was greater than the mode. The same pattern of distribution skewness was observed in the TRPS measurements. The mode and mean values of the particle size distribution obtained with TRPS were higher than the ones obtained with NTA, ranging from 129 to 141 nm for the mean and from 117 to 130 nm for the mode. The polydispersity of the VLP samples was evaluated using a percentile diameter ratio (D90-D10)/D50, usually a named span. The calculated values for span using TRPS were in the lower range (0.359–0.461) in comparison to the ones obtained with NTA (0.47–1.09). No correlation exists between monovalent or pentavalent VLPs and the calculated values of span for TRPS or NTA.

The concentration of total particles determined with NTA was one order of magnitude higher in comparison to the TRPS. The

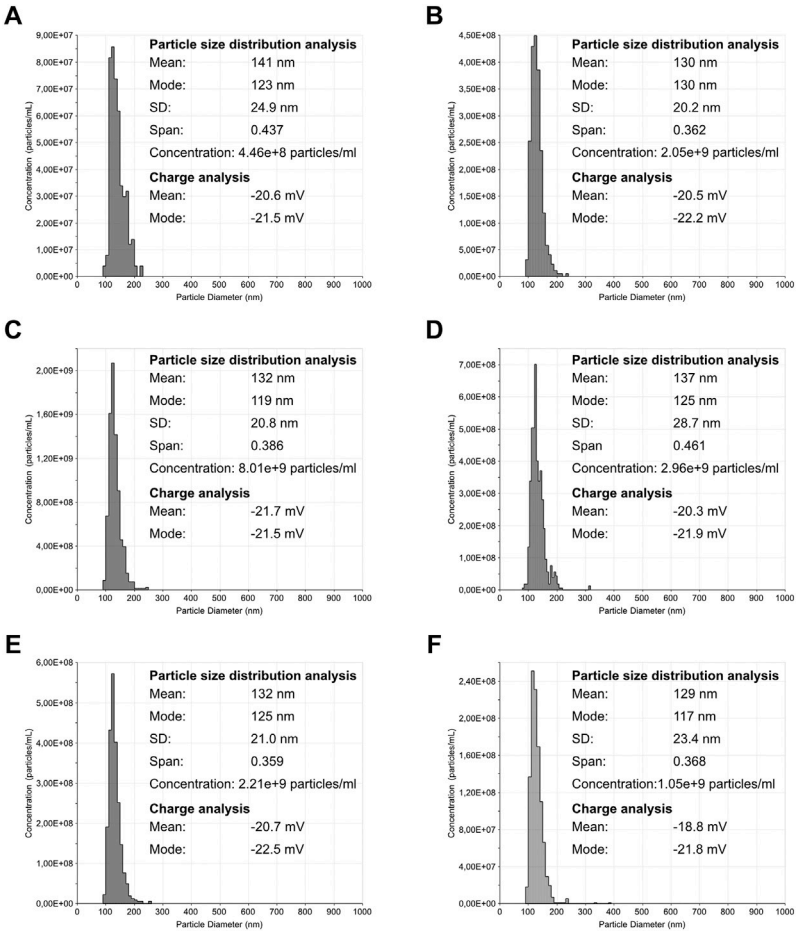

FIGURE 6 | Tunable resistive pulse sensing analysis of influenza VLPs. Particle size distribution analysis of purified samples. The bin size for all histogram was defined as 10 nm. **(A)** H1 Mono VLP, **(B)** H1 Penta VLP, **(C)** H3 Mono VLP, **(D)** H3 Penta VLP, **(E)** B Mono VLP, **(F)** B Penta VLP.

concentration in NTA ranged from 1.83×10^{10} to 8.60×10^{10} total particles/ml and in TRPS from 4.46×10^{8} to 8.01×10^{9} total particles/ml.

Zeta potential analysis of the different VLPs ranged from −18.8 to −21.7 mV. Although for H1 Mono and H1 Penta VLP samples the measured zeta potential was very similar (−20.6 and −20.5 mV), the same cannot be observed for the other VLP samples. The pentavalent H3 and B VLPs were less negatively charged, having a zeta potential of −20.3 and −18.8 mV respectively, in comparison with −21.7 mV for H3 Mono and −20.7 mV for B Mono.

Secondary Structure Analysis and Thermal Stability Evaluation

To investigate influenza VLP secondary structure, circular dichroism (CD) analysis of purified VLPs was performed (**Figure 7**). Although CD spectra at 20°C of the different VLPs present distinct shapes and magnitudes, they display minima near 210 and 222 nm, suggesting the presence of predominantly helix-α secondary structure type. An exception is made for H1 Mono VLP, where magnitude is the lowest and the α-helix signature is not that evident (**Figure 7A**). As we increase the temperature (from 20°C to 90°C) it is possible to observe a loss of signal, which is indicative of temperature-dependent loss of secondary structure. This signal decrease is more evident for H3 Mono (**Figure 7C**), B Mono (**Figure 7E**), and B Penta (**Figure 7F**) VLPs.

VLP thermal stability was evaluated by monitoring the CD signal at 210 and 222 nm as a function of temperature (**Figures 8**, **9**). For H1 Mono VLPs (**Figure 8A**) it is not possible to observe a significant shift in the structure following the 210 nm wavelength. However, we can observe a sigmoidal behavior and a T_m of 56.1°C following the 222 nm wavelength (**Figure 9A**). Considering the 222 nm wavelength, H1 Penta VLPs are more stable than H1 Mono VLPs (ΔT_m >12°C) (**Figures 9A,B**). Contrarily, for the H3 subtype, the monovalent VLPs appear to be more stable than the pentavalent VLPs, irrespective of the wavelength (**Figures 8C**,D, **9C**,D). B VLPs present the highest T_m at 222 nm, with values of 83.0°C for B Mono (**Figure 9E**) and 84.4°C for B Penta

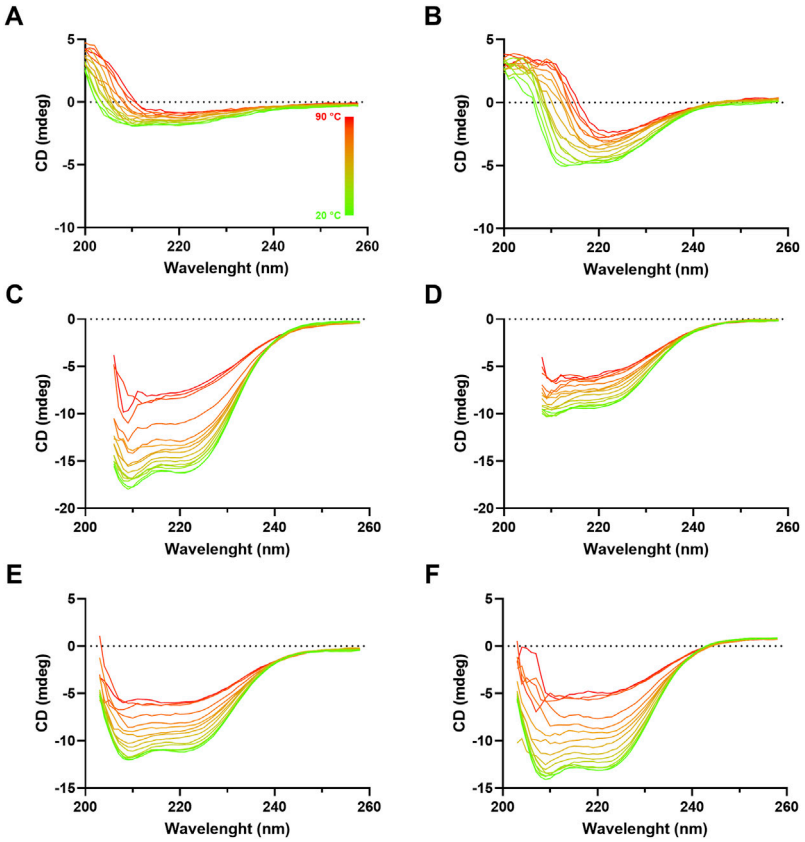

FIGURE 7 | Circular dichroism spectra of influenza VLPs. Far UV (260–195 nm) CD spectra analysis of purified samples (SEC fraction selected) at different temperatures, ranging from 20°C (green) to 90°C (red), pH 7. mdeg: milidegrees. **(A)** H1 Mono VLP, **(B)** H1 Penta VLP, **(C)** H3 Mono VLP, **(D)** H3 Penta VLP, **(E)** B Mono VLP, **(F)** B Penta VLP.

(**Figure 9F**). Pentavalent VLP is slightly more stable than the monovalent, for both wavelengths. From the CD signal at 210 nm the obtained values for Tm are 71.8°C for B Mono (**Figure 8E**) and 76.2°C for B Penta (**Figure 8F**), respectively.

DISCUSSION

Influenza VLPs of different groups (A and B), subtypes (H1 and H3), and valences (mono and pentavalent) were produced using the IC-BEVS and characterized biochemically and biophysically. These analyses provide us insights into VLP titer, process-impurities content, morphology, size distribution, surface charge, secondary structure, and thermal stability. VLPs with spherical and pleomorphic morphology were identified, displaying HA on their surface, resembling the influenza virus. Differences were observed for HA titer and DNA, total protein, and baculovirus content across the bioprocess. Although most of the particles present similar secondary structure content and their surface charge is within the same range of values, significant variations in terms of thermal stability were observed.

VLPs Bioprocess and Biochemical Characterization

The differences in VLP formats (mono or pentavalent), groups (A and B), and subtypes (H1 and H3) may impact upstream and downstream processing stages. Cell concentration and viability profiles followed similar trends in all groups/subtypes and valences studied. Cell viability and HA titer were used to decide the time of harvest. As the expression system used is lytic, we need to consider that cell viability will decrease significantly after infection releasing a considerable amount of host cell impurities. Therefore, it is critical to balance the titer with cell viability as it will impact the downstream processing and product quality. For the case of B VLPs, increasing culture time did not affect cell viability and improved HA titer. No significant differences were observed in terms of impurity content removal when compared to the other VLPs, meaning that it is worth extending cell culture. On the other hand, H3 Mono VLP presented the lowest cell viability at the time of harvest, which was then reflected in terms of impurity content at the initial stage of the purification process, requiring a more robust downstream process. Moreover, the HA titer for this VLP is the lowest observed, meaning that some process optimizations should be

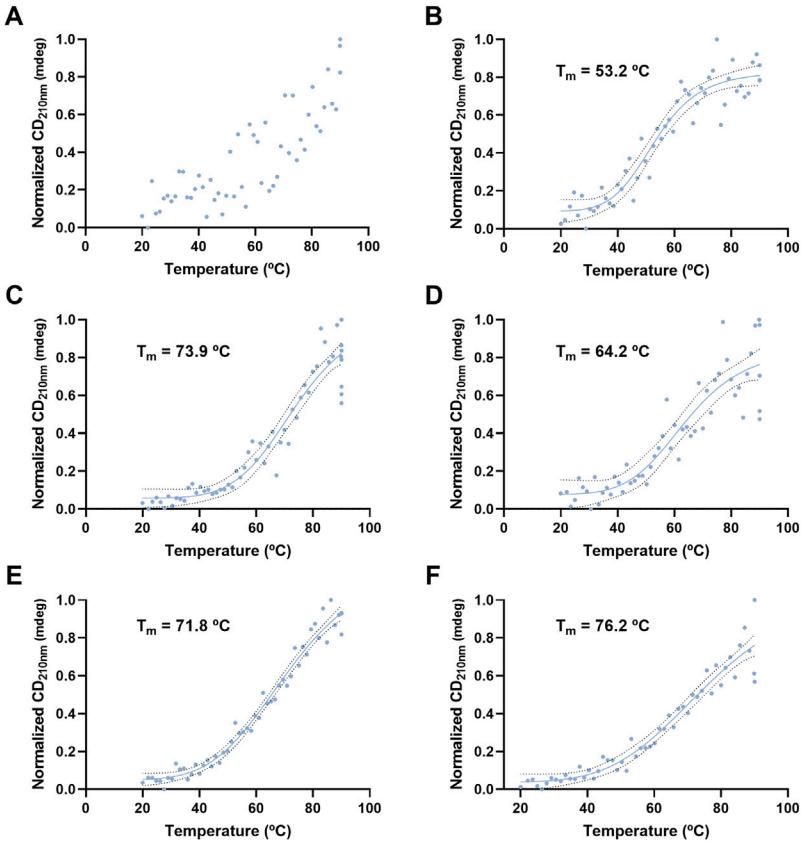

FIGURE 8 | Thermal stress analysis of influenza VLPs using circular dichroism. Temperature ramp for VLP secondary structure analysis during thermal stress. CD signal was followed at 210 nm. Data was normalized (0–1) for plotting. mdeg: millidegrees. **(A)** H1 Mono VLP, **(B)** H1 Penta VLP, **(C)** H3 Mono VLP, **(D)** H3 Penta VLP, **(E)** B Mono VLP, **(F)** B Penta VLP. Indirect measurement of T_m values was estimated by interpolation applying a sigmoidal regression.

taken into consideration (e.g. increase genetic stability of baculovirus and/or protein construct, tailor-made supplementation strategies, perfusion cultures).

We confirmed that all particles incorporated both M1 and respective HA proteins. Biochemical analysis was performed to assess downstream process efficiency in terms of DNA, total protein and baculovirus removal. No evident relation between the subtype, group, or VLP valency was observed. Nevertheless, these analytics can give us insightful information for bioprocess improvement. Further studies to identify which are the host-specific proteins from a baculovirus expression system included in our VLPs will be interesting and can be evaluated by mass spectrometry proteomic analysis (Shaw et al., 2008; Hutchinson et al., 2014; Wang et al., 2017).

VLP Morphology, Surface Charge and Size Distribution

It is widely reported that influenza viruses are pleomorphic, presenting spherical but also filamentous shapes (Harris et al., 2006; Harris et al., 2013; Calder et al., 2010). In this work, we report TEM imaging of VLPs demonstrating similarity to what is expected for the native virus, in terms of size, morphology and ultrastructural details, namely HA characteristic spikes. These VLPs show a predominantly spherical morphology being also possible to identify other vesicles and baculovirus. These are critical product-related impurities, as their surface properties are usually very similar to the ones of VLPs. Although some reports suggest that these species may have a positive impact on the immune response, there is still a concern from the regulatory authorities on live contaminating viruses or virus genomes in human vaccines due to their potential side effects. In this sense, these impurities should be monitored and quantified, enforcing their removal during the bioprocess (Margine et al., 2012; Thompson et al., 2015; Deng, 2018; Lavado-García et al., 2020). Imaging tools are also useful to identify VLP aggregates and not properly formed particles or evaluate membrane protein density. For example, the H3 Mono and H3 Penta VLPs seem to have a lower HA density in the membrane surface when compared to the other VLPs. This observation is in agreement with the HA titers, which are the lowest observed. Systematic analysis of TEM images can be performed to do a semi-quantification of VLPs and product-related impurities, allowing the monitoring of the process and

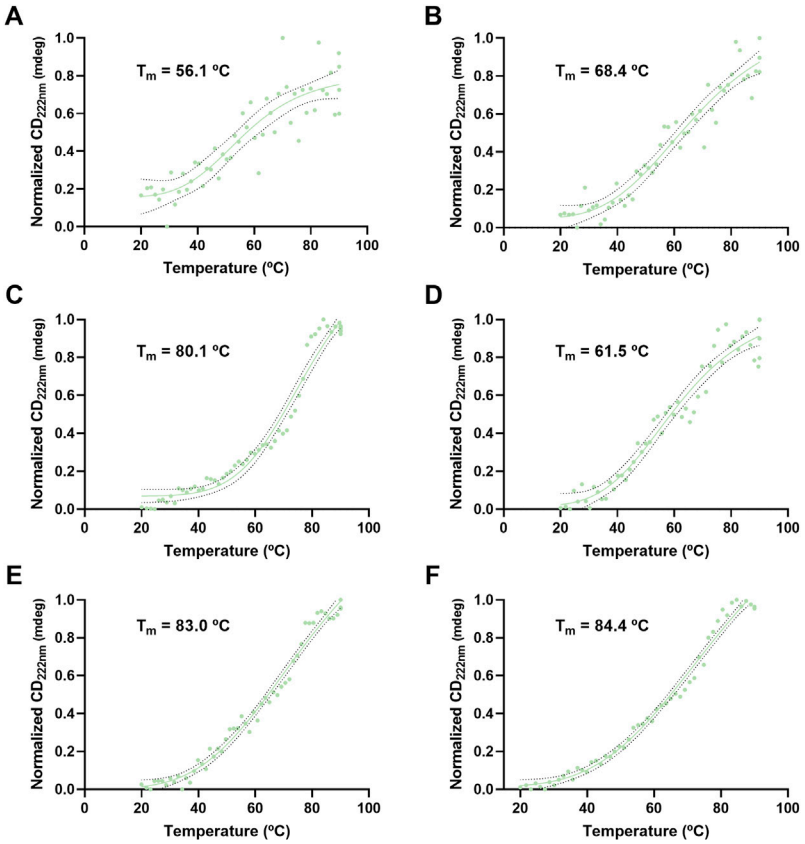

FIGURE 9 | Thermal stress analysis of influenza VLPs using circular dichroism. Temperature ramp for VLP secondary structure analysis during thermal stress. CD signal was followed at 222 nm. Data was normalized (0–1) for plotting. mdeg: milidegrees. **(A)** H1 Mono VLP, **(B)** H1 Penta VLP, **(C)** H3 Mono VLP, **(D)** H3 Penta VLP, **(E)** B Mono VLP, **(F)** B Penta VLP. Indirect measurement of T_m values was estimated by interpolation applying a sigmoidal regression.

the optimization of process conditions, e.g., pH or conductivity. Moreover, a deeper characterization of the final product can be performed using cryo-EM (McCraw et al., 2018).

Particle size and size distribution observed by TEM are in agreement with NTA and TRPS measurements. There is no correlation between size or size distribution with the group/subtype of VLPs. The values obtained for the VLP diameter using both techniques are in agreement with the expected size diameter of an influenza virus (80–130 nm) (Tidona and Darai, 2011) and recent reports of VLP size diameter measured by DLS (126 ± 11 nm) (Wu et al., 2010). The difference between the measured size diameters observed for NTA and TRPS can be explained by the different size measurements principle used. NTA determines size distributions and concentrations of particles based on their Brownian motion, calculating the diffusion coefficient of each particle in the dispersant through the Stokes-Einstein equation. The particles' hydrodynamic diameter is then calculated as a diameter of an equivalent sphere with the same diffusion coefficient (Kim et al., 2019). TRPS on the other hand uses a single dynamically resizable nanopore. When particles cross the pore, there is a change in electrical resistance, producing a pulse in electrical current. This pulse record is then interpreted to access information on geometric particle diameters, particle counts, size distributions, concentrations, and charge (Willmott, 2018).

The observed polydispersity measured through the distribution span reported for both techniques is also different, being on average two times higher in NTA. A closer analysis of the NTA particle size distributions reveals the presence of a secondary population to the left and right of the main population peak, which might not only contribute to the increase in particle dispersion but also for particle counts. TEM imaging reveals the presence of particles with dimensions above and below the VLPs observed. The secondary populations observed in NTA are not evident in TRPS, which might be related to the combination of the nanopore selected and operating parameters. While increasing pore dimensions (through the selection of a wider nanopore membrane, or by increasing the membrane stretch) increases the capability of measuring particles with higher diameters, this also reduces the signal-to-noise ratio of particles at the lower end of detection. The inverse operation will lead to opposite outcomes; lower pore dimensions will provide a reduced capability of measuring particles with

higher diameters but will improve the detection of smaller particles.

In this study, and apart from H1 Mono VLPs, NTA yields on average a particle concentration 20 times higher in comparison to TRPS. Further work is still needed to access the reproducibility of the results. These differences are related to the measurement principle of both techniques. However, a recent study (Vogel et al., 2021), where these two sizing techniques were compared, among others, for the measurement of different particle types [synthetic NIST (National Institute of Standards and Technology)-traceable particles, liposomes and exosomes], show that NTA and TRPS can be used to obtain concentration and size distributions comparable within an order of magnitude. In addition to concentration and size measurements, TRPS enables also the measurement of zeta potential. The results obtained are in line with reported values for influenza VLPs (−24 ± 0.2 mV) (Hu et al., 2017). Having access to this surface property can help in the design of the purification process and associated buffers as well as understanding how formulation can impact particle stability.

VLPs Structure and Thermal Stability

VLP secondary structure was assessed to better understand VLP major components. The presence of a double minima near 210 and 222 nm in the CD spectra suggests that VLP contain a considerable amount of α-helix content, as reported for influenza HA protein (Flanagan and Skehel, 1977). This suggests that the majority of the CD signal observed derives from HA, although we cannot rule out to also be derived from M1 (the VLP scaffold), HCP, or other cellular components. In fact, H1 Mono VLP is the one presenting the lowest CD signal and the highest ratio of HA and impurities, meaning that impurities can be contributing to the α-helix content. There are algorithms available that allow CD signal deconvolution, meaning determination and quantification of each type of secondary structure present in the sample. Here, we evaluated DICHROWEB and CAPITO servers (Whitmore and Wallace, 2008; Wiedemann et al., 2013). Both presented results consistent with the majority of the secondary structure content being α-helix, with no differences among the VLPs studied (data not shown). Nevertheless, the deconvolutions were considered inconclusive as RMSD (root-mean-square deviation) values are higher than the recommended threshold and our data does not fit properly with the data sets available for calibration. Further optimization of the experimental conditions are still needed to improve acquisition parameters, for example, recording CD signal at lower wavelengths and having a reliable analysis. Moreover, the differences observed in thermal stability suggest that CD is a useful tool to evaluate VLP behavior upon changes in process conditions. Interestingly, the thermal shift assay method was also evaluated as a tool to assess stability, but no significant shifts in the structure were observed at the conditions evaluated (data not shown). Using CD, it is also possible to evaluate other temperature ranges, pHs, the effect of cryopreservants, and perform batch-to-batch comparison (Kissmann et al., 2011; Khrustalev et al., 2020).

Hemagglutinin biological activity was confirmed with HA assay. Moreover, a previous study comparing HA assay and biolayer interferometry analysis showed a correlation between both methods, also confirming that these VLPs are also able to bind to sialic acid glycoconjugates, their receptors in cells (Carvalho et al., 2017).

Besides the methods used here, other options and orthogonal tools may be considered, depending on the resources available and specific needs, as reported in **Table 1**. The methods selected should fit the purpose: in-process monitoring or final product characterization. Bioprocess optimization will require information about titer, particle size, and size distribution, as well as impurity removal. Hemagglutination assay can provide a measurement of HA content during the entire bioprocess. This can also be obtained using orthogonal tools, such as BLI or SPR, presenting several advantages (Nilsson et al., 2010; Carvalho et al., 2017), however at a higher cost of investment. Evaluation of particle size and concentration is also fundamental and requires in-process tools such as NTA, TRPS, or DLS. These methods can give us complementary insights into particles' characteristics. Particle size and size distribution can be assessed using both NTA and TRPS methods which provide a particle by particle measurement whereas the traditional DLS offers an ensemble measurement. If particle charge is important at this point of the process, TRPS or other zeta potential analyzers should be considered instead. Impurities such as DNA, total protein and, for the expression system used, baculovirus content need to be monitored.

Product characterization implies a set of analytical tools to look at morphology, protein identity, thermal stability, and aggregation propensity, among others. The selection of the analytical method will depend on the depth of VLP characterization. TEM is critical for particle integrity and assessing the presence of HA spikes. It is a gold standard technique for direct particle detection and an immediate overview of the relative amount and shape of the particles. It requires a contrast medium for sample visualization, being that negative staining is the most common. The staining does not penetrate the membrane but the particle is enveloped with the staining compound, which can be challenging when dealing with enveloped VLPs. Moreover, VLP samples can be degraded during sample preparation. More structural information, at the atomic range level, can be obtained with cryo-EM. This technique enables the characterization of the 3D structure of macromolecules, allowing the visualization of viruses and VLPs in their native conformation. It does not require a contrast solution and due to a rapid freezing process sample damage is reduced. However, the costs are higher and the sample preparation is laborious comparing with TEM (Richert-Pöggeler et al., 2019; González-Domínguez et al., 2020). Methods such as CD or DSC allow thermal stability assessment. DSC enables direct characterization of thermal unfolding of biomolecules without the need for reporters. CD follows unfolding transition temperature (Tm) and provides information on secondary structure. However, these methods are optimized for proteins and have limitations, in particular when we are analyzing complex particles, such as VLPs. Although we are characterizing a purified sample, VLPs are complex and

heterogeneous entities, and we need to consider not only HA but all the other proteins present. We should bear in mind that like all the spectroscopies if there is heterogeneity all we can observe is an average of the population. Western blot is the traditional method for identity. Higher resolution techniques, such as peptide mapping using MS tools, can give detailed information regarding protein sequence.

The complexity of influenza VLPs (e.g. enveloped particles, multi-protein display) and the expression system (e.g. product and process-related impurities) makes VLP characterization and process monitoring challenging. In this work we (1) demonstrated the feasibility of the methods investigated to characterize the different influenza VLPs produced, and (2) established a criteria grid to aid the selection of the critical and most suitable methods for in-process monitoring and final product characterization, guiding bioprocess optimization. Importantly, the applicability of the methods herein studied can potentially be extended to other VLPs or viruses, produced in IC-BEVS or other virus-based expression systems.

DATA AVAILABILITY STATEMENT

The raw data supporting the conclusion of this article will be made available by the authors, without undue reservation.

AUTHOR CONTRIBUTIONS

Conceptualization: SC and RS; Methodology: SC and RS; Investigation: SC, RS, and MS; Formal analysis: SC, RS, and AR; Visualization: SC, RS, and AR; Writing–original draft preparation: SC, RS, and AR; Writing–review and editing: SC, RS, AR, CP, MC, and PA; Supervision: CP, AR, MC, and PA; Project administration: CP and AR; Funding acquisition: CP, AR, MC, and PA.

FUNDING

This work was funded by Fundação para a Ciência e Tecnologia (FCT, Portugal) through the following initiatives: PhD fellowship SFRH/BD/52302/2013 MolBioS Program (SC), Post-Doctoral fellowship SFRH/BPD/121558/2016 (RS), "Investigador FCT" Program (IF/01704/2014) (AR), and Exploratory Research and Development Projects (EXPL/BBB-BIO/1541/2013 and IF/01704/2014/CP1229/CT0001) (AR). This work was also supported by EU-funded project "EDUFLUVAC" (FP7-HEALTH-2013-INNOVATION−1, GA n. 602640). iNOVA4Health (UIDB/04462/2020, and UIDP/04462/2020), a program financially supported by Fundação para a Ciência e Tecnologia / Ministério da Educação e Ciência, through national funds is acknowledged. Funding from Programa INTERFACE, through Fundo de Inovação, Tecnologia e Economia Circular (FITEC), is gratefully acknowledged.

ACKNOWLEDGMENTS

The authors acknowledge Mafalda Moleirinho, Hugo Ferreira, and Daniela Sequeira for their assistance in some analytical methods. Piergiuseppe Nestola is also acknowledged for useful discussion during the conceptualization of the work. The authors acknowledge RedBiotec for kindly providing the baculovirus. Erin M. Tranfield and Ana Laura Sousa from the Electron Microscopy facility, IGC, are also acknowledged for the microscopy support.

SUPPLEMENTARY MATERIAL

The Supplementary Material for this article can be found online at: https://www.frontiersin.org/articles/10.3389/fbioe.2022.805176/full#supplementary-material

REFERENCES

Calder, L. J., Wasilewski, S., Berriman, J. A., and Rosenthal, P. B. (2010). Structural Organization of a Filamentous Influenza A Virus. *Proc. Natl. Acad. Sci.* 107, 10685–10690. doi:10.1073/pnas.1002123107

Carvalho, S. B., Freire, J. M., Moleirinho, M. G., Monteiro, F., Gaspar, D., Castanho, M. A. R. B., et al. (2016). Bioorthogonal Strategy for Bioprocessing of Specific-Site-Functionalized Enveloped Influenza-Virus-Like Particles. *Bioconjug. Chem.* 27, 2386–2399. doi:10.1021/acs.bioconjchem.6b00372

Carvalho, S. B., Moleirinho, M. G., Wheatley, D., Welsh, J., Gantier, R., Alves, P. M., et al. (2017). Universal Label-free In-Process Quantification of Influenza Virus-like Particles. *Biotechnol. J.* 12, 1700031. doi:10.1002/biot.201700031

Carvalho, S. B., Fortuna, A. R., Wolff, M. W., Peixoto, C., Alves, P. M., Reichl, U., et al. (2018). Purification of Influenza Virus-like Particles Using Sulfated Cellulose Membrane Adsorbers. *J. Chem. Technol. Biotechnol.* 93, 1988–1996. doi:10.1002/jctb.5474

Carvalho, S. B., Silva, R. J. S., Moleirinho, M. G., Cunha, B., Moreira, A. S., Xenopoulos, A., et al. (2019). Membrane-Based Approach for the Downstream Processing of Influenza Virus-Like Particles. *Biotechnol. J.* 14, 1800570. doi:10.1002/biot.201800570

Deng, F. (2018). Advances and Challenges in Enveloped Virus-like Particle (VLP)-based Vaccines. *J. Immunol. Sci.* 2, 36–41. doi:10.29245/2578-3009/2018/2.1118

Flanagan, M. T., and Skehel, J. J. (1977). The Conformation of Influenza Virus Haemagglutinin. *FEBS Lett.* 80, 57–60. doi:10.1016/0014-5793(77)80406-7

González-Domínguez, I., Puente-Massaguer, E., Cervera, L., and Gòdia, F. (2020). Quality Assessment of Virus-Like Particles at Single Particle Level: A Comparative Study. *Viruses* 12, 223. doi:10.3390/v12020223

Harris, A., Cardone, G., Winkler, D. C., Heymann, J. B., Brecher, M., White, J. M., et al. (2006). Influenza Virus Pleiomorphy Characterized by Cryoelectron Tomography. *Proc. Natl. Acad. Sci.* 103, 19123–19127. doi:10.1073/pnas.0607614103

Harris, A. K., Meyerson, J. R., Matsuoka, Y., Kuybeda, O., Moran, A., Bliss, D., et al. (2013). Structure and Accessibility of HA Trimers on Intact 2009 H1N1 Pandemic Influenza Virus to Stem Region-Specific Neutralizing Antibodies. *Proc. Natl. Acad. Sci.* 110, 4592–4597. doi:10.1073/pnas.1214913110

Hu, C.-M. J., Chien, C.-Y., Liu, M.-T., Fang, Z.-S., Chang, S.-Y., Juang, R.-H., et al. (2017). Multi-Antigen Avian Influenza a (H7N9) Virus-like Particles: Particulate Characterizations and Immunogenicity Evaluation in Murine and Avian Models. *BMC Biotechnol.* 17, 2. doi:10.1186/s12896-016-0321-6

Huang, X., Wang, X., Zhang, J., Xia, N., and Zhao, Q. (2017). Escherichia Coli-Derived Virus-like Particles in Vaccine Development. *Npj Vaccin.* 2, 3. doi:10.1038/s41541-017-0006-8

Hutchinson, E. C., Charles, P. D., Hester, S. S., Thomas, B., Trudgian, D., Martínez-Alonso, M., et al. (2014). Conserved and Host-Specific Features of Influenza Virion Architecture. *Nat. Commun.* 5, 4816. doi:10.1038/ncomms5816

Khrustalev, V. V., Kordyukova, L. V., Arutyunyan, A. M., Poboinev, V. V., Khrustaleva, T. A., Stojarov, A. N., et al. (2020). The Cytoplasmic Tail of Influenza A/H1N1 Virus Hemagglutinin Is β-Structural. *J. Biomol. Struct. Dyn.*, 1–20. doi:10.1080/07391102.2020.1860827

Kim, A., Ng, W. B., Bernt, W., and Cho, N.-J. (2019). Validation of Size Estimation of Nanoparticle Tracking Analysis on Polydisperse Macromolecule Assembly. *Sci. Rep.* 9, 2639. doi:10.1038/s41598-019-38915-x

Kissmann, J., Joshi, S. B., Haynes, J. R., Dokken, L., Richardson, C., and Middaugh, C. R. (2011). H1N1 Influenza Virus-Like Particles: Physical Degradation Pathways and Identification of Stabilizers. *J. Pharm. Sci.* 100, 634–645. doi:10.1002/jps.22304

Lavado-García, J., González-Domínguez, I., Cervera, L., Jorge, I., Vázquez, J., and Gòdia, F. (2020). Molecular Characterization of the Coproduced Extracellular Vesicles in HEK293 during Virus-Like Particle Production. *J. Proteome Res.* 19, 4516–4532. doi:10.1021/acs.jproteome.0c00581

Margine, I., Martinez-Gil, L., Chou, Y.-y., and Krammer, F. (2012). Residual Baculovirus in Insect Cell-Derived Influenza Virus-like Particle Preparations Enhances Immunogenicity. *PloS one* 7, e51559. doi:10.1371/journal.pone.0051559

McCraw, D. M., Gallagher, J. R., Torian, U., Myers, M. L., Conlon, M. T., Gulati, N. M., et al. (2018). Structural Analysis of Influenza Vaccine Virus-like Particles Reveals a Multicomponent Organization. *Sci. Rep.* 8, 10342. doi:10.1038/s41598-018-28700-7

Moleirinho, M. G., Silva, R. J. S., Carrondo, M. J. T., Alves, P. M., and Peixoto, C. (2019). Exosome-based Therapeutics: Purification Using Semi-Continuous Multi-Column Chromatography. *Sep. Purif. Technol.* 224, 515–523. doi:10.1016/j.seppur.2019.04.060

Moleirinho, M. G., Fernandes, R. P., Carvalho, S. B., Bezemer, S., Detmers, F., Hermans, P., et al. (2020). Baculovirus Affinity Removal in Viral-Based Bioprocesses. *Sep. Purif. Technol.* 241, 116693. doi:10.1016/j.seppur.2020.116693

Nilsson, C. E., Abbas, S., Bennemo, M., Larsson, A., Hämäläinen, M. D., and Frostell-Karlsson, A. (2010). A Novel Assay for Influenza Virus Quantification Using Surface Plasmon Resonance. *Vaccine* 28, 759–766. doi:10.1016/j.vaccine.2009.10.070

Nooraei, S., Bahrulolum, H., Hoseini, Z. S., Katalani, C., Hajizade, A., Easton, A. J., et al. (2021). Virus-like Particles: Preparation, Immunogenicity and Their Roles as Nanovaccines and Drug Nanocarriers. *J. Nanobiotechnol.* 19, 59. doi:10.1186/s12951-021-00806-7

Pillet, S., Aubin, É., Trépanier, S., Bussière, D., Dargis, M., Poulin, J.-F., et al. (2016). A Plant-Derived Quadrivalent Virus like Particle Influenza Vaccine Induces Cross-Reactive Antibody and T Cell Response in Healthy Adults. *Clin. Immunol.* 168, 72–87. doi:10.1016/j.clim.2016.03.008

Reiter, K., Pereira Aguilar, P., Grammelhofer, D., Joseph, J., Steppert, P., and Jungbauer, A. (2020). Separation of Influenza Virus-like Particles from Baculovirus by Polymer-Grafted Anion Exchanger. *J. Sep. Sci.* 43, 2270–2278. doi:10.1002/jssc.201901215

Richert-Pöggeler, K. R., Franzke, K., Hipp, K., and Kleespies, R. G. (2019). Electron Microscopy Methods for Virus Diagnosis and High Resolution Analysis of Viruses. *Front. Microbiol.* 9, 3255. doi:10.3389/fmicb.2018.03255

Sequeira, D. P., Correia, R., Carrondo, M. J. T., Roldão, A., Teixeira, A. P., and Alves, P. M. (2018). Combining Stable Insect Cell Lines with Baculovirus-Mediated Expression for Multi-HA Influenza VLP Production. *Vaccine* 36, 3112–3123. doi:10.1016/j.vaccine.2017.02.043

Shaw, M. L., Stone, K. L., Colangelo, C. M., Gulcicek, E. E., and Palese, P. (2008). Cellular Proteins in Influenza Virus Particles. *Plos Pathog.* 4, e1000085. doi:10.1371/journal.ppat.1000085

Thompson, C. M., Petiot, E., Lennaertz, A., Henry, O., and Kamen, A. A. (2013). Analytical Technologies for Influenza Virus-like Particle Candidate Vaccines: Challenges and Emerging Approaches. *Virol. J.* 10, 141. doi:10.1186/1743-422X-10-141

Thompson, C. M., Petiot, E., Mullick, A., Aucoin, M. G., Henry, O., and Kamen, A. A. (2015). Critical Assessment of Influenza VLP Production in Sf9 and HEK293 Expression Systems. *BMC Biotechnol.* 15, 31. doi:10.1186/s12896-015-0152-x

C. Tidona and G. Darai (Editors) (2011). *The Springer Index of Viruses* (New York, NY: Springer New York). doi:10.1007/978-0-387-95919-1

Tretyakova, I., Hidajat, R., Hamilton, G., Horn, N., Nickols, B., Prather, R. O., et al. (2016). Preparation of Quadri-Subtype Influenza Virus-like Particles Using Bovine Immunodeficiency Virus Gag Protein. *Virology* 487, 163–171. doi:10.1016/j.virol.2015.10.007

Venereo-Sanchez, A., Gilbert, R., Simoneau, M., Caron, A., Chahal, P., Chen, W., et al. (2016). Hemagglutinin and Neuraminidase Containing Virus-like Particles Produced in HEK-293 Suspension Culture: An Effective Influenza Vaccine Candidate. *Vaccine* 34, 3371–3380. doi:10.1016/j.vaccine.2016.04.089

Vicente, T., Peixoto, C., Carrondo, M. J. T., and Alves, P. M. (2009). Purification of Recombinant Baculoviruses for Gene Therapy Using Membrane Processes. *Gene Ther.* 16, 766–775. doi:10.1038/gt.2009.33

Vicente, T., Roldão, A., Peixoto, C., Carrondo, M. J. T., and Alves, P. M. (2011). Large-scale Production and Purification of VLP-Based Vaccines. *J. Invertebr. Pathol.* 107, S42–S48. doi:10.1016/j.jip.2011.05.004

Vieira, H. L. A., Estêvão, C., Roldão, A., Peixoto, C. C., Sousa, M. F. Q., Cruz, P. E., et al. (2005). Triple Layered Rotavirus VLP Production: Kinetics of Vector Replication, mRNA Stability and Recombinant Protein Production. *J. Biotechnol.* 120, 72–82. doi:10.1016/j.jbiotec.2005.03.026

Vogel, R., Savage, J., Muzard, J., della Camera, G., Vella, G., Law, A., et al. (2021). Measuring Particle Concentration of Multimodal Synthetic Reference Materials and Extracellular Vesicles with Orthogonal Techniques: Who Is up to the challenge? *J. Extracell. Vesicles* 10, e12052. doi:10.1002/jev2.12052

Wang, L., Fu, B., Li, W., Patil, G., Liu, L., Dorf, M. E., et al. (2017). Comparative Influenza Protein Interactomes Identify the Role of Plakophilin 2 in Virus Restriction. *Nat. Commun.* 8, 13876. doi:10.1038/ncomms13876

Whitmore, L., and Wallace, B. A. (2008). Protein Secondary Structure Analyses from Circular Dichroism Spectroscopy: Methods and Reference Databases. *Biopolymers* 89, 392–400. doi:10.1002/bip.20853

Wiedemann, C., Bellstedt, P., and Görlach, M. (2013). CAPITO-a Web Server-Based Analysis and Plotting Tool for Circular Dichroism Data. *Bioinformatics* 29, 1750–1757. doi:10.1093/bioinformatics/btt278

Willmott, G. R. (2018). Tunable Resistive Pulse Sensing: Better Size and Charge Measurements for Submicrometer Colloids. *Anal. Chem.* 90, 2987–2995. doi:10.1021/acs.analchem.7b05106

Wu, C.-Y., Yeh, Y.-C., Yang, Y.-C., Chan, J.-T., Hsiao, P.-W., Wu, H.-S., et al. (2010). Mammalian Expression of Virus-Like Particles for Advanced Mimicry of Authentic Influenza Virus. *PLoS ONE* 5, e9784. doi:10.1371/journal.pone.0009784

Conflict of Interest: The authors declare that the research was conducted in the absence of any commercial or financial relationships that could be construed as a potential conflict of interest.

Publisher's Note: All claims expressed in this article are solely those of the authors and do not necessarily represent those of their affiliated organizations, or those of the publisher, the editors and the reviewers. Any product that may be evaluated in this article, or claim that may be made by its manufacturer, is not guaranteed or endorsed by the publisher.

frontiers in Bioengineering and Biotechnology

ORIGINAL RESEARCH
published: 08 March 2022
doi: 10.3389/fbioe.2022.839374

Introduction of a Capillary Gel Electrophoresis-Based Workflow for Biotherapeutics Characterization: Size, Charge, and *N*-Glycosylation Variant Analysis of Bamlanivimab, an Anti-SARS-CoV-2 Product

Miklos Szabo[1†], *Daniel Sarkozy*[2†], *Marton Szigeti*[3], *Robert Farsang*[3], *Zsofia Kardos*[1], *Adam Kozma*[1], *Eszter Csanky*[1], *Doo Soo Chung*[4], *Zoltan Szekanecz*[5‡] *and Andras Guttman*[2,3*‡]

[1]Borsod Academic County Hospital, Miskolc, Hungary, [2]Horváth Csaba Memorial Laboratory of Bioseparation Sciences, Research Center for Molecular Medicine, Faculty of Medicine, Doctoral School of Molecular Medicine, University of Debrecen, Debrecen, Hungary, [3]Translational Glycomics Group, Research Institute for Biomolecular and Chemical Engineering, University of Pannonia, Veszprém, Hungary, [4]Department of Chemistry, Seoul National University, Seoul, South Korea, [5]Department of Rheumatology, Faculty of Medicine, University of Debrecen, Debrecen, Hungary

Coronavirus Disease 2019 (COVID-19) is a major public health problem worldwide with 5–10% hospitalization and 2–3% global mortality rates at the time of this publication. The disease is caused by a betacoronavirus called Severe Acute Respiratory Syndrome Coronavirus 2 (SARS-CoV-2). The receptor-binding domain (RBD) of the Spike protein expressed on the surface of the virus plays a key role in the viral entry into the host cell *via* the angiotensin-converting enzyme 2 receptor. Neutralizing monoclonal antibodies having the RBD as a target have the ability to inhibit angiotensin-converting enzyme 2 (ACE2) receptor binding, therefore, prevent SARS-CoV-2 infection, represent a promising pharmacological strategy. Bamlanivimab is the first anti-spike neutralizing monoclonal antibody, which got an emergency use authorization from the FDA for COVID-19 treatment. Albeit, bamlanivimab is primarily a neutralizing mAb, some of its effector function related activity was also emphasized. The effector function of antibody therapeutics is greatly affected by their *N*-linked carbohydrates at the conserved Fc region, possibly influenced by the manufacturing process. Various capillary gel electrophoresis methods are widely accepted in the biopharmaceutical industry for the characterization of therapeutic antibodies. In this paper we introduce a capillary gel electrophoresis based workflow for *1*) size heterogeneity analysis to determine the presence/absence of the non-glycosylated heavy chain (NGHC) fragment (SDS-CGE); *2*) capillary gel isoelectric focusing for possible *N*-glycosylation mediated charge

Abbreviations: ADCC, antibody dependent cell mediated cytotoxicity; CGE-LIF, capillary gel electrophoresis with laser induced fluorescent detection; cIEF, capillary isoelectric focusing; HC, IgG heavy chain; LC, IgG light chain; NGHC, non-glycosylated IgG heavy chain; pI, isoelectric point; PNGase F, Peptide-N4-(N-acetyl-beta-glucosaminyl) asparagine amidase; RBD, receptor binding domain; SDS-CGE, sodium dodecyl sulfate – capillary gel electrophoresis.

OPEN ACCESS

Edited by:
Pei-Hui Wang,
Shandong University, China

Reviewed by:
Lisa Holland,
West Virginia University, United States
Julia Khandurina,
Genomatica, Inc., United States
Kittikhun Wangkanont,
Chulalongkorn University, Thailand
Ahmed S Fahad,
Ragon Institute, United States

***Correspondence:**
Andras Guttman
andrasguttman@gmail.com

†These authors have contributed equally to this work and share first authorship

‡These authors have contributed equally to this work and share last authorship

Specialty section:
This article was submitted to Bioprocess Engineering, a section of the journal Frontiers in Bioengineering and Biotechnology

Received: *19 December 2021*
Accepted: *21 February 2022*
Published: *08 March 2022*

Citation:
Szabo M, Sarkozy D, Szigeti M, Farsang R, Kardos Z, Kozma A, Csanky E, Chung DS, Szekanecz Z and Guttman A (2022) Introduction of a Capillary Gel Electrophoresis-Based Workflow for Biotherapeutics Characterization: Size, Charge, and N-Glycosylation Variant Analysis of Bamlanivimab, an Anti-SARS-CoV-2 Product. Front. Bioeng. Biotechnol. 10:839374. doi: 10.3389/fbioe.2022.839374

heterogeneity determination, e.g., for excess sialylation and finally, *3*) capillary gel electrophoresis for *N*-glycosylation profiling and sequencing. Our results have shown the presence of negligible amount of non-glycosylated heavy chain (NGHC) while 25% acidic charge variants were detected. Comprehensive *N*-glycosylation characterization revealed the occurrence of approximately 8.2% core-afucosylated complex and 17% galactosylated *N*-linked oligosaccharides, suggesting the possible existence of antibody dependent cell mediated cytotoxicity (ADCC) effector function in addition to the generally considered neutralizing effect of this particular therapeutic antibody molecule.

Keywords: capillary electrophoresis, bamlanivimab, anti-SARS-CoV-2, product characterization, N-glycans

INTRODUCTION

Recently emerging viral diseases have become a significant public threat around the world. The coronavirus pandemic (COVID-19) currently represents a major public health problem worldwide since the outbreak in 2019. At the time of this publication, 5–10% of patients are hospitalized, while the mortality rate is around 2–3% globally (Salzberger et al., 2021). Severe illness typically occurs approximately 1 week after the onset of symptoms and can rapidly progress from the mild stage. The risk factors for severe COVID-19 include being male, age >65, and with comorbidities such as cardiovascular disease, lung disease, hypertension, diabetes, or obesity (Wu C. et al., 2020; Williamson et al., 2020). The most common cause of fatal outcome is pneumonia and consequent respiratory failure. The SARS-CoV-2 virus may additionally affect the heart, gastrointestinal system, liver, kidney, and the central nervous system, eventually leading to multi-organ failures (Zhu et al., 2020). The disease is caused by a new strain of betacoronavirus called Severe Acute Respiratory Syndrome Coronavirus 2 (SARS-CoV-2) (Huang et al., 2020; Zhu et al., 2020; Synowiec et al., 2021). In the viral phase of the COVID-19 disease (phase I, IIa), antiviral therapy is primarily aiming to inhibit the replication of the virus or its entry into the cell (Szekanecz et al., 2021). The Spike protein expressed on the surface of the virus plays a key role in the viral entry into the host cell. The receptor-binding domain (RBD) of the Spike protein binds to the angiotensin-converting enzyme 2 (ACE2) receptor located on the target cell plasma membrane and facilitates host cell invasion. The use of RBD targeted (neutralizing) monoclonal antibodies is one of the therapeutic options (Majumder and Minko, 2021). To avoid resistance due to the RBD modifications observed in new SARS-CoV-2 virus variants, combinations of monoclonal antibodies, specific for different epitopes, are preferentially administered.

Recently several monoclonal antibodies have been developed to treat COVID-19. Bamlanivimab (also known as LY3819253 or LY-CoV555) and etesevimab (LY3832479 or LY-CoV016) are potent anti-spike neutralizing monoclonal antibodies, which were derived from patients recovered from COVID-19 (Jones et al., 2020; Shi et al., 2020). Plasma containing antiviral antibodies obtained from such patients has been successfully used as passive immunotherapy in a number of viral infections in the past. The use of convalescent plasma in COVID-19 patients is supported by the results, that higher plasma levels of IgG against SARS-CoV-2 was associated with lower mortality (Joyner et al., 2021). Antibodies in convalescent plasma exert their effects through neutralization of pathogens and special antibody effector mechanisms (Mair-Jenkins et al., 2015). Antibodies that inhibit the binding and entry of the virus into the cell with high specificity can be obtained from the B-lymphocytes of patients who have recovered from COVID-19 disease. These neutralizing antibodies can be modified and produced in large quantities by recombinant technology. The binding site of monoclonal antibodies is mostly the receptor binding domain (RBD) of the S protein of SARS-CoV-2 (Wu Y. et al., 2020). Bamlanivimab is an IgG1 isotype monoclonal neutralizing antibody that binds to a key region of RBD that prevents the virus from entering the cell. The antibody reportedly reduced viral load as well as viral replication in the airways. In combination with etesevimab the risk of hospitalization and death could be reduced in mild to moderate SARS-CoV-2 virus infection. It may also be used prophylactically in high-risk population following exposure to SARS-CoV-2 (Gottlieb et al., 2021).

The effector function of antibody therapeutics is greatly affected by their *N*-linked carbohydrates at the conserved Fc region, influenced by the manufacturing process. Among other techniques, various capillary gel electrophoresis methods are widely utilized in the biopharmaceutical industry for the characterization of therapeutic antibodies. For size-based protein level analysis of monoclonal antibody drugs, high-resolution separation by sodium dodecyl sulfate capillary gel electrophoresis (SDS-CGE) is commonly used, featuring rapid analysis time and low volume sample requirement (Sänger-van De Griend, 2019). To yield charge heterogeneity information of therapeutic antibodies, capillary isoelectric focusing (cIEF) is an effective CE-based separation method for amphoteric protein compounds according to their isoelectric points (pI) along a continuous pH gradient (Righetti et al., 2013). On the other hand, capillary gel electrophoresis with laser induced fluorescent detection (CGE-LIF) is the separation technique of choice for *N*-glycosylation profiling and sequencing for glycan structure elucidation after derivatization with a fluorescent label of aminopyrenetrisulfonate of PNGase F released carbohydrates (Guttman, 1996).

In this paper we introduce a capillary gel electrophoresis-based characterization workflow using the model compound of bamlanivimab, in respect to linked carbohydrate mediated size,

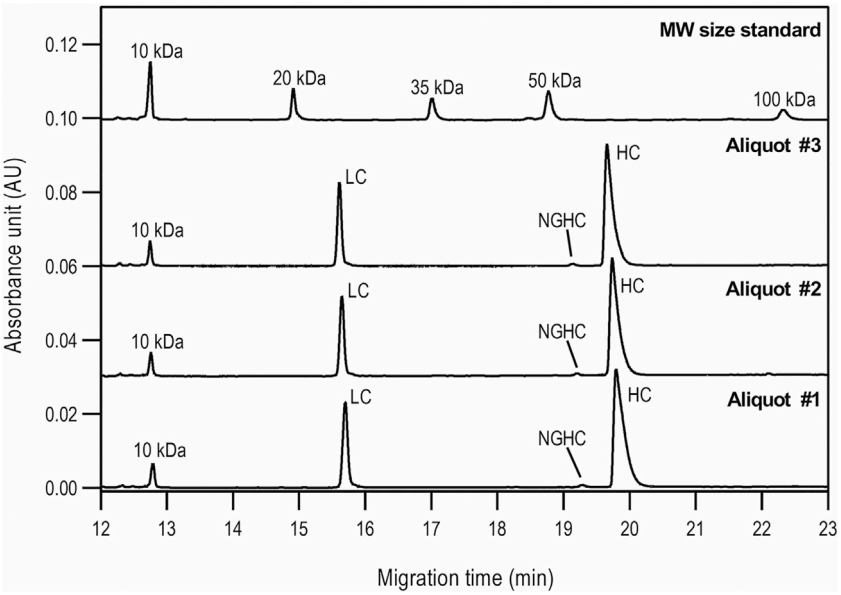

FIGURE 1 | Reduced SDS-CGE analysis of bamlanivimab. Peaks: 10 kDa – internal standard, LC – light chain, NGHC – non-glycosylated heavy chain and HC - heavy chain. Separation conditions: 30 cm total capillary length, 20 cm effective length, 50 µm i.d. BFS; separation media: SDS-MW gel buffer; 25°C separation temperature; 15 kV separation voltage; sample injection: 5.0 kV for 20 s.

TABLE 1 | Statistical evaluation of the reduced SDS-CGE analysis peak profiles of bamlanivimab.

Reduced sample preparation

Peak	Migration time (min)						%Corrected area					
	Aliquot #1	Aliquot #2	Aliquot #3	Median	Std.Dev.	% RSD	Aliquot #1	Aliquot #2	Aliquot #3	Median	Std.Dev.	% RSD
LC	15.72	15.65	15.67	15.68	0.04	0.24	31.55	31.37	30.97	31.30	0.30	0.95
NGHC	19.29	19.21	19.22	19.24	0.04	0.23	0.62	0.66	0.64	0.64	0.02	3.13
HC	19.80	19.74	19.75	19.76	0.03	0.15	67.83	67.97	68.39	68.06	0.29	0.43

charge and *N*-glycosylation variations. Capillary SDS gel electrophoresis was used for size heterogeneity analysis to learn about the presence/absence of the non *N*-glycosylated heavy chain (NGHC) fragment. Capillary gel isoelectric focusing was used for charge variant determination, e.g., for excess sialylation. Finally, capillary gel electrophoresis was applied for *N*-glycosylation profiling and sequencing.

MATERIALS AND METHODS

Chemicals and Reagents

Sodium hydroxide (S2770-100ML), hydrocloric acid (1.09058.1000), sodium cyanoborohydride in 1 M tetrahydrofuran (296813-100ML), phosphoric acid (345245-100ML), urea (U0631-500G), iminodiacetic acid (220000-500G), iodoacetamide (I6125-5G) and L-arginine (A5006-100G) were purchased from Merck (Kenilworth, NJ, United States). Glacial acetic acid (02790-101-340) and acetonitrile (00630-517-350) were from Molar Chemicals (Halasztelek, Hungary). Glycerol (24388.295), tetrahydrofuran (28553.293) and 2-mercaptoethanol (M131-250ML) were from VWR (Radnor, PA, United States). The Pharmalyte 3-10 (17-0456-01) was from GE Healthcare (Chicago, IL, United States). The Advanced cIEF Starter Kit (A80976), the SDS-MW Analysis Kit (390953) and the Fast Glycan Kit (B94499PTO) were from Bio-Science Kft (Budapest, Hungary). The PNGase F enzyme and all exoglycosidase enzymes (Neuraminidase, Galactosidase and Hexosaminidase) were from the Bio-Nanosystems Laboratory, University of Pannonia (Veszprem, Hungary). The bamlanivimab (35 mg/ml; NDC 0002-7910-01) was a kind gift of the Borsod Academic County Hospital (Miskolc, Hungary).

SDS Capillary Gel Electrophoresis

All SDS-CGE measurements were performed on a P/ACE MDQ instrument equipped with UV detection (220 ± 10 nm) (Beckman Coulter, Brea, CA, United States). The sample preparations were carried out using 80 µl of sample buffer, 5.0 µl of 2-mercaptoethanol (reduced) or 5.0 µl of 250 mM iodoacetamide (non-reduced) and

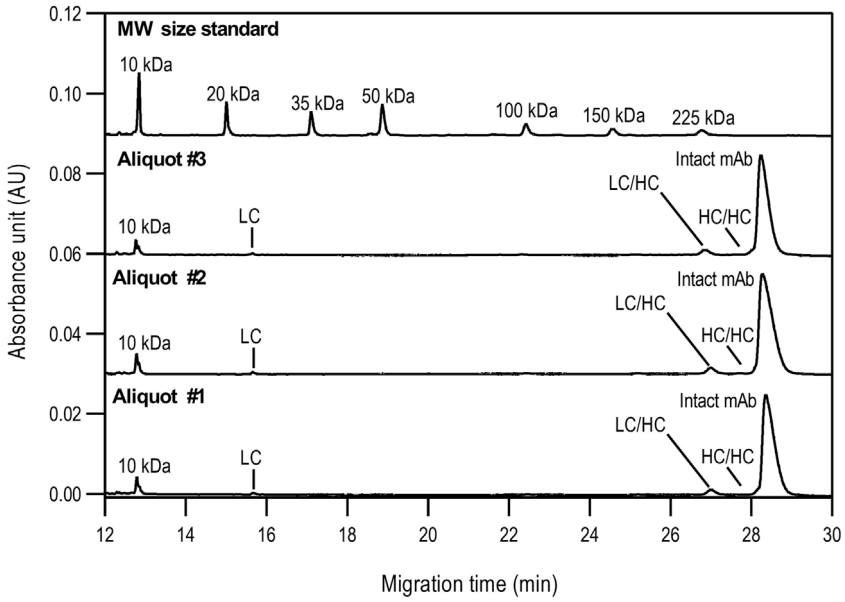

FIGURE 2 | Non-reduced SDS-CGE analysis of bamlanivimab. Peaks: 10 kDa–internal standard, LC–light chain, LC/HC–light/heavy chain complex, HC/HC–heavy/heavy chain complex, intact mAb–intact monoclonal antibody. Separation conditions were the same as in **Figure 1**.

TABLE 2 | Statistical evaluation of the non-reduced SDS-CGE analysis peak profiles of bamlanivimab.

Non-reduced sample preparation

Peak	Migration time (min)						%Corrected area					
	Aliquot #1	Aliquot #2	Aliquot #3	Median	Std.Dev.	% RSD	Aliquot #1	Aliquot #2	Aliquot #3	Median	Std.Dev.	% RSD
LC	15.68	15.71	15.69	15.69	0.02	0.12	0.76	0.82	0.81	0.80	0.03	4.04
LC/HC	27.01	27.05	27.02	27.03	0.02	0.08	3.43	3.71	3.68	3.61	0.15	4.26
HC/HC	27.79	27.79	27.82	27.80	0.01	0.05	0.12	0.11	0.12	0.12	0.01	4.95
Intact mAb	28.36	28.32	28.42	28.37	0.05	0.18	95.69	95.36	95.39	95.48	0.18	0.19

2.0 µl of 10 kDa internal standard for 10 µl of 10 mg/ml (100 µg) bamlanivimab. The samples were incubated at 70°C for 15 min prior to analysis. The instrument was equipped with a 30 cm total length (20 cm effective length, 50 µm i.d.) bare fused silica (BFS) capillary. The capillary was filled with the SDS-MW separation gel buffer and 15 kV separation voltage was applied in reversed polarity mode at 25°C capillary temperature. The sample was introduced by applying 5.0 kV for 20 s. The capillary was conditioned prior and in between every run by rinsing with 0.1 M NaOH, 0.1 M HCl and HPLC grade water, respectively.

Isoelectric Point Determination With cIEF

Capillary gel isoelectric focusing-based isoelectric point (pI) determination was accomplished in the P/ACE MDQ instrument equipped with UV detection (280 ± 10 nm) using a 30 cm total length (20 cm effective length, 50 µm i.d.) NCHO coated capillary. The separation and sample storage temperatures were set to 20 and 10°C, respectively. The cIEF analysis workflow was carried out in two major steps: *1*) sample focusing by applying 833 V/cm electric field in normal polarity mode for 15 min between the anolyte (200 mM phosphoric acid) and catholyte (300 mM sodium hydroxide, and 2) mobilization was performed using 1000 V/cm electric field in normal polarity mode between the anolyte and the chemical mobilizer of 350 mM acetic acid for 45 min. The capillary was filled with 2.0 µl of 10 mg/ml of bamlanivimab diluted with 240 µl of Master Mix including the cIEF separation gel buffer, urea, Pharmalyte 3-10, L-arginine, iminodiacetic acid and the pI markers 7.0 and 10. The separation capillary was rinsed with 6 M urea and HPLC grade water prior and between every runs.

N-Glycan Analysis and Sequencing With CGE-LIF

N-glycosylation analysis was also carried out using the P/ACE MDQ instrument equipped with LIF detection (ex.: 488 nm, em.:

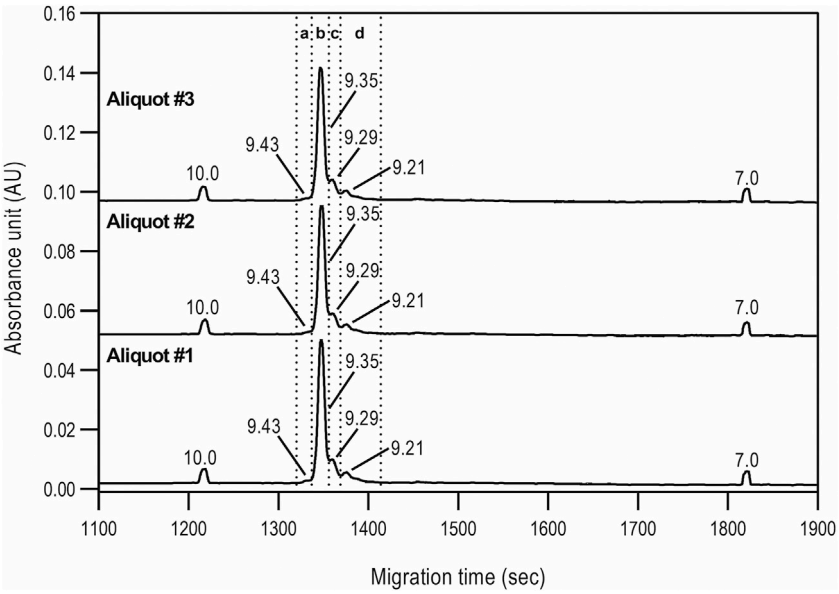

FIGURE 3 | cIEF analysis of bamlanivimab. Section a: Basic peaks; Section b: Main peak; Section c: Acidic peaks region 1; Section d: Acidic peaks region 2. Separation conditions: 30 cm total capillary length, 20 cm effective length, 50 µm i.d. NCHO coated capillary; applied focusing electric field strength: 833 V/cm; mobilization electric field strength: 1,000 V/cm; 20°C separation temperature; sample injection: 2.0 µl of sample was mixed into the Master Mixture and introduced by applying 25 psi for 100 s–total capillary fill.

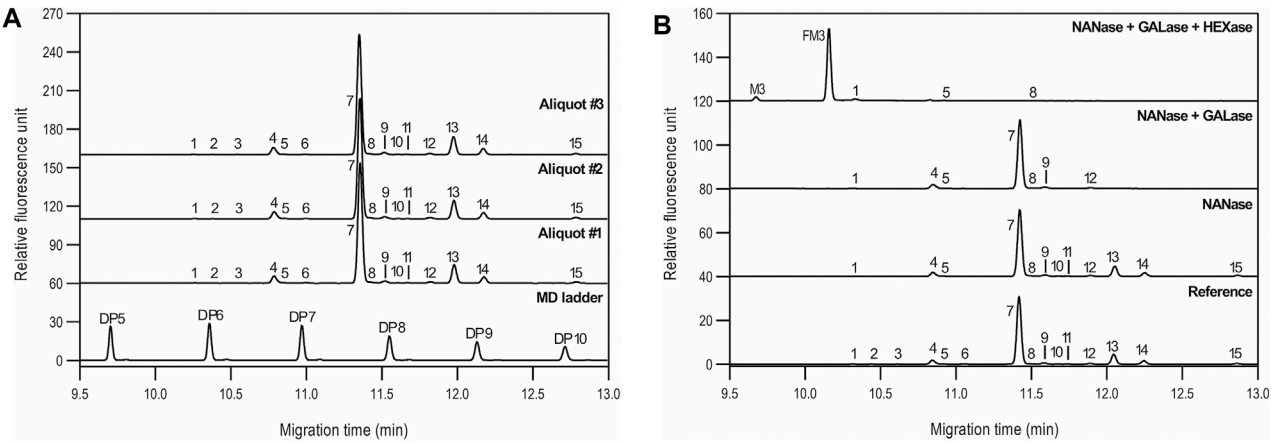

FIGURE 4 | *N*-glycan profiling **(A)** and sequencing **(B)** of bamlanivimab with CGE-LIF. Peaks: as listed in **Table 4**. Separation conditions: 50 cm total capillary length, 40 cm effective length, 50 µm i.d. BFS; separation media: HR-NCHO gel buffer; 25°C separation temperature; 30 kV separation voltage; sample injection: 1.0 psi for 5.0 s water → 5.0 kV for 20 s sample.

520 nm), using a 50 cm total length (40 cm effective length, 50 µm i.d.) BFS capillary by applying 30 kV separation voltage in reversed polarity mode at 25°C capillary temperature. The column was filled with HR-NCHO separation gel buffer and the sample was injected after introducing a water plug (1.0 psi for 5.0 s) followed by the sample introduction (2.0 kV for 2.0 s). The *N*-glycan sample preparation was based on the method introduced by Reider *et al.* (Reider et al., 2018). Briefly, 10 µl of 10 mg/ml (100 µg) bamlanivimab was denatured at 80°C for 10 min using 2.0 µl of a denaturation mixture, followed by digestion with the addition of 1.0 µl of PNGase F in 20 µl of 20 mM ammonium acetate at 37°C for 2.0 h. After the digestion step, 20 µl of the labeling solution was added (6.0 mM of APTS, 100 mM of sodium cyanoborohydride in 1 M THF and 24% of acetic acid) and incubated overnight at 37°C with open lid (evaporative labeling). Prior to injection, the excess dye was removed using 20 µl of five-fold concentrated purification beads and 185 µl of acetonitrile alternately in total of four

TABLE 3 | Statistical evaluation of the cIEF analysis peak profiles of bamlanivimab.

%Area							pI value						
Group	Aliquot #1	Aliquot #2	Aliquot #3	Meadian	Std.Dev.	% RSD	Peak	Aliquot #1	Aliquot #2	Aliquot #3	Meadian	Std.Dev.	% RSD
Basic peaks	1.45	1.46	1.42	1.44	0.02	1.58	1.00	9.43	9.43	9.43	9.43	0.00	0.03
Main peak	74.38	74.37	73.69	74.15	0.40	0.54	2.00	9.35	9.35	9.35	9.35	0.00	0.02
Acidic-1 peaks	13.48	13.27	13.95	13.57	0.35	2.57	3.00	9.29	9.29	9.29	9.29	0.00	0.02
Acidic-2 peaks	10.69	10.89	10.94	10.84	0.13	1.20	4.00	9.21	9.22	9.21	9.21	0.00	0.02

wash cycles and the APTS labeled sample was eluted by 100 µl of HPLC grade water. The samples were diluted tenfold using HPLC grade water and analyzed by the CGE-LIF system. Oligosaccharide sequencing was carried out by adding 1.0 µl of exoglycosidase enzymes from each type (Neuraminidase, Galactosidase and Hexosaminidase) to 10 µl of sample as described earlier (Szigeti and Guttman, 2017). Then, the samples were incubated at 37°C for 1.0 h. Prior to CGE-LIF analysis, 40 µl of HPLC grade water was added to the digested samples.

RESULTS

The capillary gel electrophoresis-based characterization workflow included size, charge and *N*-glycosylation variant analyses of the model mAb of bamlanivimab. Size and charge heterogeneities were investigated by SDS-CGE and cIEF, respectively. *N*-glycosylation variant analysis utilized capillary gel electrophoresis profiling after endoglycosidase release of the bound carbohydrates, fluorophore labeling as well as specific exoglycosydase array-based sequencing.

Size Heterogeneity Characterization

First, the size heterogeneity of the product was studied with special respect to the presence or absence of the NGHC fragment in reduced SDS-CGE separation modes. Purity analysis was done by SDS-CGE in non-reduced mode. In both instances, three separate aliquots of the same sample were prepared parallel and analyzed. **Figure 1** compares the injections of the reduced samples to the size standard trace. The statistical analysis of the results is listed in **Table 1**, showing the following peak area distribution: 31.3% LC, only 0.64% NGHC and 68.06% HC fragments. Please note the excellent migration time reproducibility of <0.25% RSD.

The non-reduced samples were also analyzed by SDS-CGE as shown in **Figure 2**, along with the statistical evaluation of the data obtained (**Table 2**). Similar to **Figure 1**, excellent migration time reproducibility was observed (<0.2% RSD) by injecting the parallel sample preparation products of the three separate aliquots. In this instance, in addition to the large intact monoclonal antibody peak (~95.5%), some small impurity/decomposition products were also observed including the heavy-heavy chain (HC/HC) fragment, the light-heavy chain (LC/HC) fragment and the light chain (LC). The obtained purity data corresponds with the EUA FDA certificate of bamlanivimab (>95%, https://www.cellsciences.com/PDF/CPC534.pdf).

Charge Variant Analysis

Capillary isoelectric focusing was used to investigate the charge variants of the product with special attention to the acidic forms assuming the presence of possible sialylated glycans. **Figure 3** shows the resulting cIEF traces highlighting the basic (section a), main peak (section b), and two acidic regions (sections c and d). Very little amount (<1.5%) of basic charge variants were observed. The main peak represented 74.1% of the product. Please note that the pI difference between the main peak and the basic region was less than 0.08 pH unit. The two acidic variant regions corresponded to 13.5 and 10.8%, adding up to almost 25% as acidic forms. The very small pI differences of <0.14 pH unit suggested the need for thorough glycosylation analysis with respect to sialic acid content determination as reported below.

N-Glycosylation Characterization

The asparagine-linked glycosylation of the product was thoroughly analyzed at the profile and sequence levels by CGE as shown in **Figures 4A,B**, respectively. **Figure 4A** compares the CGE-LIF traces of the independent sample preparation products of three separate aliquots of the same sample (PNGase F digestion and APTS labeling) to the maltooligosaccharide ladder (lower trace). 14 features were identified as significant, and the peaks labeled accordingly. Glucose unit (GU) values were calculated based on the triple internal standard approach our group introduced earlier (Jarvas et al., 2016) and the corresponding structures were assigned by mining publicly available databases (glycostore.org). **Table 3** lists the qualitative and quantitative results after verification by exoglycosidase array-based carbohydrate sequencing. **Figure 4B** compares the sequencing traces to the undigested reference sample (lower trace). Sialidase digestion (NANase trace) removed all sialic acids from the *N*-linked oligosaccharides, while consecutive galactosidase (GALase trace) and hexosaminidase (HEXase trace) treatment removed all galactose and N-acetylglucosamine residues. The large peak in trace HEXase (FM3) represents the core fucosylated trimannosyl chitobiose core structure. The total amount of core afucosylated glycans was ~8.2%, excluding high mannose types. The galactosylated and sialylated oligosaccharides represented 17.2 and 0.5%, while 1.3% high mannose structures were detected.

TABLE 4 | Statistical evaluation of the *N*-glycan analysis peak profiles of bamlanivimab.

Peak	ID	GU	Exoglycosidase sequencing - response			Migration time (min)					%Area				
			NANase	GALase	HEXase	Aliquot #1	Aliquot #2	Aliquot #3	Median	Std.Dev.	%RSD	Aliquot #1	Aliquot #2	Aliquot #3	Median	Std.Dev.	%RSD
1	M4	5.74	–	–	–	10.28	10.26	10.25	10.26	0.01	0.13	0.19	0.19	0.19	0.19	0.00	2.17
2	FA2G1S1	5.92	×	–	–	10.40	10.38	10.38	10.39	0.01	0.12	0.13	0.13	0.13	0.13	0.00	1.26
3	A2G2S1	6.18	×	–	–	10.57	10.55	10.55	10.56	0.01	0.12	0.12	0.11	0.11	0.11	0.00	4.37
4	A2	6.56	–	–	×	10.81	10.79	10.78	10.79	0.01	0.12	4.71	4.81	4.86	4.79	0.08	1.64
5	M5	6.67	–	–	–	10.87	10.85	10.85	10.85	0.01	0.12	0.41	0.42	0.43	0.42	0.01	2.81
6	A2B	6.89	×	–	–	11.02	11.00	10.99	11.00	0.01	0.13	0.32	0.32	0.29	0.31	0.02	5.52
7	FA2	7.49	–	–	×	11.38	11.35	11.35	11.36	0.01	0.12	73.51	73.32	73.74	73.52	0.21	0.28
8	M6	7.59	–	–	–	11.44	11.42	11.42	11.42	0.01	0.09	0.70	0.66	0.67	0.68	0.02	2.63
9	N/A	7.76	–	–	×	11.54	11.52	11.51	11.52	0.01	0.12	1.65	1.71	1.64	1.66	0.04	2.26
10	A2G1	7.90	–	×	–	11.63	11.61	11.61	11.61	0.01	0.11	0.23	0.23	0.21	0.23	0.01	5.19
11	A2B[6]G1	8.01	–	×	–	11.69	11.67	11.67	11.68	0.01	0.12	0.23	0.24	0.23	0.23	0.00	1.45
12	N/A	8.26	–	–	×	11.84	11.82	11.82	11.83	0.01	0.12	0.94	0.95	0.92	0.93	0.02	1.84
13	FA2[6]G1	8.53	–	×	–	12.00	11.98	11.97	11.98	0.01	0.11	11.67	11.73	11.55	11.65	0.10	0.82
14	FA2[3]G1	8.85	–	×	–	12.20	12.17	12.17	12.18	0.01	0.12	4.22	4.21	4.12	4.18	0.05	1.24
15	FA2G2	9.87	–	×	–	12.81	12.78	12.78	12.79	0.01	0.11	0.99	0.98	0.93	0.96	0.03	3.40
Total afucosylated (incl. high mannose) peaks (%)					9.56	%RSD median - all peaks (>0.01%)					0.12	%RSD median - all peaks (>0.01%)					2.46
Total terminal galactosylated peaks (%)					17.25	%RSD median - %area below 1%					0.12	%RSD median - %area below 1%					3.06
Total high mannose peaks (%)					1.29	%RSD median - %area between 1 and 5%					0.12	%RSD median - %area between 1 and 5%					1.71
Total sialylated peaks (%)					0.55	%RSD median - %area over 5%					0.12	%RSD median - %area over 5%					0.55

DISCUSSION

Reduced capillary SDS gel electrophoresis-based size heterogeneity analysis revealed very little amount of the non-glycosylated heavy chain fragment, suggesting that the product was >99% glycosylated (**Table 1**). Applying the same method to the non-reduced sample showed 95.5% purity (**Table 2**). Please note that while the MW of the intact form of the molecule is ~150 kDa, it migrated slower than the 225 kDa size standard. The reason for this anomaly is the significantly bulkier Y shape of the intact IgG molecule compared to the linear polypeptide standard, as was reported earlier (Guttman et al., 2021). Charge variant characterization by capillary gel isoelectric focusing showed the presence of lower than 1.5% of the basic variants, but almost 25% of acidic variants (**Table 3**). However, the very small pI difference between the main peak and even the higher acidity variant region of <0.14 pH unit, suggested the need for additional glycosylation analysis with special respect to sialic acid containing attached glycans. *N*-glycosylation profiling and sequencing revealed that the total sialylation level of the product was only ~0.5% (**Table 4**), therefore the acidic variants found during the cIEF analysis were probably the result of the number of acidic amino acids in the polypeptide backbone and possible deamidation or glycation of the product. The core fucosylation level of bamlanivimab was >90%, suggesting some antibody dependent cell mediated cytotoxicity (ADCC) effector function of the product due to the presence of approximately 8.2% afucosylated attached oligosaccharides. As a matter of fact, ADCC function of bamlanivimab was reported on FCγRIIIa expressing Jurkat cells after reacting with Spike protein expressing target cells, while complement dependent cytotoxicity (CDC) was not detected (Eli Lilly and Company, U.S. Food and Drug Administration, 2021). The interaction between the FcγRIIIa glycosylation and the lack of core fucosylation on the IgG Fc region enables greater carbohydrate-carbohydrate interactions increasing the overall binding strength (Hsieh et al., 2017; Wang et al., 2018). In addition, approximately 17% of the core fucosylated biantennary structures showed terminal galactosylation, reportedly enhancing the above suggested ADCC function (Raju and Jordan, 2012; Aoyama et al., 2019). Please note that terminal galactosylation also increases the serum half-life of the product, while the very low amount of high mannose structures found in our study (1.28%) should not significantly contribute to the opposite (Filep et al., 2021). By all means, our results suggested some ADCC function of bamlanivimab, besides the neutralizing effect of the product.

CONCLUSION

In this paper, a comprehensive capillary gel electrophoresis-based characterization workflow is presented using bamlanivimab, an anti-COVID-19 biotherapeutic product, as a model compound. The study included analyses at the intact

protein, subunit and *N*-glycosylation levels using capillary SDS gel electrophoresis and isoelectric focusing with UV detection as well as GGE-LIF, respectively. This latter was utilized for profiling and sequencing to reveal possible *N*-glycan structure–function relationships. Our results revealed the presence of negligible amount of non glycosylated HC fragment, significant amount of acidic charge variants (25%) but with very little pI shift (<0.14 pH unit) and >90% of fucosylated *N*-linked oligosaccharides. The remaining <10% core-afucosylated glycans together with the 17% terminal galactosylation suggested some ADCC effector function of the product, while the major mode of action of bamlanivimab should still be considered by its neutralizing effect.

DATA AVAILABILITY STATEMENT

The raw data supporting the conclusions of this article will be made available by the authors, without undue reservation.

AUTHOR CONTRIBUTIONS

MiS: Writing – original draft, Preparation. DS: Investigation, Formal analysis. MaS: Conceptualization, Methodology. RF: Conceptualization, Methodology. EC: Resources. ZK: Data curation. AK: Resources. ZS: Review and editing. AG: Writing – review and editing. DC: Regulatory editing. All authors contributed to manuscript revision, read, and approved the submitted version.

FUNDING

The authors gratefully acknowledge the support of the BIONANO_GINOP-2.3.2-15-2016-00017 project and the V4-Korea Joint Research Program, project National Research Development and Innovation Office (NKFIH) (NN 127062) grants of the Hungarian Government. DSC acknowledges the supports from the National Research Foundation of Korea (NRF 2018K1A3A1A39088119). This is contribution #195 from the Horváth Csaba Memorial Laboratory of Bioseparation Sciences.

REFERENCES

Aoyama, M., Hashii, N., Tsukimura, W., Osumi, K., Harazono, A., Tada, M., et al. (2019). Effects of Terminal Galactose Residues in Mannose α1-6 Arm of Fc-Glycan on the Effector Functions of Therapeutic Monoclonal Antibodies. *mAbs* 11, 826–836. doi:10.1080/19420862.2019.1608143

Eli Lilly and Company, U.S. Food and Drug Administration (2021). *Fact Sheet for Health Care Providers Emergency Use Authorization (EUA) of Bamlanivimab (B3.01-BAM-0006-EUA HCP-20210318)*. Silver Spring, MD: FDA.

Filep, C., Szigeti, M., Farsang, R., Haberger, M., Reusch, D., and Guttman, A. (2021). Multilevel Capillary Gel Electrophoresis Characterization of New Antibody Modalities. *Analytica Chim. Acta* 1166, 338492. doi:10.1016/j.aca.2021.338492

Gottlieb, R. L., Nirula, A., Chen, P., Boscia, J., Heller, B., Morris, J., et al. (2021). Effect of Bamlanivimab as Monotherapy or in Combination with Etesevimab on Viral Load in Patients with Mild to Moderate COVID-19. *JAMA* 325, 632–644. doi:10.1001/jama.2021.0202

Guttman, A., Filep, C., and Karger, B. L. (2021). Fundamentals of Capillary Electrophoretic Migration and Separation of SDS Proteins in Borate Cross-Linked Dextran Gels. *Anal. Chem.* 93, 9267–9276. doi:10.1021/acs.analchem.1c01636

Guttman, A. (1996). High-resolution Carbohydrate Profiling by Capillary Gel Electrophoresis. *Nature* 380, 461–462. doi:10.1038/380461a0

Hsieh, Y.-T., Aggarwal, P., Cirelli, D., Gu, L., Surowy, T., and Mozier, N. M. (2017). Characterization of FcγRIIIA Effector Cells Used in In Vitro ADCC Bioassay: Comparison of Primary NK Cells with Engineered NK-92 and Jurkat T Cells. *J. Immunological Methods* 441, 56–66. doi:10.1016/j.jim.2016.12.002

Huang, C., Wang, Y., Li, X., Ren, L., Zhao, J., Hu, Y., et al. (2020). Clinical Features of Patients Infected with 2019 Novel Coronavirus in Wuhan, China. *The Lancet* 395, 497–506. doi:10.1016/s0140-6736(20)30183-5

Jarvas, G., Szigeti, M., Chapman, J., and Guttman, A. (2016). Triple-Internal Standard Based Glycan Structural Assignment Method for Capillary Electrophoresis Analysis of Carbohydrates. *Anal. Chem.* 88, 11364–11367. doi:10.1021/acs.analchem.6b03596

Jones, B. E., Brown-Augsburger, P. L., Corbett, K. S., Westendorf, K., Davies, J., Cujec, T. P., et al. (2020). *LY-CoV555, a Rapidly Isolated Potent Neutralizing Antibody, Provides protection in a Non-human Primate Model of SARS-CoV-2 Infection*. Cold Spring Harbor, NY: bioRxiv.

Joyner, M. J., Carter, R. E., Senefeld, J. W., Klassen, S. A., Mills, J. R., Johnson, P. W., et al. (2021). Convalescent Plasma Antibody Levels and the Risk of Death from Covid-19. *N. Engl. J. Med.* 384, 1015–1027. doi:10.1056/nejmoa2031893

Mair-Jenkins, J., Saavedra-Campos, M., Baillie, J. K., Cleary, P., Khaw, F.-M., Lim, W. S., et al. (2015). The Effectiveness of Convalescent Plasma and Hyperimmune Immunoglobulin for the Treatment of Severe Acute Respiratory Infections of Viral Etiology: a Systematic Review and Exploratory Meta-Analysis. *J. Infect. Dis.* 211, 80–90. doi:10.1093/infdis/jiu396

Majumder, J., and Minko, T. (2021). Recent Developments on Therapeutic and Diagnostic Approaches for COVID-19. *AAPS J.* 23, 14. doi:10.1208/s12248-020-00532-2

Raju, T. S., and Jordan, R. E. (2012). Galactosylation Variations in Marketed Therapeutic Antibodies. *mAbs* 4, 385–391. doi:10.4161/mabs.19868

Reider, B., Szigeti, M., and Guttman, A. (2018). Evaporative Fluorophore Labeling of Carbohydrates via Reductive Amination. *Talanta* 185, 365–369. doi:10.1016/j.talanta.2018.03.101

Righetti, P. G., Sebastiano, R., and Citterio, A. (2013). Capillary Electrophoresis and Isoelectric Focusing in Peptide and Protein Analysis. *Proteomics* 13, 325–340. doi:10.1002/pmic.201200378

Salzberger, B., Buder, F., Lampl, B., Ehrenstein, B., Hitzenbichler, F., Holzmann, T., et al. (2021). Epidemiology of SARS-CoV-2. *Infection* 49, 233–239. doi:10.1007/s15010-020-01531-3

Sänger-van de Griend, C. E. (2019). CE-SDS Method Development, Validation, and Best Practice-An Overview. *Electrophoresis* 40, 2361–2374. doi:10.1002/elps.201900094

Shi, R., Shan, C., Duan, X., Chen, Z., Liu, P., Song, J., et al. (2020). A Human Neutralizing Antibody Targets the Receptor-Binding Site of SARS-CoV-2. *Nature* 584, 120–124. doi:10.1038/s41586-020-2381-y

Synowiec, A., Szczepański, A., Barreto-Duran, E., Lie, L. K., and Pyrc, K. (2021). Severe Acute Respiratory Syndrome Coronavirus 2 (SARS-CoV-2): a Systemic Infection. *Clin. Microbiol. Rev.* 34. doi:10.1128/CMR.00133-20

Szekanecz, Z., Bogos, K., Constantin, T., Fülesdi, B., Müller, V., Rákóczi, É., et al. (2021). Antivirális És Gyulladásellenes Kezelési Lehetőségek COVID-19-Ben. *Oh* 162, 643–651. doi:10.1556/650.2021.32230

Szigeti, M., and Guttman, A. (2017). Automated N-Glycosylation Sequencing of Biopharmaceuticals by Capillary Electrophoresis. *Sci. Rep.* 7, 11663. doi:10.1038/s41598-017-11493-6

Wang, X., Mathieu, M., and Brezski, R. J. (2018). IgG Fc Engineering to Modulate Antibody Effector Functions. *Protein Cell* 9, 63–73. doi:10.1007/s13238-017-0473-8

Williamson, E. J., Walker, A. J., Bhaskaran, K., Bacon, S., Bates, C., Morton, C. E., et al. (2020). Factors Associated with COVID-19-Related Death Using OpenSAFELY. *Nature* 584, 430–436. doi:10.1038/s41586-020-2521-4

Wu, C., Chen, X., Cai, Y., Xia, J. a., Zhou, X., Xu, S., et al. (2020a). Risk Factors Associated with Acute Respiratory Distress Syndrome and Death in Patients with Coronavirus Disease 2019 Pneumonia in Wuhan, China. *JAMA Intern. Med.* 180, 934–943. doi:10.1001/jamainternmed.2020.0994

Wu, Y., Wang, F., Shen, C., Peng, W., Li, D., Zhao, C., et al. (2020b). A Noncompeting Pair of Human Neutralizing Antibodies Block COVID-19 Virus Binding to its Receptor ACE2. *Science* 368, 1274–1278. doi:10.1126/science.abc2241

Zhu, N., Zhang, D., Wang, W., Li, X., Yang, B., Song, J., et al. (2020). A Novel Coronavirus from Patients with Pneumonia in China, 2019. *N. Engl. J. Med.* 382, 727–733. doi:10.1056/nejmoa2001017

Conflict of Interest: The authors declare that the research was conducted in the absence of any commercial or financial relationships that could be construed as a potential conflict of interest.

frontiers in Bioengineering and Biotechnology

ORIGINAL RESEARCH
published: 14 March 2022
doi: 10.3389/fbioe.2022.862456

Streamlining the Characterization of Disulfide Bond Shuffling and Protein Degradation in IgG1 Biopharmaceuticals Under Native and Stressed Conditions

*Jill Coghlan[1†], Alexander Benet[1†], Preethi Kumaran[1], Michael Ford[2], Lawrie Veale[3], St. John Skilton[3], Sergei Saveliev[4] and Anna A. Schwendeman[1,5]**

[1]Department of Pharmaceutical Sciences, College of Pharmacy, University of Michigan, Ann Arbor, MI, United States, [2]MS Bioworks, Ann Arbor, MI, United States, [3]Protein Metrics, Cupertino, CA, United States, [4]Promega Corporation, Madison, WI, United States, [5]Biointerfaces Institute, Ann Arbor, MI, United States

OPEN ACCESS

Edited by:
Anurag S. Rathore, Indian Institute of Technology Delhi, India

Reviewed by:
Alain Beck, Pierre Fabre, France
Davy Guillarme, Université de Genève, Switzerland

***Correspondence:**
Anna A. Schwendeman
annaschw@med.umich.edu

[†]These authors have contributed equally to this work and share first authorship

Specialty section:
This article was submitted to Bioprocess Engineering, a section of the journal Frontiers in Bioengineering and Biotechnology

Received: *25 January 2022*
Accepted: *16 February 2022*
Published: *14 March 2022*

Citation:
Coghlan J, Benet A, Kumaran P, Ford M, Veale L, Skilton SJ, Saveliev S and Schwendeman AA (2022) Streamlining the Characterization of Disulfide Bond Shuffling and Protein Degradation in IgG1 Biopharmaceuticals Under Native and Stressed Conditions. Front. Bioeng. Biotechnol. 10:862456. doi: 10.3389/fbioe.2022.862456

Post translational modifications (PTMs) have been shown to negatively impact protein efficacy and safety by altering its native conformation, stability, target binding and/or pharmacokinetics. One PTM in particular, shuffled disulfide bonds, has been linked to decreased potency and increased immunogenicity of protein therapeutics. In an effort to gain more insights into the effects of shuffled disulfide bonds on protein therapeutics' safety and efficacy, we designed and further optimized a semi-automated LC-MS/MS method for disulfide bond characterization on two IgG1 protein therapeutics—rituximab and bevacizumab. We also compared originator vs. biosimilar versions of the two therapeutics to determine if there were notable variations in the disulfide shuffling and overall degradation between originator and biosimilar drug products. From our resulting data, we noticed differences in how the two proteins degraded. Bevacizumab had a general upward trend in shuffled disulfide bond levels over the course of a 4-week incubation (0.58 ± 0.08% to 1.46 ± 1.10% for originator) whereas rituximab maintained similar levels throughout the incubation (0.24 ± 0.21% to 0.51 ± 0.11% for originator). When we measured degradation by SEC and SDS-PAGE, we observed trends that correlated with the LC-MS/MS data. Across all methods, we observed that the originator and biosimilar drugs performed similarly. The results from this study will help provide groundwork for comparative disulfide shuffling analysis by LC-MS/MS and standard analytical methodology implementation for the development and regulatory approval of biosimilars.

Keywords: disulfide bond shuffling, IgG1 therapeutics, biosimilars, LC-MS/MS, protein degradation

INTRODUCTION

Mass spectrometry has gained traction among the biologics community for its ability to identify a myriad of protein modifications. Being able to identify, locate and quantify protein modifications is paramount when developing new biologics and biosimilars. After all, certain modifications can be indicators of protein degradation, immunogenicity, improper manufacturing conditions, etc. N and

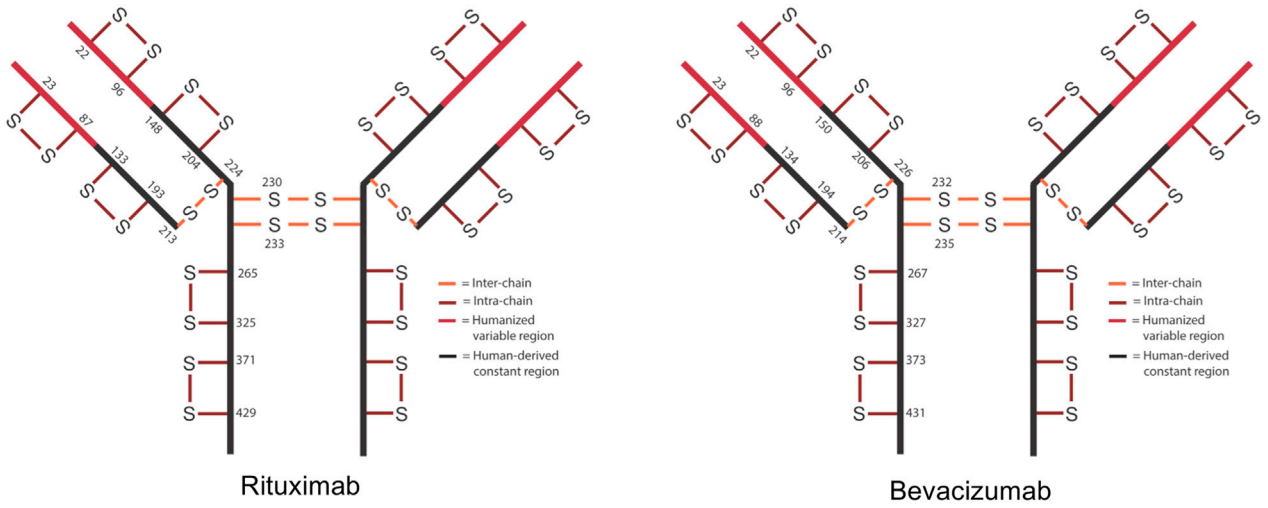

FIGURE 1 | Schematic of expected disulfide bond locations for rituximab and bevacizumab. Fc region is shown in black and Fv region is shown in red. 12 intra-chain (red) and 4 inter-chain (orange) bonds are typical for IgG1.

O-linked glycosylation is one example of a post translational modification (PTM) that has been well-studied in recent years. The presence of specific glycans can affect protein therapeutics' potency by conferring stability, controlling conformation, altering target binding, and increasing clearance rate (Kanda et al., 2007; Matsumiya et al., 2007; Goetze et al., 2011; Zheng et al., 2011; Hmiel et al., 2015; Thomann et al., 2016; Pereira et al., 2018). Aside from glycans, there are other noteworthy PTMs that influence protein activity and safety, including deamidation at asparagine and glutamine residues, oxidation at methionine and tryptophan residues, and disulfide bond shuffling (Strohl and Strohl, 2012). Disulfide bond shuffling in IgG1 therapeutics, namely bevacizumab and rituximab, is the main focus of this research as, upon our literature search, we discovered a limited number of publications studying this topic.

In IgG1s there are normally 16 disulfide bonds—4 interchain and 12 intrachain (**Figure 1**). These bonds are critical in maintaining proper protein folding and stability. Interchain bonds are more susceptible to reduction and, therefore, are more susceptible to an incomplete formation of bonds and shuffling than intrachain bonds (Cordoba et al., 2005; Liu et al., 2010; Ouellette et al., 2010; Liu and May, 2012; Hmiel et al., 2015; Lakbub et al., 2018; Weinfurtner, 2018; Nie et al., 2022). For example, the larger number and hinge region arrangement of disulfide bonds an IgG2 increases its potential for covalent dimerization, which leads to an increased binding avidity (Moritz and Stracke, 2017; Weinfurtner, 2018). Similarly, antibody-drug conjugates (ADCs) that are conjugated via thiol-maleimide chemistry are dependent upon the partial reduction of disulfide bonds. These bonds are then able to participate in forming the connection between the antibody and the drug (Liu-Shin et al., 2018). The success of ADCs in treating diseases such as cancer is evidenced by the fact that 10 ADCs are FDA approved and over 80 others are in clinical trials (Dean et al., 2021).

Then again, sometimes unconventional disulfide bond formation can be detrimental. Normally, cysteines pair with their correct partner residue, but occasionally a cysteine or "free thiol" will bond with a second cysteine in an unexpected way. This unexpected, incorrect bonding of cysteines is referred to as disulfide bond shuffling or scrambling. Usually disulfide bond shuffling occurs as a protein is exposed to stressors such as heat, oxygen radicals, high pH and agitation (Sung et al., 2016; Moritz and Stracke, 2017; Resemann et al., 2018; Dong et al., 2021). Disulfide bond shuffling can negatively impact a therapeutic protein's safety and functionality by increasing its aggregation and degradation, modifying its folding, and/or reducing its target binding (Zhang et al., 2011; Sung et al., 2016; Weinfurtner, 2018). In addition to disulfide bond shuffling, a rare modification called a trisulfide bond can occur in IgGs. A trisulfide bond is described as the insertion of a third sulfur between the cysteines of a disulfide bond. While trisulfide bonds have not yet been shown to affect a protein's safety and functionality, they are indicators of unhealthy cell cultures being used during protein production (Gu et al., 2010; Kshirsagar et al., 2012).

Disulfide bonds are clearly important contributors to the proper functioning of a therapeutic IgG1. When they are shuffled, they can have detrimental effects on the protein's stability and, therefore, potentially its safety and potency as well. Due to this, disulfide bonds are considered to be a subset of a "cysteine form" critical quality attribute (CQA) for biologics. Free thiols, unexpected linkages and modifications such as trisulfides are embedded within this CQA (Alt et al., 2016). The designation of disulfide bonds as CQAs is recognized by regulatory bodies including the FDA, EMA and ICH (Christl, XXXX; Lim, 2018; Guideline on similar biological medicinal products containing biotechnology-derived proteins as active substance: quality issues (revision 1), 2014; Teasdale et al., 2018). Additionally, an ICH guidance states that scrambled/

exchanged disulfide bonds are a common protein degradation mechanism (Teasdale et al., 2018).

It is especially important to quantify disulfide bonds during biosimilar characterization as regulators note that disulfide bonds affect the protein's physicochemical properties and can influence the efficacy of the product. In a comparison between Humira® and a biosimilar, disulfide linkages were listed as CQAs and the authors remarked that mismatched disulfide linkages could impact the conformation and function of the drug (Zhang et al., 2020). Others have conducted similar studies on disulfide bond comparisons across biosimilar and originator biologics to monitor and control changes in disulfide bond number and position. Again, these studies were completed because incorrect disulfide bond linkages can negatively affect the activity, potency, immunogenicity and overall "similarity" of biosimilars (Lu et al., 2020; Shion et al., 2016; Lamanna et al., 2017).

However, despite all of the possible negative side effects of shuffled disulfide bonds, there are more publications on the issue for IgG2 and IgG4 as compared to IgG1. It is likely that there are more publications for IgG2 and IgG4 because disulfide bond shuffling occurs more frequently in them and can sometimes be beneficial to the proper functioning of these proteins. Likewise, disulfide bond shuffling is also frequently discussed with regards to proteins derived from *E.coli* cells because *E.coli* lack an endoplasmic reticulum. For proteins produced in mammalian cell lines, such as the CHO cell lines used to produce rituximab and bevacizumab, the endoplasmic reticulum acts a center for disulfide bond modulation, checking for the proper formation of bonds (Zhang et al., 2011; Cai et al., 2021). Nevertheless, IgG1 therapeutics are not fully immune to disulfide bond shuffling.

Sung et al. (2016) have studied disulfide bond shuffling in bevacizumab under different pH and enzymatic conditions. While this research is useful in determining preferential protein digestion conditions to minimize disulfide shuffling, it does not discuss in great detail how the process of identifying disulfide bonds can be optimized. Similarly, Nie et al. (2022) analyzed two IgG1 proteins to suggest sample preparation improvements to minimize the number of the disulfide bond artifacts. Again, this group focused on sample preparation conditions rather than disulfide bond identification and quantification methods. Dong et al. (2021) studied disulfide bond shuffling in the NIST monoclonal antibody, focusing on generating a mass spectral library of disulfide linkages for the monoclonal antibody rather than discussing method optimization. Mass spectrometry instrumentation companies such as Waters and Shimadzu have also characterized disulfide bonds on biosimilar and originator IgG1 therapeutics to showcase how they can detect any product/batch variability on their latest platforms (Lu et al., 2020; Shion et al., 2016). None of these reports emphasized optimizing a disulfide bond identification and quantitation method, especially for shuffled bonds, for multiple IgG1s. Nor did any group measure the effects that normal vs. prolonged stressed conditions had on disulfide bond shuffling and subsequent IgG1 biosimilar and originator degradation.

To address this lack of knowledge, we have designed a semi-automated, streamlined method for characterizing disulfide bonds on two IgG1s, rituximab and bevacizumab, using an Agilent AssayMAP Bravo liquid handling platform and LC-MS/MS. Performing this method, in conjunction with typical degradation analytical techniques (SEC and SDS-PAGE), allowed us to increase our knowledge of how these two proteins are modified and degraded overtime. This gave us insights into antibody variability as antibodies can act differently, especially when exposed to undesirable conditions (Nowak et al., 2017; Xu et al., 2018; Halley et al., 2020). Additionally, we compared originator and biosimilars versions of the drugs to determine their batch comparability and biosimilarity levels when exposed to various periods of stress. Previous research in our lab and in other labs have shown structural and functional differences between originators and biosimilars after forced degradation, so we were curious as to how our treatment conditions may impact the overall degradation and disulfide shuffling profiles of the rituximab and bevacizumab originators and biosimilars studied here (Pisupati et al., 2017; Dyck et al., 2019; Kang et al., 2019; Shatat et al., 2021).

In sum, our analytical methodology provided us with a way to preliminarily test our hypothesis that as proteins unfold during degradation, exposing buried cysteine residues, they increase their likelihood to form shuffled disulfide bonds. Although we recognize that degradation and disulfide shuffling are not directly proportional, completing these studies helps justify future research and innovation in this space.

MATERIALS AND METHODS

IgG1 Drug Products

The following originator drugs were purchased and stored at 4°C until analysis: Avastin® (Genentech) and Rituxan® (Genentech). The following biosimilar drugs were purchased and stored at 4°C until analysis: Acellbia® (Biocad) and Avegra® (Biocad). The two rituximabs (Rituxan® and Acellbia®) are referred to as Rit throughout the manuscript. The two bevacizumabs (Avastin® and Avegra®) are referred to as Bev throughout the manuscript. Originators are referred to as OR and biosimilars are referred to as BS.

Digestion Reagents

Digestion reagents, including AccuMAP denaturing solution, 10x low pH AccuMAP reaction buffer, N-ethylmaleimide (NEM), Trypsin Platinum and AccuMAP low pH resistant rLys-C were acquired from Promega Corporation. Sample plates for the digestion reaction were purchased through Agilent.

Incubation of Proteins

Rituximab lots were aliquoted in 50 µl increments into 0.5 ml Eppendorf tubes. Bevacizumab lots were diluted from 25 mg/ml down to 10 mg/ml with water to match the aliquot concentration of rituximab. Bevacizumab samples at 10 mg/ml were aliquoted in 50 µl increments into 0.5 ml Eppendorf tubes. For each timepoint (0, 2 and 4 weeks), there were three aliquots per lot

of each mAb. Tubes were placed on an orbital shaker at 240 RPM, incubating at 37°C for up to 4 weeks. 0-week samples were instead left at 4°C and 2-week samples, upon removal from the incubator, were moved to 4°C until the 4-week samples were finished incubating.

LC-MS/MS

3 µl of 10 mg/ml antibody samples (0, 2, 4-week; $N = 3$ per sample type) were added into a 96 well Eppendorf PCR plate and placed on the Agilent AssayMAP Bravo liquid handling platform (referred to herein as the "robot"). A single solution containing Promega's AccuMAP Denaturing Solution, 10x low pH AccuMAP reaction buffer and 200 mM NEM were added in 32 µl aliquots into a 96 well Eppendorf PCR plate and placed on the robot. The addition of 17 µl of this solution into the protein plate, followed by a 30-minute incubation at 37°C, yielded denatured mAbs with blocked free cysteines. Also on the robot were two other plates, one containing an AccuMAP low pH resistant rLys-C pre-digest and a second containing a digestion solution comprised of 10x low pH reaction buffer, AccuMAP low pH resistant rLys-C, Trypsin Platinum and water. The robot added 35 µl of the pre-digest to the sample plate, incubated for 2.5 h at 37°C, then added 81 µl of digestion solution. Then samples were left at 37°C overnight. The pH for the digestion reaction was 5.4. The next day samples were acidified with 20% TFA and prepared for lyophilization prior to reconstitution and MS injection.

The samples were analyzed using an Acquity LC (Waters) interfaced to an Orbitrap Fusion Lumos mass spectrometer (ThermoFisher). The sample peptides were loaded onto a 75 µm analytical trapping column packed with Luna C18 resin (Phenomenex) then eluted at a flow rate of 350 nl/min. For the LC, a 30-minute reverse phase gradient was used. For the MS, a data dependent HCD mode was used with MS at a 60,000 FWHM resolution and MS/MS at a 15,000 FWHM resolution. 3 s cycles were used throughout the duration of the MS and MS/MS run time.

LC-MS/MS Data Processing

Data was processed using the Byos disulfide bond workflow (Protein Metrics, Inc.), accounting for trypsin and Lys-C cleavage. Sequences were searched against existing library data derived from the FASTA file of each protein. The designation of disulfide bond type (i.e. expected vs. shuffled) was based on FASTA protein sequences. By using the FASTA protein sequence and existing databases, the software was able to match the bonds detected from our samples with known, expected disulfide bonds. Label free quantitation was used to create an extracted ion chromatogram (XIC) from the summation of the MS1 isotope area(s) over an elution time range for the peptides resulting after digestion. The XIC is then integrated to determine area under the curve, and this integrated value is compared with other peptides to report the relative abundances of the peptide. The label free quantitation method we used in reporting our data was a single isotope mechanism. This means that the integrated XICs are representative of the monoisotopic, or most intense isotope, peak detected for a peptide. These monoisotope peaks can be compared with the unmodified peptides of the same protein to identify modifications (i.e., disulfide bonds) on the peptide.

For shuffled disulfide bonds, we reported the disulfide bond data as the XIC sum contribution of all shuffled disulfide bonds relative to the total XIC sum of all (shuffled and expected) detected disulfide bonds. For the trisulfide bonds, we repeated the same process looking at the total XIC sum of all trisulfides bonds compared to the XIC sum of all detected disulfide bonds. When analyzing the frequency of specific disulfide bond locations, we normalized the number of times that each bond type was measured relative to the total number of disulfide bonds. All data was analyzed for statistical significance using a 2-way ANOVA, $^{*}p < 0.05$, $^{**}p < 0.01$, $^{***}p < 0.001$, $^{****}p < 0.0001$. Each sample was run in triplicate and results were reported as averages ±standard deviation.

SEC

All samples were diluted down to 1.5 mg/ml with water. 10 µl of 1.5 mg/ml mAb samples were injected onto the column (Acquity UPLC BEH 450 SEC 2.5 µm, 4.6 × 150 mm, Waters) attached to an Acquity UPLC (Waters) and run for 10 min at a flow rate of 0.4 ml/min. The column was maintained at room temperature. The mobile phase used for the isocratic method was 1x phosphate buffered saline, pH 7.4 (Gibco, Fisher Scientific). Antibodies were detected at dual wavelengths of 214 and 280 nm. Data was reported as average % contribution of each peak type (monomer, aggregate and fragment) ± standard deviation. For the aggregate and fragment peaks, our average % contribution data accounted for the summation of areas of all fragment and aggregate peaks, when applicable. % contribution values were based off of the entire area under the curve reported for each sample type. Samples were run in triplicate. A 2-way ANOVA ($^{*}p < 0.05$, $^{**}p < 0.01$, $^{***}p < 0.001$, $^{****}p < 0.0001$) was conducted to compare the statistical significance of BS and OR results for the same protein at the same timepoint.

SDS-PAGE

Representative samples from each antibody at each timepoint (0, 2, and 4 weeks) were run on an Invitrogen NuPAGE 3%–8% Tris-Acetate Gel. Protein samples were diluted from 10 mg/ml down to 0.33 mg/ml with water. To each of the 0.33 mg/ml samples, 5 µl of loading buffer (NuPAGE LDS Sample Buffer 4X, Invitrogen) were added, yielding 1:3 sample:loading buffer, with a final antibody concentration of 0.25 mg/ml 10 µl of the 0.25 mg/ml antibodies were added into individual wells. 15 µl of the ladder (HiMark^{TM} pre-stained protein standard, Invitrogen) were added into well 1. The gel was run under the following conditions: 150 V, 50 mA, 5 W for 1 h on a PowerEase500 electrophoresis system (Invitrogen). Upon completion of the run, the gel was washed 3 times with water, shaking each time for 5 min. Then the gel was washed with SimplyBlue SafeStain (Invitrogen) for 1 h with shaking and with water for 1 h with shaking. The gel was imaged using a FluorChem M Imaging System (Protein Simple).

FIGURE 2 | (A) Schematic of the Byos disulfide bond workflow. **(B)** Highlighted bevacizumab shuffled disulfide bond used for representation of LC-MS/MS data plots. Generated data depicted as a **(C)** MS1 plot; **(D)** MSMS plot; **(E)** Mass error plot; and **(F)** XIC intensity plot.

RESULTS

Disulfide Bond Quantification and Qualification by LC-MS/MS

To assess the extent and location of disulfide bond shuffling in our monoclonal antibodies, we completed a non-reduced protein digestion using a modified version of the robot's in-solution digestion protocol. After identifying the measured bond locations via LC-MS/MS, we used Protein Metrics' Byos software to designate whether each bond was an expected or shuffled disulfide bond (**Figure 2**).

Aside from designating bond type, the Byos disulfide bond workflow flags samples that need to be checked manually due to concerns over threshold, recovery and/or scores (**Figure 2A**). We confirmed that the samples marked as true positives and false positives were indeed properly labeled or changed them to true or false positives based on our manual analysis. We did so by monitoring the MS1 isotope plots, looking for the characteristic isotopic distribution for peptides, and matching it to the charge state (**Figure 2C**). We also confirmed that the MS1 plots were created by using both the most abundant isotopic peak (apex identified within the pink bar across the isotope on the isotope plot panel, **Figure 2C**) and the MSMS scan location in relation to the retention time (shown in the blue XIC intensity plot, **Figure 2F**). Users can select whether an isotope or an averagine calculation is applied for the label-free quantitation of samples. As described in the methods section, we used a single isotope mechanism. If we had chosen the averagine calculation, we would have extrapolated the monoisotopic peak via the averagine distribution, yielding a theoretical monoisotope (Mahon et al., 2012). Finally, we assessed the MSMS and mass error plots (**Figures 2D,E**) and ensured that we were seeing good fragmentation and ion coverage. If samples did not meet these criteria, they were marked as false positive and were not included in our disulfide bond analysis.

From our LC-MS/MS data we determined that the unstressed, 0-week bevacizumab samples trended towards higher shuffled disulfide bond levels initially when compared with rituximab samples. This held true for both the originator and biosimilar samples. As depicted in **Figures 3A,C**, we observed that over the course of 4 weeks under stressed conditions, both rituximab sample types had minor, possibly artificial increases in their average relative percent contribution of shuffled disulfide bonds: 0.24 ± 0.21% to 0.51 ± 0.11% for the originator and 0.27 ± 0.07% to 0.35 ± 0.08% for the biosimilar. The bevacizumab originator sample had a more pronounced increase in the average relative percent contribution of shuffled bonds, from 0.58 ± 0.08% to 1.46 ± 1.10% after the 4-week incubation. The bevacizumab biosimilar samples saw a marginal increase, potentially due to analytical variability, between the 2-week (1.10 ± 0.50%) and 4-week samples (1.25 ± 0.20%). According to our results, the bevacizumab biosimilar 0-week samples had the highest level of shuffled bonds (1.62 ± 0.78%) which is unexpected given other trends, but this can be explained by analytical variability at such low levels as well as the relatively small sample size ($n = 3$). None of the four sample types had any statistical significance in the relative percent contribution of shuffled disulfide bonds measured across all of the timepoints. This suggests that there are not any significant increases in the number of shuffled disulfide bonds over time. However, since minimal disulfide bond shuffling is expected when samples are treated at pH 7 or below (Sung et al., 2016; Dong et al., 2021), as ours were, seeing these general upwards trends in shuffling supports our hypothesis that disulfide shuffling occurs more frequently as a protein is exposed to stress and begins degrading.

In addition to monitoring the relative contribution of the shuffled disulfide bonds, we also monitored the location of the shuffled bonds to see whether they would change over time (**Figure 3B**). We studied this to see how protein residue exposure and unfolding may differ after varying incubation times. We also were curious as to whether the most prominent shuffled disulfide bond locations would be

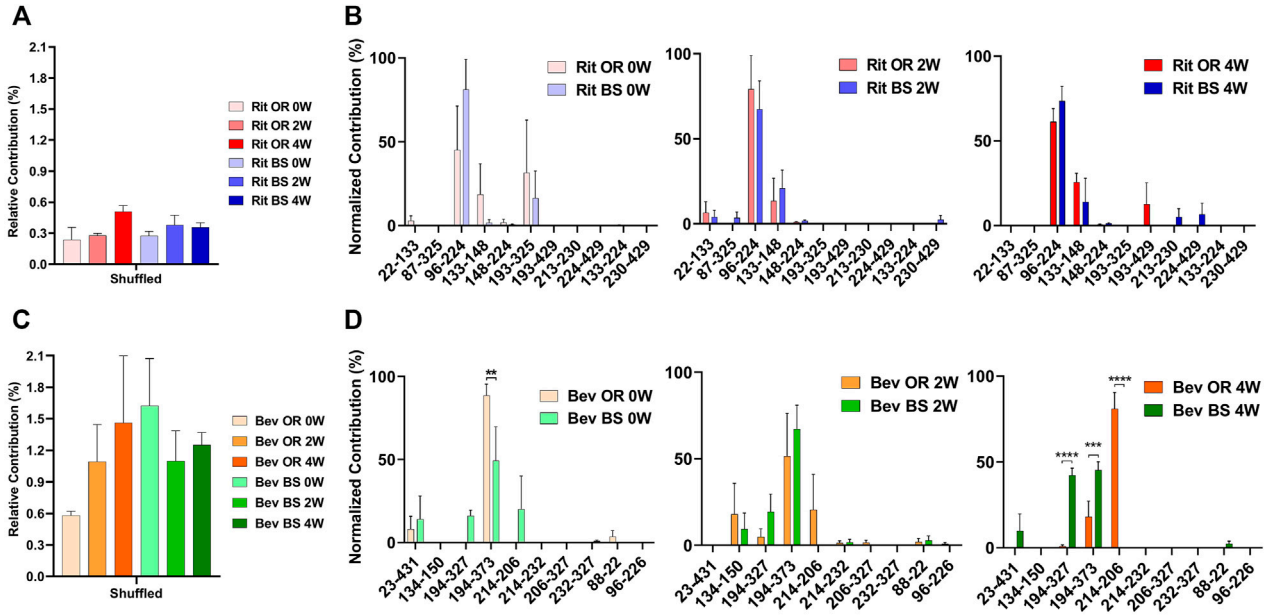

FIGURE 3 | Total shuffled bond contribution relative to the XIC sum of all identified disulfide bonds for **(A)** rituximab originator and biosimilar and **(C)** bevacizumab originator and biosimilar. Prevalence of the shuffled bond locations normalized to the total number of shuffled bonds for **(B)** rituximab originator and biosimilar and **(D)** bevacizumab originator and biosimilar ($N = 3$, mean ± SD, 2-way ANOVA, $^{*}p < 0.05$, $^{**}p < 0.01$, $^{***}p < 0.001$, $^{****}p < 0.0001$).

intrachain or interchain. As mentioned in the introduction, interchain bonds are more susceptible to reduction, incomplete formation and, therefore, shuffling than intrachain bonds. For rituximab originator and biosimilar, the shuffled bond at position Cys96-Cys224 was the most prominent across all of the timepoints. Position 224 is normally involved in an interchain bond, which may be why it was participating in the most prominent shuffled bond. Cys133-Cys148 was also relatively prominent in across all timepoints, but more so in the incubated samples. Cys193-Cys325 had a higher abundance for the unstressed sample. These bonds are all normally involved intrachain binding. There was no statistically significant difference in the bond locations for the originator vs. biosimilar.

A similar story played out for bevacizumab. Its most prominent shuffled bond location was at Cys194-Cys373 for all samples except bevacizumab originator at 4-weeks, whose most prominent location was Cys214-Cys206. Cys194, Cys373 and Cys206 are typically involved in intrachain bonds but Cys214 is typically involved in an interchain bond. Other common shuffled bond locations included Cys194-Cys327 (intrachain) and Cys214-Cys206. Unlike rituximab, there were some significant differences in the bond locations between the originator and biosimilar. For the 4-week samples, Cys214-Cys206 (80.97 ± 16.49) became the most prominent disulfide bond location for the originator while Cys194-Cys327(42.20 ± 7.26) and Cys194-Cys373 (45.39 ± 8.10) were nearly equal in their contribution for the biosimilar (**Figure 3D**). It should be noted that given constraints in our current technology, we were unable to determine whether these disulfide bonds were inter- or intra-antibody.

Detection of Trisulfide Formation by LC-MS/MS

We were also curious about the number of trisulfide bonds present in the samples. By using the disulfide workflow in the Byos software and manually checking the outputs, we were able to identify 5 unique trisulfides in the bevacizumab originator samples and 8 unique trisulfides in the bevacizumab biosimilar samples. The initial average levels of trisulfides, based on XIC values for trisulfides bonds compared to all detected disulfide bonds, were 0.07 ± 0.70% for the originator and 0.19 ± 0.14% for the biosimilar. This level is low but is still worth mentioning because it was significantly greater than rituximab, which had no detectable trisulfides. These were most commonly found at position Cys22-Cys96 in the variable region of the antibody, which is an expected disulfide bond location (**Figure 4B**).

Protein Degradation Measurement by SEC

Since our research hypothesis hinges on the fact that stressed proteins degrade and, in doing so, increase their propensity for disulfide bond shuffling, we wanted to verify that we were indeed seeing protein degradation via more traditional chromatography methods. To track protein degradation over time, we measured the changes in percent aggregates, fragments and monomer for each sample type by size exclusion chromatography (**Figure 5**; **Table 1**). In this study we observed a small increase in aggregates from 0 to 4 weeks for the rituximabs—0.76 ± 0.02% to 1.37 ± 0.08% for the originator and 2.11 ± 0.05% to 2.41 ± 0.11% for the biosimilar. We also measured more fragments than aggregates initially in rituximab, with fragment formation in the rituximab samples slightly increasing over time. The originator fragment

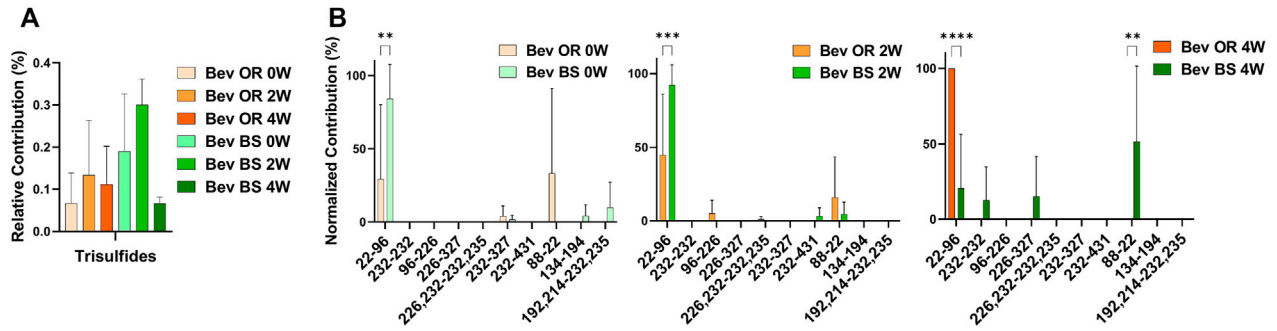

FIGURE 4 | Trisulfide bonds detected for bevacizumab samples by LC-MS/MS. **(A)** Total trisulfide bond contribution relative to the XIC sum of all identified disulfide bonds for bevacizumab OR (0 week—peach, 2 weeks—orange, 4 weeks—red orange) and BS (0 week—teal, 2 weeks—green, 4 weeks—dark green). **(B)** Prevalence of the shuffled bond locations normalized to the total number of shuffled bonds for bevacizumab OR (0 week–peach, 2 weeks—orange, 4 weeks—red orange) and BS (0 week—teal, 2 weeks—green, 4 weeks—dark green) (N = 3, mean ± SD, 2-way ANOVA, *p < 0.05, **p < 0.01, ***p < 0.001, ****p < 0.0001).

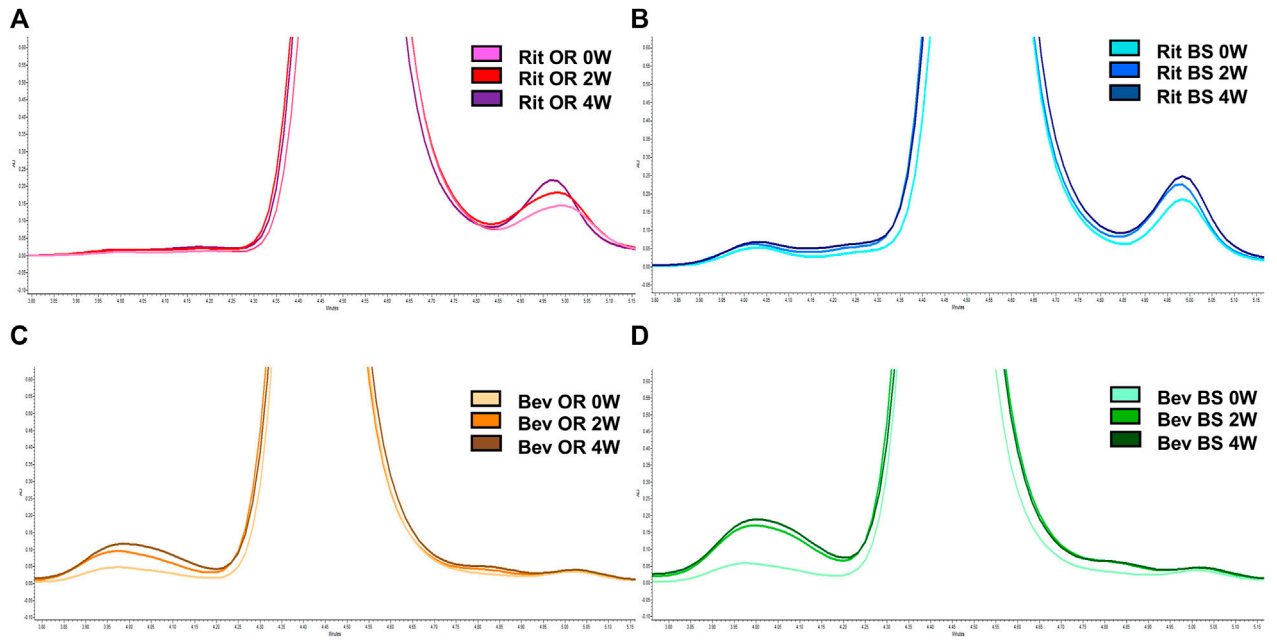

FIGURE 5 | Representative SEC chromatograms at 214 nm for 15 µg of antibody. **(A)** Rituximab OR at 0 (pink), 2 (red) and 4 (purple) weeks; **(B)** Rituximab BS at 0 (light blue), 2 (blue) and 4 (navy) weeks; **(C)** Bevacizumab OR at 0 (peach), 2 (orange), and 4 (brown) weeks; **(D)** Bevacizumab BS at 0 (teal), 2 (green) and 4 (dark green) weeks. Stressed samples were shaking at 240 RPM, incubating at 37°C for 2 or 4 weeks. Chromatograms are zoomed in to depict the increase in aggregates and/or fragments detected in each sample across each timepoint.

contribution increased from 6.76 ± 0.24% (0 weeks) to 7.61 ± 0.24% (4 weeks) and the biosimilar fragment contribution increased from 7.09 ± 0.05% (0 weeks) to 8.02 ± 0.38% (4 weeks). Conversely, we observed that the bevacizumab samples had more degradation in the form of aggregates. From 0 to 4 weeks the relative contribution of aggregates for the bevacizumab originator increased from 2.91 ± 0.39% (0 weeks) to 7.09 ± 0.37% (4 weeks) and for the biosimilar, 3.30 ± 0.06% (0 weeks) to 10.60 ± 0.52% (4 weeks). There were fragments present in the bevacizumab samples, but those stayed relatively steady over time. The originator fragment contribution was 1.76 ± 0.06% at 0 weeks and 1.78 ± 0.01% at 4 weeks. The biosimilar fragment contribution was 1.91 ± 0.07% at 0 weeks and 1.75 ± 0.01% at 4 weeks.

We noticed that there was a greater decrease in the percent monomer for bevacizumab compared to rituximab (**Table 1**). The percent monomer for the rituximab originator changed from 92.48 ± 0.26% to 91.03 ± 0.26% and the biosimilar changed from 90.79% ± 0.01 to 89.57 ± 0.50% over the course of 4 weeks. The percent monomer for the bevacizumab originator changed from 95.34 ± 0.33% to 91.14 ± 0.38% and the biosimilar changed from 94.78 ± 0.02% to 87.65 ± 0.53% over the course of 4 weeks. The

TABLE 1 | SEC data depicted as average % concentration contributions of monomer, aggregate, fragment peaks (*N* = 3, mean ± SD). Aggregates and fragments include summations of multiple peaks, where applicable. Stressed samples were shaking at 240 RPM, incubating at 37°C for 2 or 4 weeks. All samples were diluted to 1.5 mg/ml to load 15 µg of antibody on the column.

	% Monomer	% Aggregates	% Fragments
Rit OR 0w	92.48 ± 0.26	0.76 ± 0.02	6.76 ± 0.24
Rit OR 2w	91.15 ± 1.33	1.37 ± 0.61	7.49 ± 0.72
Rit OR 4w	91.03 ± 0.26	1.37 ± 0.08	7.61 ± 0.24
Rit BS 0w	90.79 ± 0.01	2.11 ± 0.05**	7.09 ± 0.05
Rit BS 2w	90.51 ± 0.63	1.89 ± 0.58	7.60 ± 0.40
Rit BS 4w	89.57 ± 0.50	2.41 ± 0.11*	8.02 ± 0.38
Bev OR 0w	95.34 ± 0.33	2.91 ± 0.39	1.76 ± 0.06
Bev OR 2w	92.43 ± 0.64	5.85 ± 0.78	1.71 ± 0.13
Bev OR 4w	91.14 ± 0.38	7.09 ± 0.37	1.78 ± 0.01
Bev BS 0w	94.78 ± 0.02	3.30 ± 0.06	1.91 ± 0.07
Bev BS 2w	89.88 ± 0.21****	8.38 ± 0.21***	1.74 ± 0.03
Bev BS 4w	87.65 ± 0.53****	10.60 ± 0.52****	1.75 ± 0.01

N = *3, mean ± SD, 2-way ANOVA,* *p < *0.05,* **p < *0.01,* ***p < *0.001,* ****p < *0.0001. *Denotes statistical significance of BS, compared to OR, at same timepoint for the same protein type.*

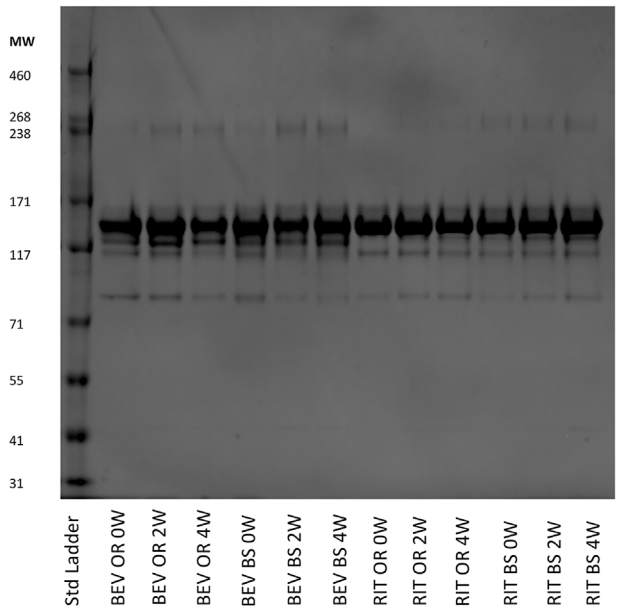

FIGURE 6 | SDS-PAGE of representative 0.25 mg/ml samples for bevacizumab OR and BS and rituximab OR and BS depicting the fragmentation and aggregation of the samples at each timepoint. Samples were incubated 0, 2 or 4 weeks at 37°C, shaking at 240 RPM.

larger reduction in percent monomer confirmed that the bevacizumab degraded more over time relative to rituximab. Given our hypothesis, this would be expected because bevacizumab had higher levels of shuffled disulfide bonds. With regards to biosimilar vs. originator comparisons, we noticed more significant differences between the two for bevacizumab than for rituximab. The biosimilar bevacizumab had a larger formation of aggregates, thus a smaller average % monomer, when compared to the originator bevacizumab.

While aggregation and fragmentation are both degradation products, it is interesting that the two IgG1s had differing degradation profiles. Then again, the two proteins varied in their LC-MS/MS disulfide bond profiles. Bevacizumab had more shuffled bonds appear over time under stressed conditions compared to rituximab. This correlates with the greater percent decrease in monomer for bevacizumab as detected by SEC across the 4-week incubation. We also saw similarities in the LC-MS/MS disulfide bond trends over time between biosimilar and originator drugs for both rituximab and bevacizumab. These trends were further confirmed by the SEC data.

Protein Degradation Characterization by SDS-PAGE

As an orthogonal method to SEC, we completed SDS-PAGE at varying protein concentrations. Shown in **Figure 6** is a gel that contains data from all of the samples across the different stressed and unstressed timepoints. The monomer bands are at ~150 kDa, which matches the molecular weights of intact rituximab (145 kDa) and bevacizumab (149 kDa).

We observed more aggregates in the bevacizumab samples at a molecular weight of ~240 kDa compared to the rituximab samples. The aggregate contributions also increased, yielding darker gel bands, in the stressed samples for both the bevacizumab originator and biosimilar. This matches our SEC data and continues to exemplify how exposure to stressed conditions degrades antibodies. We also saw fragments present at ~115 and ~85 kDa in both proteins. Since we used SDS-PAGE as a qualitative orthogonal method, we did not determine exactly which fragments these bands corresponded to. The fragment bands at 115 kDa were consistent and prominent for rituximab. The fragment bands at 85 kDa increased, becoming darker, across the 0, 2 and 4-week samples for rituximab. The fragment bands at 115 and 85 kDa were similar across the bevacizumab originator. The fragments at 115 and 85 kDa were larger in the 0-week bevacizumab biosimilar sample compared to the 2 and 4-week sample, but this could be accounted for by differences in the protein concentration loaded on the gel. In general, this SDS-PAGE data matches the SEC data. Both protein types also have a variety of other less abundant fragments below the main monomer band at ~150 kDa.

DISCUSSION

By performing the semi-automated mass spectrometry method for characterizing disulfide bonds, as well as the SEC and SDS-PAGE methods, we were able to more seamlessly identify how bevacizumab and rituximab differ in their disulfide bond profile and degradation propensity. Low levels of shuffled disulfide bonds were detected in both antibodies. The total amount of shuffled bonds and changes in shuffled bond levels over time differed between rituximab and bevacizumab. Similarly, both antibodies showed degradation over the

course of the 4-week incubation, but the two varied in how they changed over time.

Rituximab maintained relatively consistent, low levels of disulfide bonds throughout the duration of the stress experiment. At 4 weeks, we detected only 0.51 ± 0.11% shuffled disulfide bonds for the originator and 0.35 ± 0.08% for the biosimilar. Bevacizumab had higher levels of disulfide bond shuffling initially, averaging 0.58 ± 0.08% relative contribution for the originator and 1.62 ± 0.78% relative contribution for the biosimilar. By 4 weeks, the average relative percent contribution of shuffled disulfide bonds reached 1.46 ± 1.10% for the originator and 1.25 ± 0.20% for the biosimilar. We attribute the higher relative percent contribution of shuffled bonds in the 0-week bevacizumab biosimilar sample to analytical variability, especially given the low levels at which we are measuring, and sample size ($N = 3$). We did see an increase in shuffled bond contribution between the 2 and 4-week samples. This suggests that the biosimilar should follow similar disulfide shuffling trends compared to the ones we observed in the originator. We also identified trisulfide bonds in all of the bevacizumab samples but none of the rituximab samples. This perhaps points to poor bevacizumab manufacturing conditions, as trisulfide bonds are indicative of unhealthy cell cultures (Gu et al., 2010; Kshirsagar et al., 2012).

In the end, there was no statistically significant difference across the timepoints and between the originator and biosimilar for each protein. To further confirm this finding, we would need to perform these studies on additional lots of each drug product. However, that does not discount the fact that we were seeing increases in the average relative percent contribution of shuffled bonds, especially in the bevacizumab samples. After all, under neutral or slightly acidic conditions, disulfide bond shuffling should be minimal (Sung et al., 2016; Dong et al., 2021). Therefore, increases in shuffled bond contributions at low levels can still support our hypothesis—as a protein unfolds during degradation, buried cysteine residues are exposed and can participate in disulfide bond shuffling. Additionally, the higher levels of shuffled disulfide bonds present in the bevacizumab samples compared with the rituximab samples suggest that bevacizumab is overall less stable, thus more prone to degradation.

While the disulfide bond data indicated that bevacizumab has lower stability and, subsequently, a greater chance for degradation to occur, the SEC and SDS-PAGE data told their own version of the story. As depicted in **Figures 5**, **6** and **Table 1**, bevacizumab was more likely to aggregate than fragment when exposed to stress while the opposite was true for rituximab. In comparing biosimilars with their originators, we generally saw similar trends. We detected more significant differences between the bevacizumab biosimilar and originator with regards degradation overtime when compared with rituximab. According to our SEC data, the biosimilar bevacizumab had a greater increase in the % contribution of aggregates after the 2- and 4-week incubations. This also translated to an average lower % monomer for the biosimilar bevacizumab compared with the originator bevacizumab. It is not yet understood exactly why we are seeing these differences in degradation patterns, both between biosimilars and originators and across different IgG1s, but the variability in degradation is interesting given that all of the studied proteins are IgG1s. It should be noted, though, that to further bolster our findings and ensure that intra- and inter-batch variability are not dictating our results and theorized trends, we need to perform these same studies on more than one lot per originator and biosimilar. Nevertheless, these initial studies are important for proof of concept and give us an idea of what trends we may expect. They also exemplify the uniqueness and complexity of protein therapeutics, as well as documents how not all IgG1s can be expected to act similarly.

Although bevacizumab and rituximab differed in how they responded to stress conditions, the broad applicability of our methods made it possible to run samples from both proteins in tandem. The disulfide bond LC-MS/MS method was instrumental in showcasing how we can more efficiently characterize unexpected disulfide bonds in monoclonal antibodies. The established SEC and SDS-PAGE methods were critical in demonstrating the variability in degradation pathways across IgG1 therapeutics. By combining these methods, we were able paint a full picture on the stability of IgG1 therapeutics exposed to normal and stressed conditions.

In conclusion, our use of a semi-automated, streamlined approach for identifying, characterizing and quantifying disulfide bonds on rituximab and bevacizumab has allowed us to more fully understand differences in the aggregation/degradation propensity between drugs of the same IgG subclass. Many published studies have characterized aggregation/degradation profiles of these and other IgG1 therapeutics, but few have focused on providing, improving and/or optimizing methods by which to measure disulfide bond shuffling. Based on our data, disulfide bond shuffling does occur in IgG1s, even when they are unstressed. As the proteins are exposed to prolonged heat and shaking, a greater level of shuffling occurs. Similarly, we noticed that disulfide bond shuffling trends matched those of protein degradation, as measured by SEC and SDS-PAGE. This bolsters our hypothesis that as proteins unfold during degradation, exposing buried cysteine residues, they increase their likelihood to form shuffled disulfide bonds. While we recognize that correlation is not causation and other factors could be influencing IgG1 degradation propensity, this initial study justifies our further exploration into how disulfide bond shuffling and protein degradation may be linked.

The implementation of our semi-automated LC-MS/MS method, SEC and SDS-PAGE during antibody development can be useful to a number of stakeholders including the pharmaceutical industry and regulatory agencies. By identifying shuffled disulfide bonds upfront, companies can save themselves the inevitable headache that will occur if a product fails to meet its designated specifications. This would be especially beneficial to the pharmaceutical industry as disulfide bond characterization is a CQA that is monitored during the development of new therapeutics and biosimilars. Companies can also reduce project related time, money and operator variability by implementing robotics and established MS data processing workflows in their protein characterization. With regards to

regulatory agencies, our experimental workflow can become a standardized way to characterize expected and shuffled disulfide bonds within a protein therapeutic. Providing a standardized disulfide bond identification method in product specific guidances would help streamline the approval of BLAs. In sum, our methodology for identifying, quantifying and characterizing disulfide bonds and protein degradation profiles provides the groundwork necessary to further standardize such methods across the pharmaceutical industry and regulatory bodies.

DATA AVAILABILITY STATEMENT

The raw data supporting the conclusion of this article will be made available by the authors, without undue reservation.

AUTHOR CONTRIBUTIONS

JC, AB, and AS proposed the research topic and conceptualized the research studies. AB and AS designed the experiments. AB performed preliminary studies to show proof of concept. JC and PK conducted optimized versions of the preliminary studies for digestion sample preparation for LC-MS/MS, SEC and SDS-PAGE. SS designed digestion parameters using Promega materials and acted as a reference for questions regarding non-reduced digestion. MF performed LC-MS/MS analysis, generated raw data and provided instrumental method information. JC, LV, and SJS adapted Promega workflows to identify, quantify, and qualify disulfide bonds. JC wrote the draft manuscript. LV, SJS, AS, and AB edited the manuscript.

FUNDING

JC was supported by the Cellular Biotechnology Training Program under the National Institutes of Health, USA award number (NIH T32GM008353).

ACKNOWLEDGMENTS

We would like to acknowledge Protein Metrics, MS Bioworks and members of the AS lab for allowing us to design **Figure 2** based off of a Byos disulfide bond workflow application note.

REFERENCES

Alt, N., Zhang, T. Y., Motchnik, P., Taticek, R., Quarmby, V., Schlothauer, T., et al. (2016). Determination of Critical Quality Attributes for Monoclonal Antibodies Using Quality by Design Principles. *Biologicals.* 44, 291–305. doi:10.1016/j.biologicals.2016.06.005

Cai, C. X., Schneck, N. A., Cozine, T., Ivleva, V. B., Ragheb, D., Gollapudi, D., et al. (2021). Investigation of Cysteine Modifications in Recombinant Protein Tetanus Toxoid Heavy Chain Fragment C. *J. Am. Soc. Mass. Spectrom.* 32, 1837–1840. doi:10.1021/JASMS.1C00075/SUPPL_FILE/JS1C00075_SI_001.PDF

Christl, L. (XXXX). *Overview of the Regulatory Pathway and FDA's Guidance for the Development and Approval of Biosimillar Products in the US*. Silver Springs, MD: FDA

Cordoba, A. J., Shyong, B.-J., Breen, D., and Harris, R. J. (2005). Non-enzymatic Hinge Region Fragmentation of Antibodies in Solution. *J. Chromatogr. B.* 818, 115–121. doi:10.1016/j.jchromb.2004.12.033

Dean, A. Q., Luo, S., Twomey, J. D., and Zhang, B. (2021). Targeting Cancer with Antibody-Drug Conjugates: Promises and Challenges. *mAbs.* 13, 1951427-1–1951427-23. doi:10.1080/19420862.2021.1951427

Dong, Q., Yan, X., Liang, Y., Markey, S. P., Sheetlin, S. L., Remoroza, C. A., et al. (2021). Comprehensive Analysis of Tryptic Peptides Arising from Disulfide Linkages in NISTmAb and Their Use for Developing a Mass Spectral Library. *J. Proteome Res.* 20, 1612–1629. doi:10.1021/ACS.JPROTEOME.0C00823/SUPPL_FILE/PR0C00823_SI_001.XLSX

Dyck, Y. F. K., Rehm, D., Joseph, J. F., Winkler, K., Sandig, V., Jabs, W., et al. (2019). Forced Degradation Testing as Complementary Tool for Biosimilarity Assessment. *Bioengineering.* 6, 62. doi:10.3390/bioengineering6030062

Goetze, A. M., Liu, Y. D., Zhang, Z., Shah, B., Lee, E., Bondarenko, P. V., et al. (2011). High-mannose Glycans on the Fc Region of Therapeutic IgG Antibodies Increase Serum Clearance in Humans. *Glycobiology.* 21, 949–959. doi:10.1093/glycob/cwr027

Gu, S., Wen, D., Weinreb, P. H., Sun, Y., Zhang, L., Foley, S. F., et al. (2010). Characterization of Trisulfide Modification in Antibodies. *Anal. Biochem.* 400, 89–98. doi:10.1016/j.ab.2010.01.019

Guideline on similar biological medicinal products containing biotechnology-derived proteins as active substance: quality issues (revision 1) (2014). Eur. Med. *Agency*. London, 1-9. Available at: www.ema.europa.eu (Accessed December 10, 2021).

Halley, J., Chou, Y. R., Cicchino, C., Huang, M., Sharma, V., Tan, N. C., et al. (2020). An Industry Perspective on Forced Degradation Studies of Biopharmaceuticals: Survey Outcome and Recommendations. *J. Pharm. Sci.* 109, 6–21. doi:10.1016/j.xphs.2019.09.018

Hmiel, L. K., Brorson, K. A., and Boyne, M. T. (2015). Post-translational Structural Modifications of Immunoglobulin G and Their Effect on Biological Activity. *Anal. Bioanal. Chem.* 407, 79–94. doi:10.1007/s00216-014-8108-x

Kanda, Y., Yamada, T., Mori, K., Okazaki, A., Inoue, M., Kitajima-Miyama, K., et al. (2007). Comparison of Biological Activity Among Nonfucosylated Therapeutic IgG1 Antibodies with Three Different N-Linked Fc Oligosaccharides: the High-Mannose, Hybrid, and Complex Types. *Glycobiology.* 17, 104–118. doi:10.1093/GLYCOB/CWL057

Kang, J., Halseth, T., Vallejo, D., Najafabadi, Z. I., Sen, K. I., Ford, M., et al. (2019). Assessment of Biosimilarity under Native and Heat-Stressed Conditions: Rituximab, Bevacizumab, and Trastuzumab Originators and Biosimilars. *Anal. Bioanal. Chem.* 412 (412), 763–775. doi:10.1007/S00216-019-02298-9

Kshirsagar, R., McElearney, K., Gilbert, A., Sinacore, M., and Ryll, T. (2012). Controlling Trisulfide Modification in Recombinant Monoclonal Antibody Produced in Fed-Batch Cell Culture. *Biotechnol. Bioeng.* 109, 2523–2532. doi:10.1002/BIT.24511

Lakbub, J. C., Shipman, J. T., and Desaire, H. (2018). Recent Mass Spectrometry-Based Techniques and Considerations for Disulfide Bond Characterization in Proteins. *Anal. Bioanal. Chem.* 410, 2467–2484. doi:10.1007/S00216-017-0772-1

Lamanna, W. C., Mayer, R. E., Rupprechter, A., Fuchs, M., Higel, F., Fritsch, C., et al. (2017). The Structure-Function Relationship of Disulfide Bonds in Etanercept. *Sci. Rep.* 7, 1–8. doi:10.1038/s41598-017-04320-5

Lim, S. (2018). *Overview of the Regulatory Framework and FDA's Guidance for the Development and Approval of Biosimilar Products in the US*. Silver Springs, MD: FDA.

Liu, H., Chumsae, C., Gaza-Bulseco, G., Hurkmans, K., and Radziejewski, C. H. (2010). Ranking the Susceptibility of Disulfide Bonds in Human IgG1 Antibodies by Reduction, Differential Alkylation, and LC–MS Analysis. *Anal. Chem.* 82, 5219–5226. doi:10.1021/AC100575N/SUPPL_FILE/AC100575N_SI_002.PDF

Liu, H., and May, K. (2012). Disulfide Bond Structures of IgG Molecules. *MAbs* 4, 17–23. doi:10.4161/MABS.4.1.18347

Liu-Shin, L., Fung, A., Malhotra, A., and Ratnaswamy, G. (2018). Influence of Disulfide Bond Isoforms on Drug Conjugation Sites in Cysteine-Linked IgG2 Antibody-Drug Conjugates. *MAbs* 10, 583–595. doi:10.1080/19420862.2018.1440165/SUPPL_FILE/KMAB_A_1440165_SM5845.ZIP

Lu, Y., Seng Wong, C., Xing, J., and Zhan, Z. (2020). *Characterization of Disulfide Bonds in Bevacizumab Biosimilar Using A Q-TOF Mass Spectrometer*. Singapore: National University of Singapore.

Mahon, D., Sen, K. I., Kil, Y. J., and Mehndiratta, P. (2012). *Isotope Selection in Label-free Quantitation and its Effects in Biopharmaceutical Characterization*Summit, NJ and Cupertino, CA: Celgene Corp. and Protein Metrics Inc.

Matsumiya, S., Yamaguchi, Y., Nagano, H., Otaki, S., Satoh, M., Shitara, K., et al. (2007). Structural Comparison of Fucosylated and Nonfucosylated Fc Fragments of Human Immunoglobulin G1. *J. Mol. Biol.* 368, 767–779. doi:10.1016/j.jmb.2007.02.034

Moritz, B., and Stracke, J. O. (2017). Assessment of Disulfide and Hinge Modifications in Monoclonal Antibodies. *Electrophoresis.* 38, 769–785. doi:10.1002/elps.201600425

Nie, S., Greer, T., Huang, X., Zheng, X., and Li, N. (2022). Development of a Simple Non-reduced Peptide Mapping Method that Prevents Disulfide Scrambling of mAbs without Affecting Tryptic Enzyme Activity. *J. Pharm. Biomed. Anal.* 209, 114541. doi:10.1016/j.jpba.2021.114541

Nowak, C., K. Cheung, J., M. Dellatore, S., Katiyar, A., Bhat, R., Sun, J., et al. (2017). Forced Degradation of Recombinant Monoclonal Antibodies: A Practical Guide. *MAbs.* 9, 1217–1230. doi:10.1080/19420862.2017.1368602

Ouellette, D., Alessandri, L., Chin, A., Grinnell, C., Tarcsa, E., Radziejewski, C., et al. (2010). Studies in Serum Support Rapid Formation of Disulfide Bond between Unpaired Cysteine Residues in the VH Domain of an Immunoglobulin G1 Molecule. *Anal. Biochem.* 397, 37–47. doi:10.1016/j.ab.2009.09.027

Pereira, N. A., Chan, K. F., Lin, P. C., and Song, Z. (2018). The "Less-Is-More" in Therapeutic Antibodies: Afucosylated Anti-cancer Antibodies with Enhanced Antibody-dependent Cellular Cytotoxicity. *MAbs.* 10, 693–711. doi:10.1080/19420862.2018.1466767

Pisupati, K., Tian, Y., Okbazghi, S., Benet, A., Ackermann, R., Ford, M., et al. (2017). A Multidimensional Analytical Comparison of Remicade and the Biosimilar Remsima. *Anal. Chem.* 89, 4838–4846. doi:10.1021/acs.analchem.6b04436

Resemann, A., Liu-Shin, L., Tremintin, G., Malhotra, A., Fung, A., Wang, F., et al. (2018). Rapid, Automated Characterization of Disulfide Bond Scrambling and IgG2 Isoform Determination. *MAbs.* 10, 1200–1213. doi:10.1080/19420862.2018.1512328

Shatat, S. M., Al-Ghobashy, M. A., Fathalla, F. A., Abbas, S. S., and Eltanany, B. M. (2021). Coupling of Trastuzumab Chromatographic Profiling with Machine Learning Tools: A Complementary Approach for Biosimilarity and Stability Assessment. *J. Chromatogr. B.* 1184, 122976. doi:10.1016/j.jchromb.2021.122976

Shion, H., Du, M., and Yu, Y. Q. (2016). Automated Disulfide Bond Mapping in Comparing Innovator and Biosimilar mAbs Using UNIFI Software | Waters. Available at: https://www.waters.com/nextgen/en/library/application-notes/2016/automated-disulfide-bond-mapping-comparing-innovator-biosimilar-mabs.html (Accessed December 10, 2021).

Strohl, W. R., and Strohl, L. M. (2012). *"Development Issues: Antibody Stability, Developability, Immunogenicity, and Comparability," in Therapeutic Antibody Engineering*. Cambridge: Woodhead Publishing, 377–595. doi:10.1533/9781908818096.377

Sung, W.-C., Chang, C.-W., Huang, S.-Y., Wei, T.-Y., Huang, Y.-L., Lin, Y.-H., et al. (2016). Evaluation of Disulfide Scrambling during the Enzymatic Digestion of Bevacizumab at Various pH Values Using Mass Spectrometry. *Biochim. Biophys. Acta (Bba) - Proteins Proteomics.* 1864, 1188–1194. doi:10.1016/j.bbapap.2016.05.011

A. Teasdale, D. Elder, and R. W. Nims. (Editor) (2018). "ICH Q5C Stability Testing of Biotechnological/Biological Products," in *ICH Quality Guidelines: An Implementation Guide*. (Hoboken: John Wiley & Sons Inc.), ,345–374.

Thomann, M., Reckermann, K., Reusch, D., Prasser, J., and Tejada, M. L. (2016). Fc-galactosylation Modulates Antibody-dependent Cellular Cytotoxicity of Therapeutic Antibodies. *Mol. Immunol.* 73, 69–75. doi:10.1016/j.molimm.2016.03.002

Weinfurtner, D. (2018). "CHAPTER 1.4. Analysis of Disulfide Bond Formation in Therapeutic Proteins," in *Oxidative Folding of Proteins: Basic Principles, Cellular Regulation and Engineering*. Cambridge: Royal Society of Chemistry, 81, 98. doi:10.1039/9781788013253-00081

Xu, Y., Wang, D., Mason, B., Rossomando, T., Li, N., Liu, D., et al. (2018). Structure, Heterogeneity and Developability Assessment of Therapeutic Antibodies. *MAbs.* 11, 239–264. doi:10.1080/19420862.2018.1553476

Zhang, E., Xie, L., Qin, P., Lu, L., Xu, Y., Gao, W., et al. (2020). Quality by Design-Based Assessment for Analytical Similarity of Adalimumab Biosimilar HLX03 to Humira®. *AAPS J.* 22, 69–14. doi:10.1208/S12248-020-00454-Z/FIGURES/7

Zhang, L., Chou, C. P., and Moo-Young, M. (2011). Disulfide Bond Formation and its Impact on the Biological Activity and Stability of Recombinant Therapeutic Proteins Produced by *Escherichia coli* Expression System. *Biotechnol. Adv.* 29, 923–929. doi:10.1016/j.biotechadv.2011.07.013

Zheng, K., Bantog, C., and Bayer, R. (2011). The Impact of Glycosylation on Monoclonal Antibody Conformation and Stability. *MAbs.* 3, 568–576. doi:10.4161/MABS.3.6.17922

Conflict of Interest: Author MF was employed by the company MS Bioworks. Authors LV and SJS were employed by the company Protein Metrics. Author SS was employed by the company Promega Corporation.

The remaining authors declare that the research was conducted in the absence of any commercial or financial relationships that could be construed as a potential conflict of interest.

Publisher's Note: All claims expressed in this article are solely those of the authors and do not necessarily represent those of their affiliated organizations, or those of the publisher, the editors and the reviewers. Any product that may be evaluated in this article, or claim that may be made by its manufacturer, is not guaranteed or endorsed by the publisher.

frontiers | Frontiers in Bioengineering and Biotechnology

ORIGINAL RESEARCH
published: 05 April 2022
doi: 10.3389/fbioe.2022.753481

Identification of Recombinant Chimpanzee Adenovirus C68 Degradation Products Detected by AEX-HPLC

Thomas W. Powers[1], *Elise K. Mullins*[1], *Kun Zhang*[1], *Joseph J. Binder*[2], *Olga Friese*[1], *Herbert A. Runnels*[1] *and Lawrence C. Thompson*[1]*

[1]Analytical Research and Development, Biotherapeutic Pharmaceutical Sciences, Pfizer Inc., Chesterfield, MO, United States, [2]Cancer Vaccines and Immunotherapeutics, Pfizer Inc., San Diego, CA, United States

Physicochemical tests represent important tools for the analytical control strategy of biotherapeutics. For adenoviral modalities, anion-exchange high performance liquid chromatography (AEX-HPLC) represents an important methodology, as it is able to simultaneously provide information on viral particle concentration, product purity and surface charge in a high-throughput manner. During product development of an adenoviral-based therapeutic, an accelerated stability study was performed and showed changes in each of the AEX-HPLC reportable attributes. These changes also correlated with a decrease in product infectivity prompting a detailed characterization of the impurity and mechanism of the surface charge change. Characterization experiments identified the impurity to be free hexon trimer, suggesting that capsid degradation could be contributing to both the impurity and reduced particle concentration. Additional mass spectrometry characterization identified deamidation of specific hexon residues to be associated with the external surface charge modification observed upon thermal stress conditions. To demonstrate a causal relationship between deamidation and surface charge changes observed by AEX-HPLC, site-directed mutagenesis experiments were performed. Through this effort, it was concluded that deamidation of asparagine 414 was responsible for the surface charge alteration observed in the AEX-HPLC profile but was not associated with the reduction in infectivity. Overall, this manuscript details critical characterization efforts conducted to enable understanding of a pivotal physicochemical test for adenoviral based therapeutics.

Keywords: adenovirus, AEX-HPLC, deamidation, hexon, mass spectometry, kinetics, non-human primate

OPEN ACCESS

Edited by:
Christopher Mark Smales, University of Kent, United Kingdom

Reviewed by:
John Liddell, Centre for Process Innovation, United Kingdom
Sofia Baptista Carvalho, Instituto de Biologia e Tecnologia Experimental, Portugal
Anurag S. Rathore, Indian Institute of Technology Delhi, India

***Correspondence:**
Lawrence C. Thompson
Lawrence.Thompson@pfizer.com

Specialty section:
This article was submitted to Bioprocess Engineering, a section of the journal Frontiers in Bioengineering and Biotechnology

Received: *04 August 2021*
Accepted: *09 March 2022*
Published: *05 April 2022*

Citation:
Powers TW, Mullins EK, Zhang K, Binder JJ, Friese O, Runnels HA and Thompson LC (2022) Identification of Recombinant Chimpanzee Adenovirus C68 Degradation Products Detected by AEX-HPLC. Front. Bioeng. Biotechnol. 10:753481. doi: 10.3389/fbioe.2022.753481

INTRODUCTION

Non-human primate adenoviral vectors are attractive for use in human vaccine and immuno-oncological applications as they maintain many of the attributes that make adenovirus appealing as a therapeutic vector while having reduced host pre-existing antivector immunity (Capone et al., 2013; Cheng et al., 2015; Zhang et al., 2017; Zhao et al., 2018; Mullins et al., 2021). Recent successes using these constructs include modified chimpanzee adenovirus type 3–vectored ebolavirus vaccine (cAd3-EBO) (Stanley et al., 2014; Ledgerwood et al., 2017) and replication-deficient simian adenoviral vectored vaccine ChAdOx1 nCoV-19 against SARS-CoV-2 (Folegatti et al., 2020; Ewer et al., 2021; Putter, 2021).

As with any therapeutic product, the analytical control strategy exists for the purpose of ensuring product safety and efficacy of these vectors. The analytical control strategy must include methods that demonstrate product quality throughout manufacturing, shipping, and storage. Cell-based bioassays are an important component of the analytical control strategy, as they provide *In vitro* measurements of critical quality attributes like infectivity, protein expression/function, etc. (Ich, 1999; FDA, 2011; CHMP, 2019; FDA, 2020). While these assays are vital to evaluate overall potency, everyday use of these bioassays is resource and reagent intensive. Therefore, it is desirable to have higher throughput physicochemical techniques as a part of the analytical control strategy that give an analogous assessment of product quality but can be run routinely during process development, formulation development, and on fully purified products. For adenoviruses, these options vary but include many well-known techniques such as AEX-HPLC (Blanche et al., 2000; Klyushnichenko et al., 2001; Kuhn et al., 2007; Whitfield et al., 2009; Kramberger et al., 2015), RP-HPLC (Lehmberg et al., 1999; Blanche et al., 2001; Vellekamp et al., 2001; Chelius et al., 2002; Takahashi et al., 2006; Benevento et al., 2014; Pérez-Berná et al., 2014; van Tricht et al., 2018), capillary electrophoresis (CE) (van Tricht et al., 2017), analytical ultracentrifugation (AUC) (Berkowitz and Philo, 2007; Berkowitz, 2008; Yang et al., 2008) and differential centrifugal sedimentation (DCS) (Bondoc and Fitzpatrick, 1998; Shih et al., 2010). AEX-HPLC is the most widely applied of these for in-process, release and stability testing, as AEX-HPLC can simultaneously determine viral particle concentration, product purity and surface charge.

A subset of the methods in the analytical control strategy should be capable of detecting product deterioration over time, which classifies the methods as stability-indicating assays. Performing accelerated stability studies, in which materials are subjected to elevated temperatures compared to recommended storage conditions, enables a more rapid product degradation and is often used to determine which methods are stability indicating, including both physiochemical assays and bioassays. Correlating the changes between physiochemical assays and bioassays provides information about which quality attributes may play important functional roles. In the current study, two chimpanzee adenovirus C68 constructs (heretofore known as AdC68) (Farina et al., 2001; Cohen et al., 2002; Xiang et al., 2002; Tatsis et al., 2006) were subjected to an accelerated stability study and the resulting materials were characterized with analytical assays in place to support the overall control strategy. The data revealed several changes in the AEX-HPLC profile, which correlated with overall decreases in product infectivity. Specifically, AEX-HPLC results demonstrated changes in viral particle concentration, product purity and surface charge. While these results demonstrated that AEX-HPLC was a powerful stability indicating tool, the method is unable to characterize specific attributes that change on the adenovirus quaternary structure and/or the underlying adenovirus DNA and protein components.

In an effort to better understand the attributes that changed in the AEX-HPLC data, and to further understand if these attributes were responsible for the observed decrease in infectivity, we present a characterization strategy for the identification of adenovirus molecular modifications and product related impurities. This strategy utilizes the power of mass spectrometry to identify changes in quality attributes at the molecular level and reveal degradation hotspots. The implementation of these approaches was supplemented by analytical fraction collection, enabling a targeted assessment of AEX-HPLC peaks. As chemical modifications were identified, the locations of the attributes were modeled in-silico. Furthermore, site-specific mutagenesis was performed to mimic the modifications and assess the impact of the attributes both on the AEX-HPLC assay and on the product infectivity. The study documented herein provides an in-depth evaluation of attributes and modifications that are responsible for changes in the AEX-HPLC assay and enhances knowledge around quality attributes for adenoviral vectors.

MATERIALS AND METHODS

Materials and Formulation

Two AdC68 constructs were manufactured within Pfizer. AdC68 material was formulated in A195 buffer (Xiang et al., 2002): 10 mM Tris, 75 mM NaCl, 5% w/v sucrose, 0.02% (w/v) 80 polysorbate 80, 1.0mM MgCl2, 0.1 mM EDTA, 0.5% (v/v) ethanol, 10 mM L-histidine, pH 7.4 (Mullins et al., 2021).

Accelerate Stability of Adenovirus Material

An accelerated stability study was performed in which adenovirus material was incubated at 26.5°C for up to 12 weeks. Throughout product development, these conditions were demonstrated to yield significant product degradation. A bulk AdC68 material was incubated at 26.5°C, and incremental time points were pulled from the bulk material and frozen at -80°C prior to analysis.

Determination of the Adenoviral Infectivity by a Cell-Based Adenovirus Titer Immunoassay

An adenoviral infectivity method was developed to monitor infectivity. For this assay, cultures of HEK293 cells (Cell biolabs, Catalog No. AD-100) were grown in a flask containing Dulbecco's modified medium (Gibco, Catalog No. 11995) supplemented with 10% Heat Inactivated Fetal Bovine Serum (Gibco, Catalog No. 10082) and 1x Penicillin-Streptomycin (Gibco, Catalog No. 15140) in a 5% CO_2 atmosphere at 37°C. HEK293 cells were seeded into a 24-well flat bottom cell culture plate at 2.2E5 cells/well and then incubated in a 37°C, 5% CO_2 incubator. A dilution series of adenovirus sample was prepared in cell culture medium. The dilution series was then added to the wells of the cell assay plate about 1 h after cell seeding. The assay plate was then incubated for 2 days. The cells were then fixed with cold methanol at -20°C and then stained with a polyclonal antibody against adenovirus Hexon proteins, which is expressed upon infection of the cells with adenovirus sample. Positive stained cells in assay wells were counted under microscope fitted with a ×10 lens. Cells per view field were recorded and used to calculate the adenovirus sample infectivity, reported as infectious units (IFU)/mL as well as viral particles (vp)/IFU.

AEX-HPLC

Analytical AEX-HPLC

The analytical AEX-HPLC method was used to determine product purity, virus particle concentration, and surface charge through the measurement of relative retention time. The analytical AEX-HPLC method used a high affinity, anion exchange column (GE Healthcare, Resource Q, 1 ml 15 μm, 6.4 × 30 mm, Part No. 17-1177-01) to separate the AdC68 and impurities. AdC68 samples were diluted with formulation buffer and analyzed against a standard curve that ran from 0.25E11 VP/mL to 3.0E11 VP/mL. Elution of the bound molecules was achieved using a salt gradient with a flow rate of 1.0 ml/min over the course of 30 min. The mobile phases consisted of 50 mM Tris, 0.05% Tween 80, 0.1 mM EDTA pH 8.0, with the addition of 1 M NaCl to mobile phase B. The gradient ranged from 10 to 100 %B. The AEX-HPLC was coupled to a fluorescence detector which was set to collect data with an excitation of 280 nm and emission of 320 nm.

Data were processed to monitor peak areas and relative retention times. Relative purity was determined by comparing area counts of the eluting peaks and was reported as a percent of the total area for all peaks. Particle concentration was achieved by correlation of the unknowns to a standard curve. Relative retention time (acidic shift) were measured by comparing the elution time of the sample to the averaged elution time of the standard curve samples. The method was qualified and determined to be adequately precise for particle concentration, purity and relative retention time.

Preparative AEX-HPLC Method

For in-depth characterization, fraction collection was utilized to isolate the impurity peak from the main peak in the AEX-HPLC profile. A CIMac Adeno 0.1 ml analytical column (Sartorius Part #110.8502-2) was set up on an Akta Explorer FPLC system. This column was utilized in order to achieve complete baseline separation of the impurity peak and main peak in a preparative scale method. An increasing salt gradient within a Tris buffer system was applied to elute the adenovirus fractions from the column. The mobile phases consisted of 50 mM Tris, pH 7.5 with the addition of 2 M NaCl to mobile phase B. The gradient ranged from 7.5 to 18 %B. Fractions were collected from bulk adenovirus material that had previously been degraded at 26.5°C for 12 weeks. For the fraction collection experiments, a series of 500 μL injections were made across the column with several fractions taken throughout the run. The column was flushed and then this was repeated several times to yield enough fractionated material for additional experiments.

Characterization of Adenoviral Capsid by Mass Spectrometry

Characterization of Intact Capsid Proteins by RP-HPLC/MS

The denatured capsid proteins were chromatographically separated on a Phenomenex Jupiter C4, 5 μm, 2 × 150 mm, 300Å analytical column (Part #00F-4167-B0) using an Agilent 1200 HPLC system similar to what was described previously (Vellekamp et al., 2001; Mullins et al., 2021) with the following alterations. The column was held at a temperature of 5 0°C with a gradient consisting of 20–100% acetonitrile with trifluoroacetic acid (TFA) over 90 min with a flow rate of 0.2 ml/min. Prior to analysis, samples were denatured with acetonitrile and TFA to yield a final mixture of 20% ACN, 0.1% TFA. For each sample, 4.4E10 viral particles of adenovirus were loaded onto the column.

Intact mass spectra were acquired in two ways. The Agilent 1200 HPLC was coupled to a Thermo Orbitrap EMR mass spectrometer. Samples were analyzed in positive-ion mode with a detection range of 400–6,000 m/z. Data were collected with a resolution of 17,500 and an isCID of 50 eV. Additionally, a Bruker maXis II QTOF mass spectrometer connected to a Waters HClass UHPLC was utilized. Samples were analyzed in positive-ion mode with a detection range of 400–4,000 m/*z*. The instrument was calibrated with the Agilent Tune Mix for ESI-QTOF MS instruments. The capillary voltage was 4,000, isCID was 150 eV, collision energy was 15 eV, and the transfer time was set to 130 μs? Thermo data were processed using PMI (Protein Metrics) Intact deconvolution software and Bruker data were processed with Bruker DataAnalysis software.

Characterization of Intact Capsid Proteins by Native SEC-HPLC/MS

Fractions collected by AEX-HPLC were analyzed by native SEC-HPLC/MS. AEX-HPLC fractions were collected as described in *Preparative AEX-HPLC Method* Section. The impurity fraction was injected onto a ACQUITY UPLC Protein BEH SEC Column 200Å, 1.7 μm, 4.6 × 300 mm column (Part #186005225) using an Agilent 1200 HPLC system. The chromatography consisted of an isocratic gradient with 40 mM ammonium formate at a constant 25°C column temperature. The HPLC was connected to an Thermo Orbitrap EMR mass spectrometer with a resolution of 17,500 and an isCID of 85 eV. Data were processed using PMI (Protein Metrics) Intact deconvolution software.

Characterization of Adenoviral Peptides by RP-HPLC/MS/MS

AdC68 was denatured and digested similar to what was described previously for human Ad5 (Benevento et al., 2014) with the following alterations. Prior to digestion, six vials of AdC68 reference material were pooled together, diluted to a total volume of 10 ml with formulation buffer, and concentrated in an Ultra-15 10 kD MWCO centrifugal filter (M012160) at 3,300 g for 20 min. The retentate was removed (~500 μL) and denatured with 500 μL of 50 mM Tris pH 8.0 with 10% sodium deoxycholate at 95°C for 5 min. The sample was then reduced with 10 μL of 1 M DTT at 56°C for 5 minutes and alkylated with 20 μL of 1 M IAA at 37°C for 15 min in the dark. The sample was mixed with 9 ml of 50 mM Tris pH 8.0 with 0.02% sodium deoxycholate and an additional buffer exchange was performed in an Ultra-15 10 kD MWCO centrifugal filter at 3,300 g for 20 min. An additional 10 ml of 50 mM Tris pH 8.0 with 0.02% sodium deoxycholate was added to the sample and centrifugation was repeated to remove excess sodium deoxycholate. The retentate were then removed and the filter was washed with 50 mM Tris pH 8.0 with 0.02% sodium deoxycholate to yield a final sample volume of 500 μL.

TABLE 1 | Infectivity & AEX-HPLC data from the AdC68 #1 accelerated stability time course.

	Infectivity assay	AEX-HPLC			Infectivity per particle load
Sample	**IFU/mL**	**% Purity**	**VP/mL**	**RRT**	**VP/IFU**
T0	3.08E9	98.7	2.1E11	1.001	68
1w	1.87E9	95.3	1.7E11	1.009	91
2w	1.47E9	91.8	1.4E11	1.018	95
4w	6.63E8	86.4	1.0E11	1.032	151
8w	2.10E7[a]	80.5	7.0E10	1.048	3326[a]
12w	3.16E6[a]	64.7	4.0E10	1.054	12,671[a]

Abbreviations: IFU, infectivity units; VP, viral particles; RRT, relative retention time.
[a]Extrapolated, outside the calibrated method range.

TABLE 2 | Infectivity & AEX-HPLC data from the AdC68 #2 accelerated stability time course.

	Infectivity assay	AEX-HPLC			Infectivity per particle load
Sample	**IFU/mL**	**% Purity**	**VP/mL**	**RRT**	**VP/IFU**
T0	2.68E9	96.7	2.0E11	0.998	75
1w	1.54E9	93.4	1.6E11	1.008	104
2w	1.48E9	92.5	1.5E11	1.016	101
4w	5.26E8	90.2	1.3E11	1.030	247
8w	2.08E7[a]	85.9	9.0E10	1.050	4330[a]
12w	2.10E6[a]	81.5	7.0E10	1.058	33,261[a]

Abbreviations: IFU, infectivity units; VP, viral particles; RRT, relative retention time.
[a]xtrapolated, outside the calibrated method range.

The sample was digested with 20 µg trypsin for 15 min at 37°C followed by DNase1 digestion (20U) for 15 min at 37°C. Enzymatic digestion was quenched by the addition of 50 µL of 10% TFA and precipitate was removed by centrifugation at 20,000 g for 2 min. The supernatant was removed and added to an HPLC vial for analysis.

Fractions from the preparative AEX-HPLC method were digested using the approach outlined above. Fractions were concentrated to 500 µL prior to denaturation with 500 µL of 50 mM Tris pH 8.0 with 10% sodium deoxycholate at 95°C for 5 min. Reduction, alkylation, buffer exchange and digestion followed the experimental procedure described for the unfractionated adenovirus material. Proteolytic digested material was chromatographically separated on an Acquity UPLC BEH C18, 2.1 × 300 mm, 1.7 µm, 130Å analytical column (Part #186005792) using an Agilent 1260 HPLC. The column was held at a temperature of 60°C with a gradient consisting of 1–98% acetonitrile with trifluoroacetic acid over 315 min with a flow rate of 0.2 ml/min.

The Agilent 1260 HPLC was coupled to a Thermo Q-Exactive Plus Orbitrap mass spectrometer. Samples were analyzed in positive-ion mode with a detection range of 300–1650 m/z. The instrument utilized an internal lock mass ion of hexakis (1H,1H,3H-perfluoropropoxy)-phosphazene at m/z 922.009798 for [M + H+]1 + for dynamic calibration. Full-scan MS spectra were acquired in the Orbitrap with a resolution of 70,000 at m/z 400. The ten most intense ions at a threshold above 2,700 were selected for collision-induced fragmentation and analyzed in the orbitrap at a normalized collision energy of 30 and an isolation width of 3.0 m/z.

The data were processed with BioPharma Finder (v3.0, ThermoFisher Scientific) and searched against a library of AdC68 protein sequences. Variable modifications, including deamidation, oxidation, NH3 loss, water loss and acetylation were included. Relative quantitation was computed in BioPharma Finder. All experiments were run in single injections, so the relative abundances reported herein represent data from one instance.

Mutagenesis

Select site-specific mutagenesis to the AdC68 construct was performed to investigate the impact of capsid deamidation. The mutation to the construct was performed by the company SGI-DNA. Mutations of N76, N414 and N76 & N414 on the hexon protein were generated, converting the DNA to encode aspartic acid from the original asparagine. Materials were manufactured and purified by Viraquest Inc., North Liberty, IA.

RESULTS

AEX-HPLC is a Stability-Indicating Assay

Multiple recombinant AdC68 constructs were designed during development with two selected to move forward into clinical trials (heretofore named AdC68 #1 and #2). In preparation for clinical manufacturing, infectivity and an AEX-HPLC purity assays (see Materials and Methods) were developed and qualified as part of the overall analytical control strategy. These tests were then utilized to evaluate samples from the 12-weeks accelerated stability study at 26.5°C to demonstrate these assays were stability indicating. **Tables 1**, **2** show that the infectivity of both developmental drug substance constructs decreased with a corresponding loss of purity and viral particle titer. Furthermore, there was a concomitant increase in the relative retention time, indicative of an acidic shift, of the viral particle peak. All changes observed in the data herein were significantly greater than the method precision results obtained during the method qualification (data not shown), indicating real changes in each attribute. A similar observation of an AEX-HPLC acidic shift for human Ad5 has been observed and investigated previously (Blanche et al., 2001).

The data from **Table 1** can be readily visualized by inspecting overlaid chromatograms (**Figure 1**) from which the associated AdC68 #1 attribute data was calculated (**Table 1**). Sequential time points show a drop in the presumed AdC68 ("main") peak area corresponding to the loss of viral particle titer. The increase in the early eluting "impurity" peak area, along with the reduction in the "main" peak area, corresponds to a decrease in the overall purity. The rightward trajectory of the main AdC68 ("main") peak across the accelerated stability time course depicts the increase in retention time, which is a surrogate measurement of increased acidic surface charge. While cataloguing the "main" peak as the AdC68 product of interest for viral particle titer determinations

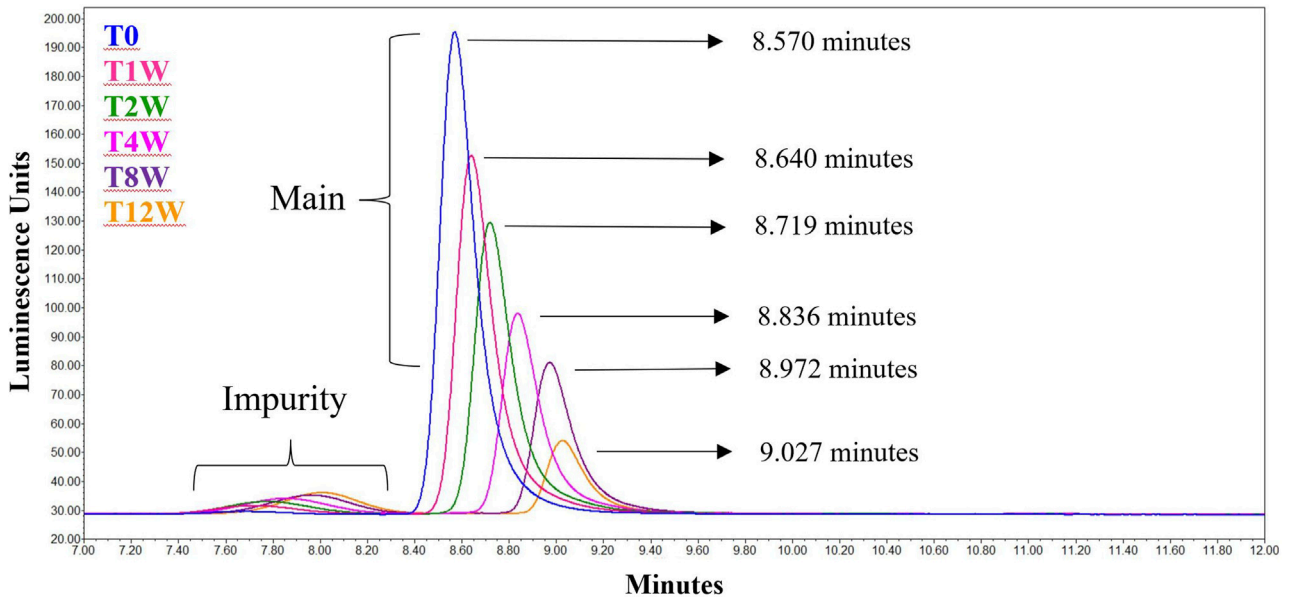

FIGURE 1 | Singlicate AEX-HPLC data from the AdC68 #1 accelerated stability time course. Peaks designated the "Main" and "Impurity" are labeled as such. The timepoints in the accelerated stability study are labeled on the figure, with blue representing the profile of the unstressed material. The retention times for each time point are shown in the figure.

(**Table 1**) was initially an anecdotal identification, additional characterization was used to confirm the "main" and "impurity" peak identities.

Analysis of AEX Fractions Demonstrates That the Impurity is Hexon Trimer

To characterize the "main" and "impurity" peak identities, 12-weeks degraded material was assessed. In **Figure 2A**, the unfractionated sample was shown to contain ample amounts of both "impurity" and "main" peaks in the analytical AEX-HPLC method. A modified, preparative AEX-HPLC method (see Materials and Methods) was then used to collect fractions of the "main" and "impurity" peaks. After several cycles of fractionation, like fractions were pooled together, concentrated and re-evaluated with the analytical AEX-HPLC method to ensure that the isolated peaks were in fact purified representations of "impurity" and "main" peaks (**Figures 2B,C**).

These fractions were then evaluated to determine their protein composition. Using a RP-HPLC/MS method similar to that described previously (Takahashi et al., 2006), the individual proteins within the samples were separated from each other for identification. The RP-HPLC/UV data demonstrated that the "impurity" peak contained primarily a single protein (**Figure 2D**), whereas the "main" peak contained many proteins and was representative of the chromatographic profile expected for adenovirus material (**Figure 2E**). The proteins from the "impurity" and "main" peaks were further examined by MS, which was directly coupled to the RP-HPLC separation. MS data confirmed that the "impurity" peak was comprised almost entirely of hexon protein, while the "main" peak contained all the proteins expected in a AdC68 viral particle, including hexon (**Figures 2D,E**) (Rux and Burnett, 2004; Russell, 2009; Nemerow et al., 2012; Ahi and Mittal, 2016). These observations were also consistent with an additional AdC68 construct (**Supplementary Figure S1**). The masses of hexon from both the main and impurity peaks are provided in **Table 3**. The observed masses of hexon for both the "main" and "impurity" peaks (104,844.8–104,847.7 Da) were abnormally high, especially when compared to hexon from an unstressed sample (104,842.1 Da), possibly indicative of deamidation of the protein.

RP-HPLC/MS is a denaturing analysis such that secondary, tertiary or quaternary structure of the proteins/complex are not retained. While the RP-HPLC/MS data demonstrated the presence of monomeric hexon, hexon is known to form noncovalent trimers on the adenovirus surface (Pichla-Gollon et al., 2007). To determine if the impurity, now identified as hexon, had such high-order structure, nSEC-HPLC/MS was implemented. The data clearly showed that the non-denatured, fraction collected impurity had a mass consistent with hexon trimer (**Table 3**). The higher-than-expected mass defect is likely explained by a combination of multiple deamidations, poor desolvation, and challenges with deconvolution at higher m/z.

HPLC-MS/MS and Directed Mutagenesis Confirms Deamidation is Responsible for the Observed Acidic Shift

With the identification of the major impurity concluded, the cause of the acidic shift was investigated by peptide mapping MS experiments. RP-HPLC-MS/MS data from the unfractionated

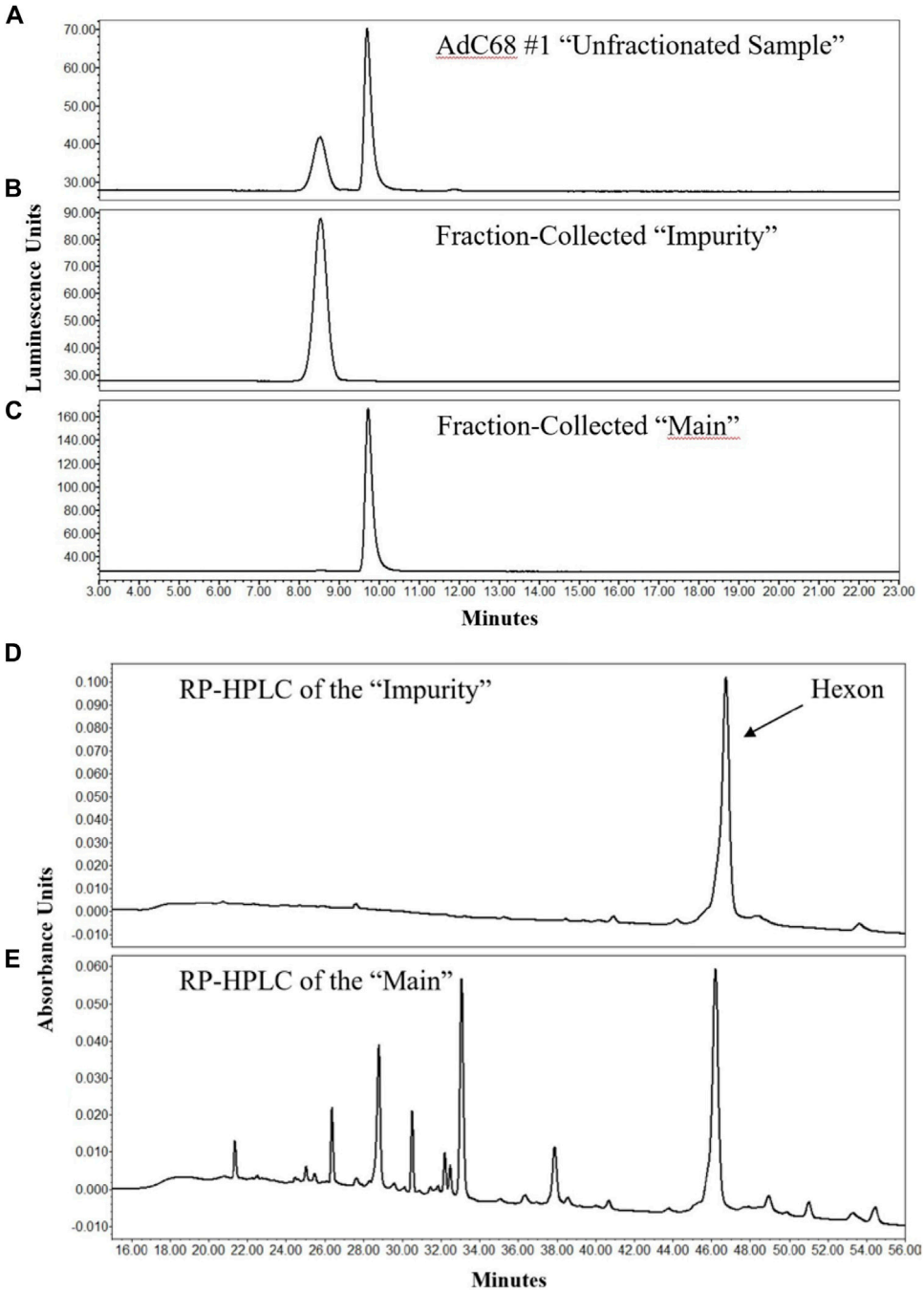

FIGURE 2 | AEX-HPLC and RP-HPLC profiles of the 12-weeks accelerated stability sample. The chromatographic profile of the unfractionated 12-weeks stability sample is shown in **(A)**. After enrichment of the "Impurity" and "Main" peaks by the preparative AEX-HPLC assay, efficient enrichment was demonstrated of the "Impurity" **(B)** and "Main" **(C)** peaks by the analytical AEX-HPLC method. Analyses of fractionated "Impurity" and "Main" peaks by RP-HPLC are shown in **(D,E)**, respectively.

sample time points in the accelerated stability study were collected and searched against various chemical modifications, including deamidation. While several modifications were observed across the entire adenoviral proteome, four hexon deamidation sites were evaluated extensively, including two that changed to a significant degree. Over the time-course, N76 and N414 reached almost 70 and 90% deamidation, respectively (**Figure 3A**). Conversely, many other sites of deamidation were observed but did not change significantly, including hexon N486 and N533 (**Figure 3A**).

The relative retention time shift from AEX-HPLC and the percent deamidation of N414 by RP-HPLC-MS/MS were plotted on the same graph and fitted to a single exponential equation to assess the relationship between deamidation and the relative

TABLE 3 | Observed Masses for deconvoluted hexon by RP-HPLC/MS and nSEC-HPLC/MS.

Sample	RP-HPLC/MS		nSEC/MS	
	Observed Mass (Da)	Theoretical Mass of monomer (Da)	Observed Mass (Da)	Theoretical Mass of trimer (Da)
AdC68 #1 "Main"	104847.2	104842.0	NT	314526.0
AdC68 #1 "Impurity"	104845.2		314545.2	
AdC68 #2 "Main"	104844.8		NT	
AdC68 #2 "Impurity"	104847.7		314559.7	
AdC68 #2 Unfractionated Non-Stressed Sample	104842.1		NT	

NT, denotes not tested.

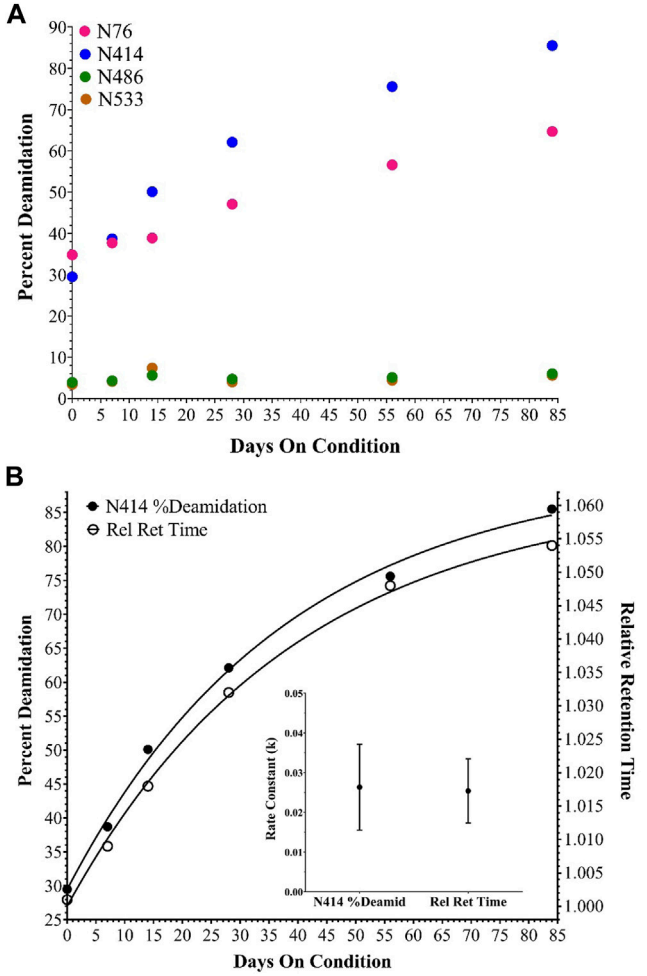

FIGURE 3 | Deamidation of selected hexon asparagine residues during the accelerated stability time course. **(A)** shows percent deamidation determined for N76, 414, 486 and 533 in AdC68 #1. **(B)** shows percent deamidation for N414 and the AEX-HPLC relative retention time shift both fit to a single exponential equation [Y=Y0 + (Plateau-Y0)*(1-exp (-K*x)], the calculated rate constants and the associated error for AdC68 #1.

retention time shift. For AdC68 #1, the generated curves and associated rate constants align excellently with each other (**Figure 3B**). Both curves showed good correlation with a single exponential equation indicating a single kinetic process and both rate constants were within error of matching. These observations were also consistent with an additional AdC68 construct (**Supplementary Figure S2**).

The pooled "impurity" and "main" peaks, along with the unfractionated sample from the 0 and 12-weeks timepoints, were also characterized by RP-HPLC-MS/MS. Specifically, the purpose of this study was to quantitate the deamidation sites of interest established in **Figure 3A** to ensure that deamidation events were not isolated to the "impurity" peak but also occurred on the intact adenoviral capsid prior to degradation. The data showed similar levels of N414 deamidation across the 12-weeks unfractionated sample and the "main" and "impurity" fractions (**Figure 4**). The data show somewhat higher levels of N76 deamidation in the "impurity" fraction compared to the "main" fraction (**Figure 4**). In both cases, the level of deamidation in the "main" fraction and the unfractionated sample at the 12-weeks accelerated timepoint were significantly higher than the 0-weeks timepoint. These observations were also consistent with an additional AdC68 construct (data not shown).

To conclude the deamidation inquiry, three hexon mutants were constructed: N414D and N76D single mutants and the N414D/N76D double mutant. These would mimic 100% deamidation at either or both sites for the asparagine residues that showed appreciable increases in deamidation upon accelerated stability. N414D was able to replicate and produce viable, infectious virus (data not shown). To assess the impact of the deamidation mutant on the relative retention time, the N414D mutant was tested by the analytical AEX-HPLC method, alongside the samples from the accelerated stability study (**Figure 5**). Upon analysis, the modified capsid eluted at a late relative retention time, consistent with the expectation that deamidation causes the AEX-HPLC retention shift in the non-mutant AdC68 accelerated stability samples (**Figure 5**). In contrast, the N76D single and N414D/N76D double mutant could not produce virus at any appreciable level. As such, the impact to infectivity and relative retention time shift could not be assessed.

DISCUSSION

As presented in the manuscript, AEX-HPLC represents an important physiochemical method for the adenovirus analytical control strategy. The AEX-HPLC assay is a critical

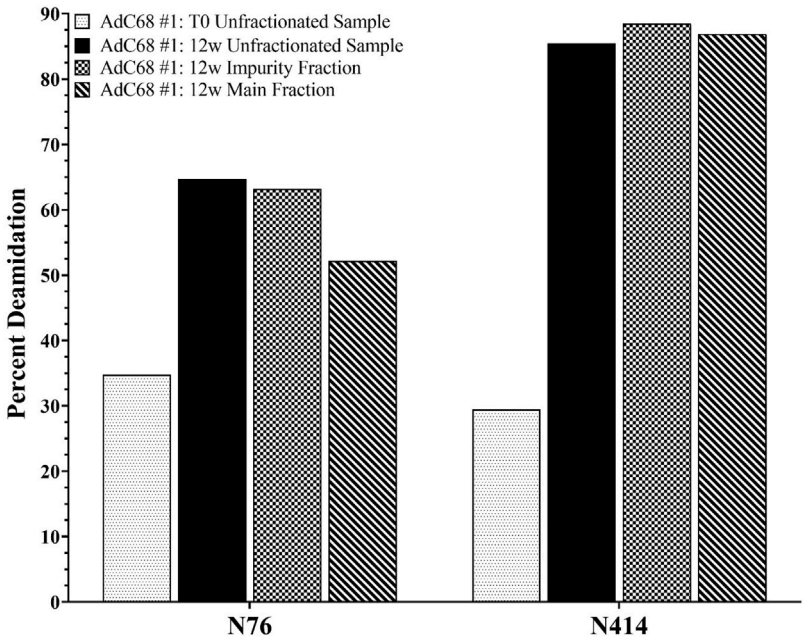

FIGURE 4 | Deamidation level of selected hexon asparagine residues from the 0- and 12-weeks accelerated stability unfractionated samples and the associated "Impurity" and "Main" peaks fractions.

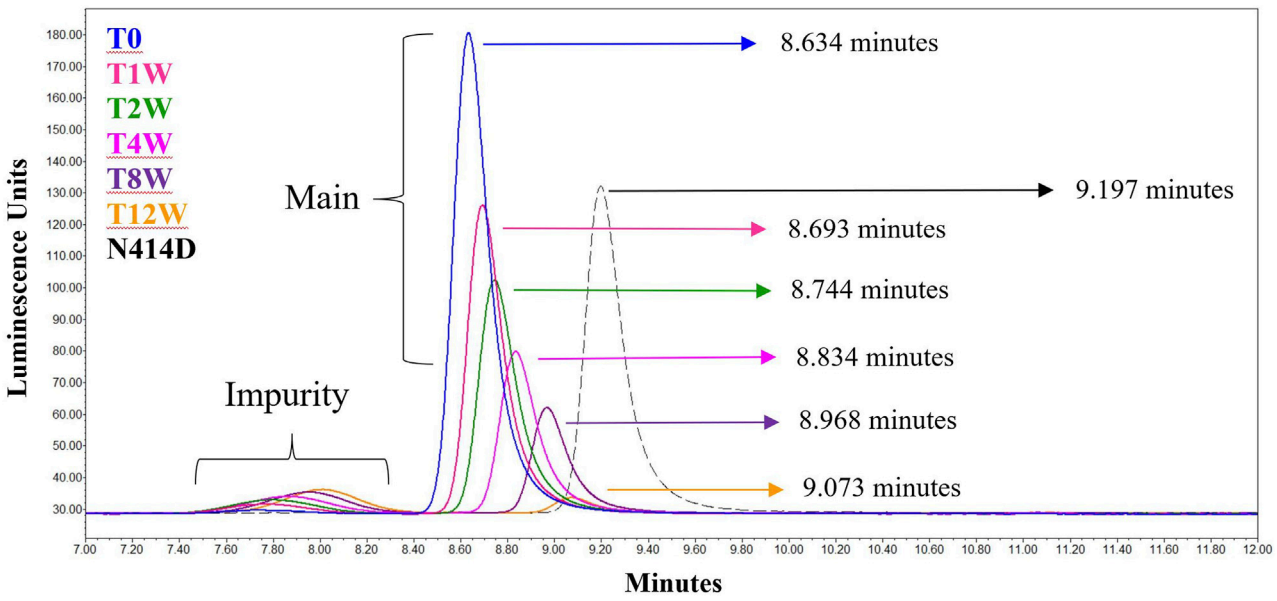

FIGURE 5 | AEX-HPLC of the N414D mutant overlaid with the singlicate AdC68 #1 accelerated stability time course. The timepoints in the accelerated stability study are labeled on the figure, with blue representing the profile of the unstressed material. The gray dashed line represents the N414D mutant. The retention times for each time point and for the mutant are shown in the figure.

assay for adenovirus-based therapeutics as it is stability indicating (documented herein), higher throughput, and can be reflective of lower-throughput, more resource intensive bioassays. As demonstrated, when the AEX-HPLC assay was used to characterize samples following accelerated stability conditions at 26.5°C, changes in viral particle concentration, particle purity and relative retention time shift were all observed (**Table 1**; **Figure 1**). While these changes were observed and correlated

with a drop in infectivity, additional work was needed to 1) understand what attributes were driving these changes and 2) assess whether the specific changes were responsible for the reduced infectivity.

Interpretation of Viral Particle Titer and Particle Purity Results

As observed in **Table 1** and **Figure 1**, viral particle concentration was reduced after accelerated stability conditions, as reflected by the drop in signal in the AEX-HPLC chromatogram. However, based on the magnitude of the particle concentration change *vs.* the magnitude of the decrease in infectivity, the change in particle concentration alone does not account for the decrease in infectivity. This is further demonstrated in the VP/IFU (**Table 1**) column, which adjusts the infectivity response to the particles dosed. The readout shows substantial reduction in per particle infectivity for the stressed samples.

Similarly, **Table 1** and **Figure 1** demonstrate a decrease in particle purity after accelerated stability conditions, as reflected by the increase in the "impurity" peak. As with particle concentration, the reduced purity alone would not account for the magnitude of reduced infectivity in the stressed samples. That said, the reduction in particle purity observed by AEX-HPLC does provide an avenue to investigate the mechanism of the viral particle concentration decrease, as the concentration decrease is likely linked to the increase of the impurity.

To understand the identity of the impurity, fractions were collected from the "impurity" and "main" peak observed by the analytical AEX-HPLC method after 12 weeks at 26.5°C. The profile from the unfractionated sample is shown in **Figure 2A**. A modified, preparative AEX-HPLC method was used for fraction collection to enable more concentrated fractions. Efficient enrichment of the "impurity" and "main" peaks were confirmed with the analytical AEX-HPLC method (**Figures 2B,C**). After successful enrichment, the "impurity" and "main" fractions were characterized by RP-HPLC/MS to identify differences between the fractions. Interestingly, the "impurity" fraction consisted primarily of a single protein (**Figure 2D**), which was identified as hexon by RP-HPLC/MS (**Table 3**). The "main" peak contained a profile indicative of adenovirus with many capsid proteins (**Figure 2E**), including hexon. RP-HPLC/MS was also used to confirm the identities of the capsid proteins from the "main" peak in an unstressed material, with the mass of hexon shown in **Table 3**. When compared with a representative unstressed and unfractionated sample, the mass of the "main" and "impurity" fractions from the sample subjected to 12 weeks at 26.5°C had higher observed masses by approximately 2–5 Daltons. This is possibly indicative of several asparagine deamidations, which is frequently observed in accelerated stability studies.

While the "impurity" was identified as hexon, we were interested in whether that "impurity" was monomeric or trimeric hexon, as it is noted that hexon exists as a trimer in the assembled adenovirus capsid (Pichla-Gollon et al., 2007). To assess this, the impurity peaks were evaluated by native SEC-MS, with a gradient that consisted of non-organic mobile phases and gentle MS source parameters directed at keeping non-covalent complexes assembled. The resulting spectra resulted in deconvolved masses between 314,545.2 and 314,559.7 Da, approximately three times the mass of the hexon in the RP-HPLC/MS data, indicating the impurity observed by AEX-HPLC is in fact hexon trimer (**Table 3**). A comparison of the observed to theoretical mass (314,526.0 Da) represents a large mass defect, but this defect can be explained by several sources. The theoretical mass does not consider hexon deamidation. As shown in the RP-HPLC/MS data, the observed hexon in the "impurity" and "main" peaks likely has several sites of deamidation present. If the monomeric hexon has on average 3 deamidations present on the capsid, the theoretical mass for the average trimer would be 9 Da higher than the theoretical mass listed in **Table 3**. Furthermore, deconvolution of spectra from native SEC-MS is challenging due to a limited number of charge states, higher m/z measurements, and poorer desolvation, often resulting in larger than expected masses. Given challenges in characterizing native spectra, and the fact that we know there is significant deamidation present on the hexon proteins in the 12-weeks accelerated stability sample, we feel that the observed mass is indeed reflective of hexon trimer.

Linking Capsid Deamidation to an Acidic Shift in the AEX-HPLC Profile

As the change in purity and particle titer have been accounted for, the cause of the relative retention time shift was then explored. In previous work on human adenovirus (Blanche et al., 2001), a similar shift was observed and was isolated to the deamidation of four accessible hexon asparagine-glycine (NG) residue pairs. Such NG pairs are known hotspots for deamidation (Geiger and Clarke, 1987). The recombinant AdC68 constructs studied in the current manuscript had 3 such NG pairs in its hexon primary sequence: N414, N486 & N533, two of which align with the human adenovirus structure. Instead of focusing the search on just these residues, MS/MS data were evaluated in a data dependent manner to see if other sites of modifications were present and changing. Interestingly, N76 which has an asparagine-threonine (NT) pair, showed a deamidation propensity like N414, albeit at a slightly slower rate. The deamidation levels of N76, N414, N486 and N533 are plotted in **Figure 3A**. Overall, the high level of hexon deamidation aligns with the hypothesis of deamidation from the RP-HPLC/MS data at the intact capsid protein level. Furthermore, N414 deamidation was contrasted with the relative retention time, and the curves showed good correlation with a single exponential equation indicating a single kinetic process and similar rate constants (**Figure 3B**). N414 is at the external surface of the hexon trimer (**Figure 6**) and could be directly responsible for the acidic shift in the surface charge observed by AEX-HPLC.

To confirm this hypothesis, site-directed mutagenesis of N414 to D414 was performed, which mimics 100% deamidation at the N414 site. As expected, when the N414D mutant was run by AEX-HPLC, alongside the accelerated stability samples, the relative retention time was in line with the expected result based on the single exponential equation (**Figure 5**). While the

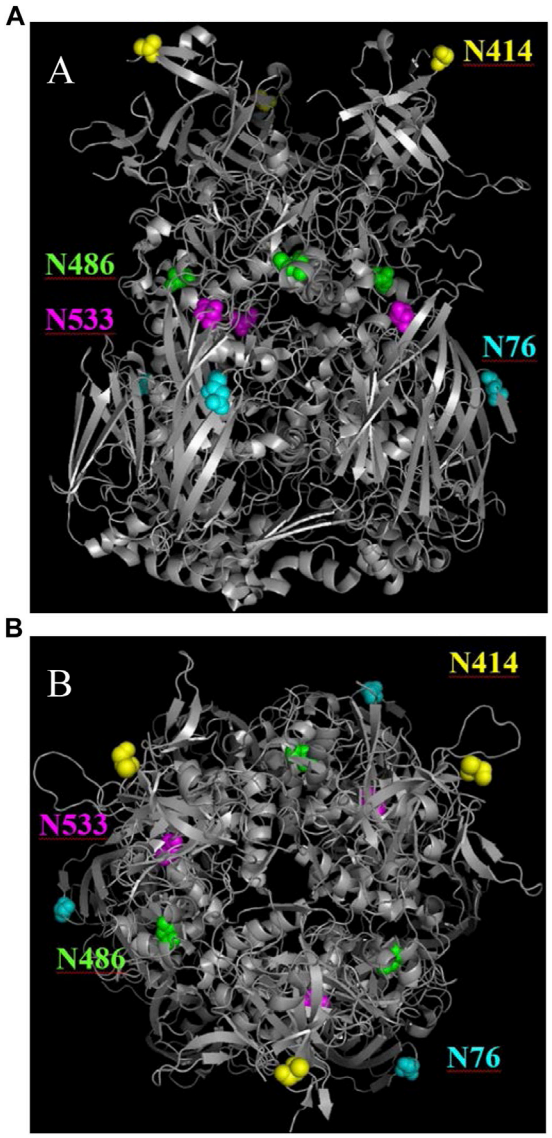

FIGURE 6 | Ribbon diagrams of the hexon AdC68 crystal structure (2obe.pdb) with selected asparagine residues highlighted. **(A)** demonstrates that N414 is on the surface and N76 is buried within the trimer. **(B)** demonstrates that N486 and N533 are buried within the hexon.

relative retention time shift was explained by deamidation at N414, this mutation did not impact infectivity.

While deamidation at N76 is not unexpected based on the NT amino acid motif, structural analysis (**Figure 6**) shows that the N76 residue exists at the outer surface of the hexon trimer in a region that is buried on the viral particle surface (Reddy, 2017; Matteson et al., 2018). As such, we wanted to ensure that the deamidation was not observed only on the "impurity" fraction, which represents free hexon trimer. Therefore, we digested both the unfractionated 0-weeks and 12-weeks accelerated stability samples in addition to the "impurity" and "main" fractions and assessed the level of deamidation for both N76 and N414 (**Figure 4**). There is significant evidence that both N76 and N414 deamidation occurs on the "main" peak, which represents the assembled adenovirus capsid, as evidenced by the increase in deamidation compared to the 0-weeks sample. Furthermore, N414 was at roughly equivalent levels across all samples. While N76 deamidation was moderately more prominent in the "impurity" fraction compared to the "main" fraction, the abundance of deamidation in both fractions were still significantly larger than the 0-weeks sample. Thus, while moderate N76 deamidation may occur after particle degradation, there is still evidence that significant N76 deamidation occurs on assembled adenovirus capsid.

Site-directed mutagenesis of N76 to D76, as a mimic for the 100% deamidated residue was performed to investigate the impact of N76 deamidation on the relative retention time shift and infectivity. However, we were unable to form assembled particles after making this mutation. Collectively, evidence of deamidation at N76 at higher rates in the "impurity" peak and the inability to form capsids after site directed mutagenesis of N76 to D76, suggests that this modification may be deleterious to assembled capsids. Whatever the mechanism for its alteration, deamidation of N76 seems to be detrimental to the structural integrity of the viral capsid and might be a site of interest in future molecular designs to stabilize the product for long-term storage.

CONCLUSION

At a high level, the manuscript overviews a critical method to support the analytical control strategy for adenovirus-based therapeutics. The analytical AEX-HPLC provides information on viral particle titer, particle purity, and surface charge. During development, it was determined that accelerated stability conditions impacted all reportable attributes in the AEX-HPLC assay and also resulted in a decrease in infectivity. While changes in purity and titer may account for some of the infectivity loss, there appears to be an additional mechanism driving infectivity loss. Deamidation accounts for the change in surface charge, but N414 deamidation did not impact infectivity. A new site of deamidation was identified and preliminary data suggests that this site may be deleterious to the capsid. A full assessment of the impact of N76 deamidation on infectivity would be an enlightening follow up manuscript. The current manuscript establishes AEX-HPLC as a stability-indicating method, bolsters the understanding of attributes that underpin changes in the AEX-HPLC profile, and establishes the AEX-HPLC approach as a platform method that can be applied to multiple candidates to accelerate product development.

DATA AVAILABILITY STATEMENT

The datasets presented in this article are not readily available because Raw data may be deemed proprietary by legal. Requests to access the datasets should be directed to lawrence.thompson@pfizer.com.

AUTHOR CONTRIBUTIONS

TP, EM, KZ, JB, and LT designed the study. TP, EM, KZ, and LT performed the experiments. TP, EM, KZ, JB, OF, HR, and LT analysed the results. TP, EM, KZ, and LT wrote the manuscript. All authors contributed to the research and reviewed the manuscript.

FUNDING

Funded as part of ongoing research and development within Worldwide Research, Development and Medical by Pfizer, Inc.

ACKNOWLEDGMENTS

This is a short text to acknowledge the contributions of specific colleagues, institutions, or agencies that aided the efforts of the authors.

SUPPLEMENTARY MATERIAL

The Supplementary Material for this article can be found online at: https://www.frontiersin.org/articles/10.3389/fbioe.2022.753481/full#supplementary-material

REFERENCES

Ahi, Y. S., and Mittal, S. K. (2016). Components of Adenovirus Genome Packaging. *Front. Microbiol.* 7, 1503. doi:10.3389/fmicb.2016.01503

Benevento, M., Di Palma, S., Snijder, J., Moyer, C. L., Reddy, V. S., Nemerow, G. R., et al. (2014). Adenovirus Composition, Proteolysis, and Disassembly Studied by In-Depth Qualitative and Quantitative Proteomics. *J. Biol. Chem.* 289 (16), 11421–11430. doi:10.1074/jbc.m113.537498

Berkowitz, S. A. (2008). Determining the Concentration and the Absorptivity Factor at 260 Nm in Sodium Dodecyl Sulfate of the Adenovirus Reference Material Using Analytical Ultracentrifugation. *Anal. Biochem.* 380 (1), 152–154. doi:10.1016/j.ab.2008.05.014

Berkowitz, S. A., and Philo, J. S. (2007). Monitoring the Homogeneity of Adenovirus Preparations (A Gene Therapy Delivery System) Using Analytical Ultracentrifugation. *Anal. Biochem.* 362 (1), 16–37. doi:10.1016/j.ab.2006.11.031

Blanche, F., Cameron, B., Barbot, A., Ferrero, L., Guillemin, T., Guyot, S., et al. (2000). An Improved Anion-Exchange HPLC Method for the Detection and Purification of Adenoviral Particles. *Gene Ther.* 7 (12), 1055–1062. doi:10.1038/sj.gt.3301190

Blanche, F., Cameron, B., Somarriba, S., Maton, L., Barbot, A., and Guillemin, T. (2001). Stabilization of Recombinant Adenovirus: Site-Directed Mutagenesis of Key Asparagine Residues in the Hexon Protein. *Anal. Biochem.* 297 (1), 1–9. doi:10.1006/abio.2001.5210

Bondoc, L., and Fitzpatrick, S. (1998). Size Distribution Analysis of Recombinant Adenovirus Using Disc Centrifugation. *JIMB* 20, 317–322.

Capone, S., D'Alise, A. M., Ammendola, V., Colloca, S., Cortese, R., Nicosia, A., et al. (2013). Development of Chimpanzee Adenoviruses as Vaccine Vectors: Challenges and Successes Emerging from Clinical Trials. *Expert Rev. Vaccin.* 12 (4), 379–393. doi:10.1586/erv.13.15

Chelius, D., Hühmer, A. F. R., Shieh, C. H., Lehmberg, E., Traina, J. A., Slattery, T. K., et al. (2002). Analysis of the Adenovirus Type 5 Proteome by Liquid Chromatography and Tandem Mass Spectrometry Methods. *J. Proteome Res.* 1 (6), 501–513. doi:10.1021/pr025528c

Cheng, C., Wang, L., Ko, S.-Y., Kong, W.-P., Schmidt, S. D., Gall, J. G. D., et al. (2015). Combination Recombinant Simian or Chimpanzee Adenoviral Vectors for Vaccine Development. *Vaccine* 33 (51), 7344–7351. doi:10.1016/j.vaccine.2015.10.023

Chmp (2019). *European Pharmacopoeia 10th Edition 5.14. Gene Transfer Medicinal Products for Human Use.* European Medicines Agency Committee for Medicinal Products for Human Use.

Cohen, C. J., Xiang, Z. Q., Gao, G. P., Ertl, H. C. J., Wilson, J. M., and Bergelson, J. M. (2002). Chimpanzee Adenovirus CV-68 Adapted as a Gene Delivery Vector Interacts with the Coxsackievirus and Adenovirus Receptor. *J. Gen. Virol.* 83 (Pt 1), 151–155. doi:10.1099/0022-1317-83-1-151

Ewer, K. J., Barrett, J. R., Belij-Rammerstorfer, S., Sharpe, H., Makinson, R., Morter, R., et al. (2021). T Cell and Antibody Responses Induced by a Single Dose of ChAdOx1 nCoV-19 (AZD1222) Vaccine in a Phase 1/2 Clinical Trial. *Nat. Med.* 27 (2), 270–278. doi:10.1038/s41591-020-01194-5

Farina, S. F., Gao, G.-p., Xiang, Z. Q., Rux, J. J., Burnett, R. M., Alvira, M. R., et al. (2001). Replication-defective Vector Based on a Chimpanzee Adenovirus. *J. Virol.* 75 (23), 11603–11613. doi:10.1128/jvi.75.23.11603-11613.2001

Fda (2020). *Guidance for Industry: Chemistry, Manufacturing, and Control (CMC) Information for Human Gene Therapy Investigational New Drug Applications (INDs)*. U.S. Department of Health and Human Services Food and Drug Administration Center for Biologics Evaluation and Research.

Fda (2011). *Guidance for Industry: Potency Tests for Cellular and Gene Therapy Products*. U.S. Department of Health and Human Services Food and Drug Administration Center for Biologics Evaluation and Research.

Folegatti, P. M., Ewer, K. J., Aley, P. K., Angus, B., Becker, S., Belij-Rammerstorfer, S., et al. (2020). Safety and Immunogenicity of the ChAdOx1 nCoV-19 Vaccine against SARS-CoV-2: a Preliminary Report of a Phase 1/2, Single-Blind, Randomised Controlled Trial. *Lancet* 396 (10249), 467–478. doi:10.1016/S0140-6736(20)31604-4

Geiger, T., and Clarke, S. (1987). Deamidation, Isomerization, and Racemization at Asparaginyl and Aspartyl Residues in Peptides. Succinimide-Linked Reactions that Contribute to Protein Degradation. *J. Biol. Chem.* 262 (2), 785–794. doi:10.1016/s0021-9258(19)75855-4

Ich (1999). *Q6b Specifications: Test Procedures and Acceptance Criteria for Biotechnological/Biological Products*. International Conference On Harmonisation Of Technical Requirements For Registration Of Pharmaceuticals For Human Use.

Klyushnichenko, V., Bernier, A., Kamen, A., and Harmsen, E. (2001). Improved High-Performance Liquid Chromatographic Method in the Analysis of Adenovirus Particles. *J. Chromatogr. B Biomed. Sci. Appl.* 755 (1-2), 27–36. doi:10.1016/s0378-4347(00)00597-1

Kramberger, P., Urbas, L., and Štrancar, A. (2015). Downstream Processing and Chromatography Based Analytical Methods for Production of Vaccines, Gene Therapy Vectors, and Bacteriophages. *Hum. Vaccin. Immunother.* 11 (4), 1010–1021. doi:10.1080/21645515.2015.1009817

Kuhn, I., Larsen, B., Gross, C., and Hermiston, T. (2007). High-performance Liquid Chromatography Method for Rapid Assessment of Viral Particle Number in Crude Adenoviral Lysates of Mixed Serotype. *Gene Ther.* 14 (2), 180–184. doi:10.1038/sj.gt.3302851

Ledgerwood, J. E., DeZure, A. D., Stanley, D. A., Coates, E. E., Novik, L., Enama, M. E., et al. (2017). Chimpanzee Adenovirus Vector Ebola Vaccine. *N. Engl. J. Med.* 376 (10), 928–938. doi:10.1056/nejmoa1410863

Lehmberg, E., Traina, J. A., Chakel, J. A., Chang, R.-J., Parkman, M., McCaman, M. T., et al. (1999). Reversed-phase High-Performance Liquid Chromatographic Assay for the Adenovirus Type 5 Proteome. *J. Chromatogr. B: Biomed. Sci. Appl.* 732 (2), 411–423. doi:10.1016/s0378-4347(99)00316-3

Matteson, N. L., Barry, M. A., and Reddy, V. S. (2018). Structure-based Assessment of Protein-Protein Interactions and Accessibility of Protein IX in Adenoviruses with Implications for Antigen Display. *Virology* 516, 102–107. doi:10.1016/j.virol.2018.01.007

Mullins, E. K., Powers, T. W., Zobel, J., Clawson, K. M., Barnes, L. F., Draper, B. E., et al. (2021). Characterization of Recombinant Chimpanzee Adenovirus C68 Low and High-Density Particles: Impact on Determination of Viral Particle Titer. *Front. Bioeng. Biotechnol.* 9, 753480. doi:10.3389/fbioe.2021.753480

Nemerow, G. R., Stewart, P. L., and Reddy, V. S. (2012). Structure of Human Adenovirus. *Curr. Opin. Virol.* 2 (2), 115–121. doi:10.1016/j.coviro.2011.12.008

Pérez-Berná, A. J., Mangel, W. F., McGrath, W. J., Graziano, V., Flint, J., and San Martín, C. (2014). Processing of the L1 52/55k Protein by the Adenovirus Protease: a New Substrate and New Insights into Virion Maturation. *J. Virol.* 88 (3), 1513–1524. doi:10.1128/jvi.02884-13

Pichla-Gollon, S. L., Drinker, M., Zhou, X., Xue, F., Rux, J. J., Gao, G.-P., et al. (2007). Structure-based Identification of a Major Neutralizing Site in an Adenovirus Hexon. *J. Virol.* 81 (4), 1680–1689. doi:10.1128/jvi.02023-06

Putter, J. S. (2021). Immunotherapy for COVID-19: Evolving Treatment of Viral Infection and Associated Adverse Immunological Reactions. *Transfus. Apher. Sci.* 60 (2), 103093. doi:10.1016/j.transci.2021.103093

Reddy, V. S. (2017). The Role of Hexon Protein as a Molecular Mold in Patterning the Protein IX Organization in Human Adenoviruses. *J. Mol. Biol.* 429 (18), 2747–2751. doi:10.1016/j.jmb.2017.06.025

Russell, W. C. (2009). Adenoviruses: Update on Structure and Function. *J. Gen. Virol.* 90 (Pt 1), 1–20. doi:10.1099/vir.0.003087-0

Rux, J. J., and Burnett, R. M. (2004). Adenovirus Structure. *Hum. Gene Ther.* 15 (12), 1167–1176. doi:10.1089/hum.2004.15.1167

Shih, S.-J., Yagami, M., Tseng, W.-J., and Lin, A. (2010). Validation of a Quantitative Method for Detection of Adenovirus Aggregation. *Bioprocessing J.* 9 (2), 25–33. doi:10.12665/J92.Shih

Stanley, D. A., Honko, A. N., Asiedu, C., Trefry, J. C., Lau-Kilby, A. W., Johnson, J. C., et al. (2014). Chimpanzee Adenovirus Vaccine Generates Acute and Durable Protective Immunity against Ebolavirus challenge. *Nat. Med.* 20 (10), 1126–1129. doi:10.1038/nm.3702

Takahashi, E., Cohen, S. L., Tsai, P. K., and Sweeney, J. A. (2006). Quantitation of Adenovirus Type 5 Empty Capsids. *Anal. Biochem.* 349 (2), 208–217. doi:10.1016/j.ab.2005.11.014

Tatsis, N., Tesema, L., Robinson, E. R., Giles-Davis, W., McCoy, K., Gao, G. P., et al. (2006). Chimpanzee-origin Adenovirus Vectors as Vaccine Carriers. *Gene Ther.* 13 (5), 421–429. doi:10.1038/sj.gt.3302675

van Tricht, E., de Raadt, P., Verwilligen, A., Schenning, M., Backus, H., Germano, M., et al. (2018). Fast, Selective and Quantitative Protein Profiling of Adenovirus-Vector Based Vaccines by Ultra-performance Liquid Chromatography. *J. Chromatogr. A* 1581-1582, 25–32. doi:10.1016/j.chroma.2018.10.045

van Tricht, E., Geurink, L., Backus, H., Germano, M., Somsen, G. W., and Sänger–van de Griend, C. E. (2017). One Single, Fast and Robust Capillary Electrophoresis Method for the Direct Quantification of Intact Adenovirus Particles in Upstream and Downstream Processing Samples. *Talanta* 166, 8–14. doi:10.1016/j.talanta.2017.01.013

Vellekamp, G., Porter, F. W., Sutjipto, S., Cutler, C., Bondoc, L., Liu, Y.-H., et al. (2001). Empty Capsids in Column-Purified Recombinant Adenovirus Preparations. *Hum. Gene Ther.* 12 (15), 1923–1936. doi:10.1089/104303401753153974

Whitfield, R. J., Battom, S. E., Barut, M., Gilham, D. E., and Ball, P. D. (2009). Rapid High-Performance Liquid Chromatographic Analysis of Adenovirus Type 5 Particles with a Prototype Anion-Exchange Analytical Monolith Column. *J. Chromatogr. A* 1216 (13), 2725–2729. doi:10.1016/j.chroma.2008.11.010

Xiang, Z., Gao, G., Reyes-Sandoval, A., Cohen, C. J., Li, Y., Bergelson, J. M., et al. (2002). Novel, Chimpanzee Serotype 68-based Adenoviral Vaccine Carrier for Induction of Antibodies to a Transgene Product. *J. Virol.* 76 (6), 2667–2675. doi:10.1128/jvi.76.6.2667-2675.2002

Yang, X., Agarwala, S., Ravindran, S., and Vellekamp, G. (2008). Determination of Particle Heterogeneity and Stability of Recombinant Adenovirus by Analytical Ultracentrifugation in CsCl Gradients. *J. Pharm. Sci.* 97 (2), 746–763. doi:10.1002/jps.21008

Zhang, C., Chi, Y., and Zhou, D. (2017). Development of Novel Vaccines against Infectious Diseases Based on Chimpanzee Adenoviral Vector. *Methods Mol. Biol.* 1581, 3–13. doi:10.1007/978-1-4939-6869-5_1

Zhao, H., Xu, C., Luo, X., Wei, F., Wang, N., Shi, H., et al. (2018). Seroprevalence of Neutralizing Antibodies against Human Adenovirus Type-5 and Chimpanzee Adenovirus Type-68 in Cancer Patients. *Front. Immunol.* 9, 335. doi:10.3389/fimmu.2018.00335

Conflict of Interest: TP, EM, KZ, JB, OF, HR, and LT were employed by the company Pfizer Inc.

Publisher's Note: All claims expressed in this article are solely those of the authors and do not necessarily represent those of their affiliated organizations, or those of the publisher, the editors and the reviewers. Any product that may be evaluated in this article, or claim that may be made by its manufacturer, is not guaranteed or endorsed by the publisher.

frontiers | Frontiers in Chemistry

ORIGINAL RESEARCH
published: 13 April 2022
doi: 10.3389/fchem.2022.887960

Extreme Point Sort Transformation Combined With a Long Short-Term Memory Network Algorithm for the Raman-Based Identification of Therapeutic Monoclonal Antibodies

Jin Ling[1], *Luxia Zheng*[1], *Mingming Xu*[1], *Gang Chen*[1], *Xiao Wang*[2], *Danzhuo Mao*[2] *and Hong Shao*[1]*

[1]NMPA Key Laboratory for Quality Control of Therapeutic Monoclonal Antibodies, Shanghai Institute for Food and Drug Control, Shanghai, China, [2]NMPA Key Laboratory for Quality Analysis of Chemical Drug Preparations, Shanghai Institute for Food and Drug Control, Shanghai, China

Therapeutic monoclonal antibodies (mAbs) are a new generation of protein-based medicines that are usually expensive and thus represent a target for counterfeiters. In the present study, a method based on Raman spectroscopy that combined extreme point sort transformation with a long short-term memory (LSTM) network algorithm was presented for the identification of therapeutic mAbs. A total of 15 therapeutic mAbs were used in this study. An in-house Raman spectrum dataset for model training was created with 1,350 spectra. The characteristic region of the Raman spectrum was reduced in dimension and then transformed through an extreme point sort transformation into a sequence array, which was fitted for the LSTM network. The characteristic array was extracted from the sequence array using a well-trained LSTM network and then compared with standard spectra for identification. To demonstrate whether the present algorithm was better, ThermoFisher OMNIC 8.3 software (Thermo Fisher Scientific Inc., U.S.) with two matching modes was selected for comparison. Finally, the present method was successfully applied to identify 30 samples, including 15 therapeutic mAbs and 15 other injections. The characteristic region was selected from 100 to 1800 cm^{-1} of the full spectrum. The optimized dimensional values were set from 35 to 53, and the threshold value range was from 0.97 to 0.99 for 15 therapeutic mAbs. The results of the robustness test indicated that the present method had good robustness against spectral peak drift, random noise and fluorescence interference from the measurement. The areas under the curve (AUC) values of the present method that were analysed on the full spectrum and analysed on the characteristic region by the OMNIC 8.3 software's built-in method were 1.000, 0.678, and 0.613, respectively. The similarity scores for 15 therapeutic mAbs using OMNIC 8.3 software in all groups compared with that of the relative present algorithm group had extremely remarkable differences ($p < 0.001$). The results suggested that the extreme point sort transformation combined with the LSTM network algorithm enabled the characteristic extraction of the therapeutic mAb Raman spectrum. The present method is a proposed solution to rapidly identify therapeutic mAbs.

Keywords: Raman spectroscopy, long-short term memory network, therapeutic monoclonal antibody, extreme point sort transformation, algorithm study

OPEN ACCESS

Edited by:
Christopher Mark Smales, University of Kent, United Kingdom

Reviewed by:
Zufang Huang, Fujian Normal University, China
Rajapandiyan Panneerselvam, SRM University, India

***Correspondence:**
Hong Shao
shaohong@smda.sh.cn

Specialty section:
This article was submitted to Analytical Chemistry, a section of the journal Frontiers in Chemistry

Received: *02 March 2022*
Accepted: *23 March 2022*
Published: *13 April 2022*

Citation:
Ling J, Zheng L, Xu M, Chen G, Wang X, Mao D and Shao H (2022) Extreme Point Sort Transformation Combined With a Long Short-Term Memory Network Algorithm for the Raman-Based Identification of Therapeutic Monoclonal Antibodies. Front. Chem. 10:887960. doi: 10.3389/fchem.2022.887960

INTRODUCTION

Biologics, especially therapeutic monoclonal antibodies (mAbs), have been progressively utilized in clinics over the last decade and have been established as a major therapeutic modality to treat severe human diseases (Singh et al., 2018; Li et al., 2020). To date, approximately 80 antibody-based biopharmaceutical products have been approved for therapeutic use worldwide in 2019, and 42 therapeutic mAbs have been marketed in China (Castelli et al., 2019). Over 100 mAbs are in development, and new therapeutic mAbs are marketed every year (Ettah and Ashton, 2018; Castelli et al., 2019). Meanwhile, the number of counterfeits is increasing. Therapeutic mAb products are commonly colourless injections or white freeze-dried powder, which are easy to make counterfeit (Loethen et al., 2015). Therapeutic mAbs are considered an attractive target for counterfeiters for another important reason: they are very expensive (Degardin et al., 2017). Therefore, strict control of therapeutic mAb products is required to fight against the counterfeit of mAbs (Frosch et al., 2019). Velpandian et al. did a protein analysis using Bradford assay and SDS-PAGE to confirm the presence of bevacizumab in 16 samples including six suspected and 10 others. The results suggested that the counterfeit bevacizumab can be preliminarily identified by simple methods (Velpandian et al., 2016). These simple methods can only differentiate the therapeutic mAbs from the protein-free counterfeits. Legrand et al. reported a strategy based on the concomitant use of capillary zone electrophoresis analysis (CZE-UV), size exclusion chromatography coupled to multi-angle light scattering (SEC-MALS) and liquid chromatography hyphenated to tandem mass spectrometry (LC-MS/MS) which enables the structural identification of mAbs in addition to comprehensive characterization and quantification in samples in potentially counterfeit samples (Legrand et al., 2022). Although the concomitant use of several analysis methods can provide an accurate result, it is complicated and takes a long time.

Various rapid analysis methods based on spectrum and chromatography can allow quick identification and quality assurance in pharmacies, medical facilities, pharmaceutical warehouses, etc., (Igne et al., 2015; Hattori et al., 2018; Tobias et al., 2021). These analysis methods usually take a few minutes to give a result, which will enhance public safety. In particular, Raman spectroscopy is fast and easy to operate and provides molecular fingerprints by detecting unique vibrations from atomic bonds within a molecular structure (McAvan et al., 2020). A Raman spectrum usually contains functional groups and an overall chemical arrangement that could be used for molecular structure analysis (Lanzarotta et al., 2020). As a result, the Raman technique has been widely employed in the pharmaceutical industry and in the random inspection of small molecule drugs (Lawson and Rodriguez, 2016). Several applications have been reported for mAb analysis. A Raman spectroscopy-based nutrient control strategy was developed to enable dual control of lactate and glucose levels for a fed-batch CHO cell culture process for mAb production, which could benefit both cell metabolism and mAb product quality (T et al., 2021). Yilmaz and his colleagues demonstrated the possibility of subclass-independent quantitative mAb prediction by Raman spectroscopy in real time (Yilmaz et al., 2020). The applicability of Raman spectroscopy to detect posttranslational modifications (PTMs) and degradation seen in mAbs in the manufacturing process has been investigated (McAvan et al., 2020). The reports highlighted Raman spectroscopy as a technique to suit the application of mAb analysis, as it is information-rich, minimally invasive, insensitive to water background and requires little to no sample preparation (Jones et al., 2019).

A long short-term memory (LSTM) network is a novel recurrent neural network (RNN) architecture in conjunction with an appropriate gradient-based learning algorithm (Yu et al., 2021). Unlike RNN networks, the LSTM network has a hidden inner state that enables applying the previous sequence input to a later calculation and avoids gradient disappearance through a gating unit system. Efficient processing of sequences of data and effective propagation of information along the sequence are commonly observed in LSTM networks. Therefore, LSTM networks have been successfully applied to process time-series and position-series data, for example, stemming from speech or video and natural language sentences. Some studies are currently attempting to use LSTM networks to analyse Raman spectra. Yu et al. presented Raman spectroscopy combined with an LSTM network to predict eight strains isolated from the marine organism *Urechis unicinctus* and compared them with a method using a normal convolutional neural network (CNN) (Yu et al., 2021). The proposed LSTM methods achieved average isolation-level accuracies greater than 94%, which is higher than that of the normal CNN network. Wang and his colleagues presented a rapid method to screen hepatitis B patients using serum Raman spectroscopy combined with LSTM networks. In a previous report, principal component analysis (PCA) was selected to extract key features of spectral data for dimensional reduction of the multidimensional spectrum, followed by training of the LSTM network. Meanwhile, a fully connected layer (FCL) was used for the classification of HBV (Wang et al., 2020).

Spectral characteristic extraction is very important in the signal preprocessing step (Fukuhara et al., 2019; Galeev et al., 2019; Ling et al., 2020). Original spectral data usually contain many invalid data points, which will cause a serious performance loss and low accuracy rate. Without preprocessing characteristic extraction, model training will be difficult. FCL is usually used as a classifier at the terminal of the model. However, artificial neural networks are nonlinear fitting models, and adding an FCL classifier may cause overfitting in some cases, especially in small-sample-size

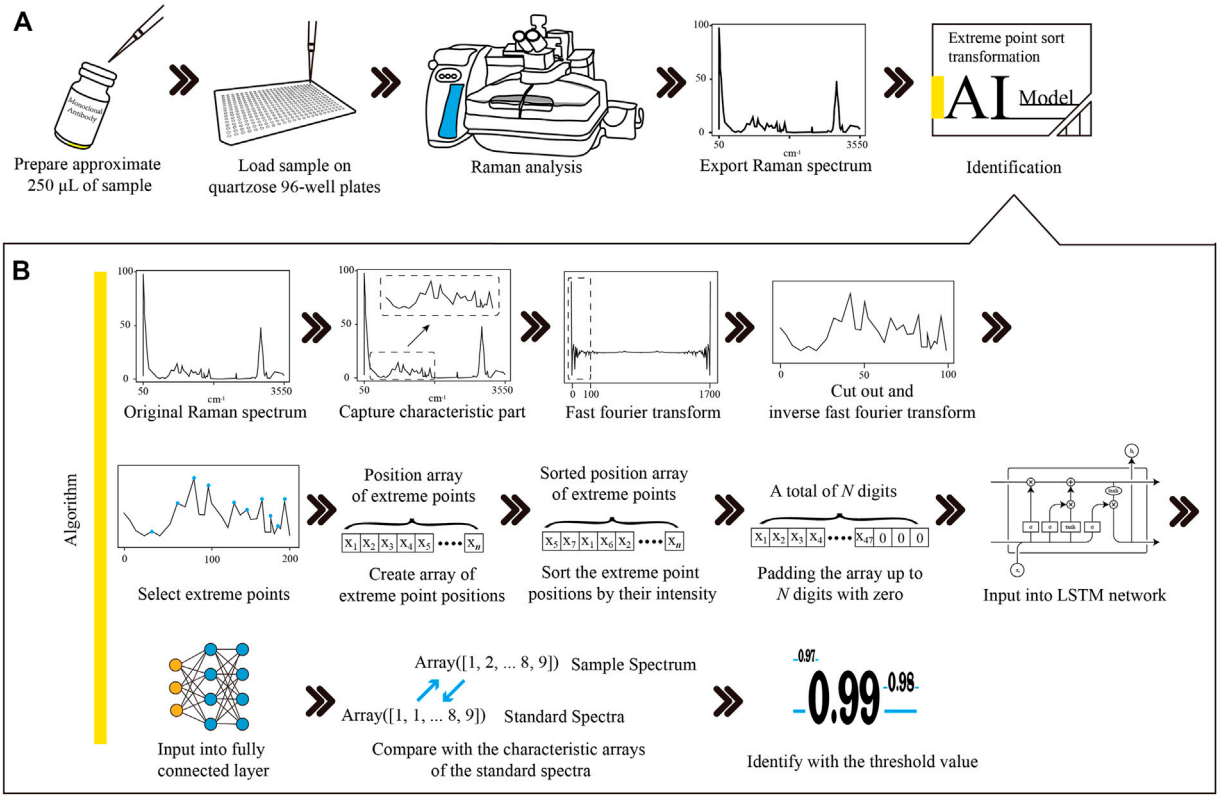

FIGURE 1 | The workflow of Raman-based therapeutic mAb identification and the procedures of Raman spectrum transformation combined with LSTM network modelling. **(A)** The therapeutic mAb sample was loaded into a quartzose 96-well plate. Raman analysis was performed to obtain the Raman spectrum of the sample. The Raman spectrum was exported into the CSV file and then input into the LSTM network model for identification. **(B)** The characteristic region of the Raman spectrum was extracted from the original spectrum. The noises of the characteristic region were removed, and the dimension was reduced with FFT and IFFT filtering. The positions of the extreme points were picked up and then sorted by the intensity of each point to create an array. The array was padded up to *N* digits with zero to satisfy the requirement of the input layer of the LSTM network model. The LSTM layer sequentially connected to the FCL formed the hidden layers of the model. The similarity of the sample spectrum and the standard spectrum was calculated by comparing their outputs from the FCL. The sample was identified as the therapeutic mAb, and the similarity value was higher than the threshold. mAb, monoclonal antibody; LSTM, long short-term memory; CSV, comma separated value; FFT, fast Fourier transformation; IFFT, inverse fast Fourier transformation; FCL, fully connected layer.

training. In the present study, we introduce a novel Raman spectrum detection approach with LSTM networks for therapeutic mAb identification. First, fast Fourier transformation (FFT) and inverse fast Fourier transformation (IFFT) are performed on the spectral characteristic region to remove spectral noise and reduce dimensions. Extreme point sort transformation is a critical step to convert the spectrum into a sequence array that involves the peak absolute positions and their relative intensities. The sequence array can be considered a number-labelled sentence, which fits the LSTM network. LSTM networks are well trained and then employed to extract the characteristics of the sequence array deeply into a characteristic array. The extracted characteristic array will be compared with the characteristic arrays extracted from standard spectra using the same method to obtain a similarity score. The sample will be identified as a therapeutic mAb class where the similarity score is higher than the threshold value of the therapeutic mAb class.

METHODS

Therapeutic Monoclonal Antibodies

A total of 15 therapeutic mAbs from seven manufacturers, including adalimumab, bevacizumab, ranibizumab, tocilizumab, evolocumab, secukinumab, rituximab, trastuzumab, pertuzumab, denosumab, ixekizumab, ustekinumab, guselkumab, emicizumab, and etanercept, were selected for the study. Eleven effect targets and four protein formats of mAbs were involved when choosing therapeutic mAbs. Information on the 15 therapeutic mAbs is shown in **Supplementary Table S1**. They were labelled from 0 to 14 for artificial intelligence identification.

Raman Analysis

As shown in **Figure 1A**, approximate 250 μL of therapeutic mAb injections were loaded into a 96-well quartzose plate for Raman scanning. Sufficient injection fluid had to be added to make the fluid level flush with the rim of the tiny cup. ThermoFisher

Scientific DXR confocal Raman microscopy (Thermo Fisher Scientific Inc., U.S.) was employed for analysis, which was equipped with a 20× objective, a 532 nm laser and a 532 nm filter. A full spectral range of 57–3,417 cm^{-1} was set to acquire the Raman spectrum. Data acquisition was performed using ThermoFisher OMIC 8.3 software (Thermo Fisher Scientific Inc., U.S.) with a 10 mW laser power, 10 s exposure time, and 20 scans. For each therapeutic mAb, 18 samples in three batches were randomly selected to collect spectra. Raman spectra were acquired from five random points on each sample. Finally, a total of 1,350 Raman spectra were obtained to build a Raman spectrum database for 15 therapeutic mAbs.

Dataset Preparation

Spectra were exported as comma-separated values (CSV) files using ThermoFisher OMIC 8.3 software. The CSV file contained the Raman shift values and the numeric value of the intensity for every single point of the Raman spectrum. These numeric values of both Raman shift and intensity in CSV files were read by Python v3.8.5 and then inserted into a MySQL v5.7.20 (MySQL AB, Sweden) database table to create an in-house dataset with some basic information, such as mAb name, specifications, and date of analysis. Numeric labels of data from 0 to 14 were assigned to each mAb. Before data processing, all numeric value data with labels were exported from the database into a text file to obtain high loading performance.

Data Transformation

Here, we present an extreme point sort transform for the array of Raman spectra, which transforms array-type spectrum data into a list of sequence numbers. First, the characteristic part of the mAbs, ranging from 100–1,800 cm^{-1} in the Raman spectrum, was captured. Then, noise removal and dimensionality reduction were performed on the characteristic region using FFT and IFFT. The FFT formula is shown as follows:

$$X(k) = \sum_{n=0}^{N-1} x(n) e^{-j\left(\frac{2\pi}{N}\right)nk} \quad (k = 0, 1, \ldots, M-1) \tag{1}$$

where k is the consecutive integers from 0 to M−1, n is the sequence number of the time-domain signal array, and M is the total number of array elements.

After FFT processing, the low-frequency range was picked to perform IFFT to obtain a noise removed and a low-dimensional spectrum. The IFFT formula is shown as follows:

$$\mathrm{x(n)} = \frac{1}{N} \sum_{n=0}^{N-1} X(k) e^{j\left(\frac{2\pi}{N}\right)nk} \quad (n = 0, 1, \ldots, N-1) \tag{2}$$

where n is the consecutive integers from 0 to N−1, k is the sequence number of the frequency-domain signal array, and N is the total number of the low-frequency range array elements.

The positions of extreme points of the spectrum were extracted using the Scipy library. The first extreme point was removed and then sorted by their intensities in descending order. The extreme point array was padded up to N digitals with zero to match the input dimension of the model.

Data visualization after each processing step was performed using the Matplotlib library. The data labels were converted into one-hot labels using the Keras library. The dataset containing all numeric values and labels was split randomly into a training dataset and validation dataset with a split ratio of 0.8, which means that 80% of the data were used for model training and the other 20% were used for model validation. The test dataset was created using 20 additional Raman spectra of each therapeutic mAb. These spectra were never used before as a test set.

Long Short-Term Memory Modelling

As shown in **Figure 2**, the training process was marked within a light blue full line box, and the predicting process was marked within a green dashed line box. The well-trained models were employed for spectral characteristic extraction to obtain a characteristic array, which was compared to the characteristic arrays of standard spectra for final identification.

All training and predictions were carried out on a SuperMicro 7049GR GPU server equipped with Dual Intel(R) Xeon(R) Gold 6,149 CPUs, 128 Gb of DDR4 RAM and Quad Nvidia RTX 3090 24 Gb graphics cards. The operating system was the 64-bit CentOS Linux system v7.5. TensorFlow v2.0.0 was employed to train and validate the LSTM network models.

As shown in **Supplementary Table S2**, the LSTM network model contains one embedding layer, one bidirectional LSTM layer, one FCL, one dropout layer and one output layer to form the output prediction. The dimension of the LSTM layer is 64. The numbers of nodes in the FCL and output layer were 32 and 15, respectively. The activation function of the FCL and output layer were the rectified linear unit (ReLU) function and Softmax function, respectively. The softmax function defined in **Eq. 3** was applied in the last layer to produce the prediction probability over the 15 output classes (Hsieh et al., 2020).

$$f(s)_i = \frac{e^{s_i}}{\sum_{j=1}^{C} e^{s_j}} \tag{3}$$

where s_i are the scores inferred by the net for each class in C.

The categorical cross-entropy was selected as the loss function, which was defined in **Eq. 4**. The goal of the network is to minimize CE.

$$\mathrm{CE} = -log \frac{e^{s_p}}{\sum_{j}^{C} e^{s_j}} \tag{4}$$

where s_p is the score for the positive class.

Adam is selected as the optimizer. The learning rate was set as 0.001, and the number of epochs was set as one to five.

Similarity Scoring

Characteristics of the Raman spectrum were extracted as a characteristic array using extreme point sort transformation and the LSTM network model. The characteristic array of the sample spectrum was compared with that of standard spectra to obtain the cosine similarity score using the Sklearn library. The threshold value of the cosine similarity score was set as the lowest score, which was calculated by comparing each standard spectrum to the remaining standard spectra. The sample

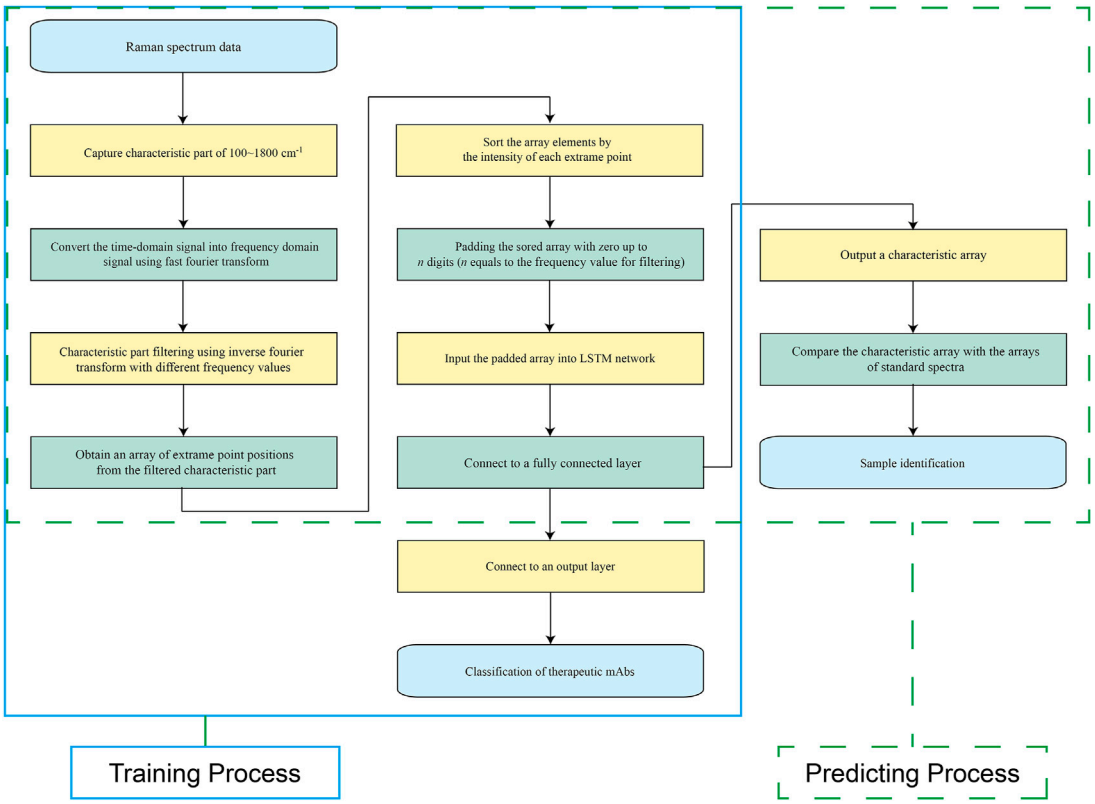

FIGURE 2 | Schematic view of the training process and prediction process. The training process is marked with a light blue full line box, and the prediction process is marked with a green dashed line box.

spectrum was identified when the cosine similarity score was higher than the threshold value.

Production of Simulative Spectra

Spectral peak drift, random noise and fluorescence interference were considered to test the robustness of the method. Elements in the spectral intensity array were integrally shifted to the left or right with 1–20 digitals to simulate spectral peak drift of 1–20 cm^{-1}. The blank positions produced while shifting were filled with the adjacent value. For simulated random noise on the spectrum, every single element in the spectral intensity array was multiplied by a random percentage. The range of the random percentage is 60–100% or 100–140%. For simulated fluorescence interference, a positive half-sine part wave overlapped in the 0–1800 cm^{-1} range of the original spectrum. The sine wave amplitude was set as 60–140% of the maximum peak intensity. The signal frequency and sampling frequency were both set as 1. The sine wavelength was set as a random integer in the range of 3,600–7,200. The reverse arrangement of the elements in 0–1800 digital positions was picked up as a positive half-sine part to create the simulative spectrum.

Evaluation of Prediction

The loss, precision, accuracy and recall were used to evaluate the model since they are commonly used in most cases for evaluations. The loss values were calculated using the categorical cross-entropy formula described above. The precision, accuracy and recall were calculated as follows:

$$Precision = \frac{tp}{tp + fp} \tag{5}$$

$$Accuracy = \frac{tp + tn}{tp + tn + fp + fn} \tag{6}$$

$$Recall = \frac{tp}{tp + fn} \tag{7}$$

where tp is true positives, fp is false-positives, tn is true negatives, and fn is false negatives.

A confusion matrix was established to investigate the classification performance. Each column of the matrix stands for a predicted label, while each row represents a true label. The receiver operating characteristic (ROC) curve was drawn with the true positive rate and false-positive rate.

Tests of the prediction performance for the present method and ThermoFisher OMNIC 8.3 software built-in method (analysed on full spectrum and characteristic region, respectively) were performed using a total of 300 Raman spectra (20 Raman spectra for each therapeutic mAb) test set with labels. The ThermoFisher OMNIC 8.3 software built-in method was used to match the spectrum with the user's

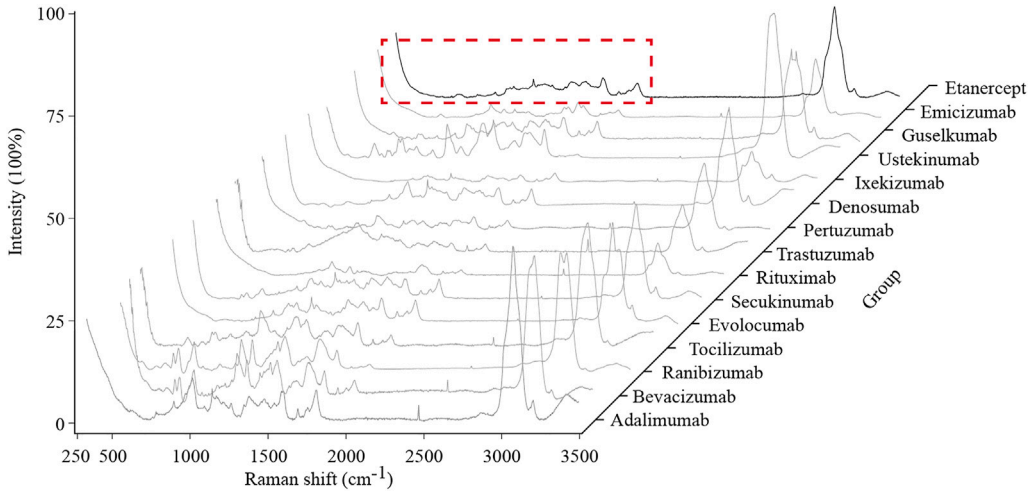

FIGURE 3 | Typical Raman spectra of the 15 therapeutic mAbs. The characteristic region of the Raman spectrum is marked with a red dashed line box.

standard spectrum library. The match parameter of the analysis region was set as the full spectrum or a range of 100–1800 cm^{-1} for full spectrum analysis or characteristic region analysis, respectively.

Sample Identification

A total of 30 samples, including 15 therapeutic mAb injections, three biochemical drug and biological product injections, and 12 chemical drug injections, were selected for the identification test using the present method. A sample is identified when the similarity score is higher than the threshold value of the standard spectrum. If the similarity score was lower than every threshold value, it was identified as "not matched".

RESULTS

Identification Approach

As shown in **Figure 1**, an optimized Raman identification approach for therapeutic mAbs was proposed. Approximately 250 μL of sample was loaded on a quartzose 96-well plate, followed by Raman analysis to obtain the spectrum. The spectral data were exported into a CSV file with 3,417 data points for data analysis.

Characteristic Region Acquirement

Fifteen typical spectra of therapeutic mAbs are shown in **Figure 3**. By comparing each spectrum manually, a range of 100–1800 cm^{-1} was selected as the characteristic region, which is information-rich.

Data Transformation

The data visualizations of the extreme point sort transformation of three therapeutic antibodies are shown in **Figure 4**, which provides insights into the operating mode of the novel data transformation and the conversion process of spectral features. As shown in **Figure 4**, the original Raman spectrum had a full scan range of 57–3,417 cm^{-1}. After interception, a characteristic region with a range of 100–1800 cm^{-1} was drawn as a new subspectrum (**Figure 4**, Line 4). The target dimensional value for each therapeutic mAb is listed in **Table 1**, which was used for spectral dimensionality reduction. The filtered spectrum and the extreme points demonstrated that approximately 10 extreme points in each filtered spectrum could be extracted as a sequence array. The elements of the extreme point positions were sorted by their corresponding intensity. Finally, the sorted array was padded with zero to the digitals of the target dimensional value for input of the LSTM network (**Figure 4**, Line 7).

Model Training

A total of 15 models were trained for the extraction of spectral characteristics. The primary parameters and training results of the optimized model for the identification of therapeutic mAbs are listed in **Table 1**. The optimized target dimensional values were set from 35 to 53. The epoch for training had a range of one to five. The accuracy and validation accuracy of the 15 models ranged from 0.8644 to 0.9975 and 0.9796 and 0.9983, respectively. The optimized threshold values ranged from 0.97 to 0.99.

Robustness Test

To test the robustness of the algorithm, a total of 36,000 simulated spectra were created manually. The average accuracy results (n = 20) are shown in **Figure 5A**. Fourteen of fifteen therapeutic mAb simulated spectra with an offset of wavenumbers under ±5 cm^{-1} could be identified using the present method to achieve an accuracy over 95%. The simulated spectra of therapeutic mAbs labelled 0, 1, 2, and 6 were correctly identified, while the offsets of the wavenumber were under ±10 cm^{-1}. As shown in **Figure 5B**, all simulated spectra with a random incremental range of 10% or −10% intensity could be identified and achieved an accuracy over

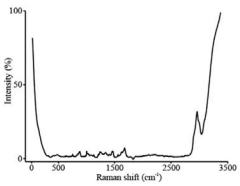

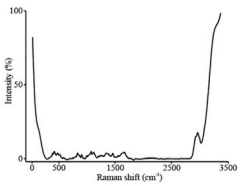

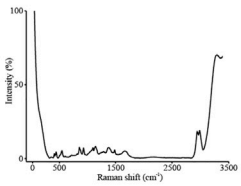

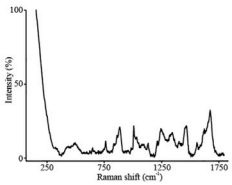

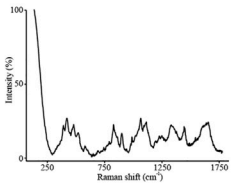

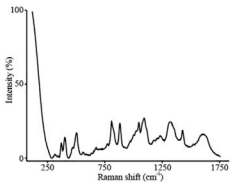

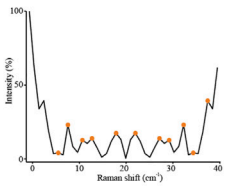

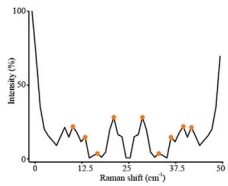

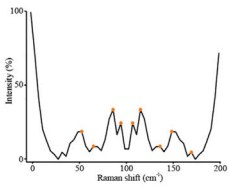

Label	0	1	2
Sample name	Adalimumab	Bevacizumab	Ranibizumab
Original raman spectrum			
Characteristic part of the spectrum			
Filtered spectrum with exetreme points			
Exetreme point positon array	[6, 8, 11, 13, 18, 22, 27, 29, 32, 34, 37]	[10, 13, 16, 20, 27, 31, 34, 37, 39]	[13, 16, 21, 23, 26, 28, 33, 36, 41]
Sorted and padded array	[37, 8, 32, 18, 22, 13, 27, 11, 29, 6, 34, 0, 0, 0, 0, 0, 0, 0, 0, 0, 0, 0, 0, 0, 0, 0, 0, 0, 0, 0, 0, 0, 0, 0, 0, 0, 0, 0, 0, 0]	[20, 27, 10, 37, 39, 13, 34, 16, 31, 0, 0, 0, 0, 0, 0, 0, 0, 0, 0, 0, 0, 0, 0, 0, 0, 0, 0, 0, 0, 0, 0, 0, 0, 0, 0, 0, 0, 0, 0, 0, 0, 0, 0, 0, 0, 0, 0]	[21, 28, 23, 26, 13, 36, 16, 33, 41, 0, 0, 0, 0, 0, 0, 0, 0, 0, 0, 0, 0, 0, 0, 0, 0, 0, 0, 0, 0, 0, 0, 0, 0, 0, 0, 0, 0, 0, 0, 0, 0, 0, 0, 0, 0, 0, 0, 0, 0]

FIGURE 4 | Visualization examples of the original Raman spectra, characteristic region of Raman spectra, characteristic region converted by extreme point transformation, sorted, and padded array of adalimumab, bevacizumab and ranibizumab.

TABLE 1 | The primary parameters and training results of the optimized model for the identification of therapeutic monoclonal antibodies.

Label	Dimensional value	Epoch	Loss	Accuracy	Validation loss	Validation accuracy	Threshold
0	40	3	0.0297	0.9975	0.0104	0.9975	0.99
1	47	5	0.0239	0.9929	0.0168	0.9948	0.99
2	49	1	0.3597	0.8839	0.0364	0.9869	0.99
3	42	5	0.0396	0.9875	0.0185	0.9915	0.99
4	48	3	0.0316	0.9909	0.0063	0.9983	0.99
5	46	1	0.4435	0.8605	0.0805	0.9694	0.98
6	41	2	0.0726	0.9774	0.0286	0.9906	0.99
7	35	1	0.4377	0.8644	0.0585	0.9796	0.99
8	42	3	0.0556	0.9821	0.0291	0.9888	0.97
9	53	3	0.0451	0.9853	0.00204	0.9908	0.99
10	39	2	0.0902	0.9729	0.0379	0.9856	0.99
11	47	3	0.0394	0.988	0.0096	0.9973	0.99
12	47	1	0.3216	0.9027	0.0371	0.9877	0.97
13	40	1	0.3225	0.9041	0.0203	0.9903	0.99
14	35	1	0.4184	0.8676	0.0658	0.9794	0.99

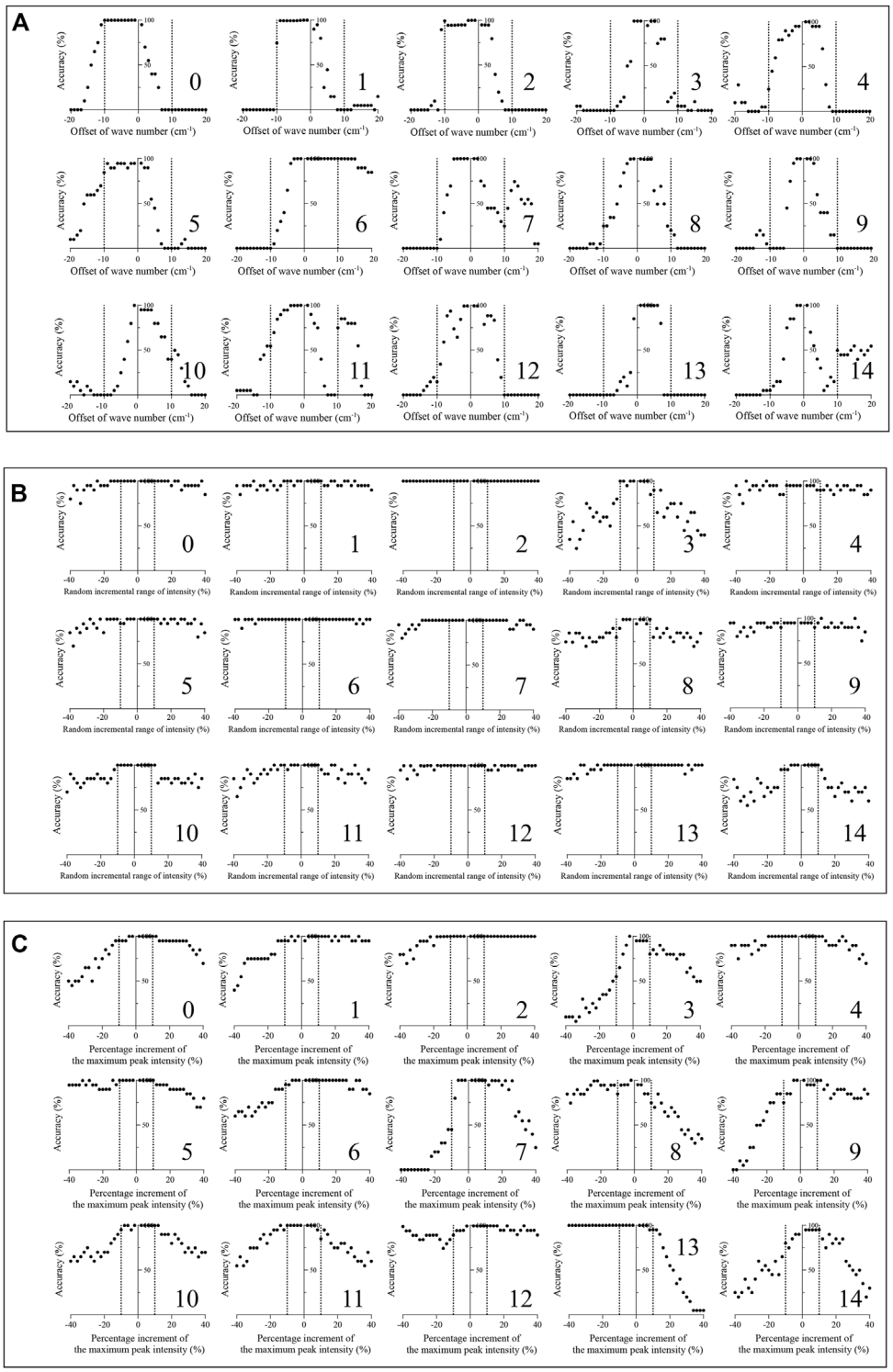

FIGURE 5 | Robustness test of the present algorithm on 15 therapeutic mAbs. **(A)** The classification effect of the present algorithm against simulated spectral peak drift (n = 20); **(B)** The classification effect of the present algorithm against simulated spectral noise (n = 20); **(C)** The classification effect of the presented method against simulated spectral florescence interference (n = 20).

95%. The simulated spectra of therapeutic mAbs labelled two could be correctly identified, while the random incremental range of intensity was in the range of ±40%. As shown in **Figure 5C**, all simulated spectra with a 10% or −10% increment of the maximum peak intensity could be identified and achieved an accuracy over 95%. The results indicated that

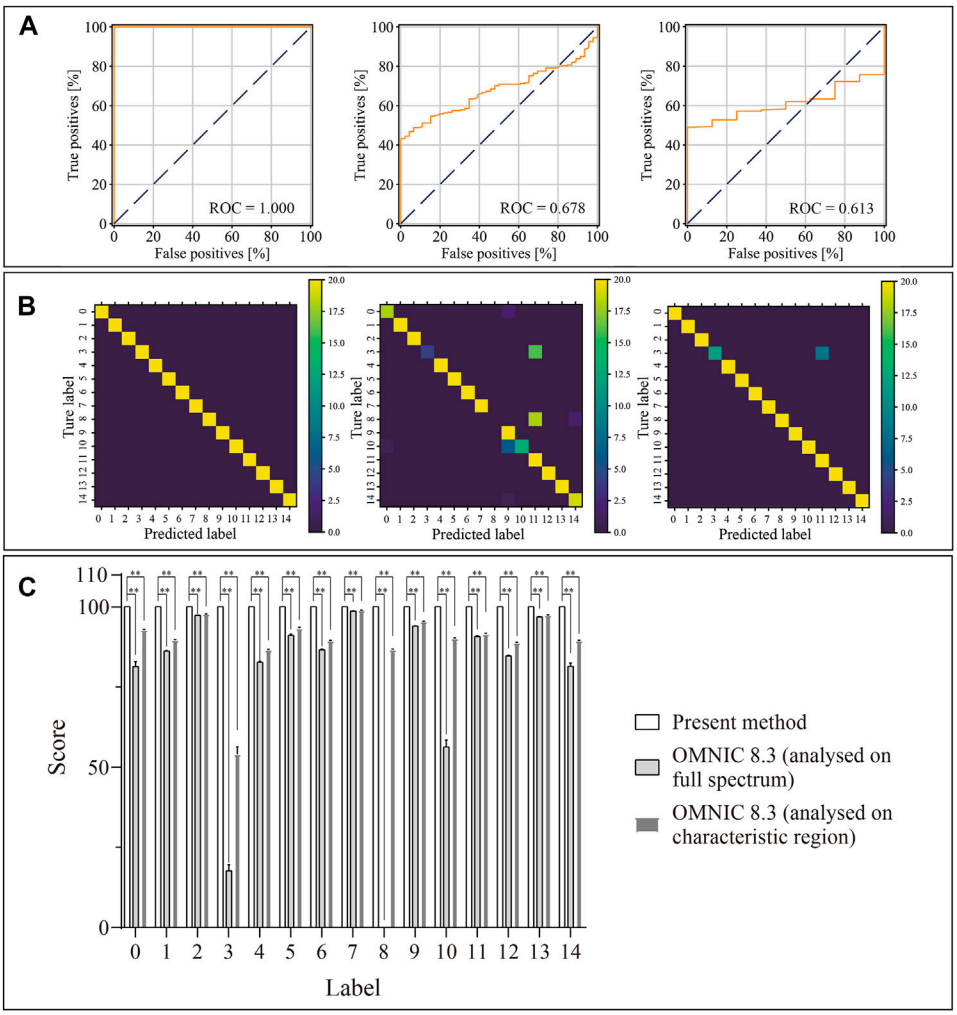

FIGURE 6 | Predicted results of the 15 therapeutic mAbs using the presented method, OMNIC 8.3 software (analysed on the full spectrum) and OMNIC 8.3 software (analysed on the characteristic region). **(A)** Receiver operating characteristic curves of the present algorithm, OMNIC 8.3 software build-in algorithm (analysed on full spectrum) and OMNIC 8.3 software build-in algorithm (analysed on characteristic region); **(B)** Confusion matrixes of the presented method, OMNIC 8.3 software build-in algorithm (analysed on full spectrum) and OMNIC 8.3 software build-in algorithm (analysed on characteristic region) are plotted based on the matching extent between the predicted labels and true labels; **(C)** The matching scores are calculated by model prediction using test samples (n = 20). $^{**}p < 0.01$.

the present algorithm had good robustness against spectral peak drift, random noise and fluorescence interference.

Model Evaluation

Figure 6 shows the ROC curves of the prediction results, confusion matrixes and similarity scores. As shown in **Figure 6A**, the areas under the curve (AUC) values of the present algorithm, OMNIC 8.3 software built-in algorithm analysed on the full spectrum and analysed on the characteristic region were 1.000, 0.678 and 0.613, respectively. In the confusion matrix, the diagonal shows the percent of correct prediction records for each therapeutic mAb, and the off-diagonals show the percent of misclassifications for each therapeutic mAb (**Figure 6B**). The similarity scores of classification for 15 therapeutic mAbs using the present algorithm were 100. The similarity scores for 15 therapeutic mAbs using OMNIC 8.3 (analysed on the full spectrum) were 81.40 ± 1.40, 86.13 ± 0.17, 97.27 ± 0.04, 17.85 ± 1.84, 82.70 ± 0.22, 91.07 ± 0.32, 86.59 ± 0.21, 98.59 ± 0.02, 0, 93.93 ± 0.08, 56.36 ± 2.13, 90.74 ± 0.17, 84.65 ± 0.19, 96.83 ± 0.04 and 81.41 ± 0.98. The similarity scores for 15 therapeutic mAbs using OMNIC 8.3 (analysed in the characteristic region) were 92.76 ± 0.11, 89.58 ± 0.13, 97.68 ± 0.04, 54.07 ± 2.27, 86.49 ± 0.18, 93.20 ± 0.26, 89.33 ± 0.14, 98.83 ± 0.02, 86.63 ± 0.17, 95.32 ± 0.06, 90.10 ± 0.15, 91.47 ± 0.16, 88.71 ± 0.14, 97.36 ± 0.03 and 89.37 + 0.16. All groups compared with the relative present algorithm group had extremely remarkable differences ($p < 0.001$). The results suggested a high classification performance for the present algorithm. These results suggested that the extreme point sort transformation combined with the LSTM network algorithm has an excellent classification performance for Raman-based therapeutic mAb identification.

TABLE 2 | Application of the presented method to identify 30 injections, including 15 monoclonal antibodies and 15 other injections.

Sample ID	Category	Sample	Prediction	Similarity score	Matched
1	Therapeutic antibody	Adalimumab	Adalimumab	0.999	Yes
2		Bevacizumab	Bevacizumab	0.998	Yes
3		Ranibizumab	Ranibizumab	0.998	Yes
4		Tocilizumab	Tocilizumab	0.999	Yes
5		Iloeuvumab	Iloeuvumab	0.997	Yes
6		Scuciumab	Scuciumab	0.990	Yes
7		Rituximab	Rituximab	0.992	Yes
8		Trastuzumab	Trastuzumab	0.999	Yes
9		Pertuzumab	Pertuzumab	0.988	Yes
10		Denosumab	Denosumab	0.996	Yes
11		Ixekizumab	Ixekizumab	0.999	Yes
12		Ustekinumab	Ustekinumab	0.997	Yes
13		Guselkumab	Guselkumab	0.986	Yes
14		Almezumab	Almezumab	0.998	Yes
15		Etanercept	Etanercept	0.999	Yes
16	Biochemical drug and biological product	Human immunoglobulin for intravenous injection	NM	—	—
17		Tetanus immunoglobulin injection	NM	—	—
18		Atosiban acetate injection	NM	—	—
19	Chemical drug	Potassium and magnesium aspartate injection	NM	—	—
20		Compound aminobarbital injection	NM	—	—
21		Dopamine hydrochloride injection	NM	—	—
22		Lidocaine hydrochloride injection	NM	—	—
23		Tramadol hydrochloride injection	NM	—	—
24		Aminotoluene acid injection	NM	—	—
25		Epinephrine hydrochloride injection	NM	—	—
26		Bupivacaine hydrochloride injection	NM	—	—
27		Potassium chloride injection	NM	—	—
28		Sodium chloride injection	NM	—	—
29		Invert sugar injection	NM	—	—
30		Sterile water for injection	NM	—	—

NM: not matched.

Sample Identification

A total of 30 samples, including 15 therapeutic mAb injections and 15 other injections, were tested using the present method. As shown in **Table 2**, 15 therapeutic mAbs were correctly identified, and 15 non-antibody samples were identified as "not matched".

DISCUSSION

Raman spectroscopy has been increasingly studied for protein sample analysis, which could indeed offer the possibility of detecting protein bands and chemicals with few preparations and little cost for a few seconds to a few minutes of measurement (Li et al., 2012; Neugebauer et al., 2015; Degardin et al., 2017; Zhang et al., 2019). The injection of therapeutic mAb usually contains antibody proteins and pharmaceutical excipients (Singh et al., 2018; Grilo and Mantalaris, 2019). They are both important components of the injection. The characteristic responses of complex components could be obtained as a spectrum using Raman spectroscopy (Wang et al., 2018). The antibody proteins and pharmaceutical excipients equally contribute to the spectrum. Therefore, it is possible to screen therapeutic mAbs utilizing Raman spectroscopy. However, most Raman peaks of therapeutic mAbs have lower intensities than those of chemical drugs. As a result, the therapeutic mAb spectra could not be identified using the previous algorithm, which is suitable for chemical drugs.

For the analysis method, LSTM networks achieve a better classification effect than other methods (Fan et al., 2019). A bidirectional long short-term memory (Bi-LSTM) network is the process of making any neural network have sequence information in both directions backwards (future to past) or forwards (past to future) (Neishabouri et al., 2021). Bidirectional input flows in two directions, making a Bi-LSTM network preserve the future and past information. In a previous study, 1,200 data points of the Raman spectrum were directly input into the LSTM network, which caused 800 epochs of training (Yu et al., 2021). Excessive training epochs will lead to overfitting of the model. Like sample pretreatment in the field of chemical analysis, preprocessing of spectral data plays an important role in data analysis. In the present study, we provide an extreme point sort transformation to convert the characteristic region of the Raman spectrum to a sequence array. The spectral peak positions and relative intensities, two critical spectral characteristics, were involved in the array. This is an efficient transformation that even the Raman analysis under the influence, and only a few effects would be observed at the identification stage.

FCLs and the softmax function are commonly used in classification models. FCLs are added at the end of the sequence model to make the model end-to-end trainable. The

FCLs learn a function between the high-level features given as an output from the previous layers. The softmax function transforms any input values into values between 0 and 1 so that they can be interpreted as probabilities. However, inappropriate parameters of FLCs may lead to overfitting of the model, which will enable counterfeit drugs to be identified as genuine. The result is not accepted in the application of counterfeit drug identification. Therefore, the FLC was only employed in the training process for the fitting model. Then, the model extracted the characteristics from sample spectra followed by calculating the similarity score with standard spectra to classify samples with the threshold value. This step reduces the false-positive rate to avoid identifying the counterfeit drug as genuine.

In summary, we propose a novel extreme port sort transformation combined with an LSTM network algorithm to identify 15 therapeutic mAbs with Raman spectra. The extreme port sort transformation converted the characteristic region of the Raman spectrum into a sequence array containing the original spectral peaks and intensity profile. The characteristic array was extracted from the sequence array by the LSTM network model. The final identification was based on the comparison of the characteristic array. The algorithm was successfully applied in therapeutic mAb identification using an independent test dataset. The algorithm was compared with ThermoFisher OMNIC 8.3 build-in spectrum matching algorithms, and the results indicated that the present algorithm provides a better classification performance.

DATA AVAILABILITY STATEMENT

The datasets generated for this study can be found here: https://github.com/ttelva2/EPSTLSTM.git.

AUTHOR CONTRIBUTIONS

HS, GC and JL contributed to the conception and design of the study. JL, LZ, MX, XW and DM performed the Raman analysis and the method tests. JL organized the database, did the algorithm research and wrote the draft of the manuscript. GC and HS contributed to the manuscript's revision.

FUNDING

This research was financially supported by Shanghai Municipal Drug Administration Research Projects (Grand No. ZX-2021-07) and Shanghai Public Service Platform for Research and Development Projects (Grand No. 19DZ2294600).

SUPPLEMENTARY MATERIAL

The Supplementary Material for this article can be found online at: https://www.frontiersin.org/articles/10.3389/fchem.2022.887960/full#supplementary-material

REFERENCES

Castelli, M. S., McGonigle, P., and Hornby, P. J. (2019). The Pharmacology and Therapeutic Applications of Monoclonal Antibodies. *Pharmacol. Res. Perspect.* 7, e00535. doi:10.1002/prp2.535

Dégardin, K., Desponds, A., and Roggo, Y. (2017). Protein-based Medicines Analysis by Raman Spectroscopy for the Detection of Counterfeits. *Forensic Sci. Int.* 278, 313–325. doi:10.1016/j.forsciint.2017.07.012

Ettah, I., and Ashton, L. (2018). Engaging with Raman Spectroscopy to Investigate Antibody Aggregation. *Antibodies* 7, 24. doi:10.3390/antib7030024

Eyster, T. W., Talwar, S., Fernandez, J., Foster, S., Hayes, J., Allen, R., et al. (2021). Tuning Monoclonal Antibody Galactosylation Using Raman Spectroscopy-Controlled Lactic Acid Feeding. *Biotechnol. Prog.* 37, e3085. doi:10.1002/btpr.3085

Fan, X., Ming, W., Zeng, H., Zhang, Z., and Lu, H. (2019). Deep Learning-Based Component Identification for the Raman Spectra of Mixtures. *Analyst* 144, 1789–1798. doi:10.1039/c8an02212g

Frosch, T., Wyrwich, E., Yan, D., Domes, C., Domes, R., Popp, J., et al. (2019). Counterfeit and Substandard Test of the Antimalarial Tablet Riamet by Means of Raman Hyperspectral Multicomponent Analysis. *Molecules* 24, 3229. doi:10.3390/molecules24183229

Fukuhara, M., Fujiwara, K., Maruyama, Y., and Itoh, H. (2019). Feature Visualization of Raman Spectrum Analysis with Deep Convolutional Neural Network. *Analytica Chim. Acta* 1087, 11–19. doi:10.1016/j.aca.2019.08.064

Galeev, R. R., Semanov, D. A., Galeeva, E. V., Falaleeva, T. S., Aryslanov, I. R., Saveliev, A. A., et al. (2019). Peak Window Correlation Method for Drug Screening Using Raman Spectroscopy. *J. Pharm. Biomed. Anal.* 163, 9–16. doi:10.1016/j.jpba.2018.09.041

Grilo, A. L., and Mantalaris, A. (2019). The Increasingly Human and Profitable Monoclonal Antibody Market. *Trends Biotechnol.* 37, 9–16. doi:10.1016/j.tibtech.2018.05.014

Hattori, Y., Seko, Y., Peerapattana, J., Otsuka, K., Sakamoto, T., and Otsuka, M. (2017). Rapid Identification of Oral Solid Dosage Forms of Counterfeit Pharmaceuticals by Discrimination Using Near-Infrared Spectroscopy. *Bme* 29, 1–14. doi:10.3233/bme-171708

Hsieh, C.-H., Li, Y.-S., Hwang, B.-J., and Hsiao, C.-H. (2020). Detection of Atrial Fibrillation Using 1D Convolutional Neural Network. *Sensors* 20, 2136. doi:10.3390/s20072136

Igne, B., Talwar, S., Feng, H., Drennen, J. K., and Anderson, C. A. (2015). Near-Infrared Spatially Resolved Spectroscopy for Tablet Quality Determination. *J. Pharm. Sci.* 104, 4074–4081. doi:10.1002/jps.24618

Jones, R. R., Hooper, D. C., Zhang, L., Wolverson, D., and Valev, V. K. (2019). Raman Techniques: Fundamentals and Frontiers. *Nanoscale Res. Lett.* 14, 231. doi:10.1186/s11671-019-3039-2

Lanzarotta, A., Kimani, M. M., Thatcher, M. D., Lynch, J., Fulcher, M., Witkowski, M. R., et al. (2020). Evaluation of Suspected Counterfeit Pharmaceutical Tablets Declared to Contain Controlled Substances Using Handheld Raman Spectrometers. *J. Forensic. Sci.* 65, 1274–1279. doi:10.1111/1556-4029.14287

Lawson, L. S., and Rodriguez, J. D. (2016). Raman Barcode for Counterfeit Drug Product Detection. *Anal. Chem.* 88, 4706–4713. doi:10.1021/acs.analchem.5b04636

Legrand, P., Dembele, O., Alamil, H., Lamoureux, C., Mignet, N., Houzé, P., et al. (2022). Structural Identification and Absolute Quantification of Monoclonal Antibodies in Suspected Counterfeits Using Capillary Electrophoresis and Liquid Chromatography-Tandem Mass Spectrometry. *Anal. Bioanal. Chem.* 414, 2699–2712. doi:10.1007/s00216-022-03913-y

Li, H., Er Saw, P., and Song, E. (2020). Challenges and Strategies for Next-Generation Bispecific Antibody-Based Antitumor Therapeutics. *Cell Mol. Immunol.* 17, 451–461. doi:10.1038/s41423-020-0417-8

Li, S.-X., Chen, Q.-Y., Zhang, Y.-J., Liu, Z.-M., Xiong, H.-L., Guo, Z.-Y., et al. (2012). Detection of Nasopharyngeal Cancer Using Confocal Raman

Spectroscopy and Genetic Algorithm Technique. *J. Biomed. Opt.* 17, 125003. doi:10.1117/1.JBO.17.12.125003

Ling, J., Li, G., Shao, H., Wang, H., Yin, H., Zhou, H., et al. (2020). Helix Matrix Transformation Combined with Convolutional Neural Network Algorithm for Matrix-Assisted Laser Desorption Ionization-Time of Flight Mass Spectrometry-Based Bacterial Identification. *Front. Microbiol.* 11, 565434. doi:10.3389/fmicb.2020.565434

Loethen, Y. L., Kauffman, J. F., Buhse, L. F., and Rodriguez, J. D. (2015). Rapid Screening of Anti-infective Drug Products for Counterfeits Using Raman Spectral Library-Based Correlation Methods. *Analyst* 140, 7225–7233. doi:10.1039/c5an01679g

McAvan, B. S., Bowsher, L. A., Powell, T., O'Hara, J. F., Spitali, M., Goodacre, R., et al. (2020). Raman Spectroscopy to Monitor Post-Translational Modifications and Degradation in Monoclonal Antibody Therapeutics. *Anal. Chem.* 92, 10381–10389. doi:10.1021/acs.analchem.0c00627

Neishabouri, A., Wahl, N., Mairani, A., Köthe, U., and Bangert, M. (2021). Long Short-term Memory Networks for Proton Dose Calculation in Highly Heterogeneous Tissues. *Med. Phys.* 48, 1893–1908. doi:10.1002/mp.14658

Neugebauer, U., Rösch, P., and Popp, J. (2015). Raman Spectroscopy towards Clinical Application: Drug Monitoring and Pathogen Identification. *Int. J. Antimicrob. Agents* 46 (Suppl. 1), S35–S39. doi:10.1016/j.ijantimicag.2015.10.014

Singh, S., Kumar, N. K., Dwiwedi, P., Charan, J., Kaur, R., Sidhu, P., et al. (2018). Monoclonal Antibodies: A Review. *Ccp* 13, 85–99. doi:10.2174/1574884712666170809124728

Tobias, S., Shapiro, A. M., Grant, C. J., Patel, P., Lysyshyn, M., and Ti, L. (2021). Drug Checking Identifies Counterfeit Alprazolam Tablets. *Drug and Alcohol Dependence* 218, 108300. doi:10.1016/j.drugalcdep.2020.108300

Velpandian, T., Nath, M., Laxmi, M., and Halder, N. (2016). Finger Printing of Counterfeit Bevacizumab and Identifying it before Clinical Use. *Natl. Med. J. India* 29, 326

Wang, W.-t., Zhang, H., Yuan, Y., Guo, Y., and He, S.-x. (2018). Research Progress of Raman Spectroscopy in Drug Analysis. *AAPS PharmSciTech* 19, 2921–2928. doi:10.1208/s12249-018-1135-8

Wang, X., Tian, S., Yu, L., Lv, X., and Zhang, Z. (2020). Rapid Screening of Hepatitis B Using Raman Spectroscopy and Long Short-Term Memory Neural Network. *Lasers Med. Sci.* 35, 1791–1799. doi:10.1007/s10103-020-03003-4

Yilmaz, D., Mehdizadeh, H., Navarro, D., Shehzad, A., O'Connor, M., and McCormick, P. (2020). Application of Raman Spectroscopy in Monoclonal Antibody Producing Continuous Systems for Downstream Process Intensification. *Biotechnol. Prog.* 36, e2947. doi:10.1002/btpr.2947

Yu, S., Li, X., Lu, W., Li, H., Fu, Y. V., and Liu, F. (2021). Analysis of Raman Spectra by Using Deep Learning Methods in the Identification of Marine Pathogens. *Anal. Chem.* 93, 11089–11098. doi:10.1021/acs.analchem.1c00431

Zhang, C., Springall, J. S., Wang, X., and Barman, I. (2019). Rapid, Quantitative Determination of Aggregation and Particle Formation for Antibody Drug Conjugate Therapeutics with Label-free Raman Spectroscopy. *Analytica Chim. Acta* 1081, 138–145. doi:10.1016/j.aca.2019.07.007

Conflict of Interest: The authors declare that the research was conducted in the absence of any commercial or financial relationships that could be construed as a potential conflict of interest.

Publisher's Note: All claims expressed in this article are solely those of the authors and do not necessarily represent those of their affiliated organizations, or those of the publisher, the editors and the reviewers. Any product that may be evaluated in this article, or claim that may be made by its manufacturer, is not guaranteed or endorsed by the publisher.

frontiers | Frontiers in Bioengineering and Biotechnology

ORIGINAL RESEARCH
published: 24 May 2022
doi: 10.3389/fbioe.2022.816275

Biophysical Characterization of the Oligomeric States of Recombinant Immunoglobulins Type-M and Their C1q-Binding Kinetics by Biolayer Interferometry

*Anne Chouquet[1], Andrea J. Pinto[1], Julia Hennicke[2], Wai Li Ling[1], Isabelle Bally[1], Linda Schwaigerlehner[2], Nicole M. Thielens[1], Renate Kunert[2] and Jean-Baptiste Reiser[1]**

[1]Institut de Biologie Structurale, UMR 5075, Univ. Grenoble Alpes, CEA, CNRS, IBS, Grenoble, France, [2]Department of Biotechnology, University of Natural Resources and Life Sciences, Vienna, Austria

OPEN ACCESS

Edited by:
Anurag S. Rathore,
Indian Institute of Technology Delhi, India

Reviewed by:
Kathrin Göritzer,
St George's, University of London, United Kingdom
Christopher Mark Smales,
University of Kent, United Kingdom

***Correspondence:**
Jean-Baptiste Reiser
jean-baptiste.reiser@ibs.fr

Specialty section:
This article was submitted to Bioprocess Engineering, a section of the journal Frontiers in Bioengineering and Biotechnology

Received: 16 November 2021
Accepted: 19 April 2022
Published: 24 May 2022

Citation:
Chouquet A, Pinto AJ, Hennicke J, Ling WL, Bally I, Schwaigerlehner L, Thielens NM, Kunert R and Reiser J-B (2022) Biophysical Characterization of the Oligomeric States of Recombinant Immunoglobulins Type-M and Their C1q-Binding Kinetics by Biolayer Interferometry. Front. Bioeng. Biotechnol. 10:816275. doi: 10.3389/fbioe.2022.816275

Immunoglobulins type-M (IgMs) are one of the first antibody classes mobilized during immune responses against pathogens and tumor cells. Binding to specific target antigens enables the interaction with the C1 complex which strongly activates the classical complement pathway. This biological function is the basis for the huge therapeutic potential of IgMs. But, due to their high oligomeric complexity, *in vitro* production, biochemical characterization, and biophysical characterization are challenging. In this study, we present recombinant production of two IgM models (IgM617 and IgM012) in pentameric and hexameric states and the evaluation of their polymer distribution using different biophysical methods (analytical ultracentrifugation, size exclusion chromatography coupled to multi-angle laser light scattering, mass photometry, and transmission electron microscopy). Each IgM construct is defined by a specific expression and purification pattern with different sample quality. Nevertheless, both purified IgMs were able to activate complement in a C1q-dependent manner. More importantly, BioLayer Interferometry (BLI) was used for characterizing the kinetics of C1q binding to recombinant IgMs. We show that recombinant IgMs possess similar C1q-binding properties as IgMs purified from human plasma.

Keywords: immunoglobulins, IgM, complement, C1q, recombinant expression, biophysical characterization, protein–protein interaction, biolayer interferometry

Abbreviations: sv-AUC/AUC, sedimentation velocity analytical ultra-centrifugation; BLI, biolayer interferometry; CLR, collagen-like region of C1q; ELISA, enzyme-linked immunosorbent assay; H/H chain, heavy chain; L/L chain, light chain; gC1q, globular head of C1q; Ig/Igs, immunoglobulin/s; IgG/IgGs, immunoglobulin/s G; IgM/IgMs, immunoglobulin/s M; J/J chain, joining chain; EM, electron microscopy; MP, mass photometry; PCR, polymerase chain reaction; RIfS, reflectometric interference spectroscopy; SEC, size exclusion chromatography; SEC-MALLS, multi-angle laser light scattering coupled to size exclusion chromatography; SPR, surface plasmon resonance; TEM, transmission electron microscopy; PAGE, polyacrylamide gel electrophoresis.

1 INTRODUCTION

Immunoglobulins of type M (IgMs) are the first Igs produced and secreted by B cells during early infection and immune reaction stages in adults. They are highly oligomeric polypeptides composed of a heavy chain (H) and a light chain (L). Each chain contains an N-terminal variable domain and one (for the L chain) or four (for the H chain) C-terminal constant domains. In serum, IgMs are mainly found as an assembly of H_2L_2 protomer subunits in a pentameric form $(H_2L_2)_5$ containing an additional covalently linked peptide called the joining (J) chain, but also to a lesser extent (less than 5%), in hexameric form $(H_2L_2)_6$, devoid of J chain (for reviews Gong and Ruprecht, 2020; Jones et al., 2020; Keyt et al., 2020). IgMs are also highly glycosylated with 5–6 different N-linked glycosylation chains that can account for up to 10–15% of their total molecular weight (Arnold et al., 2005). The overall assembly of IgMs is now revealed by modern high-resolution electron microscopy (EM) methods. They have been observed as star-shaped structures with a compact Fc core and orbiting, labile, and flexible Fab arms. While hexamers have the expected 6-fold symmetry, the pentamers possess a pseudo-hexameric symmetry in which five IgM protomers occupy five of the six symmetric positions and the J chain the sixth position (Hiramoto et al., 2018; Li et al., 2020; Kumar et al., 2021).

In addition to their antigen recognition function, IgMs fulfill their immune effector function by being one of the most potent activators of the classical pathway of the complement system. The binding of complexes between specific surface-exposed antigens and IgMs to the first recognition component of the classical pathway (CP), the C1q molecule, initiates a regulated amplifying proteolytic cascade, which in turn enables the formation of the membrane attack complex and the elimination of the pathogen or infected cell targets (Ricklin et al., 2010; Cedzyński et al., 2019). C1q is found in high concentration in human serum as part of the CP initiation C1 complex together with the $C1r_2C1s_2$ pro-enzyme tetramer. It is a 460-kDa highly flexible glycoprotein assembled from 18 polypeptide chains of 3 types (A, B, and C). These are organized into six ABC heterotrimers forming six Ig recognition domains, the globular heads (gC1q), attached to collagen-like regions (CLR). The C1q assembly has been depicted as a "bouquet of tulips" or an "Eiffel tower" (Kishore and Reid, 2000; Diebolder et al., 2014; Sharp et al., 2019).

Methods to measure direct binding characteristics of Igs to C1q as functional quality attributes are rather limited in number (reviewed in Harboe et al., 2011). Traditional methods employ enzyme-linked immunosorbent assay (ELISA) to measure equilibrium and end-point deposition of Igs on coated C1q and *vice versa* (exemplified in Duncan and Winter, 1988; Idusogie et al., 2000). More recently, label-free and real-time methods such as surface plasmon resonance (SPR) or biolayer interferometry (BLI) have been used to characterize the binding kinetics between C1q and IgGs (Moore et al., 2010; Patel et al., 2015; Zhou et al., 2018) or IgMs (Bally et al., 2019).

In the present study, we report productions of our IgM models, IgM617 and IgM012, in pentameric and hexameric forms and their biochemical and functional quality characterization using analytical ultracentrifugation (AUC), size exclusion chromatography coupled to multi-angle laser light scattering (SEC-MALLS), mass photometry (MP), transmission electron microscopy (TEM), and in-house ELISA for detection of complement activation. More importantly, we also report protocols to evaluate their bindings to C1q with BLI and compare their binding kinetics.

2 MATERIALS AND METHODS

2.1 Immunoglobulins Type-M Genetic Constructs

IgM617 is originally expressed by the EBV-transformed B cell line HB617 and directed against glycosphingolipids overexpressed on the tumor cell surfaces to elicit cytotoxic T-cells (Vorauer-Uhl et al., 2010). IgM012 was developed after a class switch of an HIV broadly neutralizing human IgG-targeting mannose carbohydrate structures of the HIV1 envelope protein gp120 (Wolbank et al., 2003). Light chain (L), heavy chain (H), and joining chain (J) cDNAs of both IgM models were codon-optimized and sub-cloned into separate pIRES vectors as described in Chromikova et al. (2015b), into pCEP4 vectors as described in Hennicke et al. (2017), and into pcDNA3.1(+) vectors. For the last constructs, IgM chain cDNAs were amplified by the polymerase chain reaction (PCR) using conventional protocols and the pIRES constructs as templates. Additional flanked NheI and BamHI restriction sites were also introduced by PCR. The genes were then inserted individually with classical ligation techniques into pcDNA3.1(+) vectors (Invitrogen) containing a resistance cassette for either Geneticin (H chain), Zeocin (L chain), or hygromycin (J chain).

2.2 Cell Lines and Expression of Immunoglobulins Type-M Models

IgM617-HLJ and IgM012-HLJ were expressed using 1) CHO DG44 cell lines by co-transfection with pIRES constructs and generation of stable cells lines (Chromikova et al., 2015b), 2) HEK293E cell lines after co-transfection with pCEP4 vectors and transient expression (Hennicke et al., 2019), or 3) HEK293F after co-transfection or serial transfections with pcDNA3.1(+) vectors and generation of stable cell lines.

Transfection and cultivation conditions of CHO DG44 and HEK293E cell lines have been described previously (Chromikova et al., 2015b; Hennicke et al., 2020). To generate stable HEK293F cell lines expressing either IgM617-HL or IgM012-HL, cells were simultaneously co-transfected with H-chain- and L-chain-containing pcDNA3.1(+) plasmids using 293 fectin according to the manufacturer's protocol (Invitrogen) and grown in FreeStyle 293 expression medium supplemented with 400 μg/ml G418 (Invitrogen) and 10 μg/ml Zeocin (Invitrogen). These cells were then transfected with J-chain-containing pcDNA3.1(+) plasmids in the same way, and the stable transfectants producing either IgM617-HLJ or IgM012-HLJ were generated using cultivation in a medium supplemented with additional 100 μg/ml hygromycin (Sigma-Aldrich). The stable cells expressing each IgM construct were then cultivated

in Freestyle 293 expression medium under antibiotic pressures and passaged every 3–4 days when cell density approached 3.10^6 cells/ml.

2.3 Recombinant Immunoglobulins Type-M Purification

All IgMs were purified from harvested supernatants according to Hennicke et al. (2017). In brief, POROS CaptureSelect™ IgM Affinity Matrix (Thermo Fisher Scientific) was used for affinity chromatography. Culture supernatants were directly applied to the packed column, and the IgMs were eluted with 1 M arginine and 2 M $MgCl_2$, pH 3.5 or pH 4.0. The collected fractions were immediately neutralized with 1 M Tris pH 8.5. The IgM-containing fractions were then pooled, dialyzed against the next-step equilibration buffer and concentrated. For a second purification step consisting of a size exclusion chromatography (SEC), they were applied on a Superose™ 6 increase 10/300 or 16/600 column (GE Healthcare/Cytiva) equilibrated in 0.1 M sodium phosphate pH 7.4, 0.2 M NaCl or in 0.025 M Tris–base, 0.137 M NaCl, and 0.003 M KCl, pH 7.4 at a flow rate of 0.5 ml/min. Highly multimeric IgMs were eluted as a single peak separated from lower or higher oligomeric states and from nucleic acid contaminants. Identification of purified IgMs by SDS-PAGE was performed as described in Vorauer-Uhl et al. (2010) using native PAGE 3–12% Bis–Tris gels followed by Coomassie Blue staining.

2.4 C1q Purification From Plasma

C1q was purified from human serum according to the well-established protocol. Briefly, IgG-ovalbumin-insoluble immune aggregates were prepared as described by Arlaud et al. (1979). Human serum, obtained from the Etablissement Français du Sang Rhône-Alpes, was incubated after clarification by centrifugation with immune aggregates on ice for 45 min. C1/immune complexes were then collected by centrifugation and extensively washed with 20 mM Tris, 120 mM NaCl, and 5 mM $CaCl_2$ at pH 7.4. Following C1r and C1s release by washing with buffer containing EDTA, C1q was eluted from immune aggregated with 50 mM Tris and 700 mM NaCl at pH 10.0 and separated from the immune complex by centrifugation. C1q samples were further purified to homogeneity by CM-cellulose chromatography.

2.5 Analytical Ultracentrifugation

Sedimentation velocity Analytical ultracentrifugation (sv-AUC) experiments were conducted in an XLI analytical ultracentrifuge (Beckman, Palo Alto, CA) using an ANTi-60 rotor, double channel Ti center pieces (Nanolytics, Germany) of 12- or 3-mm optical path length equipped with sapphire windows and the reference channel being typically filled with the sample solvent. Acquisitions were performed overnight at 4°C and at 20,000 rpm (32,000 g) using absorbance (280 nm) and interference detection. Data processing and analysis were completed using the program SEDFIT (Schuck, 2000) from P. Schuck (NIH, United States), REDATE (Zhao et al., 2015) and GUSSI (Brautigam, 2015) from C. Brautigam (United States), and using standard equations and protocols described previously (Salvay et al., 2008; Le Roy et al., 2013, 2015).

2.6 Size Exclusion Chromatography—Multi-Angle Laser Light Scattering Analyses

SEC combined with online detection by MALLS, refractometry, and UV-Vis was used to measure the absolute molecular mass in solution. The SEC runs were performed using a Superose™ 6 increase 10/300 column (GE Healthcare/Cytiva) equilibrated in 0.025 M Tris–Base, 0.137 M NaCl, and 0.003 M KCl, pH 7.4. Protein sample of 50 µl, concentrated to about 1 mg/ml, was injected with a constant flow rate of 0.5 ml/min, and separation was performed at room temperature. Online MALLS and differential refractive index detection were performed using a DAWN-HELEOS II detector (Wyatt Technology Corp.) with a laser emitting at 690 nm and an Optilab T-rEX detector (Wyatt Technology Corp.), respectively. Weight-averaged molar mass determination was performed with ASTRA6, using the "protein conjugate" module. The following refractive index increments and UV-Vis absorbance values were used: *dn/dc* protein = 0.185 ml/g; *dn/dc* glycosylation = 0.15 ml/g; A_{280} = 1.38 ml/mg.cm.

2.7 Mass Photometry

Coverslips (high-precision glass coverslips, 24 × 50 mm^2, No. 1.5H; Marienfeld, Lauda-Königshofen, Germany) were cleaned by sequential sonication in Milli-Q H_2O, 50% isopropanol (HPLC grade)/Milli-Q H_2O, and Milli-Q H_2O (5 min each), followed by drying with a clean nitrogen stream. To keep the sample droplet in shape, reusable self-adhesive silicone culture wells (Grace Bio-Labs reusable CultureWell™ gaskets) were cut into 4–10 segments. To ensure proper adhesion to the coverslips, the gaskets were dried well using a clean nitrogen stream. To prepare a sample carrier, gaskets were placed in the center of the cleaned coverslip and fixed tightly by applying light pressure with the back of a pipette tip. Protein landing was recorded using a Refeyn One^{MP} (Refeyn Ltd., Oxford, United Kingdom) MP system by forming a droplet of each IgM sample at a final concentration of 10 nM in 0.025 M Tris–Base, 0.137 M NaCl, 0.003 M KCl, pH 7.4. Movies were acquired for 120 s (12,000 frames) with Acquire^{MP} (Refeyn Ltd., v2.1.1) software using standard settings. Contrast-to-mass (C2M) calibration was performed using a mix of proteins with molecular weights of 66, 146, 500, and 1,046 kDa. Data were analyzed using Discover^{MP} (Refeyn Ltd., v2.1.1), and analysis parameters were set to T1 = 1.2 for threshold 1. The values for number of binned frames (nf = 8), threshold 2 (T2 = 0.25), and median filter kernel (=15) remained constant. The mean peak contrasts were determined in the software using Gaussian fitting. The mean contrast values were then plotted and fitted to a line. The experimental masses were finally obtained by averaging replicates using independent recombinant IgM preparations (2–4), and errors were the standard deviation.

2.8 Transmission Electron Microscopy

About 4 µl of diluted IgM samples (60–80 ng) were applied to a carbon film evaporated onto a mica sheet. The carbon film was

then floated off the mica in ~100 µl 2% sodium silicotungstate (SST, Agar Scientific) and transferred onto a 400 mesh Cu TEM grid (Delta Microscopies). Images were acquired using a CETA camera on a Tecnai F20 TEM microscope operating at 200 keV.

2.9 Complement Activation—Enzyme-Linked Immunosorbent Assays

The activation of the classical complement pathway was monitored by an ELISA based on the detection of C4b deposition according to Bally et al. (2019); Hennicke et al. (2020). In brief, 200 ng of IgMs diluted in PBS were adsorbed on a MaxiSorp 96-well plate (Thermo Fisher Scientific) by incubating overnight at 4°C. After washing, unspecific binding was prevented by saturation with PBS complemented with 2% bovine serum albumin (BSA, Sigma-Aldrich) for 1 h at 37°C. Replicate wells were then incubated with either normal human serum (NHS) diluted 25 times in a buffer containing 5 mM Veronal, 150 mM NaCl, 5 mM $CaCl_2$, 1.5 mM $MgCl_2$ at pH 7.4, C1q-depleted serum (NHSΔ, CompTech) diluted 25 times, or NHSΔ diluted 25 times and reconstituted with purified human C1q (4 µg/ml) for 1 h at 37°C. NHS was obtained from the Etablissement Français du Sang Rhône-Alpes (agreement number 14-1940 regarding its use in research). The reaction was stopped by washing with a buffer containing 5 mM Veronal, 150 mM NaCl, and 5 mM EDTA at pH 7.4. Deposited cleaved C4 form was detected with a rabbit anti-human C4 polyclonal antibody (Siemens), an anti-rabbit-HRP antibody conjugate (Sigma-Aldrich), addition of TMB (Sigma-Aldrich), and a CLARIOstar plate reader (BMG Labtech). Polyclonal IgM isolated from human serum (Sigma-Aldrich) was used as a control. Blank wells were prepared and processed similarly to wells coated with IgMs but incubated with buffer instead of NHS samples. Reported values were obtained by normalizing each data set (polyclonal IgM/NHS defined as 100) after blank subtraction and by averaging data obtained in replicated assays using independent recombinant IgM preparations (between 2 and 4); reported errors were the standard deviation of the replicates.

2.10 BioLayer Interferometry

BLI experiments were performed on an OctetRED96e from Pall/FortéBio and were recorded with the manufacturer's software (Data Acquisition v11.1). All protein samples were buffer exchanged against either 0.01 M Na_2HPO_4, 0.0018 M KH_2PO_4, 0.137 M NaCl, and 0.0027 M KCl at pH 7.4 (phosphate-buffered saline, PBS) or 0.025 M Tris, 0.15 M NaCl, and 0.003 M KCL at pH 7.4 (Tris-buffered saline, TBS) with Zeba Spin Desalting columns (Thermo Fisher Scientific) prior to loading. Commercial AR2G (amine coupling), SA (streptavidin), APS (aminopropylsilane), Protein A, and Protein L biosensors (Pall/FortéBio) or lab-made IgM-specific biosensors were tested. For the latter, mouse or goat anti-µ chain antibodies (Invitrogen) or CaptureSelect anti-IgM nanobody (Thermo Fisher Scientific) were biotinylated using NHS-PEG4-biotin EZ-link kit (Thermo Fisher Scientific) and captured onto SA biosensors. For their capture on AR2G biosensors, IgM samples were diluted in 0.01 M sodium acetate at pH 4, 4.5, 5, 5.5, or 6 (best capture at pH 6) and C1q in either 0.01 M sodium acetate at pH 4, 4.5, 5, or 5.5, 0.01 M MES at pH 6 or 6.5, or 0.01 M HEPES at pH 7 or 7.5 (best capture at pH 7.5). For their capture on SA biosensor, IgM or C1q samples were biotinylated using NHS-PEG4-biotin EZ-link kit (Thermo Fisher Scientific) according to manufacturer's conditions. No chemical treatments were applied before capturing on APS, Protein A, Protein L, or IgM-specific biosensors. AR2G biosensors were activated by dipping them in a mix of 10 mM N-hydroxysulfosuccinimide (s-NHS) and 20 mM 1-Ethyl-3-3dimethylaminopropyl (EDC) for 300 s prior to capture and quenched with 1 M ethanolamine pH 8.5 for 300 s after capture. In the case of APS biosensors, they were quenched with 50 µg/ml BSA solution for 600 s. Analyses were performed in 0.2 ml per well in black 96-well plates (Nunc F96 MicroWell, Thermo Fisher Scientific) at 25°C at 1,000 rpm agitation. Biosensors were pre-wetted in 0.2 ml PBS, 0.02% Tween-20, or analysis buffer for 10 min, followed by equilibration in pre-wetting buffer for 120 s. All ligand samples were applied at concentrations between 10 and 50 µg/ml and loaded according to the capture chemistry for between 300 and 600 s, followed by an additional equilibration step of 120 s or more in analysis buffer. For association and dissociation, all analyte samples were diluted at concentrations between 10 and 100 nM in TBS complemented with 0.002 M $CaCl_2$ and 0.02% Tween-20 as analysis buffer. Association phases were monitored during dipping the functionalized biosensors in analyte solutions for 180–300 s, and the dissociation phases were monitored in the analysis buffer for 180–300 s. To assess and monitor unspecific binding of analytes, measurements were performed using biosensors treated with the same protocols but replacing ligand solutions with analysis buffer complemented or not with 1% BSA. Since C1q unspecific binding levels were similar, further analyses were performed without BSA. Kinetics analyses were performed using Protein L biosensors which were functionalized with each IgM sample diluted at 30 µg/ml for 600 s until reaching a spectrum shift between 5.5 and 7.0 nm. The association phase of plasma C1q was monitored for 300 s with the diluted sample in analysis buffer at concentrations between 0 and 100 nM and dissociation phase for 600 s. All measurements were performed in replicates (between 2 and 4) using independent recombinant IgM preparations and loadings. Kinetics data were processed with the manufacturer's software (Data analysis HT v11.1). Signals from the reference biosensor and zero-concentration sample were subtracted from the signals obtained for each functionalized biosensor and each analyte concentration. Resulting specific kinetics signals were then fitted using a global fit method and a 2:1 heterogeneous ligand model. Reported kinetics parameter values were obtained by averaging the values obtained with replicated assays and reported errors as the standard deviation.

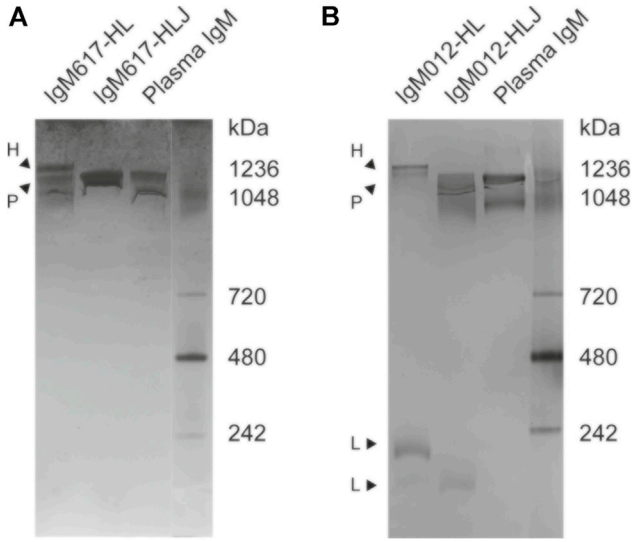

FIGURE 1 | Semi-native polyacrylamide gel electrophoresis (PAGE) analysis of purified IgM samples from HEK293F expression. Native PAGE gels followed by Coomassie Blue staining were run to identify **(A)** IgM617-HLJ and IgM617-HL and **(B)** IgM012-HLJ and IgM012-HL polymer distributions after SEC purification. IgMs purified from plasma (antibodies-online GmbH) are taken as markers along with native markers (Novex NativeMark™ Unstained Protein Standard). Suspected hexamers (H), pentamers (P), and lower assemblies (L) are indicated with arrows.

3 RESULTS

3.1 Recombinant Expression by HEK293F and Purification of Different Oligomeric Forms of Immunoglobulins Type-M

Previously, the production of recombinant IgM models using different stable and transient expression systems in mammalian cells has been intensively studied (Wolbank et al., 2003; Vorauer-Uhl et al., 2010; Chromikova et al., 2015a; Chromikova et al., 2015b; Hennicke et al., 2017; Hennicke et al., 2019; Hennicke et al., 2020). Here, we present an additional production system for the two IgM constructs, IgM617 and IgM012, using stabilized HEK293F cell lines. cDNAs of H, L, and J chains from both models were individually subcloned in pcDNA3.1(+) (**Supplementary Figure S1**). HEK293F cells were transfected with the three H, L, and J pcDNA3.1(+) constructs to obtain IgM samples in pentameric forms (IgM617-HLJ and IgM012-HLJ) or with only H and L vector constructs to obtain IgM samples in hexameric forms (IgM617-HL and IgM012-HL). After selection and culture expansion, recombinant IgMs were purified from culture media using the optimized protocol established by Hennicke et al. (2017). As previously observed in other cell lines, the retrieved yields after purification differed for recombinant IgMs with higher product titers for IgM617 than IgM012. Indeed, the final purified yield from stable HEK293F culture media of IgM617-HLJ or IgM617HL (5–10 mg/l of culture supernatant) was 25–100 times higher than that of IgM012-HLJ or IgM012-HL (less than 0.1 mg/l of culture supernatant).

3.2 Biophysical Characterization of the Oligomeric Forms of Recombinant Immunoglobulins Type-M

The oligomeric distribution and quality of purified IgM samples expressed by HEK293F cell lines were investigated using biochemical, biophysical, and structural methods.

3.2.1 SDS-PAGE

Semi-native polyacrylamide gel electrophoresis (PAGE) adapted from Vorauer-Uhl et al. (2010) showed that purified IgM617-HLJ migrated as a single and broad band while IgM617-HL migrated in a more heterogeneous manner with two major bands in the highest molecular weight range, suggesting the presence of different high oligomeric states in the absence of J chain (**Figure 1A**). Interestingly, although IgM012-HLJ and IgM012-HL behaved similarly to IgM617 constructs, additional noticeable bands at molecular weights below 242 kDa were still observed. This suggests the presence of lower assembly states (**Figure 1B**) as described by Chromikova et al. (2015b) and Hennicke et al. (2020) for the production of IgM617 and IgM012 pentamers in CHO DG44 or HEK239E cell lines.

3.2.2 Size Exclusion Chromatography—Multi-Angle Laser Light Scattering

To further characterize IgM617-HLJ and IgM617-HL homogeneity, multi-angle laser light scattering coupled to size exclusion chromatography (SEC-MALLS) was performed. The analyses presented a homogeneous sharp peak of about 895 kDa for IgM617-HLJ, which falls in the range of theoretical molecular weight of the glycosylated pentamers (891 kDa of amino acids +10–15% of glycosylation) (**Table 1** and **Figure 2A**). Surprisingly, a single mass of 947 kDa was also observed for IgM617-HL (**Table 1** and **Figure 2B**), whereas SDS-PAGE analysis showed a mixture of pentamers and hexamers (see above). The observed mass likely corresponds to average molecular weights of the different glycosylated oligomers (hexamers: 1,050 kDa +10–15%; pentamers without J chain: 875 kDa +10–15%). They might have co-eluted as a single peak from SEC, the resolution of this method being insufficient to separate hexamers and pentamers.

3.2.3 Analytical Ultracentrifugation

To further explore sample heterogeneities, sedimentation velocity Analytical ultra-centrifugation (sv-AUC) experiments were performed. Migration in the velocity field of IgM617-HLJ samples showed one main homogeneous peak at a sedimentation coefficient of about 19 S (more than 75%) and minor peaks at 12 S (12%) and 6 S (9%). It reveals the presence of a majority of pentamers but also of lower molecular weight oligomers (**Table 1** and **Figure 2C**). Migration of IgM617-HL samples appeared even more heterogeneous with two main peaks at about 21 S (between 60 and 70% depending on lots) and about 17.5 S (25–30%), which may correspond to hexamers and pentamers, but also with two minor peaks at 15 S (5%) and below 5 S (3–10%) accountable for lower molecular weight oligomers (**Table 1** and **Figure 2D**). Our AUC data on

TABLE 1 | Summary of theoretical and experimental molecular weights and of sedimentation coefficients. The theoretical peptide molecular weights are calculated based on the amino-acid primary sequences of the subcloned IgM chains using Protparam (Gasteiger et al., 2005). Experimental molecular weights were determined by SEC-MALLS and MP and sedimentation coefficients by AUC.

IgM	Oligomers	Theoretical (kDa)	SEC-MALLS (kDa)	AUC (S)	Mass photometry (kDa)
IgM617-HLJ	Pentamers	891	895	19.0 S	998 ± 6
	Tetramers	700	-	12.0 S	-
	Protomers	175	-	6.0 S	-
IgM617-HL	Hexamers	1,050	947	21.0 S	1,250 ± 54
	Pentamers	875		17.5 S	1,050 ± 43
	Tetramers	700	-	15.0 S	841 ± 37
	Protomers	175	-	5.0 S	162 ± 12
IgM012-HLJ	Pentamers	878	n.d.	n.d.	944 ± 32
	Tetramers	690	n.d.	n.d.	-
	Protomers	172	n.d.	n.d.	162 ± 14
IgM012-HL	Hexamers	1,034	n.d.	n.d.	1,166 ± 21
	Pentamers	862	n.d.	n.d.	1,052 ± 34
	Tetramers	690	n.d.	n.d.	-
	Protomers	172	n.d.	n.d.	150 ± 21

(n.d.: not determined).

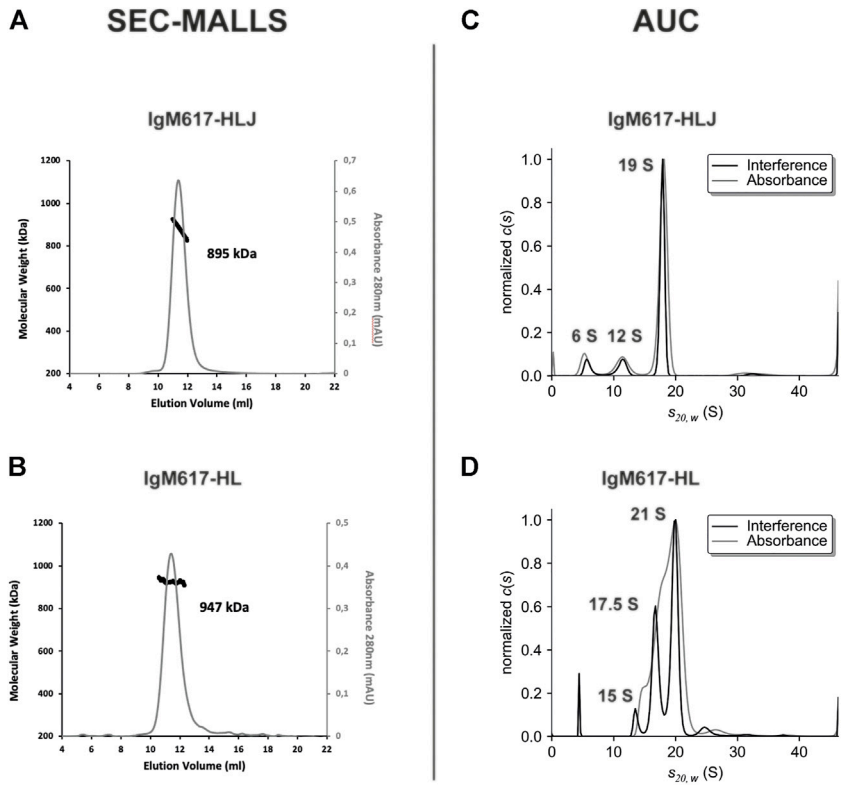

FIGURE 2 | Size exclusion chromatography coupled to multi-angle laser light scattering (SEC-MALLS) and analytical ultracentrifugation (AUC) analysis of purified IgM617 samples from HEK293F expression. The left panels show the elution profiles of the purified **(A)** IgM617-HLJ and **(B)** IgM617-HL monitored by the excess refractive index (right ordinate axis) and the molecular weight as bold line (left ordinate axis) derived from MALLS, refractometry, and UV-Vis measurements. The estimated average molecular weights are indicated on the graphs. The right panels show the sedimentation distributions of **(C)** purified IgM617-HLJ and **(D)** IgM617-HL. Calculated and corrected sedimentation coefficients $S_{20,W}$ are obtained as described in Materials and Methods and are indicated on the graphs.

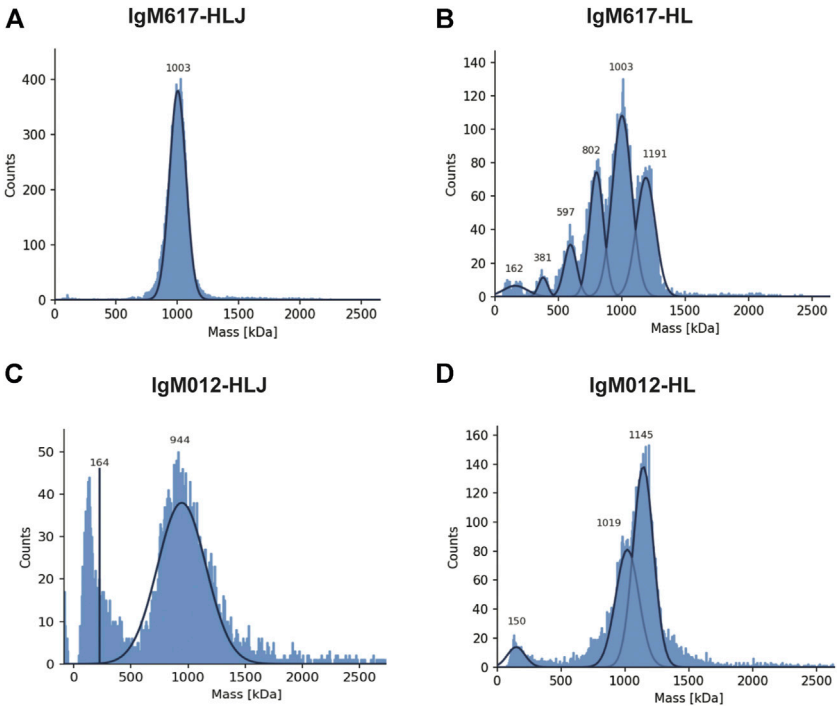

FIGURE 3 | Mass photometry (MP) analysis of recombinant IgMs produced in HEK293F. Histograms show the population distributions of purified IgMs. Shown analyses are representative of replicate experiments: **(A)** IgM617-HLJ, **(B)** IgM617-HL, **(C)** IgM012-HLJ, and **(D)** IgM012-HL. Estimated molecular weights for the shown experiments are indicated on each graph.

recombinant IgMs are in agreement with the sedimentation coefficients originally measured by Eskeland and Christensen (1975) on purified IgM from patient sera with or without J chain.

3.2.4 Mass Photometry

To assess more precisely IgM oligomeric states and experimental molecular masses, samples were further analyzed using mass photometry (MP), an emerging technique enabling accurate native mass measurements of single molecules in solution (Sonn-Segev et al., 2020). A single population with an average mass of 998 ± 6 kDa (mean ± SD over replicates) could be observed for IgM617-HLJ (**Table 1** and **Figure 3A**). The experimental mass matched the mass of fully glycosylated pentamers (891 kDa +10–15% glycosylation). By contrast, IgM617-HL data showed three main populations at 1,250 ± 54 kDa, 1,050 ± 43 kDa, and 841 ± 37 kDa (**Table 1** and **Figure 3B**) that might correspond to hexamers (1,050 kDa +10–15% glycosylation), pentamers, (875 kDa +10–15%) and tetramers (700 kDa +10–15%), respectively. Minor populations could also be observed and might correspond to lower oligomeric protomer states. This is in agreement with our sv-AUC observation of the presence of different IgM617-HL oligomers (see above). However, the oligomeric distributions appeared different and might be explained not only by the usage of different batches of IgM617-HL for the measurements but also by the methods used. IgM012-HLJ appeared with a quite homogeneous experimental mass of 944 ± 32 kDa, corresponding to pentamers (878 kDa +10–15%), although a broad mass distribution was still observed and an additional population at low molecular weight was present and might correspond to the lower assembly states (**Table 1** and **Figure 3C**). Finally, IgM012-HL behaved similarly to IgM617-HL with two main populations at 1,166 ± 21 kDa and 1,052 ± 34 kDa corresponding to hexamers (1,035 kDa +10–15%) and pentamers (862 kDa +10–15%), but low assembly states could also be observed (**Table 1** and **Figure 3D**).

3.2.5 Transmission Electron Microscopy

The structural integrity and oligomeric states of IgMs produced by HEK293F were also examined and confirmed with negative staining Transmitted electron microscopy (TEM). IgM617-HLJ (**Figure 4A**) and IgM012-HLJ (**Figure 4C**) produced in HEK293F exhibited very similar structural characteristics as previously observed for pentamers produced in HEK293E and CHO DG44 (Hennicke et al., 2020). They possessed a central circular core with projecting flexible Fab units in a star-shaped configuration, as well-known for IgMs isolated from human serum. As expected from biophysical data described previously, both IgM617-HL (**Figure 4B**) and IgM012-HL (**Figure 4D**) presented two types of distinct particles. Some had a symmetric shape and six arms, confirming the hexameric structural features of HL samples in addition to the pentamer ones, also confirmed by asymmetrical particles to which five arms could be assigned. It should be noted that IgM molecules with lower oligomeric states observed with mass photometry and AUC could not have been easily identified on TEM micrographs.

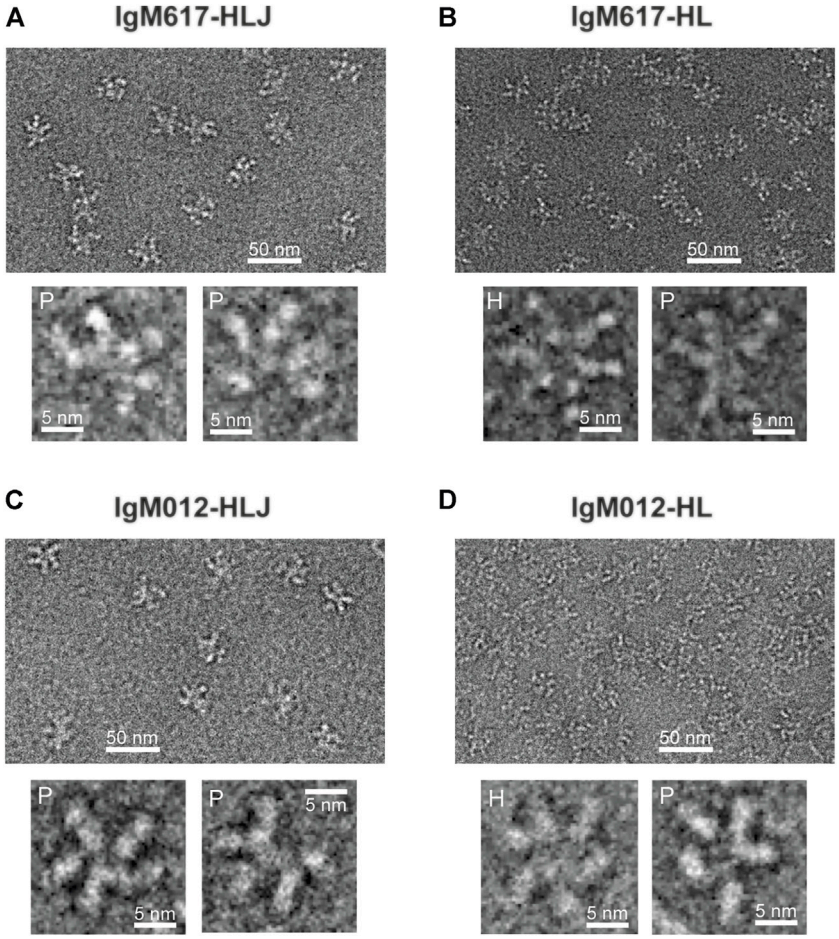

FIGURE 4 | Non-processed images of recombinant IgMs produced in HEK293F by negative stain transmission electron microscopy. Representative fields of particles with a 50 nm scale bar are shown on top of each panel with magnified views of some individual molecules shown on the lower part of each panel: **(A)** IgM617-HLJ, **(B)** IgM617-HL, **(C)** IgM012-HLJ, and **(D)** IgM012-HL. Hexamers are denoted with H and pentamers with P.

3.3 C1q-Dependent Complement Activation by Recombinant Oligomeric Immunoglobulins Type-M Forms Produced by HEK293F Cells

The capacity of the different recombinant IgM preparations to activate CP was analyzed using our in-house *in vitro* enzyme-linked immunosorbent assay (ELISA) based on the detection of C4b fragment deposition after cleavage of C4 by the C1 complex bound to coated IgM molecules (Bally et al., 2019; Hennicke et al., 2020). Although these assays do not confirm antigen-specific CP activation, they allow to demonstrate the coated IgM effector function. Assays with C1q-depleted normal human serum and C1q-reconstituted serum were used as controls for the C1q/IgM interaction dependency. Polyclonal IgMs purified from human plasma (pIgMs) were used as positive control and standard. As observed with our previous IgM617 and IgM012 productions (Hennicke et al., 2020), no significant difference was observed in the C4b deposition yields between the different coated IgM samples, whether serum-derived or recombinant. Thus, the polymer distributions may not influence the ability of IgMs to activate the proteolytic complement cascade through C1 when coated onto the ELISA surfaces (**Figure 5**).

3.4 C1q-Binding Kinetics to Immunoglobulins Type-M Measured by BioLayer Interferometry

In order to characterize the binding kinetics of IgMs to C1q, we developed new protocols using the label-free optical method based on the reflectometric inference spectroscopy (RIfS) (Hänel and Gauglitz, 2002; Gauglitz, 2020) and its setup, known as biolayer interferometry (BLI) (Abdiche et al., 2008; Sultana and Lee, 2015) on an OctetRED96e instrument. In this study, plasma-purified C1q and plasma-derived IgM preparations or recombinant IgM constructs produced in HEK293F were used, in addition to IgMs produced in CHO DG44 and HEK293E (Hennicke et al., 2020). Real-time detection of binding events at the surface of biosensors enables two strategies, using either C1q captured to the biosensor surfaces

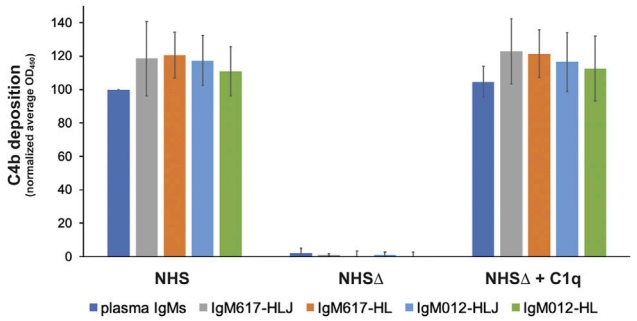

FIGURE 5 | Complement activation by the different purified IgM constructs expressed in HEK293F. Recombinant IgMs and IgMs purified from plasma were coated on microplate wells and incubated with either normal human serum (NHS), C1q-depleted NHS (NHSΔ), or reconstituted NHS (NHSΔ + C1q). C1 activity was monitored *via* C4b deposition. Reported values are average of replicated (2–4) normalized experiments (100% = IgM plasma/NHS). Errors are obtained as standard deviation between independent replicates.

as ligands and IgMs as analytes or IgMs captured to the biosensor surfaces as ligands and C1q as analytes.

The first strategy was evaluated with C1q ligand either amine coupled onto AR2G biosensors or captured by streptavidin (SA) biosensors after biotinylation. However, although high C1q densities could be reached in both cases (3–7 nm spectral shift), no binding responses could be retrieved with plasma IgM samples (**Supplementary Figure S2**).

In the second strategy, we tested several different commercial biosensors (AR2G, SA, APS, Protein A, and Protein L) and laboratory-made IgM-specific biosensors (mouse or goat anti-μ chain antibodies or CaptureSelect anti-IgM nanobody coated on SA biosensors). All biosensors could be functionalized with plasma-derived polyclonal IgMs at different high levels depending on the capture chemistry (between 1 and 7 nm spectral shift) (**Supplementary Figure S3** left panels, **Supplementary Figure S3A**). Because Protein A is specific for Fcγ regions of IgG but also for VH_3 subfamilies of Ig, both monoclonal recombinant IgM617 and IgM012 were tested, but no capture signal could be recovered for this type of biosensors, although IgM617 belongs to the VH_3 subfamily. Unspecific binding of C1q was also evaluated for all biosensor types: without any captured IgM, most of them showed either weak or no unspecific signals from C1q, contrary to previous reports (Zhou et al., 2018) (**Supplementary Figure S3** right panels). Finally, either no or too weak C1q binding signals could be retrieved from most of the IgM-functionalized biosensors, making them inapplicable for kinetics and affinity determination (AR2G, SA, Protein A, APS, and anti-μ chain antibodies) (**Supplementary Figure S3** right panels). Only protein L biosensors showed both limited unspecific C1q binding signals (**Supplementary Figure S4B**), and measurable kinetics signals on the IgM-functionalized biosensors. Therefore, pIgMs, IgM617, and IgM012 constructs were stably absorbed on Protein L biosensors until saturation was reached (4–7 nm shift) (**Supplementary Figure S4B**) and kinetics analyses were then performed by dipping the IgM-functionalized biosensors in C1q concentration series ranging from 3.13 to 100 nM with 2-fold dilution (**Figure 6**).

C1q bound to all IgMs in a biphasic manner, with two distinguishable fast and slow binding rates, and the 1:1-Langmuir model could not be applied to determine interaction kinetics parameters. The only fitting model available to account for the complicated kinetics components was the 2:1-heterogeneous-ligand model (**Figure 6**). Plasma-derived polyclonal and all recombinant monoclonal IgMs showed affinities in the nanomolar scale, ranging from about 1 to 8 nM for K_{D1} and from 4 to 26 nM for K_{D2}, depending on the sample (**Table 1**). pIgMs (K_{D1} = 2.3 nM and K_{D2} = 6.5 nM) and IgM012s (K_{D1} = 1–3 nM and K_{D2} = 4–10 nM) affinities for C1q appear higher than IgM617s (K_{D1} = 6–8 nM and K_{D2} = 7–26 nM). However, those differences may not be significant. It should be noted that for all IgM samples, the distinct slow and fast kinetics led to affinities of the same nM magnitude. No significant differences in kinetics, which could be related to the host cell lines and the differential glycosylation patterns induced by the expression system (Hennicke et al., 2020), could be observed either for IgM617 or IgM012 models. Finally, although small differences could be noted in kinetics rate values when comparing HL and HLJ constructs, it is difficult to attribute them solely to the presence of hexameric forms, since such variations are also observed either between HLJ constructs or between different preparations of the very same recombinant IgM construct (**Table 1**).

4 DISCUSSION

In the presented study, we recombinantly produced and purified two IgM models, IgM617 and IgM012 (Hennicke et al., 2017, 2019, 2020), and fully characterized their biochemical and functional quality attributes using combined biophysics techniques: AUC, SEC-MALLS, MP, and TEM to determine their oligomeric states and polymer distributions and *in vitro* complement activation based on ELISA to evaluate their functional capacities. Moreover, we used the label-free and real-time detection BLI technique and adapted protocol to quantify the kinetics of the interaction between IgMs and C1q, the recognition and activating protein of the classical complement pathway.

One challenge for studying IgM and developing potential therapeutic products is the manufacturing and characterization of recombinant molecules with high Ig productivity, high homogeneous oligomerization status and purity, and similar biological biomimetic function. In the past, several methods have been tested. In particular, IgM617 and IgM012 have been taken as IgM models to develop proofs-of-concept of recombinant production (Vorauer-Uhl et al., 2010; Mader et al., 2013; Chromikova et al., 2015b; Hennicke et al., 2017, 2019, 2020). In the present study, we complemented the panel of biophysical analysis methods by using SEC-MALLS (**Figure 2**), sv-AUC (**Figure 2**), and the new MP (**Figure 3**) to determine the oligomeric distribution of recombinant IgM samples produced in

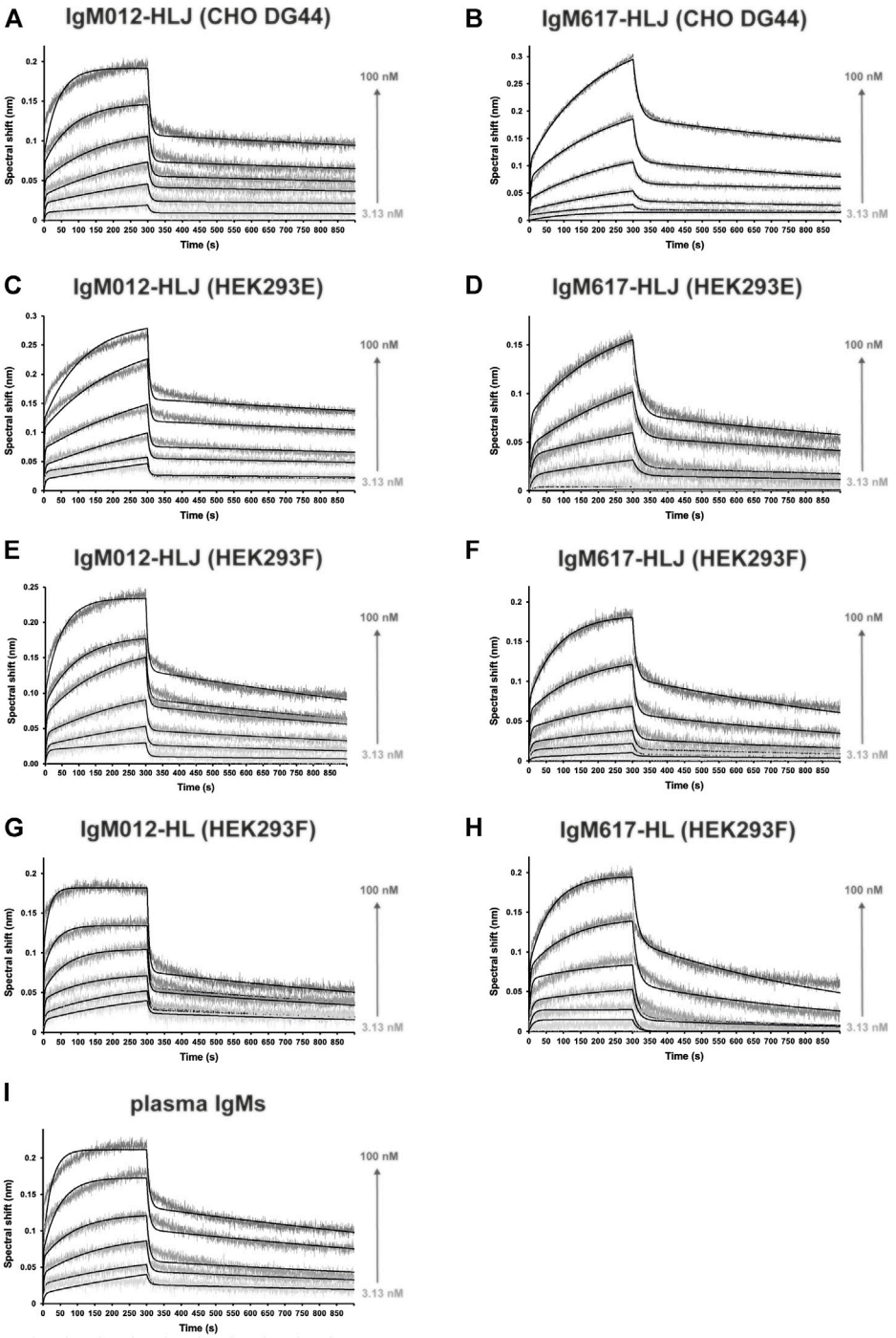

FIGURE 6 | Kinetics analysis of the interaction between C1q from plasma and the different purified and immobilized IgMs expressed in mammalian expression hosts. IgMs were captured on Protein L, and functionalized biosensors were dipped in wells containing C1q at different concentrations (3.13, 6.25, 12.5, 25, 50, and 100 nM). The binding signals (gray-scaled sensorgrams) were obtained by subtracting the signals from empty protein L biosensor and from zero-concentration samples. Fitted curves are depicted as black lines and were obtained by global fitting using a 2:1 heterogeneous ligand model. Shown kinetics analyses are representative of each binding experiment: **(A)** IgM012-HLJ expressed by CHO DG44, **(B)** IgM617-HLJ by CHO DG44, **(C)** IgM012-HLJ by HEK293E, **(D)** IgM617-HLJ by HEK293E, **(E)** IgM012-HLJ by HEK293F, **(F)** IgM617-HLJ by HEK293F, **(G)** IgM012-HL by HEK293F, **(H)** IgM617-HL by HEK293F, and **(I)** IgMs purified from plasma.

HEK293F cell line. We can thus confirm that IgM617-HLJ model can be produced as very homogeneous pentamers when H, L, and J chain genes are transfected in HEK293F for stable expression, while IgM012-HLJ retains heterogeneities with significant amounts of lower assemblies. Nevertheless, both IgM pentamers produced in HEK293F retain their structural

integrity of five-branches-star-shaped particles (**Figure 4**) as shown with negative staining TEM images and functional qualities as demonstrated with complement activation assays (**Figure 5**). One explanation for the low expression of IgM012 in recombinant expression compared to IgM617 and in general to other IgM constructs studied so far may come from the structural arrangement of its Fab. Indeed, the crystal structure of HIV-1 monoclonal antibody 2G12 Fab has revealed an unusual VH-VL domain arrangement for Fabs in which two of its Fabs assemble as a dimer with interlocked VH domain swapping, instead of the usual VH-VL monomeric assembly (Calarese et al., 2003). The VH domain exchange has been demonstrated to be mandatory for this IgG to target and recognize the specific high-mannose cluster of the glycan shield of HIV-1 (Doores et al., 2010). One can easily hypothesize that IgM012 may possess such a similar domain swapping of its Fabs and that this may constrain IgM assembly more than the regular assembly in which Fabs behave independently. These structural constraints may not be favorable and may prevent proper expression of the recombinant IgM012 constructs by the different cell lines used so far.

With this study, we show that hexamer expression of IgM617-HL, and to a lesser extent of IgM012-HL, is made possible using HEK293F stably transfected with only the H and L constructs. It was well established that the J chain expression influences the formation of the pentameric and hexameric IgM forms either *in vivo* or *in vitro*. Randall et al. (1992) first demonstrated the regulation of the pentamer/hexamer ratio in B cells by J chain gene expression with the secretion of a majority of hexamers and a minority of pentamers by cells lacking the J-chain gene. However, recombinant expression of only hexamers by J-chain-deficient cells remains challenging. Although hexamers were found to be expressed by recombinant systems, a majority of pentamers was found to be secreted by mouse hybridoma cell lines (Wiersma et al., 1998; Collins et al., 2002) or CHO-K1 (Gilmour et al., 2008). Interestingly, only Azuma et al. (2007) have succeeded to obtain a majority of hexamers by using CHO DG44 that express 20 times more hexamers than CHO co-transfected with the J-chain gene. Here, we confirm that recombinantly producing homogeneous hexameric forms of IgM remains difficult. Although IgM617 and IgM012 models can be expressed and secreted as hexamers by stable HEK293F cell lines, as shown by our different biochemical, biophysical, and structural analyses, our data also show that both sample types are not homogeneous. They present a large population of pentamers likely lacking the J chain, but also with traces of lower molecular-weighted tetramers and dimers in the purified IgM samples. Furthermore, the ratio of the distinct IgM oligomeric states appears to vary not only between IgM models but also between different production runs of the same IgM model (data not shown). In addition, data from our surface-based C1q-dependent complement activation assays do not demonstrate higher activities of hexameric-enriched IgM samples (**Figure 5**). This is in contrast to previous hemolytic assays, which have demonstrated the higher efficacy of hexameric IgM in inducing complement-dependent cytolysis compared to pentameric IgMs (Randall et al., 1990; Collins et al., 2002). As previously mentioned, the ELISA setup and the end-point measurement of C4 deposition may not be sensitive and resolutive enough to characterize differences in IgM abilities to activate the first step of complement activation (Hennicke et al., 2020).

For the first time, we present the new usage of BLI to characterize the binding kinetics and affinities of C1q to IgM antibody isotypes. Optical and surface-based methods such as SPR and BLI are popular methods for characterizing the binding properties of all antibody classes to antigens, but much less so to Ig effectors such as the complement molecule, C1q. Patel et al. (2015) and Jovic and Cymer (2019) have successfully characterized the C1q binding responses to the different IgG subtypes using SPR methods. Zhou et al. (2018) did the same using the BLI technology. Only one study has been published by Bally et al. (2019), who measured the binding kinetics between IgM fractions purified from human plasma and native C1q, as well as recombinant C1q, and a few critical mutants, using SPR.

Several experimental setups were tested in our study to define the conditions allowing reliable binding measurements between either IgM purified from human plasma or different recombinant IgM constructs and native C1q purified from human plasma. Surprisingly, and in contrast to the SPR data obtained so far when C1q was captured at the biosensor surface (Bally et al., 2019), no interaction with IgMs was detectable with the BLI method (**Supplementary Figure S2**). However, we were able to observe binding of the catalytic tetramer $C1r_2Cs_2$ to immobilized C1q with expected affinities in the nanomolar range (**Supplementary Figure S5**). These results indicate that immobilized C1q can retain some binding activities towards its partners, but that the immobilization strategy onto the BLI biosensor, either directly or by selective biotinylation of primary amines of C1q, can greatly affect its binding capabilities.

During optimization of the BLI protocols, capturing IgMs onto Protein L biosensor and using C1q as analyte proved to be the most efficient strategy since only weak or acceptable C1q unspecific binding could be detected at the used concentration range (**Supplementary Figure S4**) and specific concentration-dependent binding signals could be measured (**Figure 6**). Our method is similar to those already employed to characterize the complexes between C1q and recombinant IgGs, for which Protein L-coated sensors have been used to capture immunoglobulins for SPR or BLI, although streptavidin and biotin fusion also proved to be suitable (Zhou et al., 2018). Unfortunately, protein L was the only successful immobilization method for functionalizing BLI biosensors with IgMs. Indeed, the binding of protein L to Igs is specifically restricted to some kappa light chains, which limits the application of the method described here to IgMs containing this subtype of the L chain. Surprisingly, the binding of C1q could be measured in those conditions and without any specific antigen bound to IgMs. Similarly, complement activation could be performed by binding IgM to microtiter plates without antigen with solid-phase methods such as ELISA techniques to prove the effector function capacity of IgMs (Zwirner et al., 1998; Bally et al., 2019; Hennicke et al., 2020), whereas antigen is required in solution methods such as erythrocyte or liposome lysis (for assays review in Harboe et al., 2011). Indeed, C1q binding to IgM and subsequent activation of the complement cascade are thought to

TABLE 2 | Kinetic and affinity constants of C1q binding to different purified recombinant IgMs expressed in mammalian expression systems. Values are obtained after global fitting of the binding signals (**Figure 5**) and averaging from replicates (2–4). Affinity constants (K_{D1} and K_{D2}) are obtained from the ratio between kinetics parameters (k_{d1}/k_{a1} and k_{d2}/k_{a2}). Standard errors are obtained as standard deviation between replicates.

IgM	Source	Construct	k_{a1}	k_{d1}	K_{D1}	k_{a2}	k_{d2}	K_{D2}
			10^5/Ms	10^{-4}/s	10^{-9} M	10^7/Ms	10^{-1}/s	10^{-9} M
Total IgM	Plasma		3.04 ± 0.47	7.02 ± 1.63	**2.31 ± 0.09**	2.00 ± 0.90	1.30 ± 0.60	**6.52 ± 1.34**
IgM617	CHO DG44	HLJ	0.78 ± 0.17	6.20 ± 1.02	**8.00 ± 0.31**	0.57 ± 0.44	0.74 ± 0.08	**12.30 ± 3.87**
	HEK293E	HLJ	0.92 ± 0.16	6.26 ± 1.77	**6.82 ± 0.11**	0.86 ± 0.49	0.59 ± 0.33	**6.90 ± 1.13**
	HEK293F	HLJ	1.59 ± 0.76	11.30 ± 3.04	**7.10 ± 1.06**	0.44 ± 0.05	1.15 ± 0.53	**26.4 ± 2.89**
	HEK293F	HL	1.66 ± 0.50	9.25 ± 4.84	**5.59 ± 1.02**	0.96 ± 0.38	0.96 ± 0.47	**9.97 ± 2.00**
IgM012	CHO DG44	HLJ	2.22 ± 0.08	2.57 ± 0.37	**1.16 ± 0.01**	2.04 ± 0.31	1.34 ± 0.13	**6.54 ± 0.11**
	HEK293E	HLJ	1.64 ± 0.35	3.57 ± 0.33	**2.18 ± 0.06**	1.84 ± 0.40	1.57 ± 0.15	**8.51 ± 0.24**
	HEK293F	HLJ	2.22 ± 0.33	6.18 ± 0.08	**2.79 ± 0.03**	1.41 ± 0.34	1.34 ± 0.28	**9.50 ± 0.48**
	HEK293F	HL	4.65 ± 2.54	5.81 ± 2.61	**1.25 ± 0.31**	1.79 ± 0.51	0.73 ± 0.04	**4.09 ± 0.17**

occur physiologically only with IgM binding to a specific antigen. This latter may induce large structural changes in IgM quaternary structure and exposure of the hidden binding sites for C1q globular heads (Sharp et al., 2019). One possible explanation would be that immobilizing IgMs onto an *in vitro* surface might provoke the necessary structural feature exposures. In particular, for BLI experiments for which only IgM capture *via* Protein L allowed C1q binding, the explanation might come from the binding properties of Protein L to Ig. As shown by the 3D structure of the complex between Protein L and Fab, one Protein L domain bridges two Fab domains (Graille et al., 2001). Although this property may not strictly mimic antigen binding, it might be enough to induce an IgM conformation allowing complex formation with C1q.

As expected, the measured affinities of C1q for IgMs with BLI fall within the nM range (**Table 2**). No significant differences in affinities and kinetics rates could be observed between polyclonal IgM purified from plasma and the different recombinant monoclonal IgMs, regardless of the host cell lines, oligomeric distributions, or post-translational glycosylation pattern (Hennicke et al., 2020). Interestingly, C1q affinities for IgMs are in the same nM range as for IgG1 measured in a similar BLI configuration, although kinetics behavior differs slightly (Zhou et al., 2018). Together with the complement assays, which also showed no differences between IgM samples, our BLI data emphasize that recombinant IgM preparations retain similar abilities as physiological IgMs to bind and activate the CP *in vitro*. Our data are consistent with SPR data obtained by Bally et al. (2019) since the affinities of IgMs for C1q measured by SPR and BLI are very similar. However, the kinetics behavior appeared to be different since a 2:1 heterogeneous model was applied to fit our BLI binding data (**Figure 6**), while a 1:1 Langmuir model was sufficient to interpret SPR data. One can argue that the biphasic kinetics behavior may be raised by the heterogenous quality of native or of our recombinant IgM samples. However, no difference was observed between the most homogeneous constructs (IgM617-HLJ) and the other constructs. Thus, the differences between SPR and BLI data likely originate from either the used strategies or methods. Indeed, the employed sensor functionalization strategies were different with different capture chemistries and captured molecules (amine coupled C1q in case of SPR and Protein L/IgMs in case of BLI) and different molecules are used as analytes (IgM in case of SPR and C1q in case of BLI). The question of the used method will remain unanswered since no binding could be detected with SPR, capturing IgMs on Protein L sensors and using C1q as analytes (data not shown). The biphasic kinetics behavior of the IgM/C1q binding measured with BLI might also come from their intrinsic molecular characteristics, such as their highly oligomeric states and their flexibility. Indeed, it is expected that the single globular region of C1q may have a lower affinity for Igs than full C1q, as well as IgM protomer for C1q than full IgM. Thus, the affinities for the C1q/IgM complex formation rely on the specific multivalency that enhances the binding with an avidity effect. Furthermore, certain lability of the C1q/Ig complex formation can also influence kinetics binding. Not all gC1q bind the IgG hexamers at the same time (Ugurlar et al., 2018), although the same behavior has not been described for IgMs (Sharp et al., 2019). Finally, due to the very high flexibility of IgM and C1q molecules, structural arrangements and stabilization are expected to have an effect on the dynamics of binding events. Taken together, these molecular features would induce very complicated and heterogeneous binding kinetics for which any mathematical fitting model would not be sufficiently formulated and easy to apply to consider all possible behaviors.

In conclusion, our work presents relevant results for the development of IgM as biopharmaceuticals. This latter requires new *in vitro* methods to produce biosimilars and to characterize the quality attributes of recombinant samples to meet the regulations of various drug and health authorities around the world. For antibodies, non-clinical studies must be performed to assess first the product qualities in terms of purity and homogeneity. For example, electrophoresis is widely used so far but with the known limitations in detecting low protein amounts and the application of particular protocols necessary to characterize high molecular-weight biomolecules such as IgMs (Vorauer-Uhl et al., 2010). Our results show the relevance of additional biophysical methods to precisely determine oligomeric distributions and the molecular weight of different IgM sample states. In particular, mass photometry appears to be a reliable technique to assess rapidly the mass distribution with minimal sample amounts. The characterization of the similarity in known

Fab- and Fc-associated functions such as binding to target antigen(s) and to Fc gamma receptors, FcRn, or C1q is challenging, in particular, in finding methods to demonstrate the binding of Igs to C1q. For now, ELISA has been widely used as a surrogate for complement-dependent cytotoxicity assays in comparability studies for therapeutic Igs. SPR and BLI have proven to be alternatives with advantages like lower complexity in buffer preparations, lower hands-on manipulation, and lower sample consumption. They are also faster, more in-depth, and semi-automated interaction analysis methods with higher precisions than the endpoint measurements from ELISA (Patel et al., 2015; Zhou et al., 2018; Jovic and Cymer, 2019). With our study, we demonstrate the suitability of the BLI-based assays for the measurements of recombinant IgM/C1q interactions, and we believe that the developed protocols can be easily applied to evaluate future IgM potential therapeutic preparations in combination with the conventional biological analysis.

DATA AVAILABILITY STATEMENT

The original contributions presented in the study are included in the article/**Supplementary Material**, further inquiries can be directed to the corresponding author.

AUTHOR CONTRIBUTIONS

Conceptualization and supervision: J-BR, WL, and RK. Funding acquisition: NT, J-BR, and RK. Investigation and data: JH, LS, and RK (for IgM expression and purification in HEK293E and CHO DG44); IB, CA, AP, and J-BR (for IgM expression and purification in HEK293F); CA, AP, and J-BR (for ELISA, mass photometry and BLI measurements); and AP and WL (for electron microscopy). Expertise: NT (for $C1r_2C1s_2$ samples and SPR analysis). Manuscript writing: J-BR, WL, AP, and RK.

FUNDING

This work was supported by the French National Research Agency under Grant C1qEffero ANR-16-CE11-0019, by the program BioToP (Biomolecular Technology of Proteins) funded by the FWF under Grant W1224, and by Polymun Scientific Immunbiologische Forschung GmbH. cDNAs coding for IgM617 and IgM012 chains were provided by Polymun Scientific Immunbiologische Forschung GmbH. This work used the Biophysical, AUC, EM, and SPR/BLI platforms of the Grenoble Instruct-ERIC center (ISBG; UAR 3518 CNRS-CEA-UGA-EMBL) within the Grenoble Partnership for Structural Biology (PSB), supported by FRISBI (ANR-10-INBS-0005-02) and GRAL, financed within the University Grenoble Alpes graduate school (Ecoles Universitaires de Recherche) CBH-EUR-GS (ANR-17-EURE-0003). The EM facility is supported by the Auvergne Rhône-Alpes Region, the Fondation pour la Recherche Médicale (FRM), the Fonds FEDER, and the GIS-Infrastructures en Biologie Santé et Agronomie (IBiSA).

ACKNOWLEDGMENTS

The authors thank Caroline Mas for her assistance in the Biophysical platform and Christine Ebel and Aline Le Roy for their assistance in the AUC platform. The authors thank Guy Schoehn, head of the EM facility, for his support. IBS acknowledges integration into the Interdisciplinary Research Institute of Grenoble (IRIG, CEA). The authors would like to thank Véronique Rossi and Christine Gaboriaud from IBS for their expertise, helpful discussions, and article proofreading.

SUPPLEMENTARY MATERIAL

The Supplementary Material for this article can be found online at: https://www.frontiersin.org/articles/10.3389/fbioe.2022.816275/full#supplementary-material

REFERENCES

Abdiche, Y., Malashock, D., Pinkerton, A., and Pons, J. (2008). Determining Kinetics and Affinities of Protein Interactions Using a Parallel Real-Time Label-free Biosensor, the Octet. *Anal. Biochem.* 377, 209–217. doi:10.1016/j.ab.2008.03.035

Arlaud, G. J., Sim, R. B., Duplaa, A.-M., and Colomb, M. G. (1979). Differential Elution of Clq, Clr and Cls from Human CT Bound to Immune Aggregates. Use in the Rapid Purification of Cl Sub-components. *Mol. Immunol.* 16, 445–450. doi:10.1016/0161-5890(79)90069-5

Arnold, J. N., Wormald, M. R., Suter, D. M., Radcliffe, C. M., Harvey, D. J., Dwek, R. A., et al. (2005). Human Serum IgM Glycosylation. *J. Biol. Chem.* 280, 29080–29087. doi:10.1074/jbc.M504528200

Azuma, Y., Ishikawa, Y., Kawai, S., Tsunenari, T., Tsunoda, H., Igawa, T., et al. (2007). Recombinant Human Hexamer-Dominant IgM Monoclonal Antibody to Ganglioside GM3 for Treatment of Melanoma. *Clin. Cancer Res.* 13, 2745–2750. doi:10.1158/1078-0432.CCR-06-2919

Bally, I., Inforzato, A., Dalonneau, F., Stravalaci, M., Bottazzi, B., Gaboriaud, C., et al. (2019). Interaction of C1q with Pentraxin 3 and IgM Revisited: Mutational Studies with Recombinant C1q Variants. *Front. Immunol.* 10, 461. doi:10.3389/fimmu.2019.00461

Brautigam, C. A. (2015). Calculations and Publication-Quality Illustrations for Analytical Ultracentrifugation Data. *Methods Enzymol.* 562, 109–133. doi:10.1016/bs.mie.2015.05.001

Calarese, D. A., Scanlan, C. N., Zwick, M. B., Deechongkit, S., Mimura, Y., Kunert, R., et al. (2003). Antibody Domain Exchange Is an Immunological Solution to Carbohydrate Cluster Recognition. *Science* 300, 2065–2071. doi:10.1126/science.1083182

Cedzyński, M., Thielens, N. M., Mollnes, T. E., and Vorup-Jensen, T. (2019). Editorial: The Role of Complement in Health and Disease. *Front. Immunol.* 10, 1869. doi:10.3389/fimmu.2019.01869

Chromikova, V., Mader, A., Hofbauer, S., Göbl, C., Madl, T., Gach, J. S., et al. (2015a). Introduction of Germline Residues Improves the Stability of Anti-HIV mAb 2G12-IgM. *Biochimica Biophysica Acta (BBA) - Proteins Proteomics* 1854, 1536–1544. doi:10.1016/j.bbapap.2015.02.018

Chromikova, V., Mader, A., Steinfellner, W., and Kunert, R. (2015b). Evaluating the Bottlenecks of Recombinant IgM Production in Mammalian Cells. *Cytotechnology* 67, 343–356. doi:10.1007/s10616-014-9693-4

Collins, C., Tsui, F. W. L., and Shulman, M. J. (2002). Differential Activation of Human and guinea Pig Complement by Pentameric and Hexameric IgM. *Eur.*

J. Immunol. 32, 1802–1810. doi:10.1002/1521-4141(200206)32:6<1802::AID-IMMU1802>3.0.CO;2-C

Diebolder, C. A., Beurskens, F. J., de Jong, R. N., Koning, R. I., Strumane, K., Lindorfer, M. A., et al. (2014). Complement Is Activated by IgG Hexamers Assembled at the Cell Surface. *Science* 343, 1260–1263. doi:10.1126/science.1248943

Doores, K. J., Fulton, Z., Huber, M., Wilson, I. A., and Burton, D. R. (2010). Antibody 2G12 Recognizes Di-mannose Equivalently in Domain- and Nondomain-Exchanged Forms but Only Binds the HIV-1 Glycan Shield if Domain Exchanged. *J. Virol.* 84, 10690–10699. doi:10.1128/JVI.01110-10

Duncan, A. R., and Winter, G. (1988). The Binding Site for C1q on IgG. *Nature* 332, 738–740. doi:10.1038/332738a0

Eskeland, T., and Christensen, T. B. (1975). IgM Molecules with and without J Chain in Serum and after Purification, Studied by Ultra-centrifugation, Electrophoresis, and Electron Microscopy. *Scand. J. Immunol.* 4, 217–228. doi:10.1111/j.1365-3083.1975.tb02620.x

Gasteiger, E., Hoogland, C., Gattiker, A., Duvaud, S. e., Wilkins, M. R., Appel, R. D., et al. (2005). "Protein Identification and Analysis Tools on the ExPASy Server," in The Proteomics Protocols Handbook *Springer Protocols Handbooks*. Editor J. M. Walker (Totowa, NJ: Humana Press), 571–607. doi:10.1385/1-59259-890-0:571

Gauglitz, G. (2020). Critical Assessment of Relevant Methods in the Field of Biosensors with Direct Optical Detection Based on Fibers and Waveguides Using Plasmonic, Resonance, and Interference Effects. *Anal. Bioanal. Chem.* 412, 3317–3349. doi:10.1007/s00216-020-02581-0

Gilmour, J. E. M., Pittman, S., Nesbitt, R., and Scott, M. L. (2008). Effect of the Presence or Absence of J Chain on Expression of Recombinant Anti-kell Immunoglobulin M. *Transfus. Med.* 18, 167–174. doi:10.1111/j.1365-3148.2008.00853.x

Gong, S., and Ruprecht, R. M. (2020). Immunoglobulin M: An Ancient Antiviral Weapon - Rediscovered. *Front. Immunol.* 11, 1943. doi:10.3389/fimmu.2020.01943

Graille, M., Stura, E. A., Housden, N. G., Beckingham, J. A., Bottomley, S. P., Beale, D., et al. (2001). Complex between Peptostreptococcus Magnus Protein L and a Human Antibody Reveals Structural Convergence in the Interaction Modes of Fab Binding Proteins. *Structure* 9, 679–687. doi:10.1016/S0969-2126(01)00630-X

Hänel, C., and Gauglitz, G. (2002). Comparison of Reflectometric Interference Spectroscopy with Other Instruments for Label-free Optical Detection. *Anal. Bioanal. Chem.* 372, 91–100. doi:10.1007/s00216-001-1197-3

Harboe, M., Thorgersen, E. B., and Mollnes, T. E. (2011). Advances in Assay of Complement Function and Activation. *Adv. Drug Deliv. Rev.* 63, 976–987. doi:10.1016/j.addr.2011.05.010

Hennicke, J., Lastin, A. M., Reinhart, D., Grünwald-Gruber, C., Altmann, F., and Kunert, R. (2017). Glycan Profile of CHO Derived IgM Purified by Highly Efficient Single Step Affinity Chromatography. *Anal. Biochem.* 539, 162–166. doi:10.1016/j.ab.2017.10.020

Hennicke, J., Reinhart, D., Altmann, F., and Kunert, R. (2019). Impact of Temperature and pH on Recombinant Human IgM Quality Attributes and Productivity. *New Biotechnol.* 50, 20–26. doi:10.1016/j.nbt.2019.01.001

Hennicke, J., Schwaigerlehner, L., Grünwald-Gruber, C., Bally, I., Ling, W. L., Thielens, N., et al. (2020). Transient Pentameric IgM Fulfill Biological Function-Effect of Expression Host and Transfection on IgM Properties. *PLOS ONE* 15, e0229992. doi:10.1371/journal.pone.0229992

Hiramoto, E., Tsutsumi, A., Suzuki, R., Matsuoka, S., Arai, S., Kikkawa, M., et al. (2018). The IgM Pentamer Is an Asymmetric Pentagon with an Open Groove that Binds the AIM Protein. *Sci. Adv.* 4, eaau1199. doi:10.1126/sciadv.aau1199

Idusogie, E. E., Presta, L. G., Gazzano-Santoro, H., Totpal, K., Wong, P. Y., Ultsch, M., et al. (2000). Mapping of the C1q Binding Site on Rituxan, a Chimeric Antibody with a Human IgG1 Fc. *J. Immunol.* 164, 4178–4184. doi:10.4049/jimmunol.164.8.4178

Jones, K., Savulescu, A. F., Brombacher, F., and Hadebe, S. (2020). Immunoglobulin M in Health and Diseases: How Far Have We Come and what Next? *Front. Immunol.* 11. doi:10.3389/fimmu.2020.595535

Jovic, M., and Cymer, F. (2019). Qualification of a Surface Plasmon Resonance Assay to Determine Binding of IgG-type Antibodies to Complement Component C1q. *Biologicals* 61, 76–79. doi:10.1016/j.biologicals.2019.08.004

Keyt, B. A., Baliga, R., Sinclair, A. M., Carroll, S. F., and Peterson, M. S. (2020). Structure, Function, and Therapeutic Use of IgM Antibodies. *Antibodies* 9, 53. doi:10.3390/antib9040053

Kishore, U., and Reid, K. B. M. (2000). C1q: Structure, Function, and Receptors. *Immunopharmacology* 49, 159–170. doi:10.1016/S0162-3109(00)80301-X

Kumar, N., Arthur, C. P., Ciferri, C., and Matsumoto, M. L. (2021). Structure of the Human Secretory Immunoglobulin M Core. *Structure* 29 (6), 564–571. doi:10.1016/j.str.2021.01.002

Le Roy, A., Nury, H., Wiseman, B., Sarwan, J., Jault, J.-M., and Ebel, C. (2013). "Sedimentation Velocity Analytical Ultracentrifugation in Hydrogenated and Deuterated Solvents for the Characterization of Membrane Proteins," in Membrane Biogenesis: Methods And Protocols *Methods in Molecular Biology*. Editors D. Rapaport and J. M. Herrmann (Totowa, NJ: Humana Press), 219–251. doi:10.1007/978-1-62703-487-6_15

Le Roy, A., Wang, K., Schaack, B., Schuck, P., Breyton, C., and Ebel, C. (2015). "AUC and Small-Angle Scattering for Membrane Proteins," in Methods In Enzymology *Analytical Ultracentrifugation*. Editor J. L. Cole (Academic Press), 257–286. doi:10.1016/bs.mie.2015.06.010

Li, Y., Wang, G., Li, N., Wang, Y., Zhu, Q., Chu, H., et al. (2020). Structural Insights into Immunoglobulin M. *Science* 367, 1014–1017. doi:10.1126/science.aaz5425

Mader, A., Chromikova, V., and Kunert, R. (2013). Recombinant IgM Expression in Mammalian Cells: A Target Protein Challenging Biotechnological Production. *Abb* 04, 38–43. doi:10.4236/abb.2013.44A006

Moore, G. L., Chen, H., Karki, S., and Lazar, A. G. (2010). Engineered Fc Variant Antibodies with Enhanced Ability to Recruit Complement and Mediate Effector Functions. *mAbs* 2, 181–189. doi:10.4161/mabs.2.2.11158

Patel, R., Neill, A., Liu, H., and Andrien, B. (2015). IgG Subclass Specificity to C1q Determined by Surface Plasmon Resonance Using Protein L Capture Technique. *Anal. Biochem.* 479, 15–17. doi:10.1016/j.ab.2015.03.012

Randall, T. D., King, L. B., and Corley, R. B. (1990). The Biological Effects of IgM Hexamer Formation. *Eur. J. Immunol.* 20, 1971–1979. doi:10.1002/eji.1830200915

Randall, T. D., Parkhouse, R. M., and Corley, R. B. (1992). J Chain Synthesis and Secretion of Hexameric IgM Is Differentially Regulated by Lipopolysaccharide and Interleukin 5. *Proc. Natl. Acad. Sci. U. S. A.* 89, 962–966. doi:10.1073/pnas.89.3.962

Ricklin, D., Hajishengallis, G., Yang, K., and Lambris, J. D. (2010). Complement - a Key System for Immune Surveillance and Homeostasis. *Nat. Immunol.* 11, 785–797. doi:10.1038/ni.1923

Salvay, A. G., Santamaria, M., le Maire, M., and Ebel, C. (2008). Analytical Ultracentrifugation Sedimentation Velocity for the Characterization of Detergent-Solubilized Membrane Proteins Ca++-ATPase and ExbB. *J. Biol. Phys.* 33, 399. doi:10.1007/s10867-008-9058-3

Schuck, P. (2000). Size-Distribution Analysis of Macromolecules by Sedimentation Velocity Ultracentrifugation and Lamm Equation Modeling. *Biophys. J.* 78, 1606–1619. doi:10.1016/S0006-3495(00)76713-0

Sharp, T. H., Boyle, A. L., Diebolder, C. A., Kros, A., Koster, A. J., and Gros, P. (2019). Insights into IgM-Mediated Complement Activation Based on *In Situ* Structures of IgM-C1-C4b. *Proc. Natl. Acad. Sci.* 116 (24), 11900–11905. doi:10.1073/pnas.1901841116

Sonn-Segev, A., Belacic, K., Bodrug, T., Young, G., VanderLinden, R. T., Schulman, B. A., et al. (2020). Quantifying the Heterogeneity of Macromolecular Machines by Mass Photometry. *Nat. Commun.* 11, 1772. doi:10.1038/s41467-020-15642-w

Sultana, A., and Lee, J. E. (2015). Measuring Protein-Protein and Protein-Nucleic Acid Interactions by Biolayer Interferometry. *Curr. Protoc. Protein Sci.* 79, 19.25.1–19.25.26. doi:10.1002/0471140864.ps1925s79

Ugurlar, D., Howes, S. C., de Kreuk, B.-J., Koning, R. I., de Jong, R. N., Beurskens, F. J., et al. (2018). Structures of C1-IgG1 Provide Insights into How Danger Pattern Recognition Activates Complement. *Science* 359, 794–797. doi:10.1126/science.aao4988

Vorauer-Uhl, K., Wallner, J., Lhota, G., Katinger, H., and Kunert, R. (2010). IgM Characterization Directly Performed in Crude Culture Supernatants by a New

Simple Electrophoretic Method. *J. Immunol. Methods* 359, 21–27. doi:10.1016/j.jim.2010.05.003

Wiersma, E. J., Collins, C., Fazel, S., and Shulman, M. J. (1998). Structural and Functional Analysis of J Chain-Deficient IgM. *J. Immunol.* 160, 5979–5989.

Wolbank, S., Kunert, R., Stiegler, G., and Katinger, H. (2003). Characterization of Human Class-Switched Polymeric (Immunoglobulin M [IgM] and IgA) Anti-human Immunodeficiency Virus Type 1 Antibodies 2F5 and 2G12. *J. Virol.* 77, 4095–4103. doi:10.1128/JVI.77.7.4095-4103.2003

Zhao, H., Ghirlando, R., Alfonso, C., Arisaka, F., Attali, I., Bain, D. L., et al. (2015). A Multilaboratory Comparison of Calibration Accuracy and the Performance of External References in Analytical Ultracentrifugation. *PLoS ONE* 10, e0126420. doi:10.1371/journal.pone.0126420

Zhou, W., Lin, S., Chen, R., Liu, J., and Li, Y. (2018). Characterization of Antibody-C1q Interactions by Biolayer Interferometry. *Anal. Biochem.* 549, 143–148. doi:10.1016/j.ab.2018.03.022

Zwirner, J., Wittig, A., Kremmer, E., and Götze, O. (1998). A Novel ELISA for the Evaluation of the Classical Pathway of Complement. *J. Immunol. Methods* 211, 183–190. doi:10.1016/S0022-1759(97)00205-6

Conflict of Interest: The authors declare that the research was conducted in the absence of any commercial or financial relationships that could be construed as a potential conflict of interest.

Publisher's Note: All claims expressed in this article are solely those of the authors and do not necessarily represent those of their affiliated organizations, or those of the publisher, the editors, and the reviewers. Any product that may be evaluated in this article, or claim that may be made by its manufacturer, is not guaranteed or endorsed by the publisher.

Advantages of publishing in Frontiers

OPEN ACCESS
Articles are free to read for greatest visibility and readership

FAST PUBLICATION
Around 90 days from submission to decision

HIGH QUALITY PEER-REVIEW
Rigorous, collaborative, and constructive peer-review

TRANSPARENT PEER-REVIEW
Editors and reviewers acknowledged by name on published articles

Frontiers
Avenue du Tribunal-Fédéral 34
1005 Lausanne | Switzerland

Visit us: www.frontiersin.org
Contact us: frontiersin.org/about/contact

REPRODUCIBILITY OF RESEARCH
Support open data and methods to enhance research reproducibility

DIGITAL PUBLISHING
Articles designed for optimal readership across devices

FOLLOW US
@frontiersin

IMPACT METRICS
Advanced article metrics track visibility across digital media

EXTENSIVE PROMOTION
Marketing and promotion of impactful research

LOOP RESEARCH NETWORK
Our network increases your article's readership